Ultra-Small Magnetic Field Effects of Organic Light-Emitting Diodes Based on Tris(8-hydroxyquinoline)aluminium

Zhichao Weng

Submitted in partial fulfillment
of the requirements of the Degree of
Doctor of Philosophy

28 August 2019

School of Physics and Astronomy
Queen Mary, University of London

Queen Mary
University of London

Statement of originality

I, Zhichao Weng, confirm that the research included within this thesis is my own work or that where it has been carried out in collaboration with, or supported by others, that this is duly acknowledged below and my contribution indicated. Previously published material is also acknowledged below.

I attest that I have exercised reasonable care to ensure that the work is original, and does not to the best of my knowledge break any UK law, infringe any third party's copyright or other Intellectual Property Right, or contain any confidential material.

I accept that the College has the right to use plagiarism detection software to check the electronic version of the thesis.

I confirm that this thesis has not been previously submitted for the award of a degree by this or any other university.

.....

Zhichao Weng

28 August 2019

Parts of chapter 3 have been previously published (Zhichao Weng, William P. Gillin and Theo Kreouzis. *Scientific Reports*, **9:3439**, 1–7, (2019)).

Abstract

Magnetic field effects (namely, magnetoconductance (MC) and magnetoelectroluminescence (MEL)) in organic devices have been extensively studied in the last two decades and several theories and models have been developed to explain these interesting phenomena. In experiments the MC and MEL results are dependent on device drive conditions, materials, structures, etc. and different results can be attributed to different mechanisms under different conditions. Specifically, for Ultra-Small Magnetic Field Effects (USMFE) in organic devices, one of the most popular models is the Polaron Pair Model (PP model) which has been investigated for a decade. It is based on the effect of an external magnetic field on the singlet-triplet polaron pair interconversion and changes in ultimate singlet and triplet yields. However, in most of the Polaron Pair Model related literature, the quantitative connection between the model simulations and the experimentally obtained data (MC and MEL) is not directly made despite the polaron pair model successfully generating the USMFE MC (and MEL) typical functional forms ("W" shape).

In this work, prototype fitting of the Polaron Pair model to experimentally obtained MC (and MEL) has been carried out yielding fitting parameters, in particular, the relevant local hyperfine field B_{hf} experienced by one or more polarons in tris-(8-hydroxyquinoline)aluminium (Alq_3). Hyperfine field values are physically significant, and can be compared to experiments and calculations from the literature. The single-proton and two-proton Polaron Pair models are applied to the high resolution (μT), high sensitivity ($\sim 10^{-6}$) and high reproducibility experimentally obtained MC (and MEL) data by fitting the model to obtain different physical parameters. In particular, hyperfine field(s) obtained are: B_{hf}=(0.34$\pm$0.04)mT using the single-proton PP model and B_{hf1}=(0.63$\pm$0.01)mT, B_{hf2}=(0.24$\pm$0.01)mT using the two-proton PP model with high reproducibility across devices and independent of drive current. These values are in accord with local hyperfine fields associated with the HOMO and LUMO probability densities in the Alq_3 molecule where the electron polaron is experiencing a larger local hyperfine field while the hole polaron experiences a smaller hyperfine field. Additionally, in the single-proton PP model, a weight factor δ_{TS} is used to

describe the relative contribution of triplets and singlets to MC and the fitting yields a δ_{TS} smaller than 1, meaning singlets contribute more to the MC than triplets. However, in the developed two-proton PP model, the weight factor δ_{TS} is replaced with more explicit decay rates for dissociation and recombination of singlet and triplet PP with slightly higher dissociation rate for singlet ($\sim$44.59MHz) than triplet ($\sim$43.97MHz), and the higher dissociation rate means higher contribution to the MC, which agrees with the yielded weight factor δ_{TS} smaller than 1 from the single proton PP model. In particular, all the yielded parameters are obtained through a global fitting between the two-proton PP model and the experimentally obtained MC and MEL. Additionally, under constant current mode, the measured MC and MEL display different functional shapes instead of the same "W" shapes under constant voltage mode reported from literature. This indicates two different path ways for polaron pairs to decay with different rates. The magnitude of MEL is 100 times larger than MC, indicating that recombination process between polaron pair dominates in the whole PP dynamics, and this is also in accord with the much larger yielded singlet PP recombination rate ($\sim$87.97MHz) than the dissociation rate ($\sim$43.97MHz for triplet PP and $\sim$44.59MHz for singlet PP).

The work presented not only helps to better understand the microscopic mechanisms operating within organic devices under weak external magnetic fields, but can also function as a probe to measure the local hyperfine environments for electron and hole polarons in organic semiconductors through the macroscopic electrical and optical measurement of a working device.

Acknowledgements

First and foremost, I am grateful to both of my supervisors – Dr. Theo Kreouzis and Prof. William Gillin. My primary supervisor, Dr. Theo Kreouzis, has helped me all the way through my PhD journey. Much gratitude goes to his patience and kindness for helping me tackle different problems in the project. My researches and learning skills would have been impossible without the kind support of his. Specifically, I am very grateful for his patience and time for constantly proofreading my manuscript draft and this thesis in my final year. My secondary supervisor, Prof. William Gillin, has offered me many professional guidance and advices upon my project in my works, without whose help I would not possibly have the achievements that I got at the moment. I am also grateful for every inspiration he gave to me about the proper attitude towards scientific researches, motivating me to move forward even when there were many obstacles ahead. Once again, I am profoundly grateful and happy for their presence alongside my PhD journey for better helping me shape into a proper scientist with all the useful and professional skills.

I am also grateful to Dr. Ken Scott and Mr. Geoff Gannaway. Much gratitude goes to their kind help in the lab, without whose help I could not also win the achievements that I got at the moment. Dr. Ken Scott had always been kind in helping me build up experiment systems and offered me some practical suggestions on the experiments. Mr. Geoff Gannaway helped me a lot in the cleanroom and workshop, and many of my experiments would have been impossible without his help. Special gratitude goes to both of them.

Meanwhile, I am very thankful for the financial support from China Scholarship Council (CSC).

Additionally, I feel blessed that I am always surrounded by many kind people during my four year of PhD researches. I would like to thank all of my dearest friends both in the UK and back in my home country, China. PhD work can be tough sometimes, but I am really thankful to all of my friends who are always there backing up for me, motivating me to look on the bright side and keep moving forward. Cheers to the great friendship!

Lastly, my gratitude always goes to my dearest parents, who are always my spiritual support and guidance. I am very grateful to my parents for raising me to be a strong, independent, and kind man. They taught me how to stand for what I believe in and to be brave to chase what I dream for. Nothing would have been possible for me if without their love and support. I cannot express my gratefulness enough to both of my parents.

Publications

1. Zhichao Weng, William P. Gillin and Theo Kreouzis. Modelling and fitting the Polaron Pair Magnetoconductance model to obtain a realistic local hyperfine field in Tris-(8-hydroxyquinoline)aluminium based diodes. *Sci. Rep.*, **9**. 1-7. (2019).

2. Zhichao Weng, William P. Gillin and Theo Kreouzis. Direct probe of dynamics and local environments of spin pair in small-molecule devices. (*in preparation*)

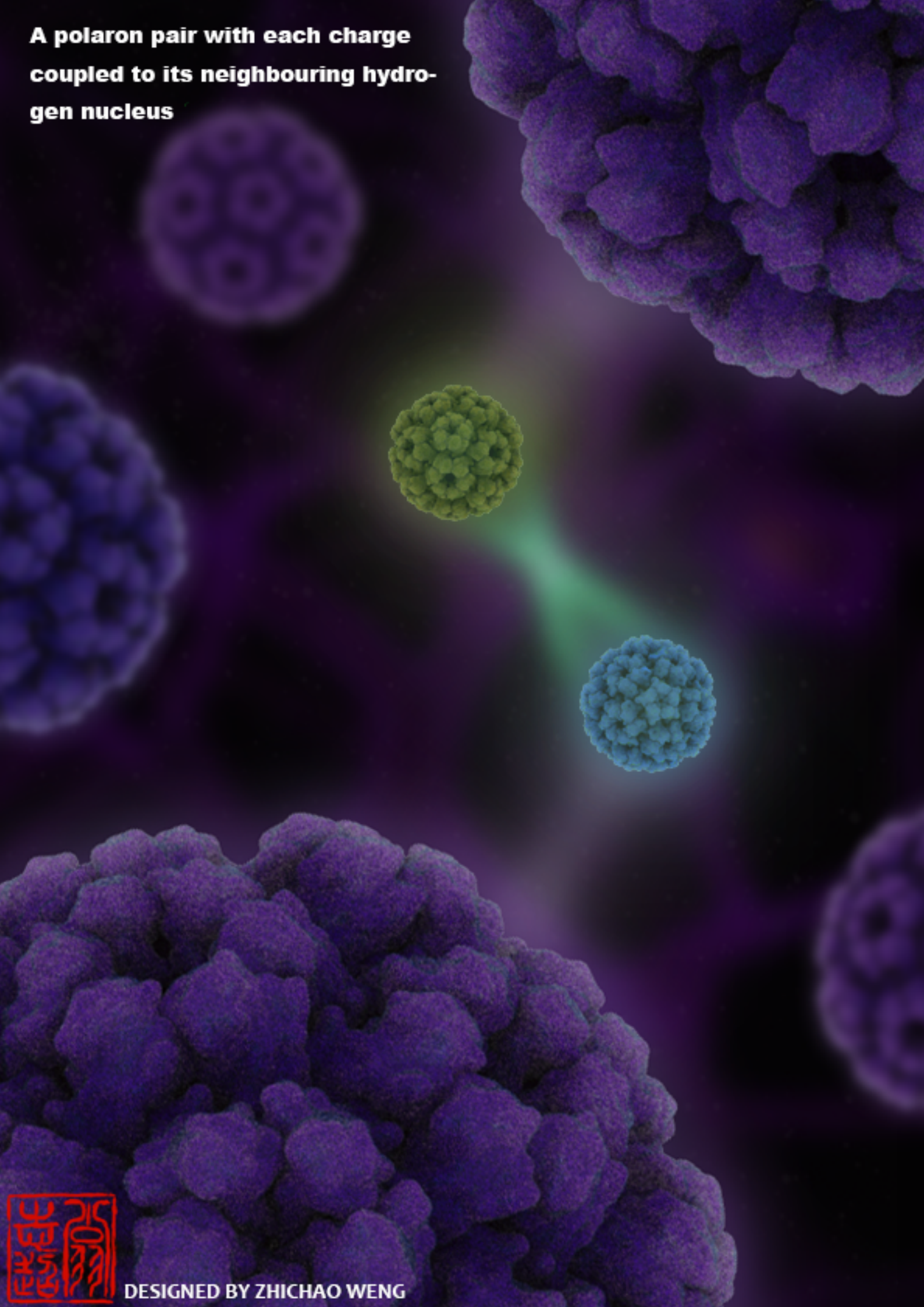
A polaron pair with each charge coupled to its neighbouring hydrogen nucleus
DESIGNED BY ZHICHAO WENG

To My Dearest Parents.

致我敬爱的父母。

Contents

List of Figures

List of Tables

Chapter 1

Introduction

1.1 Organic Molecules and Organic Semiconductors

An organic compound, as defined in chemistry, is generally the chemical compound that contains carbon atom (except for the few carbon containing compounds that are classified as inorganic compounds, such as carbides, carbonates and cyanides, etc). Normally, an organic molecule consists of carbon, hydrogen, oxygen, nitrogen, and other atoms.

Organic compounds can be categorised in 3 ways: small molecule, polymer and biomolecule.

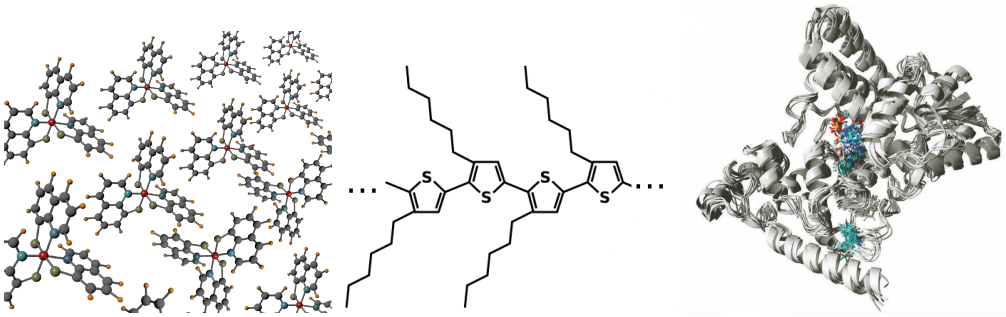

(a) (b) (c)

Figure 1.1: Three categories of molecular compounds (a) Small Molecule: Tris-(8-hydroxyquinoline)aluminium (or Alq_3) (b) Polymer: Poly(3-hexylthiophene) (or P3HT) (c) Biomolecule. (Adapted from Ref. [1])

A small molecule is defined as a molecule whose molecular weight is between 50 to 1500 Daltons [2]. Molecular weight is measured as molecular mass relative

to ^{12}C. For example, the molecular weight of water H_2O is H (1.008 Daltons) + H (1.008 Daltons) + O (15.9994 Daltons) = 18.01 Daltons. In contrast to small molecules, polymers have large molecular weights, and are also called macromolecules. Polymers take the form of repetitions of many monomers, which is the repeating unit of the polymer. The more complex biomolecules refer to the organic molecules existing specifically in biological processes like photosynthesis in plants, biomagnetoreceptions in avian systems, etc. Proteins are some of the most important biomolecules to all organisms.

Organic semiconductors differentiate themselves from other organic molecules by their specific conjugated structures based on the hybridisation of different atomic orbitals (wave functions).

In order to describe the wave-like behaviour of electrons in atoms, specific wave functions (also called atomic orbital) are used and to calculate the probability of finding an electron at certain location near the nucleus. There are three characteristic parameters in describing the wave function: the magnetic quantum number m_l, principal quantum number of the electron n and orbital angular momentum l. Different values of the quantum numbers yield different shaped atomic orbitals with different energies. For example, different values of the angular momentum l = 0, 1, 2 and 3 correspond to different atomic orbitals called s (for "sharp), p (for "principal), d (for "diffuse") and f (for "fundamental"). Additionally, the number of m_l states in each group of atomic orbitals is given by $(2l + 1)$ and with different values of magnetic quantum numbers m_l correspond to different states. Figure 1.2 shows some examples of angular distributions of the atomic orbitals of the modulus squared of the wave function.

Molecules are formed by the bonding of atoms and can also be described similarly by mathematical functions called molecular orbitals. In 1929, Sir John Lennard-Jones introduced the idea of molecular orbitals, using a Linear Combination of Atomic Orbitals. As the name suggests, the molecular orbital is a function composed of the linear combination of the atomic orbitals or wave functions. For example, if there are two individual atoms with atomic orbitals A and B and their own wavefunctions ψ_A

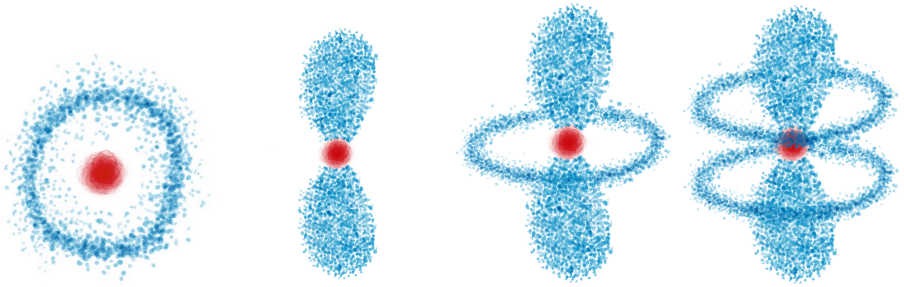

(a) Orbital s. $m = 0$, $l = 0$ (b) Orbital p. $m = 0$, $l = 1$ (c) Orbital d. $m = 0$, $l = 2$ (d) Orbital f. $m = 0$, $l = 3$

Figure 1.2: Examples of some atomic orbitals

and ψ_B. The two atoms can bond together to form a molecule C with a new molecular orbital of wave function ψ_C. Because the molecular orbital is a linear combination of atomic orbitals, we can always write the new wave function ψ_C in the form shown in equation 1.1.

$$\begin{aligned} \psi_C &= a\psi_A + b\psi_B \\ {}^*\psi_C &= b\psi_A - a\psi_B \end{aligned} \tag{1.1}$$

where a and b are just constants defining the linear combinations. In wave function 1.1, ψ_C and ${}^*\psi_C$ can correspond to a bonding orbital and anti-bonding orbital, respectively. Electrons can be confined in the bonding orbital which makes the molecule more stable, whereas electrons in the anti-bonding orbital occupy higher energy states, which can destabilise the molecule. In general, the bonding orbital has lower energy and the anti-bonding orbital has the higher energy, and electrons tend to fill in the lower energy site first. A schematic is shown in Figure 1.3

Carbon is the most important element composing any organic compounds, and its electron configuration is $1s^2 2s^2 2p^2$. The number before the orbital represents the energy level of the electron (n). The lower this number is, the lower the energy of this electron. The superscript following each orbital name represents the number of electrons at this orbital. Each orbital has a maximum electron capacity of 2. According to Pauli Exclusion Principle, no identical fermions can exist simultaneously in the same orbital. So in this specific case, only two electrons with different spin quantum numbers m_s (1/2 and -1/2 for two electrons respectively) can exist in the same orbital.

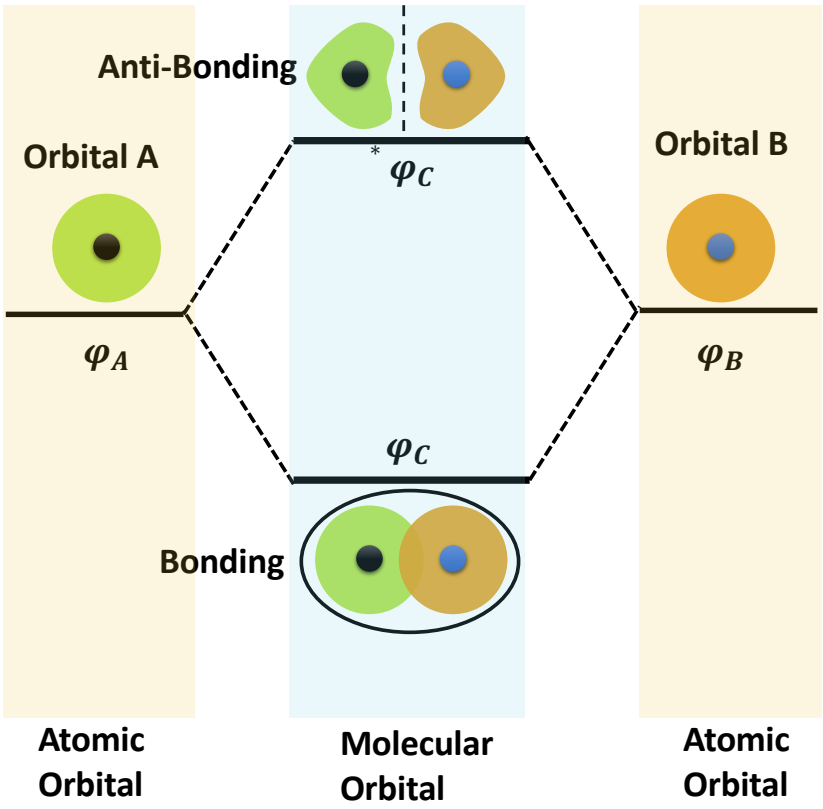

Figure 1.3: Molecular Orbital

According to the carbon electron configuration, it is suggested that the 1*s* and 2*s* orbitals are filled with electrons, leaving the remaining two electrons distributed in the 2*p* states.

Generally, there are three types of bonding between carbon atoms depending on the form of the molecule.

In Figure 1.4a, the process of *sp* hybridisation is shown. 1*s* and 2*s* are filled with two electrons and one of the electrons in the 2*s* is "promoted" to the empty p_z orbital. The remaining single 2*s* electron hybridises with one 2*p* electron by the linear combination of the wave functions forming a hybridised orbital wave function – *sp* orbital whose energy is between the 2*s* and 2*p* states, leaving two remaining 2*p* orbitals in orthogonal directions.

Something similar occurs in sp^2 and sp^3 hybridisation. For sp^2 hybridisation, after one 2*s* electron is "promoted" to the 2*p* orbital, the remaining single 2*s* electron is hybridised with two 2*p* electrons to form three hybridised sp^2 orbitals which are the

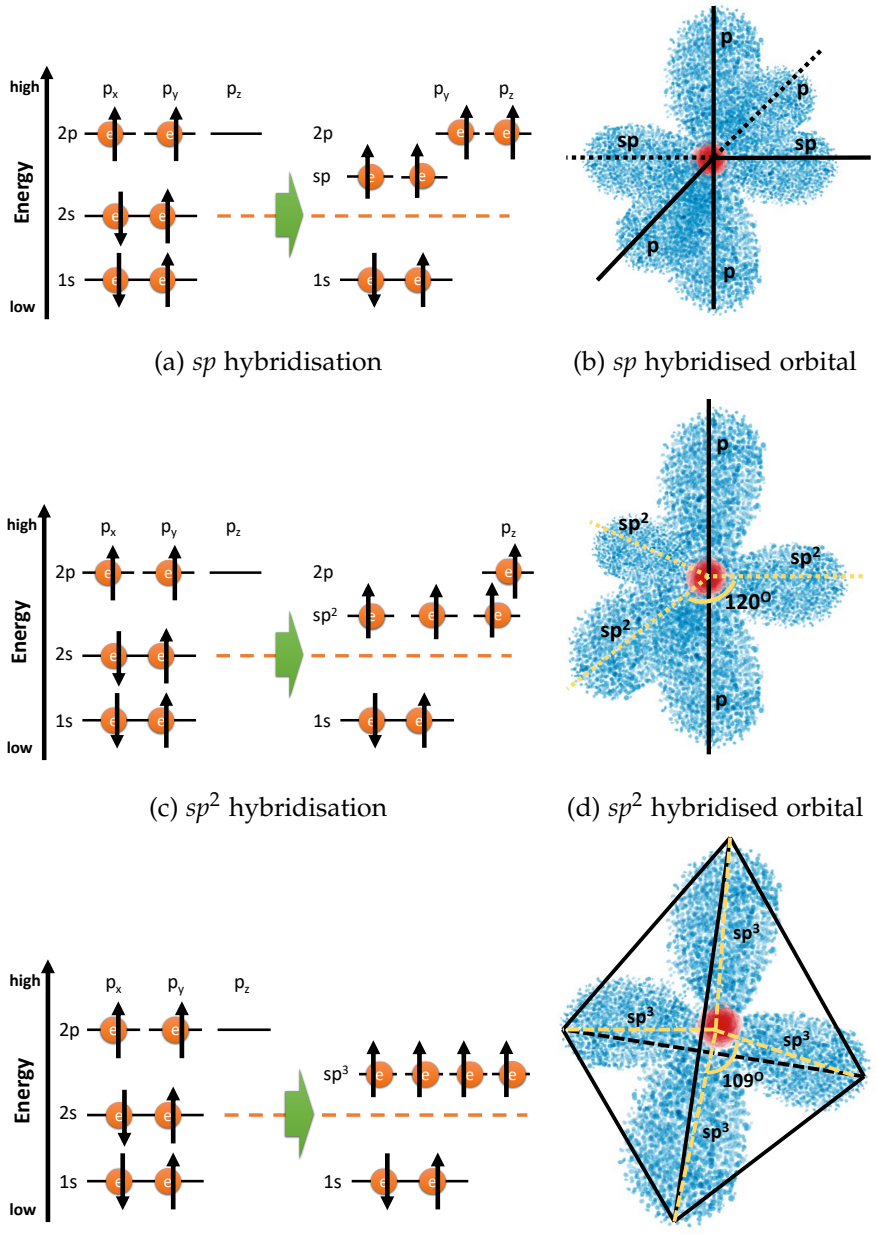

(a) *sp* hybridisation (b) *sp* hybridised orbital

(c) sp^2 hybridisation (d) sp^2 hybridised orbital

(e) sp^3 hybridisation (f) sp^3 hybridised orbital

Figure 1.4: The orbital hybridisations in carbon atom

results of the linear combinations of wave functions of one 2*s* and two 2*p* orbitals. The energy of the new hybridised sp^2 orbital is still between the energy of the 2*s* and the 2*p* orbitals. The three formed sp^2 orbitals are coplanar and separated by an angle of 120^o. Finally the remaining 2*p* electron doesn't participate in the hybridisation and this 2*p* orbital is perpendicular to the sp^2 orbital plane. In sp^3 hybridisation, after one 2*s* electron is "promoted" to the empty 2*p* orbital, the remaining single 2*s* electron is

hybridised with all $2p$ electrons to form four sp^3 hybridised orbitals separated by an angle of around 109^o in a tetrahedral structure.

When two carbon atoms form a bond together, for example, in a molecule of ethylene, the two carbon atoms bond by sharing one sp^2 hybridised orbital with each other and each will contribute one sp^2 electron in the bonding. This is called σ bond. The other two sp^2 hybridised orbitals in each atom will bond with hydrogen atoms. On the other hand, the two $2p$ orbitals of the carbon atoms are close enough to overlap with each other and form a π bond, which is perpendicular to the plane of the σ bonds and is the result of the overlap of the two p electronic wave functions. There are two ways of forming a π bond – either by p_z-p_z or p_y-p_y. The p_y-p_y bonding is the highest-energy stable configuration of ethylene. Above this energy level, there is an energy gap between the p_y-p_y bonding energy and a lowest-energy of the unstable configuration of ethylene – the lowest anti-bonding energy formed by either p_z-p_z or p_y-p_y. This energy gap between the frontier orbitals is the organic equivalent of a semiconductor band gap[3]. The orbital with the energy below this gap is the highest occupied molecular orbital (π bonding, also known as HOMO), and the orbital which lies above the energy gap is the lowest unoccupied molecular orbital ($\pi^\star$ anti-bonding, also known as LUMO). These states lay the foundation of the electrical properties in π-conjugated molecules.

There are two states for the molecule to be – neutral excited state and charged state. The neutral excited state, namely the Frenkel exciton, will be mentioned in the next section. The charged state can be formed by electrical injection of the molecule and it injects electrons into orbitals below the LUMO and holes into the orbitals above HOMO, and this yields the charges called negative or positive polarons, respectively. As there are excess electron or hole moving into the molecule, the energy levels of the molecule are rearranged to compensate for the cost of the addition of the electron or hole. This is shown in Figure 1.5 and the polaronic levels are between the energy levels of LUMO and HOMO and indicated as dashed lines.

Two common organic semiconductors are tris-(8-hydroxyquinoline)aluminium (or Alq_3) for electron transport and N,N′-Di(1-naphthyl)-N,N′-diphenyl-(1,1′-biphenyl)-

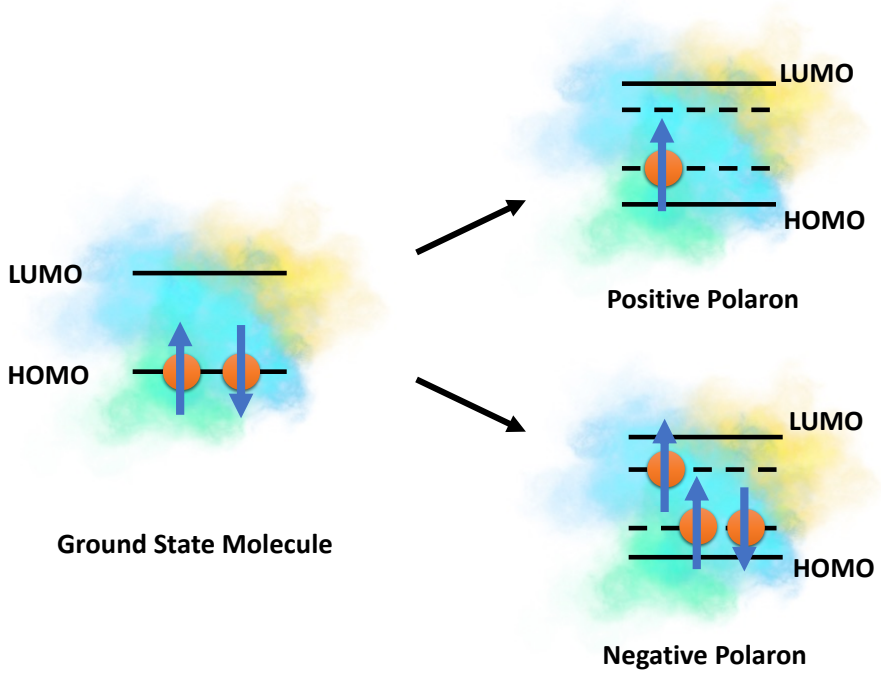

Figure 1.5: Formation of positive and negative polarons

4,4′-diamine (or NPB) for hole transport. The structures are shown in Figure 1.6

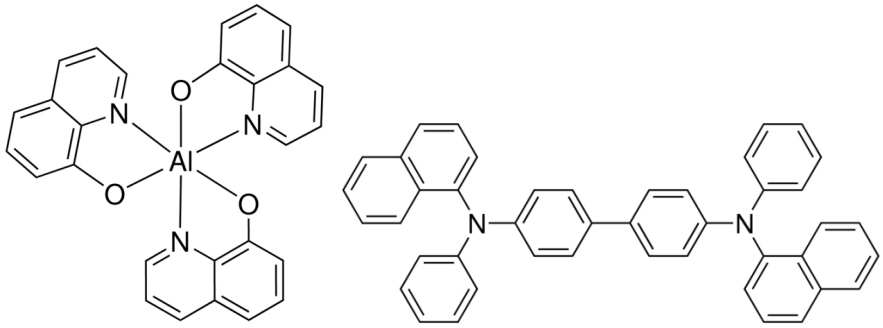

(a) Alq_3 (b) NPB

Figure 1.6: The common organic semiconductors: Alq_3 and NPB

These materials are used in device fabrication and form stable thin films, allowing in charge transport and resulting in high luminescent yields as well as being commercially available [4][5][6][7].

1.2 Organic Light-Emitting Diodes

In a two-organic-layer Organic Light-Emitting Diode, electrons are injected from the cathode and transported through the Electron Transport Layer (ETL), holes are injected from the anode and transported through the Hole Transport Layer (HTL). The two eventually meet and are bound tightly due to the strong Coulomb force between a positive and a negative charge. When an electron and hole are bound together, they tend to form a new state – excited state in the molecule and this bound charge pair is called an exciton.

There are three types of exciton in different molecular systems as shown in Figure 1.7

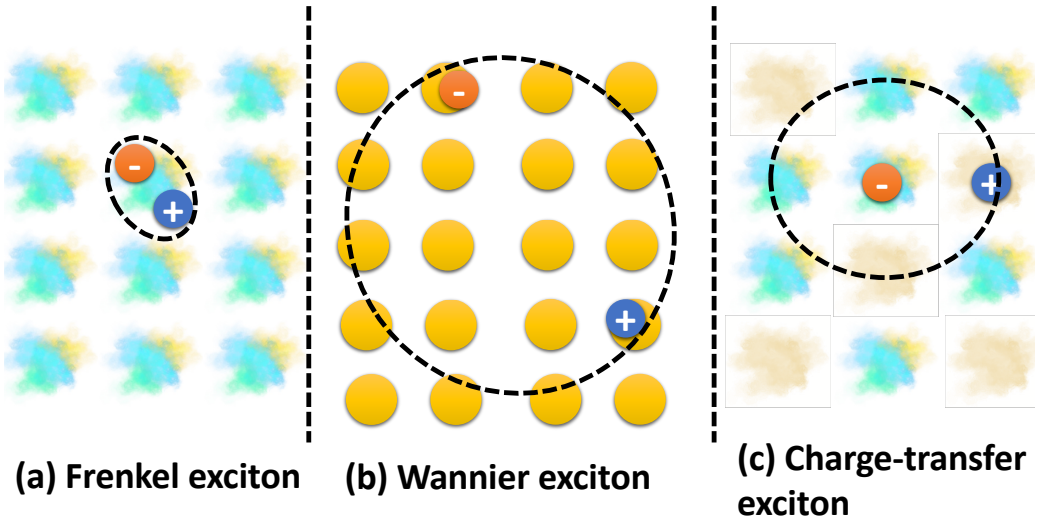

Figure 1.7: Three types of excitons

For Frenkel exciton, the distance between an electron and a hole is localised within the size of single molecule and this small distance makes the Frenkel exciton the tightest bound state, and this is also the usual situation for the excitons within a working organic light-emitting diode (OLED) [8]. For Wannier exciton, the inter chage distance is larger than that of Frenkel exciton and always exist in inorganic system such as Si or Ge, etc[8]. The third excitation state is termed Charge Transfer exciton and this state can exist in blended organic systems where multiple organic molecules coexist (type II heterojunction). Different molecules have different abilities to capture

electrons or holes, thus an electron-hole pair residing on different molecules has larger intercharge distance than the size of a single molecule.

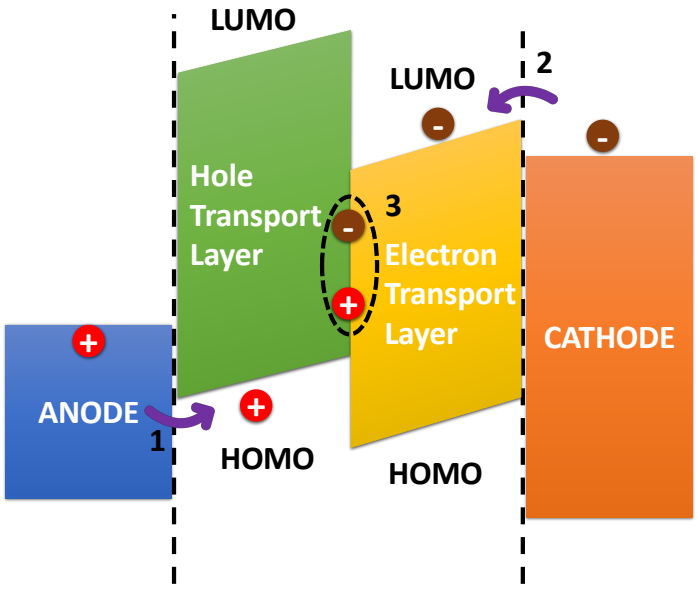

(a) OLED energy diagram

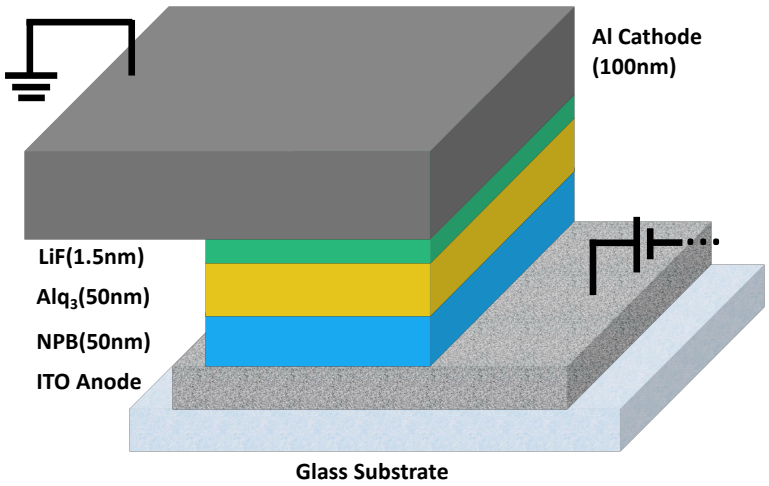

(b) OLED structure

Figure 1.8: OLED energy diagram and device strucure

Figure 1.8a shows the energy diagram of a simple structure OLED (bilayer OLED). The OLED consists of four parts, an anode, an active layer and a cathode. In the active layer, they are Electron Transport Layer (ETL) and Hole Transport Layer (HTL). As Figure 1.8a shows, there are three processes controlling the light emission in OLED. When the external bias is applied to the device, electrons from the cathode

and holes from the anode are injected into the LUMO and HOMO of the ETL and HTL, respectively. Then the electrons and holes are driven towards each other under the bias and, as the distance between the two charges becomes smaller, the Coulomb force between the two charges becomes larger, and they tend to be bound more tightly. When the two charges are close enough (the electron and hole are localised on the same molecule), they form a Frenkel exciton and subsequently, they can recombine radiatively to emit photons. At the interface of HTL:ETL (e.g. the Alq_3:NPB interface), an electron in Alq_3 is seeing a larger energy barrier to cross into NPB ($\sim$0.8eV) than an energy barrier a hole is facing when it is crossing from NPB to Alq_3 ($\sim$0.4eV) [9]. Thus, holes are easier to travel from NPB to Alq_3 than electrons crossing from the other way around. It means that holes are travelling faster into Alq_3 than electrons into NPB, and this results in that many holes encounter electrons in the Alq_3 layer, forming excitons and emission of photons.

1.3 Spins in Organic Light-Emitting Diodes

The electron is a fermion and has the spin angular momentum of $1/2$ with the "direction" of spin up $|\uparrow\rangle$ or spin down $|\downarrow\rangle$. These electrons could, for example, be in the HOMO or LUMO of a single excited neutral molecule, or in the HOMO or LUMO in a separate charged molecules.

$$\begin{aligned} |11\rangle &= \uparrow\uparrow, \\ |10\rangle &= \frac{1}{\sqrt{2}}(\uparrow\downarrow + \downarrow\uparrow), \\ |1-1\rangle &= \downarrow\downarrow, \\ |00\rangle &= \frac{1}{\sqrt{2}}(\uparrow\downarrow - \downarrow\uparrow), \end{aligned} \tag{1.2}$$

For two electrons there are 4 combinations of spins of these two spins as shown in equation 1.2. $|\mathbf{S}\ \mathbf{S}_z\rangle$ is shown in the equation 1.2 where $\mathbf{S}$ in the schematic means the total spin quantum number and $\mathbf{S}_z$ means the spin projection on the z axis. $\mathbf{S}$= 1 and 0 indicate the state of triplet and singlet states where different $\mathbf{S}_z$ in the triplet state correpond to different triplet states of $\mathbf{T}_{+1}$, $\mathbf{T}_0$ and $\mathbf{T}_{-1}$. The first three terms and the

last term in equation 1.2 correspond to the triplet and singlet states respectively and different spin configurations are also shown in Figure 1.9.

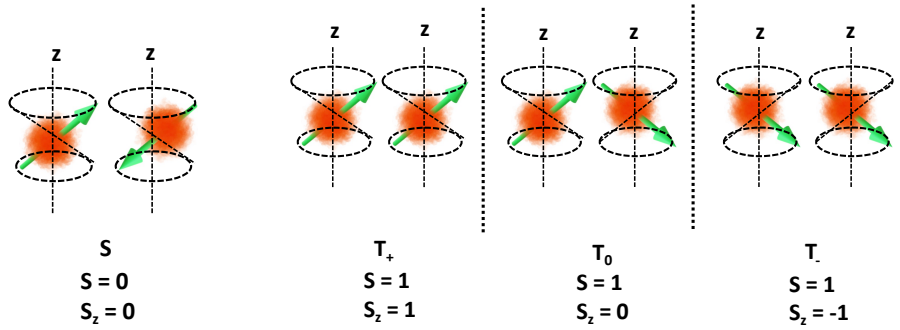

(a) singlet (b) triplet

Figure 1.9: Schematics of singlet and triplet

The singlet exciton has higher energy than the triplet due to the Pauli exclusion principle. The charges in triplet states are more separated due to their symmetric spin configurations and this longer separated inter-charge distance reduces the repulsion between charges, lowering the total energy of triplet state compared to that of a singlet state. A singlet has some probability of transforming into a lower energy triplet by spin flipping via the surrounding hyperfine field environment as shown in Figure 1.10

The Jablonski diagram in Figure 1.10 shows different transitions between different molecular energy states. A molecule can be excited and form an excited state (first singlet state or higher singlet state) by absorption of external photons. The excited molecule at higher energy state is not stable and will "de-excite" to a lower energy singlet state (i.e. $\mathbf{S}_1$ state) by **internal conversion IC** (①). Now the $\mathbf{S}_1$ state has two routes for the next energy transition, either through **intersystem crossing ISC** (②) or photon emission via fluorescence (③) back to the ground state. As the energy of $\mathbf{S}_1$ state is close to some higher energy state of the triplet, there is some probability that $\mathbf{S}_1$ will transit to the similar energy level of triplet state via, for example, the hyperfine interaction through ②. Similarly, the transitioned higher energy triplet state will undergo the same process of ① to reach a more stable and lower energy triplet state. As there are no photon emissions in processes of ① and ②, they are non-radiative

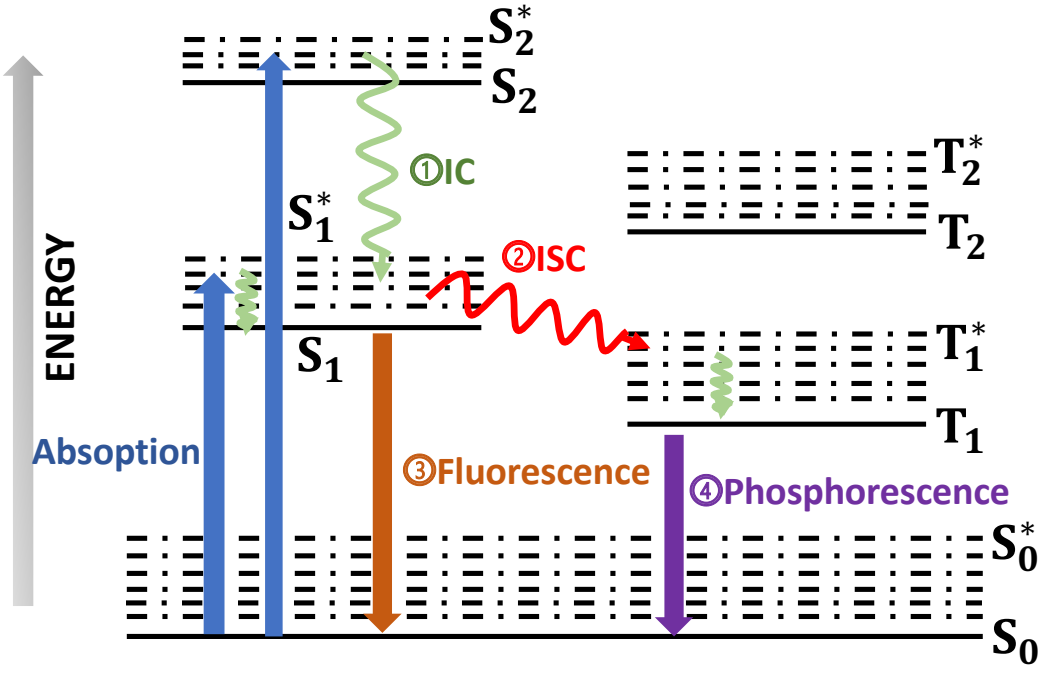

Figure 1.10: Jablonski Diagram. IC: Internal Conversion. ISC: Intersystem Crossing. $\mathbf{S}_0$: Ground State (Singlet). $\mathbf{S}_0^*$: Vibration Energy Level of Ground State. $\mathbf{S}_n$: n^{th} Singlet Excited State. $\mathbf{S}_n^*$: Vibrational Level of n^{th} Singlet Excited State. $\mathbf{T}_n$: n^{th} Triplet Excited State. $\mathbf{T}_n^*$: Vibrational Level of n^{th} Triplet Excited State.

energy transitions. However, as the triplet could not directly relax back to the ground state as this is spin forbidden, and extra spin flipping process is required for the triplet prior to relaxation back to the ground state. Compared to the direct relaxation from $\mathbf{S}_1$ to $\mathbf{S}_0$ (or fluorescence), this indirect emission process is termed phosphorescence (④). In general, photoluminescence (fluorescence and phosphorescence) is a radiative recombination process which occurs with the emission of photons. In contrast, there is another process called non-radiative recombination which occurs with the emission of phonons.

1.4 Magnetic Field Effects

Magnetic field effect in organic devices includes magnetoresistance (or magneto-conductance) and magnetoelectroluminescence, which means that the resistance (or electroluminescence) of the diode would change with external magnetic fields. There

are two categories of magnetic field effects in terms of the range of magnetic fields and they are large field effect: usually the magnetic field ranges from tens to hundreds of milliTesla and the small field effect (or ultra-small magnetic field effect) with the B field ranging even down to the scale of microTesla which is comparable or even smaller than the hyperfine field level of the organic molecule.

1.4.1 Large Field Effects

Conventional magnetic field effects in organic materials, or organic magnetoresistance (OMR), was initially brought to attention by the study of C. Taliani, et al[10] in 2002. They fabricated a new device called a spin valve to study spintronics initially. During the experiments, they found the phenomenon of spin injection and spin polarised transport in organic semiconductors. It was noticed that during the measurement of current-voltage characteristics of the spin valve device, a clear current rise was observed when an external magnetic field of 3.4 kOe (340mT) was applied, and this significant current change resulting from the application of a magnetic field (magnetoresistance) was around 30%. This initial report lead the research in organic magnetoresistance for the following decades. In the year 2003, Jan Kalinowski, et al.[11] carried out the first experiment of measuring the magnetoresistance and magnetoelectroluminescence on an Alq_3-based organic light-emitting diode. The drive voltage dependence of the positive magnetic field effect was found and a possible explanation was offered, namely, that this magnetic field effect might be due to the magnetic field dependent mixing between singlet and triplet electron-hole pairs resulting from the hyperfine interaction in the recombination process. In 2004, Z. H. Xiong, et al.[12] developed the research further in spin-valve devices with organic semiconductor spacers and a giant magnetoresistance effect, as large as 40% at low-temperature was reported. This indicated the potential for the research on OMR on organic devices, such as OLEDs. In the same year, Jan Kalinowski, et al.[13] carried out the research on magnetic field effects on the electrophosphorescence efficiency of organic devices and found an increase of 6% and 2% for tris(2-phenylpyridine) iridium [$Ir(ppy)_3$] and 2,3,7,8,12,13,17,18-octaethyl-21H,23H-porphine platinum (PtOEP) based

devices respectively when the external magnetic field increased up to 500mT. In the following year, a large amount of research on OMR was carried out. Ö.Mermer, et al. undertook some extensive studies on the OMR in Alq_3 based and polymer based devices, including the dependence on B field direction, voltage, temperature, film thickness and electrode materials of the OMR[14]. It was found that the OMR in OLED can be as large as 10% at fields of 10mT at room temperature[15]. Additionally, OMR measurements were possible on both π-conjugated polymers and small molecules based devices. Additionally, Ö.Mermer and co-workers carried out a comprehensive magnetoresistance study on a set of organic semiconductor diodes made from different π-conjugated polymers and small molecules[16]. These materials greatly differ in chemical structure, charge carrier mobility, and spin-orbit coupling strength. Large negative or positive magnetoresistance effects were observed to be dependent on material and device operating conditions. Meanwhile, Christoph Gärditz, et al. further investigate the magnetic field effect on triplet emission in Alq_3-based devices by measuring the delayed electroluminescence and phosphorescence in Alq_3-based OLED[17]. The theory of triplet-triplet annihilation has been used to explain the delayed EL in the device. In 2006, Y. Sheng, et al. started a theoretical study and computation of OMR[18]; they claimed that the OMR effect might be caused by hyperfine interaction in the molecule. At the same time, a very important empirical fitting law shown in equation 1.3 had been shown successful as a standard feature for subsequent OMR reseach.

$$MR \propto \frac{B^2}{B^2 + B_0^2} \tag{1.3}$$

where B is the external magnetic field and B_0 is a constant.

Given the large number of report on OLEDs, it became more and more important to not just observe the OMR phenomenon, but also to understand the mechanism behind this effect. As in the following years, researchers from around the world are trying to build understandings on this effect based on different experiments [19–22]. Many models were developed during this stage trying interpreting organic

magnetoresistance from different perspectives. Typical four models were used under different experimental conditions, such as materials, drive currents, B field ranges, etc. These are: the electron-hole recombination model, the triplet-polaron interaction model, the electron-hole pair model and the bipolaron model. The following sections summarizes the four models.

Electron-hole recombination model

This model used to explain the effects of doping on the magnetoresistance of the device.

In 2006, V. N. Prigodin, et al. reported a developed theory based on the electron-hole recombination model[19]. Electron-hole recombination includes the formation of the electron-hole pair (e-h pair) and the subsequent quenching of e-h pair at different rates. It is suggested that the interconversion between singlet and triplet like e-h pair is controlled by the external magnetic field. At zero field, due to the lack of Zeeman splitting, there is degeneracy in the triplet state and all triplet states can mix with the singlet state by the hyperfine field due to hydrogen nuclei. However, upon application of an external magnetic field, due to Zeeman splitting of the triplet states at large magnetic fields, only T_0 triplet state can interconvert to singlet state. This will change the recombination rate of the e-h pair, hence change the device current.

In their modelling, the whole spin Hamiltonians are expressed as in equation 1.4:

$$\begin{aligned} \hat{H} &= \hat{H}_0 + \hat{H}_{S-T}, \\ \hat{H}_0 &= g\mu_B(\mathbf{S}_1 + \mathbf{S}_2)\cdot\mathbf{H} - J(r)(1/2 + 2\mathbf{S}_1\cdot\mathbf{S}_2). \\ \hat{H}_{S-T} &= (1/2)(g_1 - g_2)\mu_B(\mathbf{S}_1 - \mathbf{S}_2)\cdot\mathbf{H} + (a_1\mathbf{I}_1\cdot\mathbf{S}_1 + a_2\mathbf{I}_2\cdot\mathbf{S}_2). \end{aligned} \tag{1.4}$$

where $\mathbf{S}_{1,2}$ is the spins for the hole and electron in the pair, respectively. And $g_{1,2}$ are the g-factors, which characterises the magnetic moment and angular momentum of an electron. $\mathbf{I}_{1,2}$ are the nuclear spins and $a_{1,2}$ are the hyperfine coupling constants, and $g = \frac{1}{2}(g_1 + g_2)$. Also, J(r) is the exchange interaction between singlet and triplet excitons and this gives the energy difference between the singlet and triplet excitons. Finally, it is the $\hat{H}_{S-T}$ Hamiltonian mixing the singlet and triplet states.

Both singlet and triplet e-h pairs experience the process of recombination and dissociation as shown in Figure 1.11.

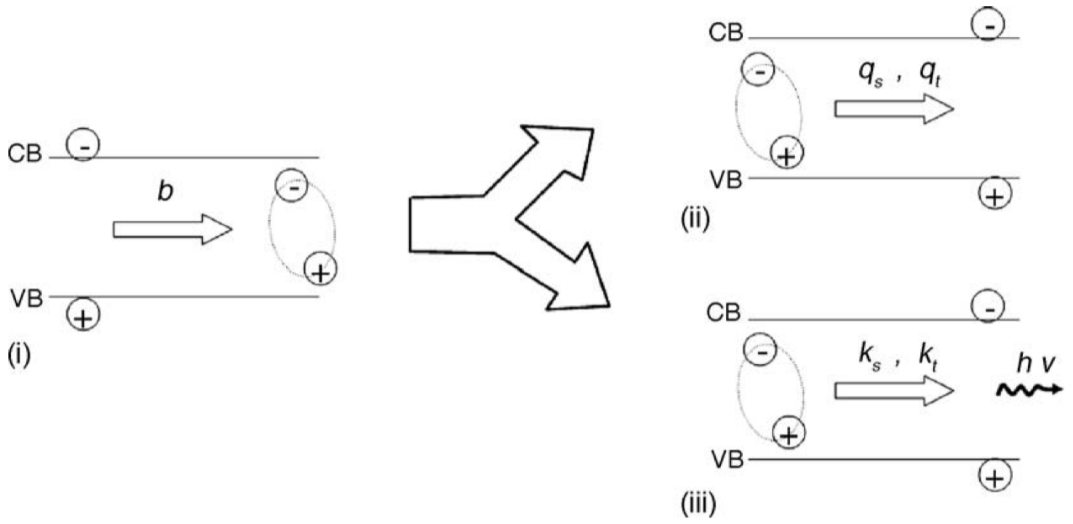

Figure 1.11: Process of e-h pair recombination and dissociation. Reproduced from [19]. (i) generation of an electron-hole pair (ii) dissociation of electron-hole pair (iii) recombination of electron-hole pair

In Figure 1.11, $q_{s,t}$ and $k_{s,t}$ are dissociation rate and recombination rate for singlets and triplets, respectively.

Finally, the magnetoresistance is expressed as in equation 1.5:

$$\begin{aligned} \frac{MR(H)}{MR_{sat}} &= f(\frac{\mu_B H}{\xi}), \\ MR_{sat} &= -\frac{1}{2}\frac{q_t}{k_t + q_t}. \end{aligned} \tag{1.5}$$

where ξ is the effective interconversion constant and is related to the spin-orbit interaction and hyperfine interaction. And the function f(x) has the asymptotes, f(x$\ll$1) $\sim x^2$ and f(x$\gg$1)-1 $\sim -1/x^2$.

V. N. Prigodin, et al. carried out a series of experiments to verify this model. They doped the phosphorescent guest material $Ir(ppy)_3$ and PtOEP with transition metal into Alq_3 to enhance the spin-orbit interaction within the device. The experiment resulted in the magnetoresistance being reduced by a factor of $\sim$ 10 for $Ir(ppy)_3$ doping, comparing to Alq_3 and disappearing in the PtOEP doped device. This is in agreement with the electron-hole recombination model as increased spin-orbit

interaction could weaken the magnetoresistance from equation 1.5 and is also in accord with more efficient energy transfer from triplets in the host molecule to the guest molecule. Additionally, the condition for observing the magnetic field effect is that the spin relaxation time τ_{spin} is long enough for the spin dynamics to be perturbed by the coupled e-h pair state, and typically for organic materials, that condition of $\tau_{spin} \gg 1/\xi$ is satisfied. Increasing spin-orbit coupling by doping phosphorescent guest molecules can decrease τ_{spin}, hence reducing the magnetoresistance.

Triplet-Polaron Interaction model

This model is used to explain the reason of the saturation of the device efficiency while the magnetoconductance is still increasing over high magnetic fields.

In 2007, Pratik Desai, et al. reported an organic magnetoresistance termed the triplet-polaron interaction model[20]. Through experiments, it was found that magnetoresistance is excitonic in nature because magnetoresistance can only be detected when there is light emission from OLEDs. Since magnetoresistance could not be solely due to a recombination current from experiments and the model of triplet-polaron interaction (trapping of charges due to triplet exciton) has been developed.

Using devices with the configuration of indium tin oxide / N,N′ -diphenyl-N,N′ bis(3-methylphenyl)-(1,1′ -biphenyl)-4,4′diamine (TPD) / Alq_3 / LiF / Al and sweeping of the different magnetic fields under different drive voltages[20] it was found that magnetoresistance appears when the drive voltage exceeds 2.2V, below which there was no light output from the device. This suggesed that organic magnetoresistance is excitonic in nature.

According to Prigodin et al., organic magnetoresistance is related to the changes in the recombination rate for electron-hole pairs, and this change is caused by the change in the singlet-triplet mixing introduced by the external magnetic field[19]. They derived an expression for the magnetoresistance, in which there are only dissociation and recombination rates for triplets. There is an implicit assumption that the dissociation rate is considerably larger than the recombination rate. Assuming that the dissociation is occurring at a significant rate means that the triplet ratio keeps

decreasing and this will in turn boost the singlet ratio, hence increasing the efficiency of the device[20]. Thus a linear correlation between the change of efficiency of the device ($\Delta\eta/\eta$) and the magnetic field effect (here, the current change ΔI/I) is expected. However, Pratik Desai and co-workers measured the relationship between $\Delta\eta/\eta$ and ΔI/I showing that the theory of Prigodin et al. is only partly correct as shown in Figure 1.12. The first part of the curve shows a clear linear relationship between $\Delta\eta/\eta$ and ΔI/I. However, the curve deviates from the linear relationship and $\Delta\eta/\eta$ begins to saturate while ΔI/I keeps increasing at higher magnetic fields. This effect indicates that the theory of Prigodin et al. does not necessarily hold true for all magnetic field ranges. Hence the theory of triplet-polaron interaction comes into development.

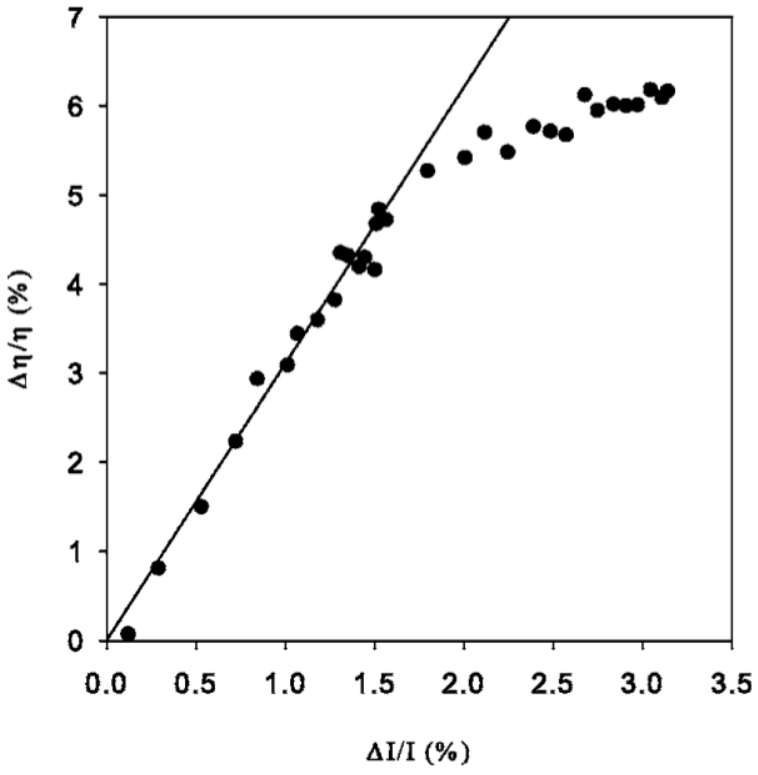

Figure 1.12: Relationship between $\Delta\eta/\eta$ and ΔI/I. Reproduced from [20].

Triplets in a working OLED have relatively long lifetime (as long as around 25μs) and these long times are enough for the triplets to diffuse throughout the whole active layer towards the electrodes[20, 23]. This slow diffusion process can result in large numbers of triplets existing in the bulk organic material. According to Ern and Merrifield[24], triplets can interact with paramagnetic centres as shown in equation

1.6

$$T_1 + D_{\pm 1/2} \overset{k_1}{\longleftrightarrow} (T_1 \cdots D_{\pm 1/2}) \overset{k_2}{\longrightarrow} D_{\pm 1/2} + S_0^* \tag{1.6}$$

where T_1 is the triplet state, $D_{\pm 1/2}$ is the free charge with spin $\pm 1/2$, ($T_1 \cdots D_{\pm 1/2}$) is a pair state, and k_1 is the formation or backscattering rate from the pair state. The righthand side of equation 1.6 shows the process of the dissociation of the triplet state into free charge carriers and vibrationally excited ground state with a rate of k_2. The lefthand side of equation1.6 shows the process of scattering and backscattering between a free charge and a triplet state, which can result in a decrease in the carrier mobility as it blocks the transport of that free charge. Therefore, with increasing density of triplets, the probability of scattering or backscattering increases and the carrier mobility should decrease.

Experimentally, it was found that efficiency increases with increasing magnetic field and this means that more singlets are generated due to triplet conversions. From equation 1.6, a low density of triplets results in less scattering (or backscattering) and hence increases the carrier mobility.

The work of Prigodin et al. is consistent with the triplet-polaron interaction model[19]. On doping Alq_3 with $Ir(ppy)_3$ and PtOEP, the organic magnetoresistance was reduced by a factor of 10 for $Ir(ppy)_3$ and disappeared for PtOEP. This is consistent as rapid removal of triplets leads to a reduction in trap sites for free charge carriers which limits the carrier mobility, thus results in reduced MR.

Therefore, in Figure 1.12, the deviation from the linear relationship can be explained as the effect of increased trapping of free charges by triplets and this may dominate the contribution to the carrier mobility in OLEDs.

Electron-Hole Pair Model

This model is used to explain how the charge carrier injection balance can have an effect on the device magnetoconductance, and this can be related to the device structuring.

In electron-hole recombination model proposed by V. N. Prigodin, et al. [19], it described how the recombination of the electron-hole pairs can affect the related rates (e.g. the recombination and dissociation rates), hence, having a final effect on the device magnetoresistance. This model is different from the electron-hole pair model, which is covered in this subsection, where the magnetoresistance of the device was modelled to be related to the competition between the electron-hole pair dissociation and different charge reactions.

In 2007, Bin Hu, et al. proposed a model involving the electron-hole pair state of injected charges[21]. Electrons and holes injected from their respective electrodes in a diode can approach each other driven by the external electric field. Over the large distances between several molecules, electrons and holes can sense each other's presence and form electron-hole pair (e-h pair) state[25][26]. However, as the electron and hole keep approaching each other, the electron-hole pair state can evolve into an exciton state as the distance between the electron and hole decreases. In the two charge state, there are singlet and triplet configurations due to different combinations of spins for each charge[25][26].

There are two processes, for either the e-h pair or exciton state, that can affect MR – the dissociation [27–31] and the charge reaction [24, 32–35]. Both of these processes can generate secondary charge carriers which will have an effect on the device current. Importantly, this generation of secondary charge carriers can be magnetic field dependent and can be changed by the application of external magnetic field. Hence the device current will show a dependence on the external magnetic field.

The whole process is illustrated in Figure1.13.

In Figure1.13, electrons and holes are injected from their respective electrodes and when they approach each other under the external electric field, e-h pair will be formed with the singlet and triplet components ($(\text{e-h})^1$ and $(\text{e-h})^3$). It is possible that the electron-hole pair state can then further evolve into an exciton state (**S** and **T**) when the distance between the electron and hole decreases.

The key point for the device current to be magnetic field dependent is the intersystem crossing as shown in Figure 1.13. As stated in reference [21], only if the magnetic

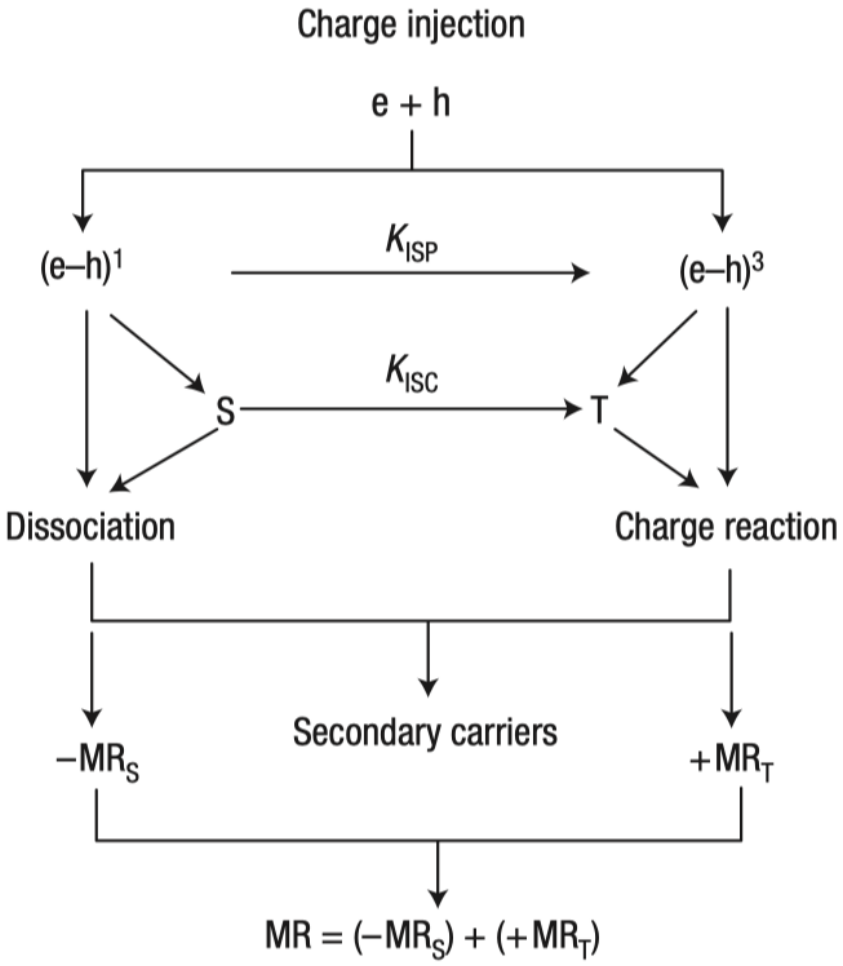

Figure 1.13: Schematic of the e-h pair model. Reproduced from reference [21]. K_{ISC}: Intersystem Crossing rate in excitonic state. K_{ISP}: Intersystem Crossing rate in pair state.

splitting caused by the external magnetic field (called external Zeeman effect, ΔE_B) is larger than the internal splitting induced by the spin-orbital coupling (internal Zeeman effect, ΔE_{ST}) can the intersystem crossing be magnetic field dependent[36]. As shown in Figure 1.14, singlet and triplet e-h pair states have similar energy levels due to similar lifetimes and binding energies, but the energy difference between the singlet and triplet excitons is significant due to the short distance spin-exchange interaction coming into play. Under no magnetic field, singlet components can transform into triplet components in both cases since the the pair states $(e\text{-}h)^1$ and $(e\text{-}h)^3$ have similar energies and the exciton S state has higher energy than the T state. However, under

external magnetic field, the external Zeeman comes into play and there would be energy splitting in triplet excited states. For the e-h pair state, the splitting would be larger with increasing magnetic field, as indicated in Figure 1.14, two $(e\text{-}h)^3$ states are at higher energy than the $(e\text{-}h)^1$ state, so can transform into $(e\text{-}h)^1$, reducing the total population of triplet e-h pairs by intersystem crossing. This is where the magnetic field dependence shows an effect. However, the total energy of the triplet exciton energy T is significantly lower than the S state and the energy splitting due to the external Zeeman effect is significantly smaller compared to the energy difference. Hence the magnetic field would have no significant effect on the intersystem crossing.

Both the singlet and triplet excited states (e-h pair state and exciton state) can experience dissociation and charge reaction to generate secondary charge carriers. However, their corresponding contributions are different due to different binding energies and lifetimes[21]. For the process of dissociation, it is noted in reference that a singlet e-h pair can be more effective than its triplet counterpart due to different dissociation rates[21, 36, 37]. With increasing external magnetic field, the population of $(e\text{-}h)^1$ increases while the population of $(e\text{-}h)^3$ decreases. And the increasing numbers of $(e\text{-}h)^1$ states will boost the dissociation and produce more secondary charge carriers, hence generating negative magnetoresistance (or positive magnetoconductance).

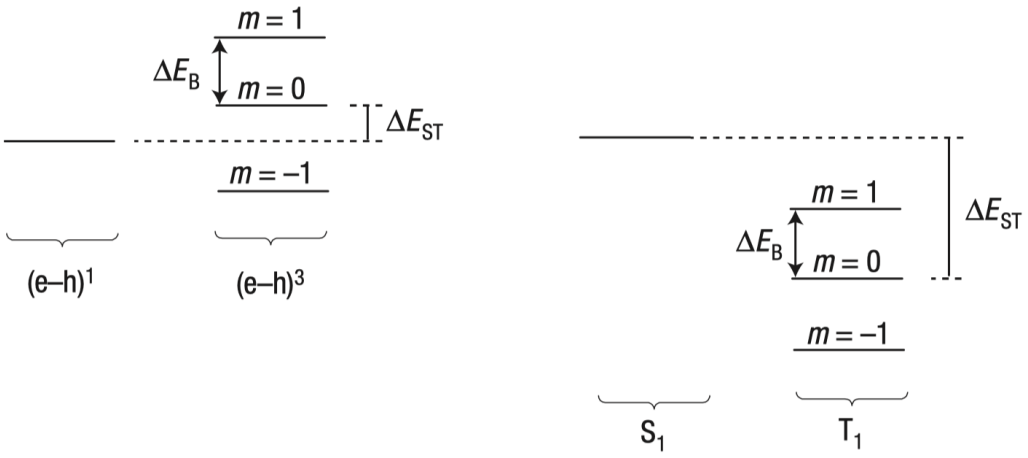

Figure 1.14: Energy level diagram of e-h pair (left) and exciton (right) under an external magnetic field. Reproduced from [21].

On the other hand, the process of charge reaction is more significant in triplet excitons due to their long lifetime. There are three types of charge reactions[34, 38–40]:

$$\begin{aligned} T + Q^* &\rightarrow S_0 + Q \text{.....} (a), \\ T + Q &\rightarrow e + h + Q \text{.....} (b), \\ T + electrode &\rightarrow e + h \text{.....} (c). \end{aligned} \tag{1.7}$$

Equation 1.7(a) is the reaction between the triplet exciton (T) and a trapped charge charge (Q^*), generating secondary charge carriers. Equation 1.7(b) is the reaction between a triplet exciton (T) and a free charge carrier (Q) to generate a free electron and hole. Equation 1.7(c) is the reaction between a triplet exciton (T) and the electrode to produce free charge carriers. All of these charge reactions can boost the numbers of free charge carriers. The e-h pair can also relax into an exciton state under electrical excitation[41]. With increasing external magnetic field, the triplet excited state ratio would be reduced due to reduced number of (e-h)^3 states and this will weaken the charge reaction hence reducing the free charges produced. This will lead to positive magnetoresistance (or negative magnetoconductance). The resulting device magnetoresistance is the sum of the dissociation and charge reaction contributions.

According to reference [21], as the charges in the charge reaction all come from excess charges in the bulk organic material, and, balancing the minority and majority charges in the injected current will boost the ratio of formed excitons to excess charge carriers within the device and this will weaken the charge reaction due to reduced numbers of charge carriers. This in turn will strengthen the dissociation of e-h pairs and result in negative magnetoresistance (or positive magnetoconductance).

This model has been verified by their experiments using an insulating thin film of Poly(methyl methacrylate) (PMMA) as a charge blocking layer in the diode to tune the balance level between the minority and majority charge carriers [21].

Bipolaron model

This model is used to explain the magnetoconductance in the unipolar devices (hole-only or electron-only organic diodes).

In 2007, P. A. Bobbert, et al. developed the bipolaron model for the explanation of organic magnetoresistance[22]. In this model, the hopping of polarons and formation of bipolarons is considered including the effect of random hyperfine fields and external magnetic fields. It is known that in organic materials, conduction is achieved by charge carrier hopping. The hopping occurs between different localised sites with an assumed Gaussian distribution of density of states (DOS)[22]. Only two polarons with opposite spin components can form a bipolaron due to the strong exchange interaction[42, 43], and this "spin blocking" effect is key to the bipolaron model.

The modelled bipolaron formation dynamics can be explained according to the reference [22]. Bipolarons are assumed to be formed at some low energy site β as shown in the inset in Figure 1.15. It is assumed that at least one polaron stays permanently at site β. In the model, a polaron from a neighbouring "branching site" α has the probability to hop to site β to form a bipolaron with different rates. There are several limitations in this model. Bipolarons formed at site β are assumed not to dissociate and hop back to site α, but the polarons at site α can originate from the "environment" with a rate of $r_{e\to\alpha}$. Additionally, the polaron at site α can hop back to the environment with a rate of $r_{\alpha\to e}$, and bipolaron fromed at site β has a probability of dissociating back to the the environment with a rate of $r_{\beta\to e}$. This whole process is shown in the inset of Figure 1.15.

The probability of bipolaron formation p_β is expressed as:

$$\begin{aligned} p_\beta &= \frac{r_{e\to\alpha}}{r_{\beta\to e}} f(B) p, \\ \text{where } f(B) &= \frac{P_P P_{AP} + 1/(4b)}{P_P P_{AP} + 1/(2b) + 1/b^2} \end{aligned} \tag{1.8}$$

Here, the branching ratio is given by b = $r_{\alpha\to\beta}$ / $r_{\alpha\to e}$. P_P and P_{AP} are the singlet probability for parallel and anti-parallel pairs. Figure 1.15 describes how the function f(B) varies with the external magnetic field normalised to the hyperfine field. From the simulation results in Figure 1.15, one can see that when the branching ratio is relatively small (meaning that bipolaron formation is not significant), f(B) is not significantly magnetic field dependent, and nor is the formation of bipolarons. However, when

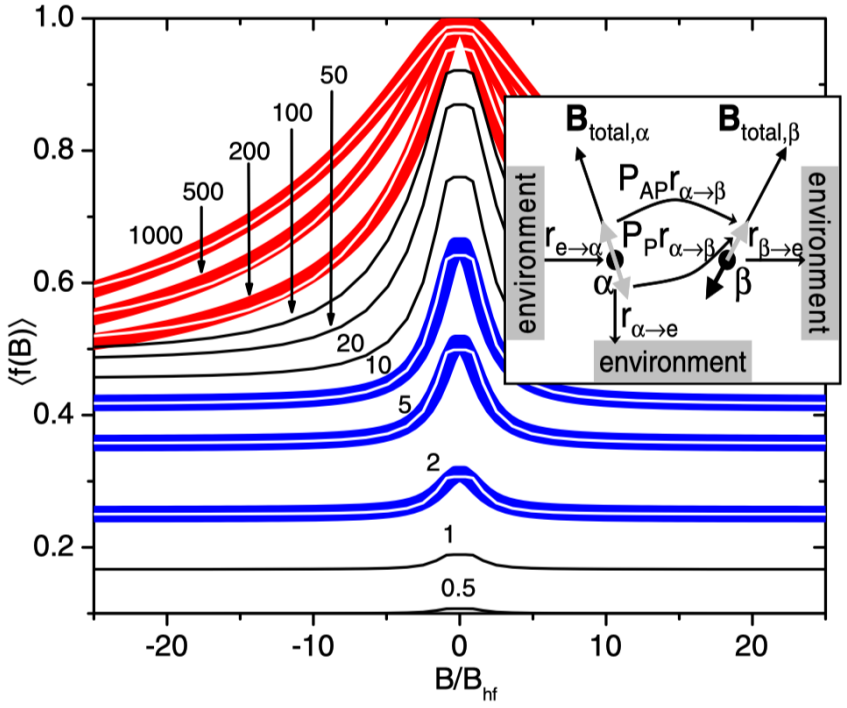

Figure 1.15: Hyperfine field average of the function f(B) under different branching ratios b. The black solid line and white solid line indicate the Lorentzian and non-Lorentzian empirical fitting law. Reproduced from [22]

the branching ratio is large, the formation of bipolarons can be significantly field dependent which can be described as non-Lorentzian behaviour, indicated by the white fitting in Figure 1.15 and this non-Lorentzian behaviour shows that the function f(B) is dependent on the branching ratio b.

In order to connect the bipolaron formation with the device magnetoresistance, Monte Carlo simulations are used by P. A. Bobbert, et al. In the simulation procedure, a random site is populated according to Fermi-Dirac distribution. At this site, the process outlined in inset of Figure 1.15 occur and are kept track of, including the site occupation, polaron spin and Coulomb field until a steady state is reached[22]. The computation of magnetoresistance is evaluated as the difference in the number of downfield and upfield hops divided by the simulation time. The result is shown in Figure 1.16, where b' is a multiplication factor of bipolaron formation or dissociation, σ is the width of the Gaussian Density of States of the localised sites, U is the Coulomb repulsion and eEa is the electric potential energy.

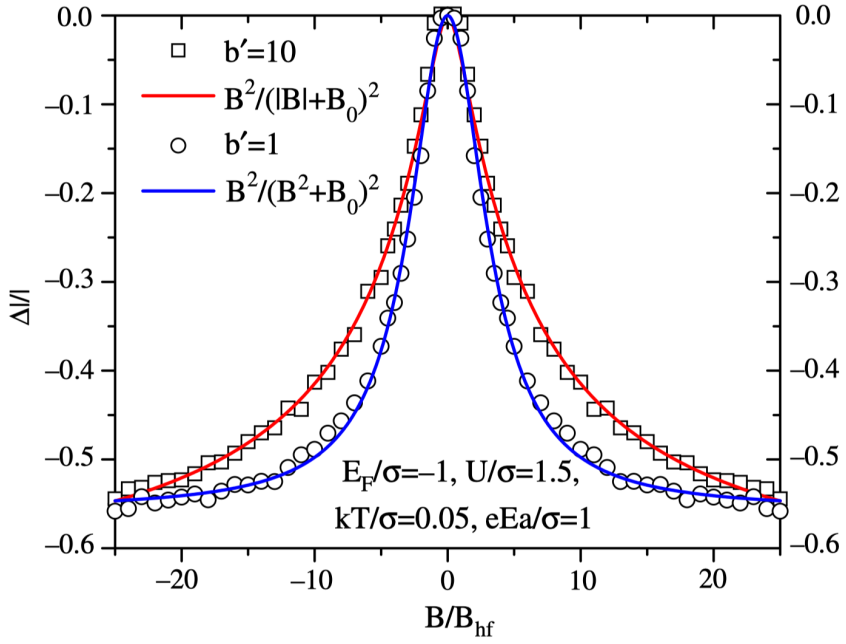

Figure 1.16: Simulation result of magnetoconductance based on bipolaron Monte Carlo Simulation. Reproduced from [22]

Generally, the bipolaron model can describe the effect of magnetoconductance in two ways[22]: (1) The negative magnetoconductance or positive magnetoresistance can be explained by the blocking of transport through bipolaron formation under relatively small drive voltages. (2) The positive magnetoconductance or negative magnetoresistance can be explained by the increase of polaron population at the cost of bipolaron formation with increasing magnetic field under relatively large drive voltages. As explained in reference [22], when the drive voltage is zero, the bipolaron is assumed to be formed at a site with low energy to offset the bipolaron formation energy U, which is a rare case. However, when the long-range Coulomb repulsion is considered, the offset energy is reduced to U-V when an electric field is applied. Hence the inclusion of V can reduce the bipolaron formation offset energy and this will boost the formation of bipolarons, hence increasing the polaron population as well for enhanced bipolaron formation.

1.4.2 Ultra-Small Magnetic Field Effect (USMFE)

Since 1976, a small magnetic field effect was found to be related to the recombination of radical ions in chemical reactions[44]. The probability of gaining a singlet state, or singlet yield, was studied under the influence of different external magnetic fields. Brian Brocklehurst found the singlet yield was a function of time and would become constant under high or zero magnetic fields. However, when the external field was small, the singlet yield would keep decaying with time as shown in Figure 1.17. This different singlet yield behaviour under low fields caught the attention of researchers.

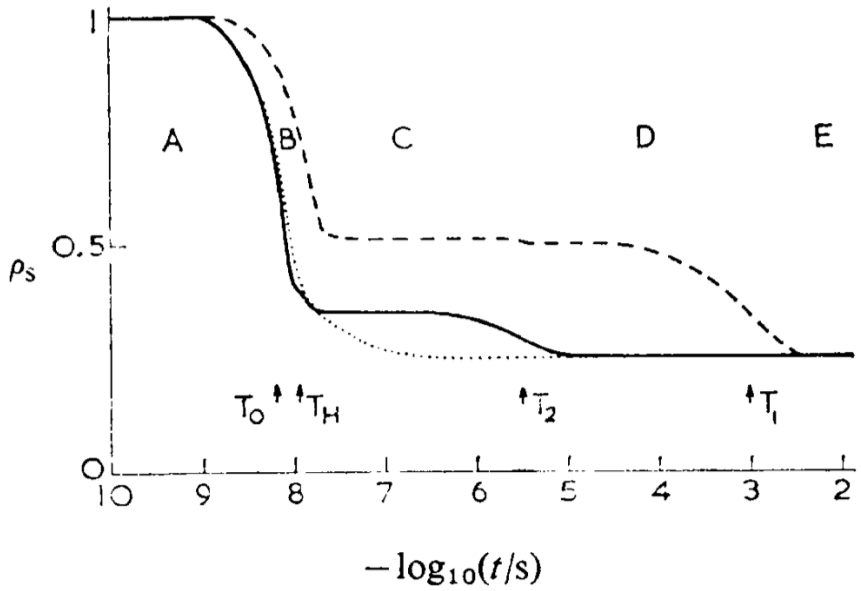

Figure 1.17: Dependence of singlet yield ρ_S on time. zero field: — very high field: - - - low field: .... Reproduced from [44]

Since then, the low field effect of radical ion pairs has been studied both experimentally and theoretically[45, 46]. Those works rendered the basics for the later radical pair model, which attempted to explain the behaviour of radical pairs during recombination in chemical reactions under low magnetic fields[47, 48]. This laid the foundation for the mechanism of avian navigation behaviour in weak geomagnetic field[49, 50].

All the previous studies were based on radical pair recombination in chemical reactions and had nothing to do with electrical devices until 2009, when F. J. Wang et al. found a low field component in magnetoresistance in a hole-unipolar diode comprised

of ITO/PEDOT-PSS/MEH-PPV/Au at 100K[51]. This low field MC appeared to be W-shaped indicating a sign reversal compared to the large field MC components[51]. They stated that the low field MC component is due to the change in mixing of spin sub-levels by hyperfine interaction within polaron pairs. This interesting effect has attracted the attention of researchers worldwide and led to more detailed studies both by experiment and theory. In 2010, Tho. D. Nguyen et al. measured the magnetoelectroluminescence (MEL) in an OLED formed by ITO/PEDOT:PSS/DOO-PPV/Ca/Al for both protonated DOO-PPV and deuterated DOO-PPV, and found the USMFE in the magnetic field range below 1mT. They provided a polaron pair model, analogous to the previous radical pair model[52]. The results are shown in Figure 1.18, and it is clear that the MEL of the deuterated material shows a narrower dip of the "W" shape effect compared to that of the protonated material. This indicates that hyperfine interaction plays an important role in ultra-small magnetic field effect and lays the basis of the polaron pair modelling.

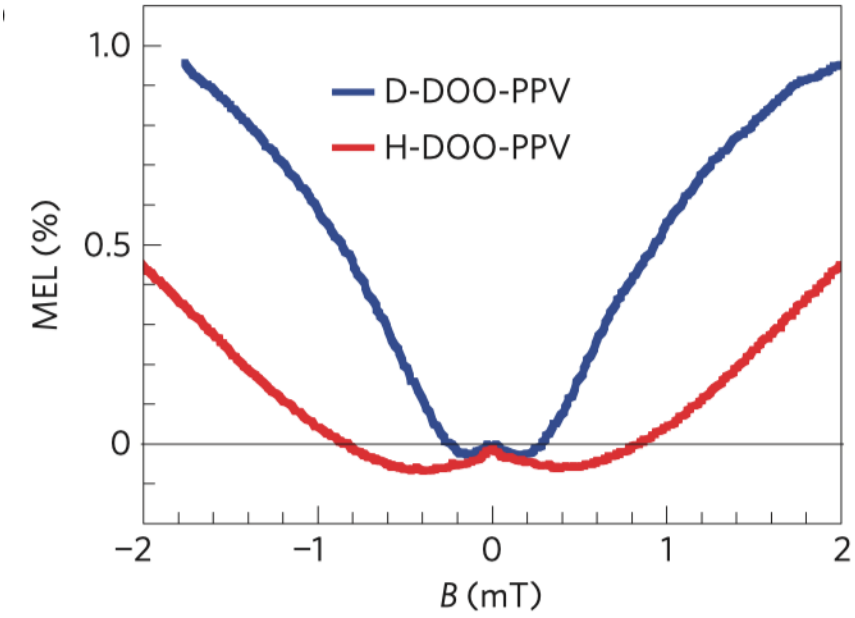

Figure 1.18: MEL results of OLEDs based on protonated and deuterated DOO-PPV polymer. Reproduced from [52]

Later in 2010, Tho. D. Nguyen et al. discovered ultra-small magnetic field effects in both unipolar and bipolar organic diodes, indicating that the polaron pair model

can not only describe opposite-charge polaron pairs but also explain same charge polaron pairs. They developed their model by including the differences between hyperfine coupling constants of negative and positive polarons and also formulated the expression for the MC of the device[53, 54]. Additionally, they found that the ultra-small magnetic field effect is directly linked to the hyperfine interactions within the material. Notably, the model simulation can reproduce the typical "W" shape experimentally observed in ultra-small magnetic field effect experiments.

In 2012, an isotope dependence experiment was carried out again but on Alq_3 based diodes and the MC and MEL were both investigated[55]. From the experiment, the MEL results showed the same isotope dependence effect as in the previous report while the MC was much less sensitive. They claimed that the isotope independence of MC might be due to an isotope independent spin mixing process in the hyperfine interaction. Specifically, a process in MC formation is modelled as the collision between a polaron and a triplet polaron-pair, and this collision is isotope insensitive. Later in 2012, Bhoj R. Gautam et al. reported the magnetic field effect on excited-state spectroscopies in polymer materials[56]. Specifically, the magnetophoto-induced absorption (MPA) and magnetophotoluminescence (MPL) behave in a correlated manner to the external magnetic fields, noticeably, in the ultra-small magnetic field range, they show a similar "W" shape to the ultra-small magnetic field effect MC and MEL previously reported. This observation again verifies the polaron pair mechanism resulting from the spin mixing of polaron pairs by the hyperfine interaction. Eitan Ehrenfreund et al. later did extensive research on the modelling of polaron pairs. This included the hyperfine interaction (both isotropic and anisotropic), the Δg mechanism for two polarons composing the polaron pair, and the spin-orbit interaction[57]. However, their work lacked comparisons between different parameter values and how they can affect the lineshape of the final MC simulation results.

In 2013, T. D. Nguyen et al. discovered the "compass effect" utilising the ultra-small magnetic field effect magnetoresistance of an organic diode[58]. It showed that both the value and direction of the local earth magnetic field can be accurately obtained. In the experiment, an external magnetic field with magnitude similar to the earth

magnetic field ($\sim 50\mu T$) was applied upon the device and the device which could rotate in relation to the direction of the local earth magnetic field, with the angle between the external magnetic field and earth's magnetic field defined as α. As shown in Figure 1.19, it shows a clear dependence of MC on the relative angle α and the sinusoidal relationship can help to locate the direction of the local earth magnetic field.

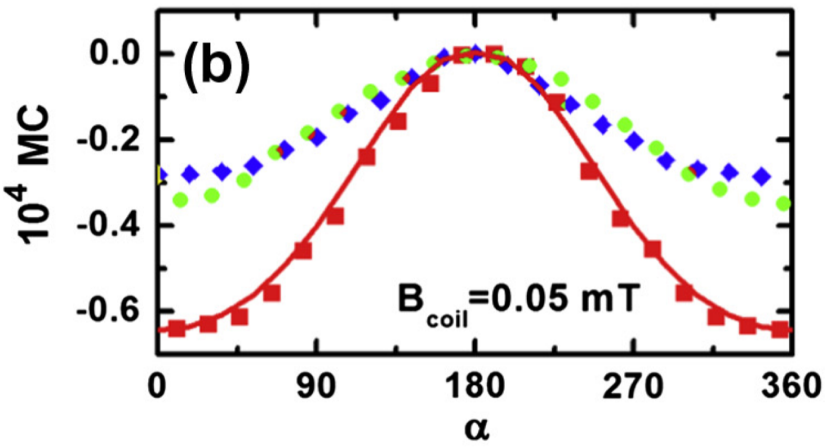

Figure 1.19: MC(α) response for three isotopes using the external magnetic field as 0.05mT. The green: protonated. The red: deuterated. The blue: ^{13}C. Reproduced from [58]

Later in 2013, Qiaoming Zhang et al. investigated the ultra-small magnetic field effect of a blended device[59]. They found that the widths of the ultra-small field broaden with an increase of Phenyl-C61-butyric acid methyl ester (PCBM) component of the blend and Super Yellow Poly(phenylenevinylene) (SY-PPV) in host material). They stated that this increases the competition ratio r (r = q/ω_{hf}, q is the dissociation rate and ω_{hf} is the hyperfine precession frequency) by increasing the dissociation rate q when PCBM is blended. P. Jassen, et al. also reported the discovery of ultra-small magnetic field effects in blend system based diodes[60, 61]. However, as these were different material system as reported before, other mechanisms other than polaron pair model come into play, such as the triplet-polaron interactions.

In 2016, Joseph E. Lawrence et al. carried out a detailed research and modelling based on magnetoelectroluminescence of OLEDs using polaron pair model[63]. As the mechanisms of magnetoresistance are still under debate, they developed a new rela-

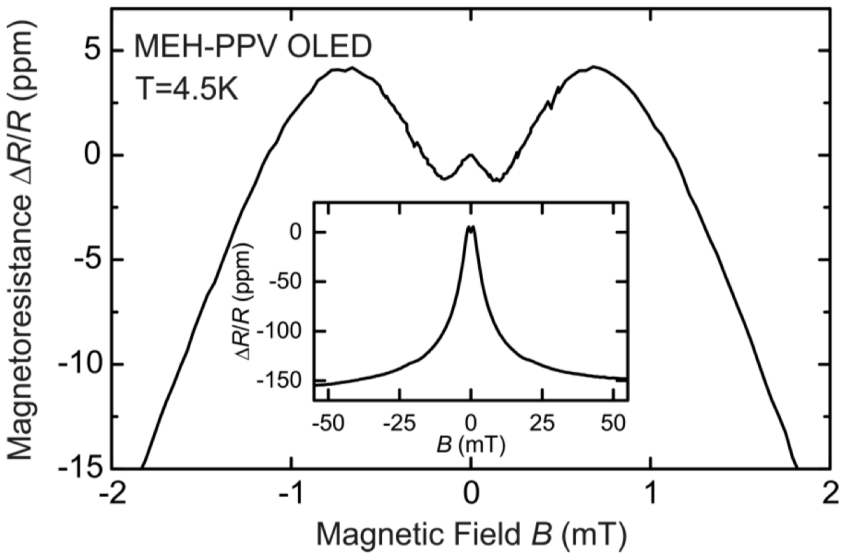

Figure 1.20: Magnetoresistance of an MEH-PPV OLED at the temperature of 4.5K. Inset shows the high magnet field effect. Reproduced from [62]

tionship between MEL and MC in OLEDs derived from the polaron pair model. This provides an alternative to compute the value of MC through known MEL simulation and modelling. Later in 2017, Philippe Klemm et al. reported a new feature in their measurements of ultra-small magnetic field effect in π-conjugated polymer devices[62]. This feature is shown in Figure 1.20 and displays a double "W" shape, differing from the typical single "W" shape previously observed. It is claimed in the paper that this additional feature might be due to the spin-spin interaction in the weakly bound polaron pairs for the spin dependent recombination process. Subsequently, in 2018, Wolfham Ratzke et al.[80] discovered the different behaviour in ultra small magnetic field effect between MC and MEL. In their results, the measured MC shows a typical "W" shape as reported before, however, for the MEL the shape becomes a monotonic function with the external magnetic field. The reason for this difference is attributed to using a constant driving current instead of a constant driving voltage as in previous reports and it is this driving condition that makes the difference. This is directly related to my experiment and will be covered in detail in Chapter 4. Additionally in their report, they managed to measure the magnetic field dependent fluorescence and phosphorescence which reflect singlets and triplets respectively. The results

showed that the magnetoelectroluminescence is dependent on the spin interconversion between singlets and triplets.

Chapter 2

Experimental Methods

2.1 Materials and Devices

2.1.1 Material Purification

The level of purity of the organic material is vital to the efficiency and performance of the organic light-emitting diodes (OLEDs) as impurities can serve as traps in the organic semiconductor and it captures charge carriers, influencing the current through the OLED.

Therefore, it is very important to ensure high purity of the organic material prior to device fabrication in order to make a good quality OLED with relatively long lifetime and good efficiency.

The three materials investigated and used in the device fabrication are N,N′-Bis(3-methylphenyl)-N,N′-diphenylbenzidine (TPD), N,N′-Di(1-naphthyl)-N,N′-diphenyl-(1,1′-biphenyl)-4,4′-diamine (NPB) and Tris-(8-hydroxyquinoline)aluminium (Alq_3). The chemical structures are shown in Figure 2.1.

All the materials are bought from Sigma-Aldrich Corp. However, the purity of these materials is not sufficient for device fabrication. Hence extra purification is needed to further purify the materials. Two stages of purification for each material were carried out. The technique used is train sublimation and a schematic is shown in Figure 2.2. Because the impurities and the target material have different sublimation points, a preset temperature that corresponds to the sublimation point of the targeted

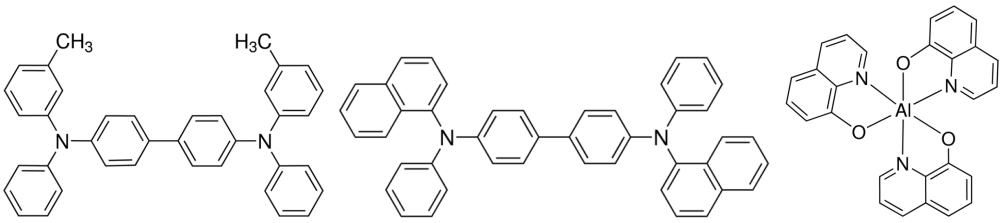

(a) TPD (b) NPB (c) Alq_3

Figure 2.1: Chemical structures of TPD, NPB and Alq_3

material is applied to the boat and the separation between the impurity and target material is achieved. However, these three materials (TPD, NPB and Alq_3) have different melting points, and the working furnace achieves relatively high temperatures (200∼300^{o}C). A material with low melting point (e.g. TPD with melting point of around 175∼177 ^{o}C) tends to turn from solid to liquid and then begins to evaporate, however, a material with high melting points (e.g. NPB and Alq_3 with melting points of 279∼283 ^{o}C and > 300 ^{o}C, respectively) will directly sublimate from the solid phase. According to different sublimation (or evaporation) conditions, a different sublimation boat is used as shown in Figure 2.3. Specifically, for the sublimation of TPD, as the material itself will melt during the high temperature, a special boat with a liquid blocker is used. This blocker can prevent the melted TPD from flowing out of the boat and keep the liquid in a limited space for better evaporation. Additionally, the filter (A/D Glass Fiber Filter, Pall Corp.) in the boat is used to keep the raw material in the boat and stop particles from flowing around to the inner tube due to pumping.

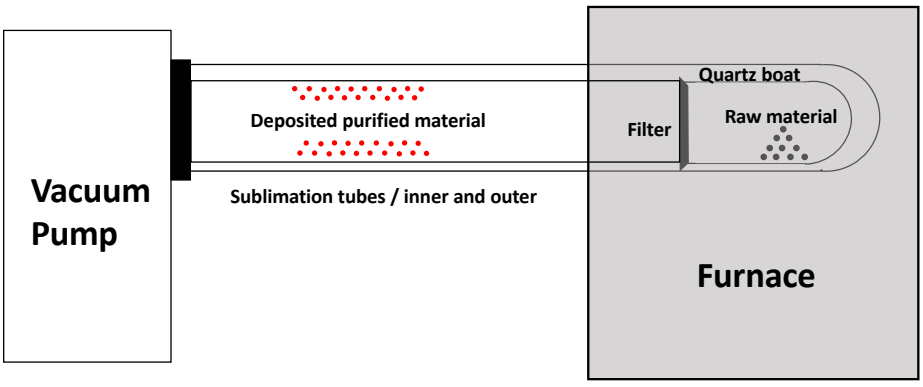

Figure 2.2: Schematic for train sublimation

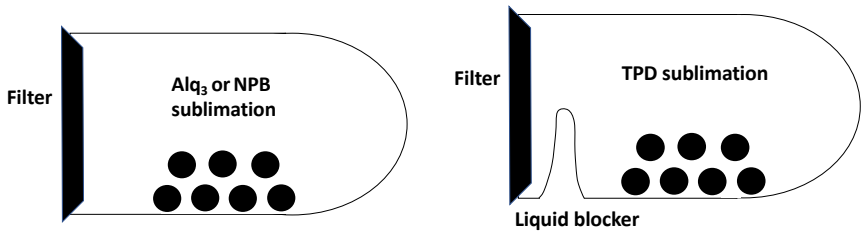

(a) Boat for gas-phase sublimation (b) Boat for liquid-phase evaporation

Figure 2.3: Different boats for different phase sublimation (evaporation)

The followings are the details of sublimation process:

Prior to any sublimation, all the sublimation tubes and boat should be cleaned properly in order for the prevention of introduction of extra impurities to the material. This is achieved by the following steps:

1. Use the tube brush to clean the inner tube, outer tube and the boat thoroughly with the laboratory detergent powder (Alconox).
2. Rinse the detergent off everything with water.
3. Set up the whole glassware by inserting the boat and inner tube into the outer tube, and fill the whole setup with de-ionised water and an appropriate amount of detergent powder.
4. Place the whole setup vertically for 20 mins in an ultrasonic bath.
5. Replace the waste liquid of step 4 with clean de-ionised water and continue with ultrasonic bath for 5 mins 3 times.
6. Fill the setup with acetone and place in ultrasonic bath for 5 mins twice.
7. Fill the setup with chloroform and place in ultrasonic bath for 5 mins twice.
8. Dry the whole setup with nitrogen, after which the cleaned setup is sealed and is ready for sublimation.

The whole glassware assembly (outer tube, inner tube and boat) needs to be set up carefully for sublimation, especially for the filter setup. Improper setup can result in contaminated purified material as the raw material might have the chance of getting out of the boat and be mixed with the purified material. The process of glassware setup is illustrated in Figure 2.4.

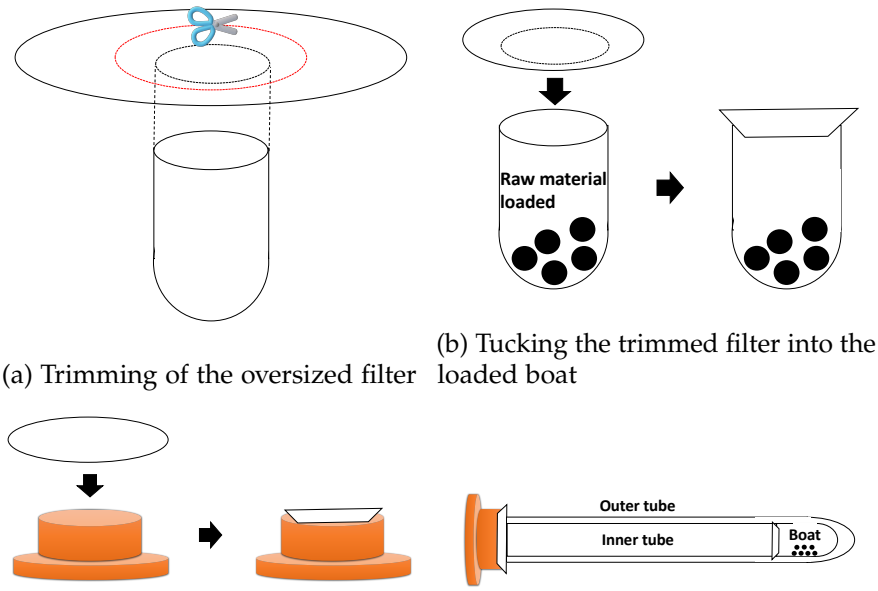

(a) Trimming of the oversized filter

(b) Tucking the trimmed filter into the loaded boat

(c) Tucking the full-size filter into the metal joint

(d) Connecting the metal joint and glassware tightly

Figure 2.4: Illustration for the glassware setup

First, the filter is oversized for the diameter of the boat, so trimming is needed for the filter to fit into the boat. Second, the boat is loaded with target organic material and tightly sealed the boat with the trimmed filter. This sealing process needs to be carefully done as the filter is very delicate and easy to break. A broken filter, with even a tiny hole on it, will fail the whole process of purification as the particles of raw material can flow out of the boat through the hole and contaminate the purified material. Thirdly, Seal the metal joint with the full-sized filter, and this metal joint connects the whole glassware with the pump directly. Last, the boat and inner tube are inserted into the outer tube and connected to the metal joint and the whole glassware together tightly and carefully. The whole setup is connected to the pump and the equipment is ready for sublimation.

The sublimation process is as follows:

1. Pumping the whole system overnight. The ideal vacuum level before any heating occurs is ideally below 10^{-6} mbar.

2. Heating of the tube furnace. At first the heating progresses slowly, as the surface area of the target material is small (particles) and water (and maybe other impurities)

from the environment might get trapped inside the powder. The first removal process is for the low-temperature sublimation (or evaporation) of impurities. The furnace is heated from room temperature to around 80 ^{o}C at a rate of 20^{o}C / hour. Because of the low pressure ambient compared to atmospheric pressure, the evaporation point of water will drop significantly and 80 ^{o}C is enough for water to evaporate. A relatively slow heating rate is chosen because there might be some chance of introducing organic impurities during the cleaning process. Since the evaporation temperature of these organics is rather low, this slow heating rate can gradually remove those organic impurities step by step, and this helps to better separate different impurities from the target material. The furnace temperature of 80^{o}C is kept overnight.

3. Different materials have different types of impurities due to their different synthesis methods. For Alq_3, the majority impurity is 8-hydroxyquinoline as it is the raw material for the synthesis of Alq_3. And 8-hydroxyquinoline has the sublimation point of $\sim 120^o$C. Hence the temperature is gradually raised to 120 ^{o}C at a rate of 10^{o}C / hour. The temperature remains constant at 120 ^{o}C overnight. In the case of TPD and NPB, the impurities are various due to the more complex synthesis processes. The procedure following is to keep heating the target material at a very slow rate until a significant vacuum drop occurs, meaning that something begins to sublimate at that temperature. A note of the vacuum reading when the pressure begins to rise is taken and the readings are tracked continuously. When the vacuum restored back to the baseline, the temperature is increased to the next level.

4. Step 3 is repeated until the target material is deposited on the wall of inner tube. Although at this specific temperature, the target material starts to sublimate and deposit, the sublimation rate is very low and is not very effective for mass sublimation and deposition. The temperature is increased carefully and appropriately at a slow rate, which will ensure that the target material and deposited material do not decompose.

5. After the first sublimation is finished, all the target material in the raw material were sublimed and deposited on the wall of the inner tube and there might be some impurities that have even higher sublimation temperatures remaining in the boat.

6. Two rounds of purification are necessary for each material to ensure high purity

Table 2.1: Different sublimation conditions for Alq_3, TPD and NPB respectively

Processes	Conditions	Alq_3	TPD	NPB
Raw amount		0.41g	0.75g	0.75g
Water removal	Temperature Heating rate Duration	85^oC 5^oC/min overnight	85^oC 5^oC/min overnight	85^oC 5^oC/min overnight
Impurity removal	Temperature Heating rate Duration	120^oC 10^oC/30min overnight	150^oC 10^oC/30min overnight	150^oC, 200^oC 10^oC/30min overnight
Target material sublimation	Temperature Heating rate Duration	270 $\sim$276^oC 10^oC/h till finished	218^oC 10^oC/h till finished	290^oC 10^oC/30min till finished
Final purification yield by mass		90.9%	76.8%	91.2%

level in the target material. The second round of purification is exactly the same as steps 1 to 5. Before any sublimation, all the glassware needs to be re-cleaned following the standard procedure. After a second round of purification, there is barely anything left in the boat and this is a sign that the twice purified material should be suitable for subsequent device fabrication.

Table 2.1 shows different conditions for Alq_3, TPD and NPB purification.

After the second round of purification is finished, the purified materials are collected and stored in a tightly sealed container which is kept in a vacuum storage desiccator.

2.1.2 Device Fabrication

Preparation for Device Fabrication: Evaporation Parameter Calibration

First, the evaporation chamber has to be clean enough for device fabrication. As the evaporation occurs at high temperature (more than 650^oC for aluminium evaporation), any impurities or other unwanted organic material attached to the chamber wall can start to evaporate together with the target material. This can introduce impurities into the device which can shorten the lifetime and lower the efficiency. Thus, it is important to clean the chamber wall and every source shells and shutters thoroughly with acetone.

Table 2.2: Calibrated parameters for device fabrication

Number	Material	TF	DENS	AI
#1	TPD	1.131	1.374	9.75
#2	Alq_3	1.410	2.166	10.85
#3	NPB	1.131	1.675	9.75
#4	LiF	1.318	2.922	11.44
#5	Al	5.387	4.332	8.17

The system is pumped and baked at high temperature (typically higher than organic evaporation point) for at least 48 hours until a significant improvement in vacuum level is achieved (typically 10^{-7} mbar).

The twice purified material is loaded into the corresponding sources in the chamber and the thickness calibration is carried out before any device fabrication. This calibration process is vital as it can directly determine the precision of thickness for different layers in the device.

For the calibration, a clean glass substrate is loaded into the evaporation chamber. The evaporation of target material is carried out to a target thickness which can be read using the thickness monitor. After the evaporation, the glass substrate is taken out and the real thickness is measured using the Dektak thickness measurement system. There are three calibration parameters for thermal evaporation – the tooling factor (TF), the density (DENS) and the acoustic impedance (AI) (or flow velocity). During the calibration process, two parameters are always considered fixed and the other one is calibrated. The density (DENS) of the material was chosen for calibration using equation 2.1:

$$DENS = DENS_{original} \times \frac{Thickness_{reading}}{Thickness_{measured}} \tag{2.1}$$

where $\text{DENS}_{original}$ is the density parameter of previous setting, $\text{Thickness}_{reading}$ is the thickness of the reading from the thickness monitor and $\text{Thickness}_{measured}$ is the thickness measured from Dektak thickness measurement system. Table 2.2 summarises all the parameters used for later device fabrication, following three rounds of calibration for each material.

Substrate Cleaning

A clean substrate is vital in order for effective photolithography. Any chemical residue or stains on the substrate can lead to the failure of the photolithography, they might cast a shadow during the UV-exposure and introduce extra shapes or detach and remove the photoresist. Hence a proper cleaning process is needed. The following steps are the detailed cleaning process:

1. Clean the indium tin oxide (ITO) coated glass substrate and beaker with laboratory detergent and distilled water.

2. Place the ITO coated substrate in ultrasonic bath with detergent and de-ionised water for 20mins.

3. Place the ITO coated substrate in ultrasonic bath with de-ionised water for 5mins three times.

4. Place the ITO coated substrate in ultrasonic bath with acetone for 5mins for twice.

5. Place the ITO coated substrate in ultrasonic bath with chloroform for 5mins for twice.

6. Blow dry the substrates with gentle nitrogen flow.

Photolithography

The ITO coated substrates are patterned using photolithography and the patterned ITO bottom electrodes provide the basis for the subsequent device fabrication and later measurement.

1. ITO-coated side of the substrate is identified with a multimeter.

2. Photoresist is spin-coated onto the ITO side of the substrate. As the photoresist is UV sensitive, the ambient light must not contain significant UV components. 8 $\sim$10 drops of photoresist are dropped with a pipette. The substrate is spin-coated at a rate of around $\sim$ 6000-7000 rpm for a minute.

3. The spin-coated substrates are cured in an oven at 90^{o}C for 15mins.

4. A mix of NaOH (87%) and distilled water at a ratio of 1:3 provides the developer.

5. The cured substrates are placed on the mask and exposed to UV light for 1min.

6. The exposed area is dissolved in the developer for 20$\sim$30s. Then the substrate is

rinsed in clean distilled water twice.

7. A mix of 50% distilled water, 48% hydrochloric acid, and 2% nitric acid provides the etching solution.

8. The etching solution is heated to 48∼50^{o}C. The substrate is placed in the warm etching solution for 1min 30s before removal.

9. The residual etching solution is rinsed with distilled water twice.

10. The standard cleaning procedure is used to clean the patterned substrates before subsequent steps.

The whole photolithography process is illustrated in Figure 2.5.

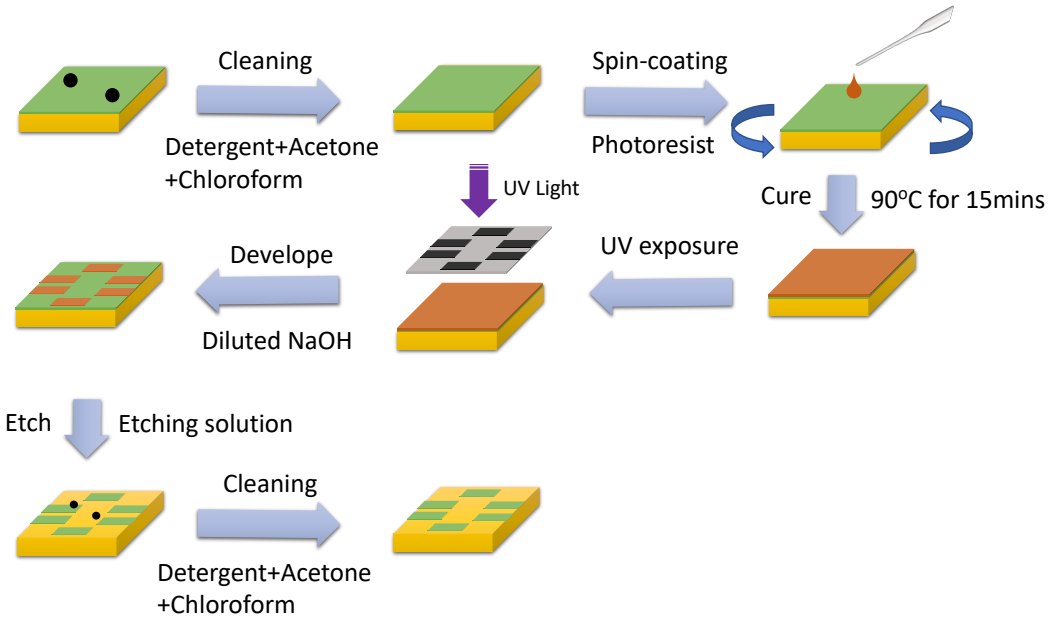

Figure 2.5: Schematic for photolithography

Oxygen Plasma Treatment

Prior to organic thin film deposition, oxygen plasma treatment must be done for two reasons: (1) to deeply clean the surface of the substrate for the removal of residual organics. (2) to lower the work function of the ITO electrode and improve the hole injection efficiency for the fabricated device.

For the first reason, because it will generate very high energy during the production of oxygen plasma, and this high energy is enough for breaking down the typical organic bonds such as C–H, C–C, C–O, etc. The oxygen plasma is highly reactive and efficient in the removal of organic contaminants.

During the process of oxygen plasma treatments, the oxygen concentration enhances greatly and decreases the electrode surface Sn:In ratio. This results in a decrease of electrons on the surface of the ITO, hence increasing the work function of the ITO electrode and improving hole injection[64–66].

The general process for oxygen plasma treatment is straightforward as follows:
1. The clean substrate is loaded into the plasma operating chamber with the ITO side facing up.
2. The plasma chamber is pumped and filled the chamber with oxygen at an ambient pressure of 2.3mbar, for 10mins.
3. The ambient pressure is adjusted to 0.2mbar and the power set to 28%. Then plasma treatment is then started. The treatment time is around 3min 30s.

After the plasma treatment, the clean substrate is immediately transferred to the thermal evaporation system, at an ambient vacuum level of around 1.5×10^{-7} mbar.

Organic Thin Film Deposition

In Figure 2.6 the schematic of the thermal evaporation system is illustrated. The whole system consists of two chambers – the load lock (**3**) and the evaporation chamber.

The clean substrate is then loaded into the load lock with the ITO side facing down. The substrate can be transferred to the cassette (**4**) in the evaporation chamber by the transfer arm (**1, 2**) and the cassette rotation rate can be set. The calibration parameters should be used in the monitor connected to the thickness measurement crystal (**5**). The source (**7, 8, 9, 10**) of the target material is preheated at correct power setting. When the deposition rate of a particular material reaches 0.05 nm/s, the main shutter (**6**) is open and the target material evaporation begins. When the thickness of the deposited target material reaches the target thickness, the main shutter is closed.

Table 2.3: Evaporation parameters for different materials.

Material	Duration/min	Power	Rate/nm· s^{-1}	Temp./^{o}C	Thick./nm	Vacuum/mbar
TPD	14.5	27%	0.23	171.8	50	10^{-7}
NPB	17	15%	0.2	192	50	10^{-7}
Alq_3	18	20%	0.17	118	50	10^{-7}
LiF	20	60%	0.02	650	1.5	10^{-7}
Al	20	38%	0.06, 0.5	– –	100	10^{-7}

The description is the general process of evaporating a specific material for the fabrication of a standard OLED, the materials NPB (or TPD), Alq_3, LiF and Al are evaporated in sequence from bottom-to-top. Detailed evaporation parameters are given in Table 2.3.

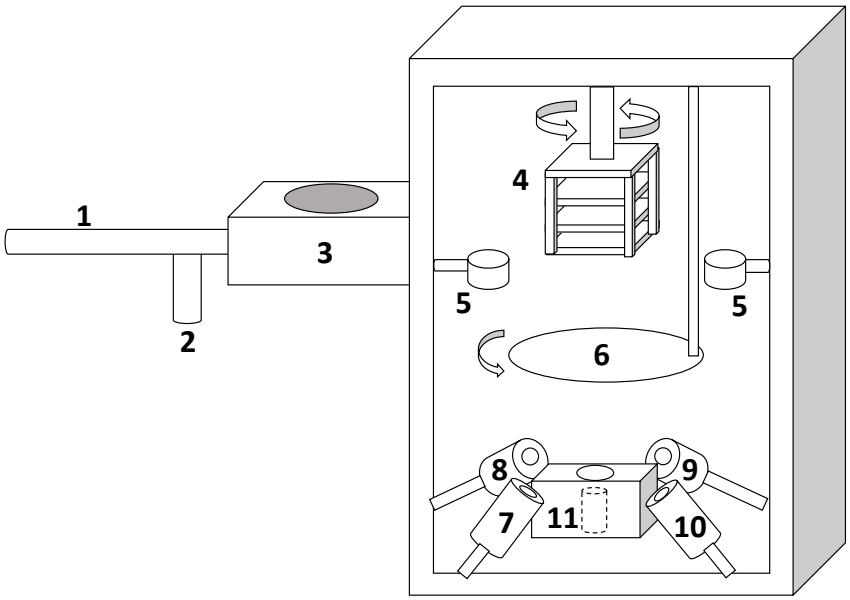

Figure 2.6: Thermal Evaporation System: 1. and 2. Transfer arm 3. Sample load lock 4. Cassette 5. Film thickness measurement crystal monitor 6. Shutter 7, 8, 9 and 10. Organic Sources for LiF, Alq_3, TPD and NPB respectively 11. Metal Source: Aluminium

In Table 2.3, there are two rates for the evaporation of Al and the slow rate (0.06 nm· s^{-1}) is applied for the first 10nm. The reason is that an initial slow growth rate can help better form a uniform thin Al film, which would have wider coverage over the deposited LiF thin film. After a thin Al film with good uniformity is grown, a

faster growth rate is then applied (in my experiment, it is 0.5 nm$\cdot$ s^{-1}) for rapidly increasing the thickness of the top electrode.

In Figure 2.7, a device and structure of a fabricated OLED are illustrated. As can be seen from Figure 2.7(a), there are four individual devices on the glass substrate and the size of the glass substrate and each device are 2cm$\times$2cm and 2mm$\times$2mm, respectively.

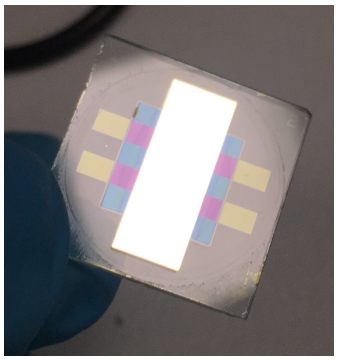

(a)

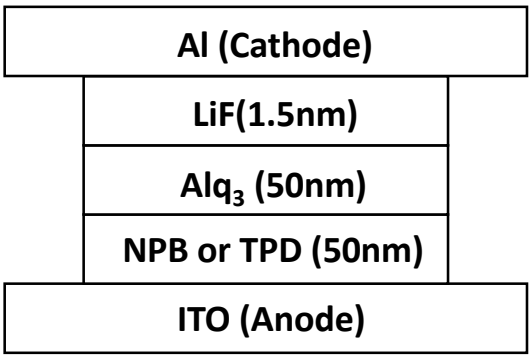

(b)

Figure 2.7: (a) A fabricated OLED (b) The structure of a fabricated OLED

2.2 Software and Equipment Engineering and Design

This section details the design and engineering of the magnetic field effect measurement system and the corresponding control software.

2.2.1 Three-Dimensional Helmholtz Coil Design

Since my work is based on ultra-small magnetic field effects, the μT range B field which is comparable to the Earth magnetic field ($\sim$50μT) has to be cancelled, leaving the applied magnetic field along a direction only towards the device. A magnetic field system has to be designed to achieve this function.

A Helmholtz coil is a known electromagnetic apparatus for producing magnetic fields. However, specific parameters and optimisation of the apparatus need to be carefully carried out so that a steady and ultra-small magnetic field can be generated.

The expression for the magnetic field produced by a single Helmholtz coil can be derived from first principles.

The magnetic field **B**, as a vector field, can be expressed as the curl of a vector potential **A** as shown in equation 2.2 and this resembles the relationship between the electric field **E** and the electric potential **V**: $\mathbf{E} = \nabla \times \mathbf{V}$

$$\mathbf{B} = \nabla \times \mathbf{A} \tag{2.2}$$

where **A** is the magnetic vector potential. **A** can be expressed as in equation 2.3:

$$\mathbf{A}(\mathbf{r}) = \frac{\mu_0}{4\pi} \int \frac{Idl}{|\mathbf{r} - \mathbf{r'}|} \tag{2.3}$$

where μ_0 is the vacuum permeability and equals to $4\pi \times 10^{-7}$ H/m. I is the current running through a single coil. dl is the unit vector along the path of the circle. And $|\mathbf{r} - \mathbf{r'}|$ is the displacement vector. This is illustrated is shown in Figure 2.8

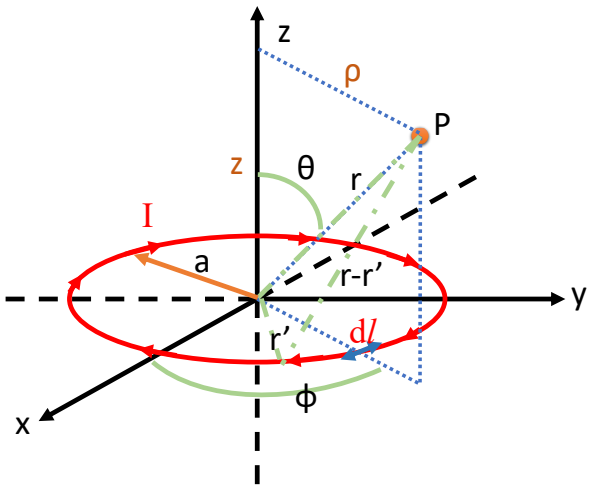

Figure 2.8: The schematic of the generated magnetic field by a single coil

The equation 2.4 and the equations in it can be written in spherical coordinates (θ, ϕ, r) in equation (a) to (d).

$$\begin{aligned}
&d\boldsymbol{l} = (-asin\phi, acos\phi, 0) \cdot d\phi \text{.....} (a), \\
&\boldsymbol{r} = (rsin\theta, 0, rcos\theta) \text{.....} (b), \\
&\boldsymbol{r'} = (acos\phi, asin\phi, 0) \text{.....} (c), \\
&|\boldsymbol{r} - \boldsymbol{r'}| = \sqrt{r^2 + a^2 - 2rasin\theta cos\phi} \text{.....} (d).
\end{aligned} \tag{2.4}$$

Noticeably, the position of point P is specifically chosen at XZ plane because of the symmetry of the magnetic field generated by a single coil for ϕ ranging from 0^o to 360^o. So in equation 2.4(b), there are only x and z components of $\boldsymbol{r}$. Additionally, the magnitude of $\boldsymbol{r'}$ is the same as a while $\boldsymbol{r'}$ is a vector and a is a scaler.

Substitute equation 2.3 with equation 2.4 and integrate over a whole circle from -π to π we obtain equation 2.5:

$$\mathbf{A}(\mathbf{r}) = \frac{\mu_0 Ia}{4\pi}\left(\int_{-\pi}^{\pi}\frac{-sin\phi}{|\mathbf{r}-\mathbf{r'}|}, \int_{-\pi}^{\pi}\frac{cos\phi}{|\mathbf{r}-\mathbf{r'}|}, 0\right)d\phi \tag{2.5}$$

In equation 2.5, because sinϕ is an odd function, the integral over a symmetric limit range would be zero, so the first term (i.e. the θ term in spherical coordinate (θ, ϕ, r)) would disappear, while the cosine function is an even function and can be integrated over half of the limit while doubling the integral as shown in equation 2.6.

$$\begin{aligned}\mathbf{A}(\mathbf{r}) &= \frac{\mu_0 Ia}{4\pi}\left(0, \int_{-\pi}^{\pi}\frac{cos\phi}{|\mathbf{r}-\mathbf{r'}|}, 0\right)d\phi \\ &= \frac{\mu_0 Ia}{4\pi}\left(0, \int_{0}^{\pi}\frac{2cos\phi}{|\mathbf{r}-\mathbf{r'}|}, 0\right)d\phi \\ &= \frac{\mu_0 Ia}{2\pi}\left(0, \int_{0}^{\pi}\frac{cos\phi}{|\mathbf{r}-\mathbf{r'}|}, 0\right)d\phi\end{aligned} \tag{2.6}$$

The vector potential now becomes a function only related to the ϕ term in the spherical coordinates, and replacing the term $|\mathbf{r}-\mathbf{r'}|$ with the expression given in equation 2.4 as resulted in equation 2.7:

$$\begin{aligned}\mathbf{A}_\phi(\mathbf{r}) &= \frac{\mu_0 Ia}{2\pi}\int_0^{\pi}\frac{cos\phi}{|\mathbf{r}-\mathbf{r'}|}d\phi \\ &= \frac{\mu_0 Ia}{2\pi}\int_0^{\pi}\frac{cos\phi}{\sqrt{r^2+a^2-2rasin\theta cos\phi}}d\phi\end{aligned} \tag{2.7}$$

It would be more straightforward to replace the spherical terms (θ, ϕ, r) in equation 2.7 with cylindrical terms (ρ, θ, z), where $r^2 = \rho^2 + z^2$, $sin\theta = \frac{\rho}{\sqrt{\rho^2+z^2}}$ and $\rho = rsin\theta$, yielding equation 2.8:

$$\mathbf{A}_\phi(\rho, \mathbf{z}) = \frac{\mu_0 Ia}{2\pi}\int_0^{\pi}\frac{cos\phi}{\sqrt{\rho^2+z^2+a^2-2a\rho cos\phi}}d\phi \tag{2.8}$$

As equation 2.8 is not in an explicit form, limit changes are needed in order to obtain a closed form with tabulated functions[67]. By replacing ϕ with $\pi + 2\varphi$ (so $d\phi = 2d\varphi$), the limits can be changed from π to $\pi/2$ as shown in equation 2.9:

$$\begin{aligned}
\mathbf{A}_\phi(\rho, \mathbf{z}) &= \frac{\mu_0 Ia}{2\pi} \int_0^{\pi} \frac{cos\phi}{\sqrt{\rho^2 + z^2 + a^2 - 2a\rho cos\phi}} d\phi \\
&= \frac{\mu_0 Ia}{\pi} \int_0^{\pi/2} \frac{cos(\pi + 2\varphi)}{\sqrt{\rho^2 + z^2 + a^2 - 2a\rho cos(\pi + 2\varphi)}} d\varphi \\
&= \frac{\mu_0 Ia}{\pi} \int_0^{\pi/2} \frac{(2sin^2\varphi - 1)}{\sqrt{\rho^2 + z^2 + a^2 - 2a\rho(2sin^2\varphi - 1)}} d\varphi \\
&= \frac{\mu_0 Ia}{\pi} \int_0^{\pi/2} \frac{(2sin^2\varphi - 1)}{\sqrt{(a+\rho)^2 + z^2 - 4a\rho sin^2\varphi}} d\varphi
\end{aligned} \tag{2.9}$$

According to [67], $k^2 = \frac{4a\rho}{(a+\rho)^2+z^2}$ is defined and equation 2.9 can be transformed into equation 2.10:

$$\mathbf{A}_\phi(\rho, \varphi) = \frac{\mu_0 I}{\pi k} \sqrt{\frac{a}{\rho}} \left[\left(1 - \frac{1}{2} k^2 \right) K(k) - E(k) \right] \tag{2.10}$$

where K(k) = $\int_0^{\pi/2} \frac{d\varphi}{\sqrt{1-k^2 sin^2\varphi}}$ and E(k) = $\int_0^{\pi/2} \sqrt{1 - k^2 sin^2\varphi} d\varphi$, which are all tabulated functions.

Using equation 2.2 and the rules for the curl (or del) in cylindrical coordinate, we can obtain equation 2.11

$$\begin{aligned}
&\mathbf{A} = (\rho, \phi, z) .....(a), \\
&\nabla \times \mathbf{A} = \left(\frac{1}{\rho} \frac{\partial A_z}{\partial \phi} - \frac{\partial A_\phi}{\partial z} \right) \rho + \left(\frac{\partial A_\rho}{\partial z} - \frac{\partial A_z}{\partial \rho} \right) \phi + \frac{1}{\rho} \left(\frac{\partial (\rho A_\phi)}{\partial \rho} - \frac{\partial A_\rho}{\partial \phi} \right) \mathbf{z} ...(b)
\end{aligned} \tag{2.11}$$

A is only the function of φ, the curl can be simplified as in equation 2.12:

$$\nabla \times \mathbf{A} = -\frac{\partial A_\phi}{\partial z} \rho + \frac{1}{\rho} \frac{\partial (\rho A_\phi)}{\partial \rho} \mathbf{z} = \mathbf{B}(\rho, z) \tag{2.12}$$

In real situations, when two Helmholtz coils are connected together, the magnetic field generated is between these two coils, that is, along the direction which is connecting the centres of two Helmholtz coils. This direction is in the z direction in Figure 2.8. During later simulations, only the B field along the z direction is considered. Hence the magnetic field generated by a single coil along z direction can be expressed as in equation 2.13:

$$\mathbf{B}_z = \frac{1}{\rho} \frac{\partial (\rho A_\phi)}{\partial \rho} = \frac{\mu_0 Ia^2}{2(a^2 + z^2)^{\frac{3}{2}}} \tag{2.13}$$

For the case of Helmholtz coil pair, the expression is modified with many turns as shown in Figure 2.9

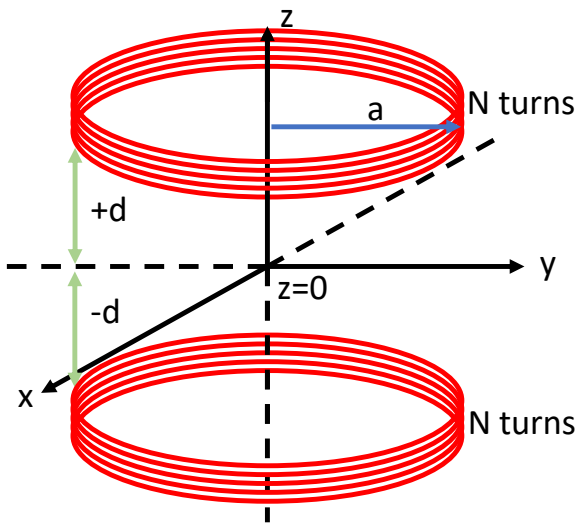

Figure 2.9: Schematic for a pair of coils with N turns, separated by a distance of 2d

Utilising the magnetic field generated by a single coil in equation 2.13, the magnetic fields generated by the pair of coils as a function of distance along z can be expressed as in equation 2.14

$$\begin{aligned} \mathbf{B}_{ztotal}(z) &= N \cdot \left(\mathbf{B}_{zupper}(+d) + \mathbf{B}_{zlower}(-d)\right) \\ &= \frac{\mu_0 I a^2 N}{2} \left[\frac{1}{(a^2 + (z+d)^2)^{\frac{3}{2}}} + \frac{1}{(a^2 + (z-d)^2)^{\frac{3}{2}}} \right] \end{aligned} \tag{2.14}$$

After obtaining of equation 2.14, it is important to know that how the generated magnetic fields change with the inter-coil distance. In these experiments, a uniform and steady magnetic field is needed.

It is obvious from Figure 2.10, in order to obtain a uniform magnetic field between the two coils (i.e. the yellow curve in Figure 2.10), the distance between two coils should be fixed as the same length of the coil radius. (i.e. d = a/2)

Also it is useful to know how the coil current changes with the number of turns as it will give information on how many turns are generally needed for a given drive current shown in Figure 2.11.

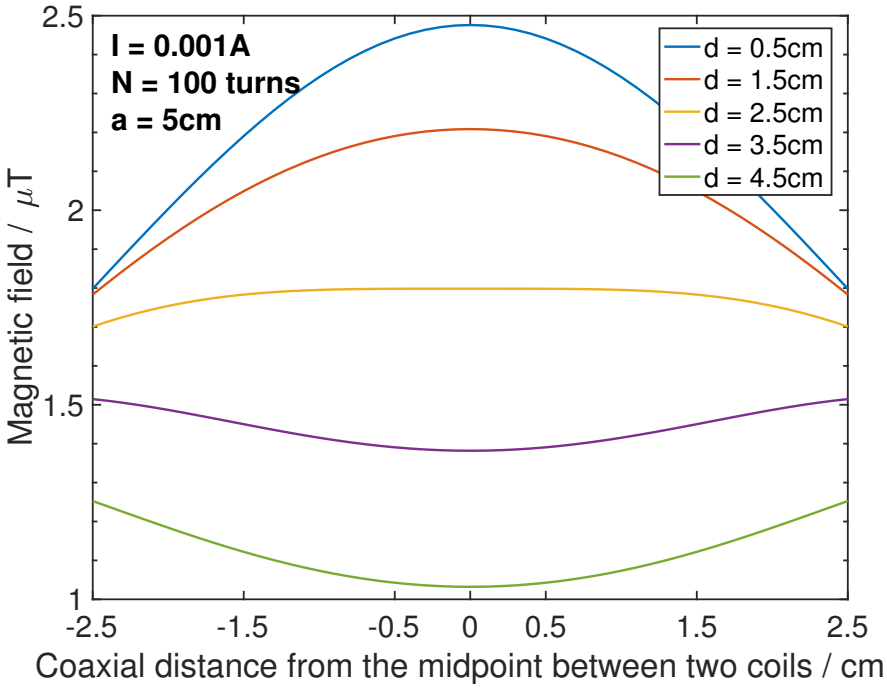

Figure 2.10: Simulation of the distance dependent magnetic fields generated by a coil pair. The coil radius is 5cm, with 100 turns and a coil current 0.001A.

From Figure 2.11, the coil current drops quadratically with the number of turns in the coils.

However, Figure 2.10 only shows the one dimensional magnetic field distribution along the coaxial distance between the two coils. In order to view the magnetic field uniformity in a three dimensional perspective, not only equation 2.14 is needed, but also the ρ term of the magnetic field **B** should be carried out in the simulation as shown in equation 2.15

$$\mathbf{B}_\rho(\rho,z) = \frac{\mu_0 I}{2\pi}\frac{z}{\rho\sqrt{(\rho+a)^2+z^2}}\left[\frac{a^2+\rho^2+z^2}{(a-\rho)^2+z^2}E(k)-K(k)\right] \tag{2.15}$$

where K(k) and E(k) are defined previously in equation 2.10. As the final 3D simulation result is shown in Figure 2.12, using the same parameters in Figure 2.10 and choosing d = a/2 where the 2D distribution of the generated magnetic field is uniform.

As can be seen from Figure 2.12(b), the magnetic field in the square region is uniformly distributed with a variation of less than 0.4 μT/cm, and this square region

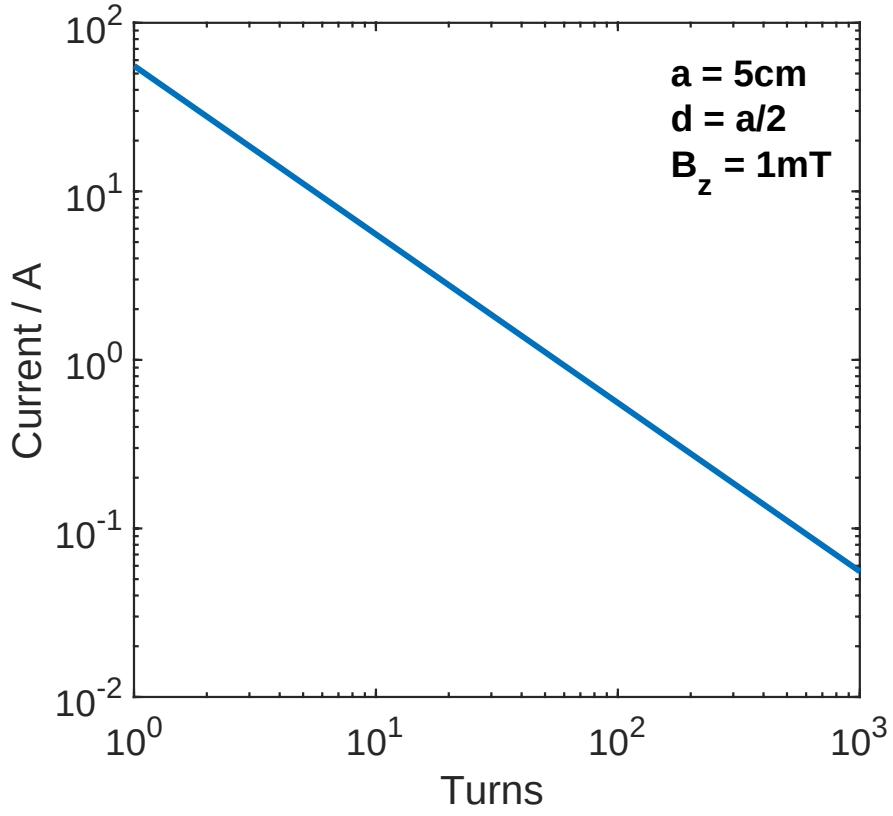

Figure 2.11: Simulation of the distance dependent magnetic fields generated by a coil pair. The coil radius is 5cm, with a feeding magnetic field 1mT.

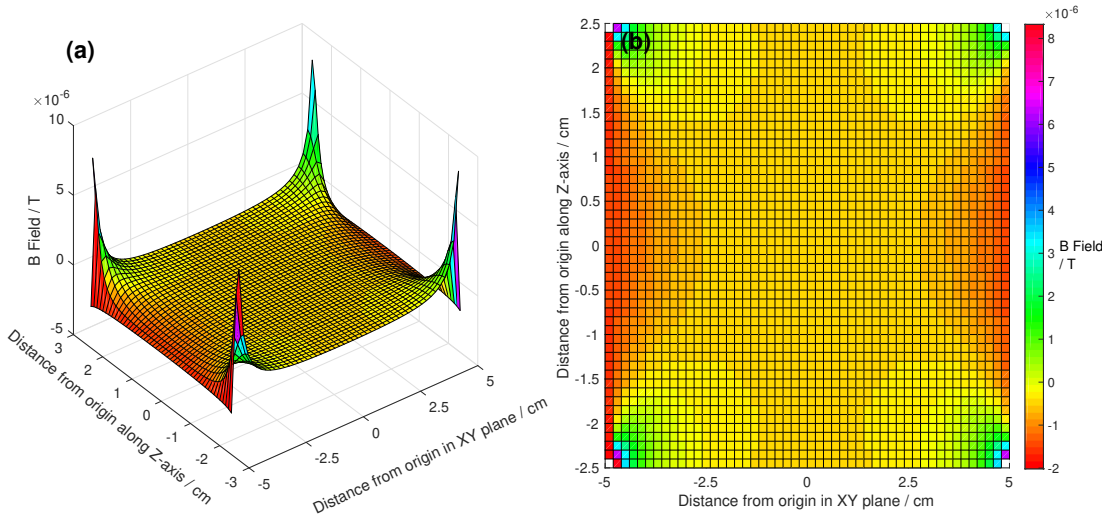

Figure 2.12: Simulation of the 3D distribution of the generated magnetic field. The coil radius is 5cm, with turns of 100 and a coil current 0.001A.

is where the device-under-test will be located.

Another factor that needs to be considered in designing the Helmholtz coil is the temperature changing due to the current running in the coils. This is important

because the amount of heat produced by running the coils determines whether extra cooling is needed. Parameters can be engineered to control the heat within a minimum. The power generated heat is given in equation 2.19, calculated using heat capacity[68].

$$\begin{aligned} P = Q &= C \cdot (\frac{\Delta T}{t}) \cdot m, \\ \frac{\Delta T}{t} &= \frac{P}{C \cdot m} = \frac{I^2 \cdot R}{C \cdot m} = \frac{I^2 \cdot \rho_{res} \frac{l}{A}}{C \cdot m} \\ &= \frac{I^2 \cdot \rho_{res} \frac{l}{A}}{C \cdot \rho_{mat} \cdot Vol} = \frac{I^2 \cdot \rho_{res} \frac{l}{A}}{C \cdot \rho_{mat} \cdot l \cdot A} \\ &= \frac{I^2 \cdot \rho_{res} \cdot l}{C \cdot \rho_{mat} \cdot l \cdot A^2} = \frac{I^2 \cdot \rho_{res}}{C \cdot \rho_{mat} \cdot A^2} \\ &= \frac{I^2 \cdot \rho_{res}}{C \cdot \rho_{mat} \cdot (\pi \cdot R_{wire})^2} \end{aligned} \tag{2.16}$$

where P is the power generated by the coil systems, Q is the heat, C is the heat capacity of the material of the wire for the coils, $\frac{\Delta T}{t}$ is the rate of the temperature change in unit time, R is the resistance of the wire, m is the mass of the coils, I is the current running through the coils, l is the length of the coil wire, A is the cross section area of the coil wire. Vol is the volume of the coil wire, ρ_{res} is the resistivity of the coil material, ρ_{mat} is the density of the coil material, R_{wire} is the radius of the wire for the coils. The current I can be expressed in the form shown in equation 2.14 as a function of $\mathbf{B}_{ztotal}$.

The results of simulation of the rate of the temperature change versus coil turns with different radii are shown in Figure 2.13

As can be seen from Figure 2.13, the rate of the temperature change decays exponentially with the number of turns in the coil, meanwhile, the thicker the wire is, the less the rate of the temperature changes at a given time. This will be an important indicator for the optimisation of the Helmholtz coil design.

However, for the previous simulations above, the situation of all the wires overlapping is assumed, and this is not realistic when a number of wires is bundled together. In a real case, when wires are coiled, because each wire will lie on top of the previous wiring, the total thickness of the wirings is increased with the number of turns, and this thickening effect can affect the generated magnetic field [68].

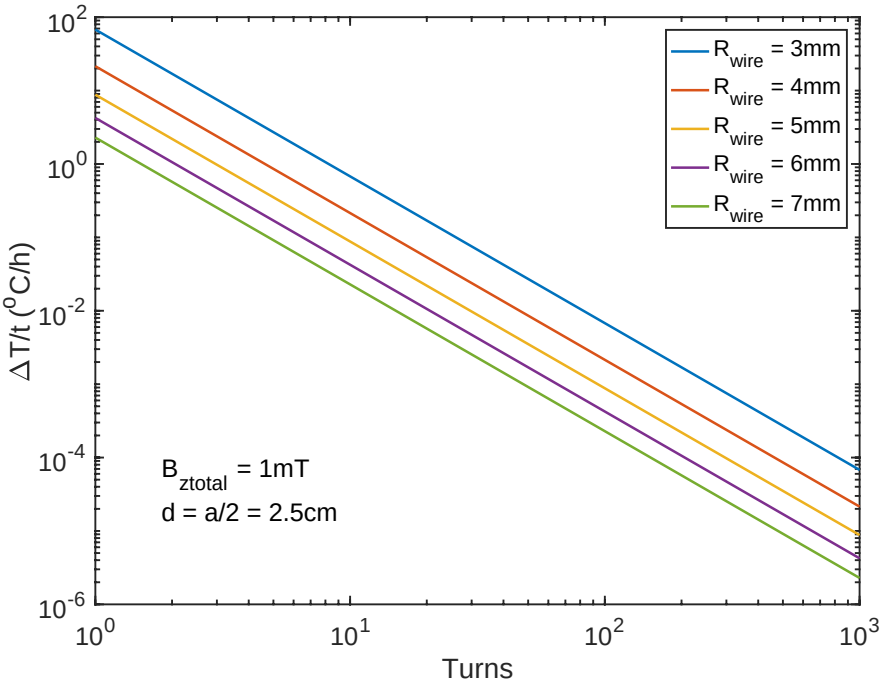

Figure 2.13: Simulation of rate of the temperature change versus coil turns. The coil radius is 5cm, and the nominal magnetic field is 1mT.

When wiring the coil, the thickening due to wires adding up can be explained in Figure 2.14(a).

According to Figure 2.14(a), the thickening due to the wiring is x and can be calculated by Pythagorean theorem:

$$\begin{aligned} (2r)^2 &= r^2 + x^2, \\ x &= \sqrt{3} \cdot r \end{aligned} \tag{2.17}$$

For Figure 2.14(b), the real situation of coil wiring thickening effect is shown. For coil I, the thickening on the x direction due to i^{th} layer is defined in equation 2.18:

$$x_i = x_1 + (i-1)\frac{\sqrt{3}}{2} \cdot 2r \tag{2.18}$$

where $x_1 = a + r$. However, in the z direction, due to the effect of the grooves, the value of z (or $z_{j,I}$) is dependent on the turn of the specific wiring and the end result can be expressed in equation 2.19

$$z_{j,I} = \begin{cases} z_1 + (j-1) \cdot 2r, & \text{if i is odd.} \\ z_1 + r + (j-1) \cdot 2r, & \text{if i is even.} \end{cases} \tag{2.19}$$

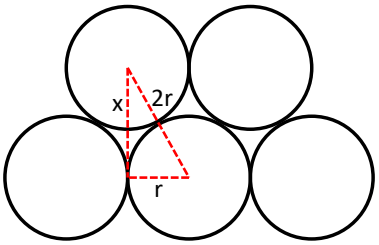

(a) Cross section of coil thickening due to wiring patterns. The wire radius is r and x is the thickened length.

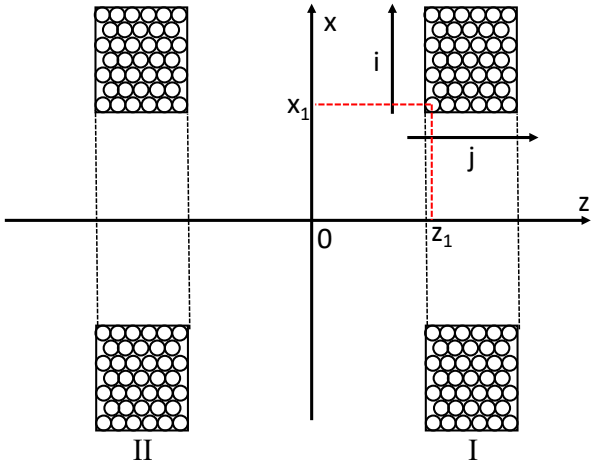

(b) Cross section of a pair of coil due to wiring effect

Figure 2.14: Illustration for the wiring effect in the coils.

Now $z_{j,I}$ and x_i can replace the terms for z and a in equation 2.13, respectively, and yield equation 2.20.

$$\mathbf{B}_{z,I} = \frac{\mu_0 I}{2} \cdot \sum_{i=1}^{N_i} \sum_{j=1}^{N_j} \frac{(x_1 + (i-1) \cdot \frac{\sqrt{3}}{2} \cdot 2r)^2}{((x_1 + (i-1) \cdot \frac{\sqrt{3}}{2} \cdot 2r)^2 + (z - z_{j,I})^2)^{\frac{3}{2}}} \tag{2.20}$$

Likewise, the expression for coil II can be derived in a similar manner, with the sign reversal of the z term ($z_{j,II} = -z_{j,I}$) and can be expressed in equation 2.21:

$$\mathbf{B}_{z,II} = \frac{\mu_0 I}{2} \cdot \sum_{i=1}^{N_i} \sum_{j=1}^{N_j} \frac{(x_1 + (i-1) \cdot \frac{\sqrt{3}}{2} \cdot 2r)^2}{((x_1 + (i-1) \cdot \frac{\sqrt{3}}{2} \cdot 2r)^2 + (z + z_{j,II})^2)^{\frac{3}{2}}} \tag{2.21}$$

Therefore, the magnetic field generated by this coil with consideration of the

wiring patterns can be expressed in equation 2.22:

$$\begin{aligned}\mathbf{B}_{z,total} &= \mathbf{B}_{z,I} + \mathbf{B}_{z,II} \\ &= \frac{\mu_0 I}{2} \cdot \sum_{i=1}^{N_i} \sum_{j=1}^{N_j} \frac{(x_1 + (i-1) \cdot \frac{\sqrt{3}}{2} \cdot 2r)^2}{((x_1 + (i-1) \cdot \frac{\sqrt{3}}{2} \cdot 2r)^2 + (z - z_{j,I})^2)^{\frac{3}{2}}} \\ &+ \frac{\mu_0 I}{2} \cdot \sum_{i=1}^{N_i} \sum_{j=1}^{N_j} \frac{(x_1 + (i-1) \cdot \frac{\sqrt{3}}{2} \cdot 2r)^2}{((x_1 + (i-1) \cdot \frac{\sqrt{3}}{2} \cdot 2r)^2 + (z + z_{j,II})^2)^{\frac{3}{2}}}\end{aligned} \tag{2.22}$$

Figure 2.15 shows the result of the $\mathbf{B}_{z,total}$ in equation 2.22 with different wire radii, adding the comparison to the result of $\mathbf{B}_{z,total}$ without any consideration of the wiring situation before (the dashed line in Figure 2.15.)

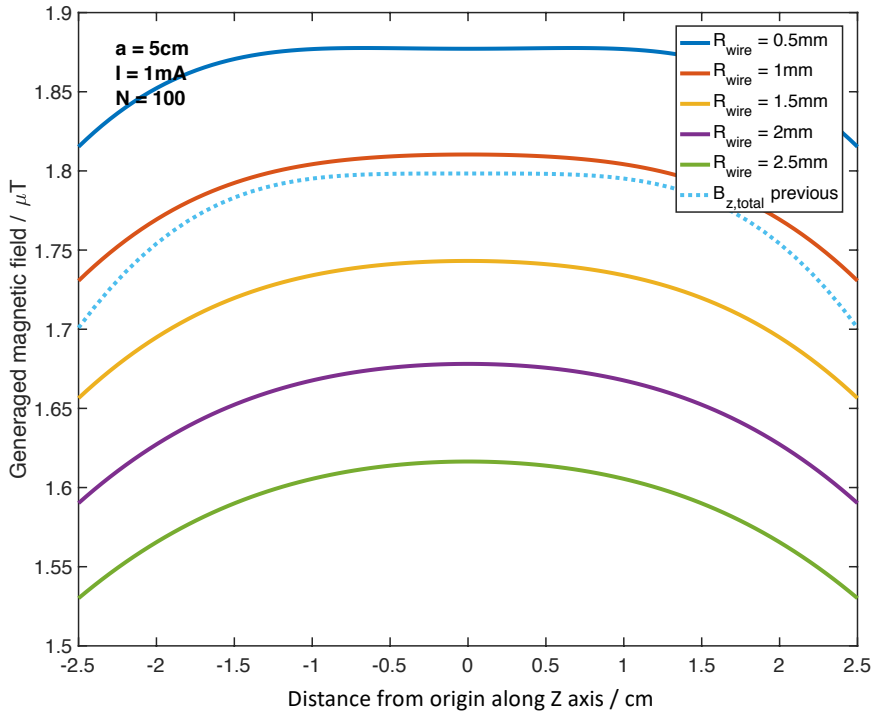

Figure 2.15: Simulation of $\mathbf{B}_{z,total}$ using equation 2.22. The coil radius is 5cm, and the feeding coil current is 1mA.

As can be seen from Figure 2.15, in a real situation where the wiring distribution is considered into the generated magnetic field, the thicker the wire used in the coils, the less uniform the generated magnetic field is for the coils. This can also be an important indicator for engineering the coil parameters for optimisations later.

Table 2.4 shows different coil parameters (such as the resolution of the magnetic fields and driving current in the Helmholtz coils) to yield different turns and the rate

Table 2.4: Coil parameter optimization. Bres: resolution of magnetic field. Ires: resolution of current.

						ΔT/h (°C/h)				ΔT/h (°C/h)				ΔT/h (°C/h)		
				Turns		0.6mm	0.8mm	1mm		0.6mm	0.8mm	1mm		0.6mm	0.8mm	1mm
Bres = 2μT	Ires = 1mA	coil radius	5cm	112	Bmax = 1mT	54.1	17.1	7	Bmax = 2mT	217	68.5	28.1	Bmax = 3mT	486.5	153.9	63.1
			7cm	156		40.1	12.68	5.2		160	50.7	20.8		360.8	114.2	46.8
			8cm	178		37.1	11.7	4.8		148	47	19.2		334	105.6	43.3
			10cm	223		33.5	11	4.3		134	42.4	17.4		301.5	95.4	39.1
			11cm	245		32.6	10.3	4.2		130	41.2	16.9		293.1	92.7	38
			13cm	290		31.1	9.8	4		125	39.4	16.1		280.1	88.6	36.3
						ΔT/h (°C/h)				ΔT/h (°C/h)				ΔT/h (°C/h)		
				Turns		0.6mm	0.8mm	1mm		0.6mm	0.8mm	1mm		0.6mm	0.8mm	1mm
Bres = 5μT	Ires = 1mA	coil radius	5cm	278	Bmax = 1mT	8.7	2.7	1.1	Bmax = 2mT	35	11.1	4.5	Bmax = 3mT	79	25	10.2
			7cm	334		8.7	2.7	1.1		35	11.1	4.5		79	25	10.2
			8cm	366		8.8	2.7	1.1		35	11.1	4.5		79	25	10.2
			10cm	436		8.7	2.7	1.1		35	11.1	4.5		79	25	10.2
			11cm	472		8.7	2.7	1.1		35	11.1	4.5		79	25	10.2
			13cm	547		8.7	2.7	1.1		35	11.1	4.5		79	25	10.2
						ΔT/h (°C/h)				ΔT/h (°C/h)				ΔT/h (°C/h)		
				Turns		0.6mm	0.8mm	1mm		0.6mm	0.8mm	1mm		0.6mm	0.8mm	1mm
Bres = 2μT	Ires = 0.1mA	coil radius	5cm	1113	Bmax = 1mT	0.5	0.2	0.07	Bmax = 2mT	2.2	0.7	0.3	Bmax = 3mT	4.9	1.6	0.64
			7cm	1334		0.5	0.2	0.07		2.2	0.7	0.3		4.9	1.6	0.64
			8cm	1465		0.5	0.2	0.07		2.2	0.7	0.3		4.9	1.6	0.64
			10cm	1744		0.5	0.2	0.07		2.2	0.7	0.3		4.9	1.6	0.64
			11cm	1889		0.5	0.2	0.07		2.2	0.7	0.3		4.9	1.6	0.64
			13cm	2185		0.5	0.2	0.07		2.2	0.7	0.3		4.9	1.6	0.64

of the temperature change for different radii of coils. As can be seen, the variables in the simulation are the resolution of the magnetic field and driving current of the coil. This is because in experiments of ultra-small magnetic field effects, the resolution of the magnetic field scanning should be explicitly small for the precision of the experiment. Thus in the simulation results of Table 2.4, very small magnetic field resolutions are used ($2\mu T$ and $5\mu T$). At the same time, the resolution of the driving current is also considered. As in a real case, some external power supply (specifically, the current supply) is needed for driving the coil, and the current resolution of the power supply determines the resolution of the drive current. Also, importantly, the finer the resolution of the current of the power supply, the more expensive equipment, and this should also be considered during the process of parameter optimisation. Additionally, the turns of the coils should be considered as well as the price of the wire (enamelled copper wire).

As this is a 3D Helmholtz coil, 3 pairs of coils with different sizes should be obtained and each pair should fit inside the outer coil pairs. So, there are several factors to be optimised for the coils. The resolution of the generated magnetic fields and the drive current, the turns of the coils and the rate of the temperature change of the coils.

From Table 2.4, the small magnetic field resolution rows (main row 1 and main row

3), the difference is the driving current resolution where main row 1 is 1mA resolution while main row 3 is 0.1mA. Although the rate of the temperature change due to the smaller current resolution (0.1mA) reduces significantly, however, the turns for the coils increase dramatically. So using the parameters in main row 3 is going to make the cost of the 3D Helmholtz coil system very high (very small current resolution power supply and large amounts of enamelled copper wire for thousands of turns of wirings.).

However, using the parameters in main row 2 can significantly drop the rate of the temperature change compared to that in main row 1, but this is at the cost of the magnetic field resolution and the turns of the wirings. This is also undesirable because it sacrifices the important factor of magnetic field resolution in order to get a small rate of the temperature change. In my experiments, the magnetic field ranges should be comparable to the Earth's magnetic field ($\sim 50\mu T$) and $5\mu T$ resolution is too big a step if the magnetic field range needs to be extensively investigated. Therefore, plan 1 (using the parameters in main row 1) is an optimal choice.

As can be seen from main row 1, the rate of the temperature change can be controlled down to a significantly small range if a relatively thicker copper wire is applied (i.e. 1mm diameter). As mentioned previously, the sizes of three pairs of coils should be considered carefully as the smallest pair should fit into other pairs. Three pairs of coils with coil radii of 5cm, 8cm and 11cm are considered optimal for this situation, with the corresponding numbers of turns: 112, 178 and 245.

A draft of the 3D Helmholtz coils is shown in Figure 2.16 using AutoCAD.

The 3D Helmholtz coil system is made with the help of Mr. Geoff Gannaway in the workshop. And the final product is shown in Figure 2.17

As can be seen from Figure 2.17, the three pairs of coils (made of Aluminium) are named Coil X, Coil Y and Coil Z, in which Coil Z is the innermost coil pair and is used for the magnetic field scanning for the device (i.e. the magnetic field provided for measurement of magnetic field effect), Coil X and Coil Y pairs are used for cancelling the external residual magnetic field (e.g. the Earth magnetic field). The device is located in the middle of the common area shared by those three pairs of coils.

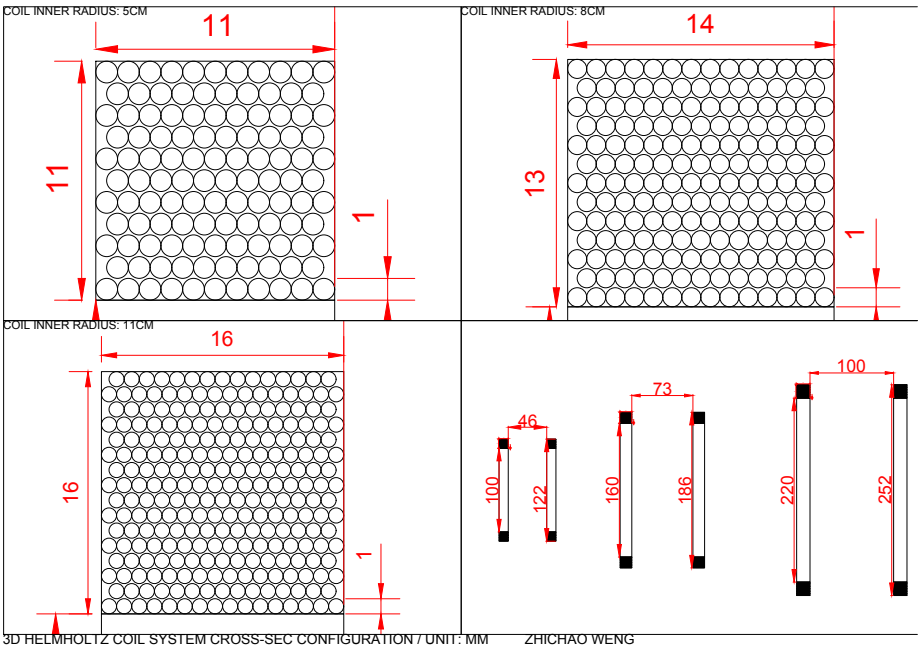

(a) Sketch for the cross section of each coil pair

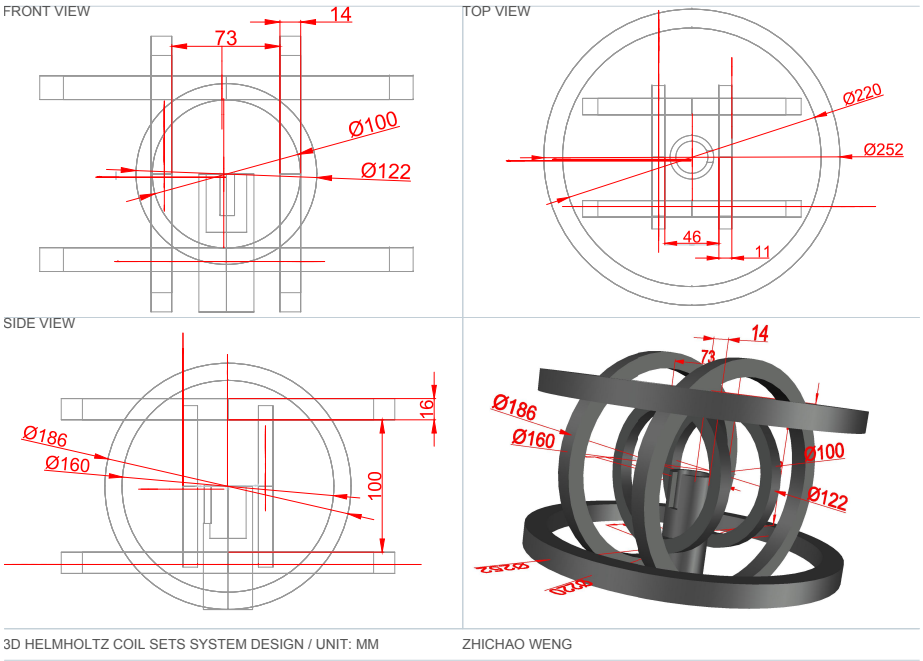

(b) Sketch for the whole set of 3D Helmholtz coil in different perspectives. unit of the length: mm

Figure 2.16: Schematics of the draft for the designed and optimised 3D Helmholtz coil

In order to test if the magnetic field generated by each pair of coils is uniform over the device in the middle, it is important to measure the magnetic field distribution for

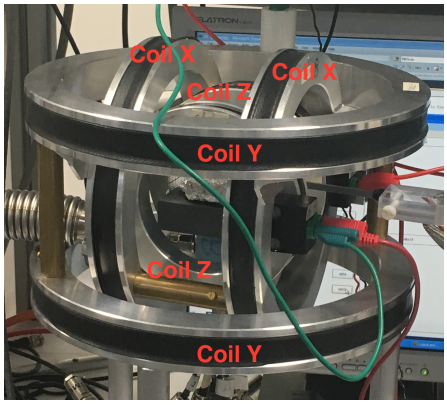

Figure 2.17: The 3D Helmholtz Coil System

Table 2.5: Statistics of the magnetic field for each coil pair

	Coil X	Coil Y	Coil Z
Average	51.68μT	49.38μT	51.06μT
Standard Deviation	0.3μT	0.3μT	0.2μT
Standard Error	0.03μT	0.05μT	0.04μT

each of the coil pairs in the regime where the device-under-test is located.

The 3D map in Figure 2.18 indicates how the magnetic field is distributed spatially. The measurement process is as follows: a point is fixed in the space within the region where the device is located. The current is fed into the coil and the static magnetic field is measured at that specific point. The current is adjusted to obtain a specific value (e.g. 50μT). The current is kept constant at that value and the Gaussmeter is moved about a point and a record of the magnetic field at different points is kept. The data can be collected and mapped against the spatial distribution of the coils and the result is analysed as shown in Figure 2.18. After the calculation according to the 3D mappings, the statistics of each coil pair are calculated as shown in Table2.5.

From Table2.5, the variations in the magnetic field are significantly small as indicated by the very small standard errors of the three pairs. This shows the great stability in producing magnetic fields within the region where the device is located.

After the magnetic field generation system is completed, it is necessary to design a control and measurement system and software to carry out measurements of ultra-small magnetic field effects.

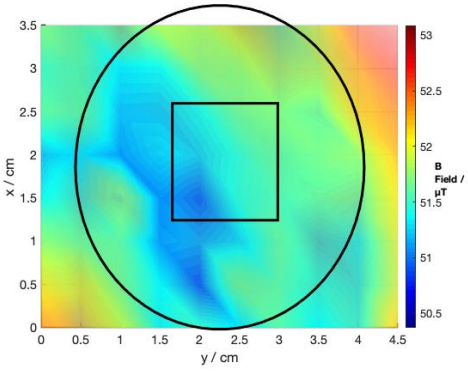

(a) Coil X: Top view of the B field distribution. Device is in the square region

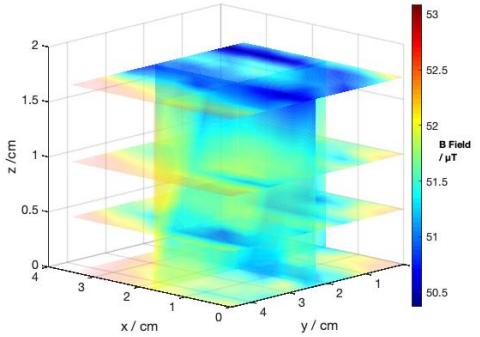

(b) Coil X: 3D map of the B field generated by Coil X pairs. Device is at 0.5 $\sim$ 1cm along z axis

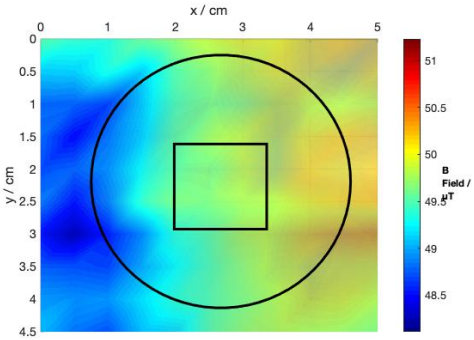

(c) Coil Y: Top view of the B field distribution. Device is in the square region

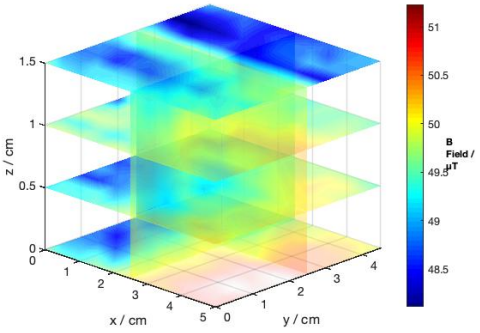

(d) Coil Y: 3D map of the B field generated by Coil Y pairs. Device is at 0.5 $\sim$ 1cm along z axis

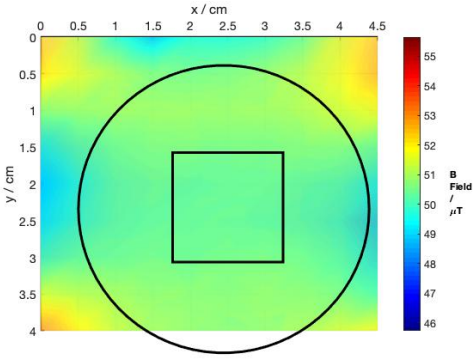

(e) Coil Z: Top view of the B field distribution. Device is in the square region

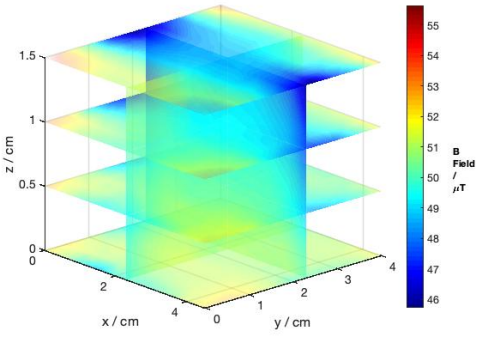

(f) Coil Z: 3D map of the B field generated by Coil Z pairs. Device is at 0.5 $\sim$ 1cm along z axis

Figure 2.18: 3D map of the B field generated by three pairs

2.2.2 Magnetic field effect measurement system and control software design

It is necessary to control the magnetic field generation system using a control software for measurements to be possible.

The magnetic field effect measurement system is assembled first. As shown in Figure 2.19, the measurement system is composed of several components serving different functions.

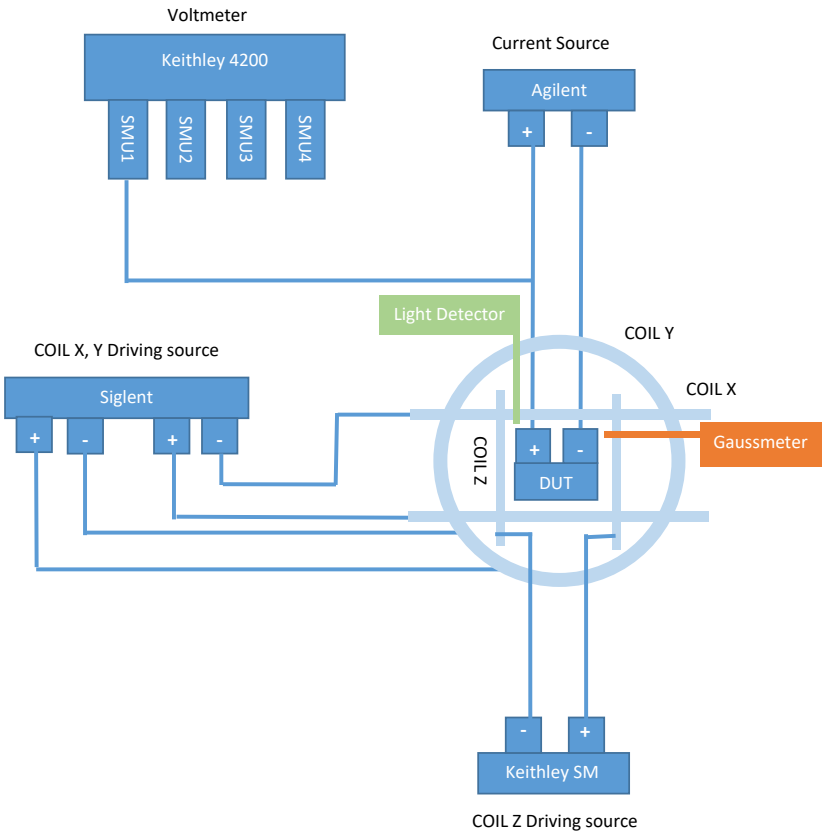

Figure 2.19: The ultra-small magnetic field effect measurement system

A power supply (or current supply) is needed for driving the coils to reach a given value of magnetic field. A device current source is also needed for driving the device-under-test (DUT) and a "voltmeter" is needed to record any device voltage changes. Equipment for measuring and recording the magnetic field and light intensity generated by the DUT are also needed (Gaussmeter and light detector).

A Keithley Semiconductor Characterization System (Model 4200-SCS) is used and programmed as a precision "voltmeter" to record the device voltage changes. A Semiconductor Characterization System is necessary for measuring the ultra-small magnetic field effect ($\sim 10^{-4}\%$). This measurement can only be achieved by a high precision measuring system. The Keithley Semiconductor Characterization System

(Model 4200-SCS) can perform 6-digit precision measurements and make the small effect ($\sim 10^{-5}$%) measurable. For the device driving current supplier, a Precision Source/Measure Unit (Agilent B2900) is used. This supply only provides a current but other measurements are not required. This specific model can supply a current with a very high resolution (100pA) when the current in the range is up to $10\mu A$. As for the coil current supply, the only requirement is that the current resolution should be 1mA as indicated by the final optimisation result in subsection **2.2.1**. A DC power supply (Siglent, SPD3303X) with a current resolution of 1mA provides drive current for the coil pairs (two coil pairs for cancelling the environmental residual magnetic fields). Since there are only two sets of outputs available for Siglent power supply, so another power supply (Keithley, 2400 SourceMeter) is needed for the drive current for the third pair of coils (the scanning B field for the device). Another reason for choosing a separate power supply to drive the third coil is to avoid any signal intercross. The precision of the Gaussmeter is vital to the experiment as this directly determines the recorded magnetic field which the device is actually experiencing. By using a Gaussmeter (LakeShore DSP Gaussmeter, Model 475) with a specific high sensitivity Hall probe, the resolution of the magnetic field measurement can reach 0.15μT. For light detection and measurements, an optical power meter (Newport, 1830-C) is used with a precision of 4-1/2 digit.

It is important to design the sequence of each signal (device driving current starting and ending time, coil magnetic field changing time, etc) before designing the algorithm for the controlling software. Figure 2.20 shows the control sequence for different operations and is the foundation for that software algorithm.

As shown in Figure 2.20, the device is switched with a specific drive current (I_0) before any other control commands. This allows the device to settle before any measurement takes place. After the settling time for the device, the magnetic field of the coil is generated and yield the 1st target magnetic field value B_1. Then the magnetic field, device voltage and device light output are recorded consecutively as indicated in Figure 2.20. After the measurements, the magnetic field is switched from B_1 to the next target magnetic field B_2, and the same sequence occurs until all the

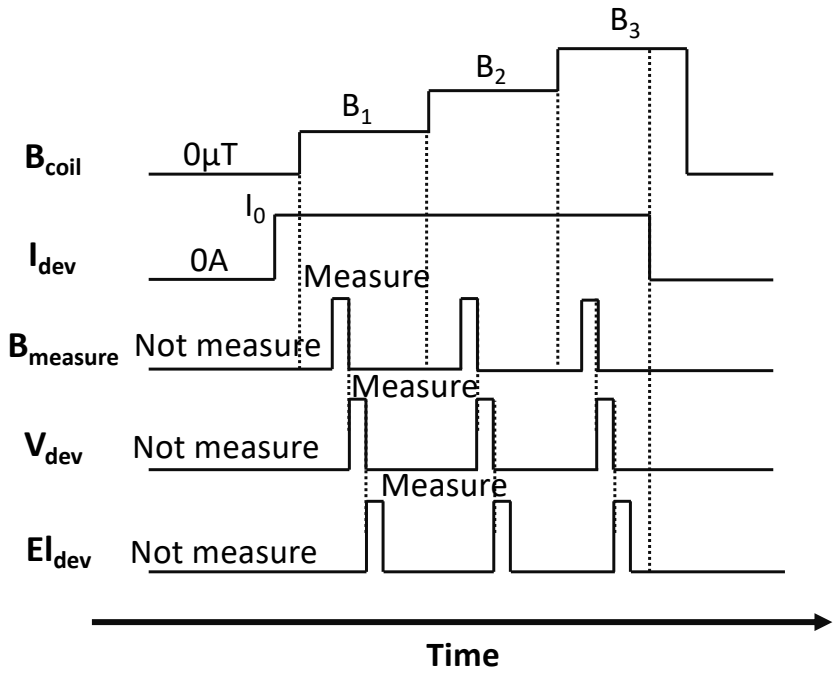

Figure 2.20: The designed controlling sequence for the ultra-small magnetic field effect measurement

measurement are completed for all the target magnetic fields. The device is switched off before turning the magnetic field to null. Noticeably, the device is always kept on until all the measurements are completed.

The algorithm of the control software is based on Visual Basic .NET due to its straightforward coding style and easy graphical user interface (GUI) based on Visual Studio platform.

Figure 2.21, this is the top level of the whole algorithm with many functional blocks built in. In total, there are 6 functional blocks in this top level flowchart, namely: the Input block, the Initialisation block, the coil driving current calculating block, the device sourcing block, the measurement block and the output block. Generally, the software can be considered as a "blackbox" with an input and an output, and inside the "blackbox" the core functional part is a self-looping process to complete the magnetic field effect measurement. There follows a detailed description and explanation of each functional block.

Input block: The structure of the input block is shown in Figure 2.24. This is the entrance block to the whole software where the target magnetic fields and target

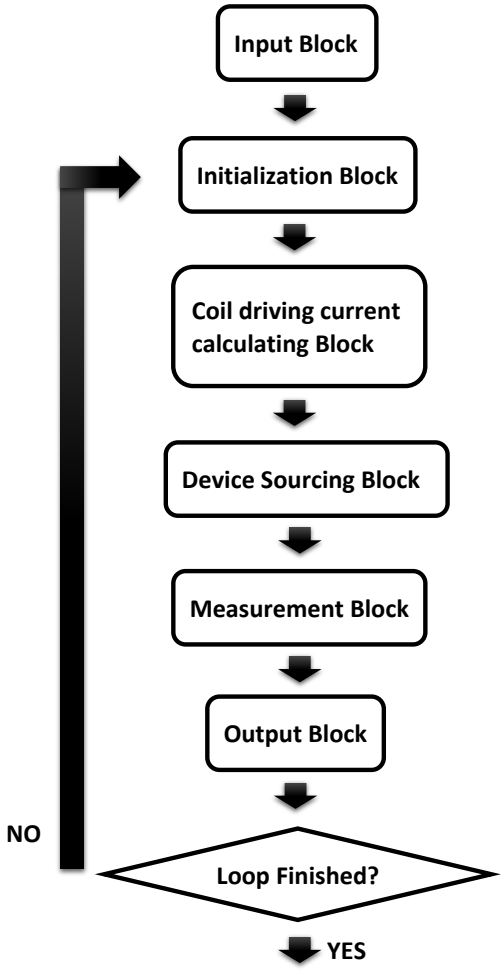

Figure 2.21: Top level flowchart for the control software

device driving current are defined as matrices.

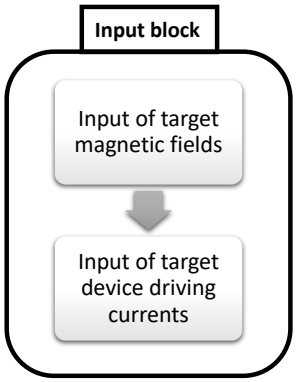

Figure 2.22: Structure for the input block

Initialisation block: the software will initialise the equipment to be used to ensure

it works as expected. There are three devices that need initialisation: the light detector, the Keithley "voltmeter" and the device current sourcing equipment. Noticeably, it is this initialisation that commands the Keithley Semiconductor Characterization System and Agilent Precision Source/Measure Unit to function as a "voltmeter" and a device current source, respectively. The initialisation of the light detector switches on the auto-ranging in the power meter, increasing the precision of the collected data.

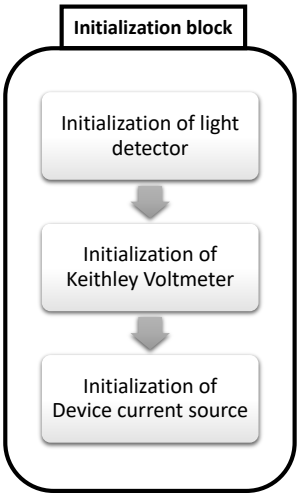

Figure 2.23: Structure for the initialisation block

Coil Driving Current Calculating Block: The drive current corresponding to different target magnetic fields has to be calculated and sent to the power supply of the Helmholtz coils. In this block, the linear relationship between **B** and the coil current **I** as shown in equation 2.22 is used, and all the other parameters can be treated as a constant $\mathbf{K}_{coil}$. There is a shift between the driving current and the target magnetic field due to the environmental magnetic field. This block finds this environmental magnetic field first and then feeds it into the linear calculation formula to calculate the coil drive current corresponding to the target magnetic field. The code used is as follows:

```
   Blocal = 0
Do Until z = 3
Blocal = B_Reading() + Blocal 'B_Reading() is the function built
for measuring the magnetic field by the Gaussmeter
```

```
System.Treading.Thread.Sleep(3000) 'wait for 3 seconds for the next
measurement
z = z + 1
Loop
Blocal = -(Blocal / 3)
Do Until x = size
designedIcoil(x) = (designedBfield(x) + Blocal) / Kcoil
x = x + 1
Loop
```

Having calculated the coil driving current `designedIcoil` it can be directly sent to the power supply for the Helmholtz coil pairs.

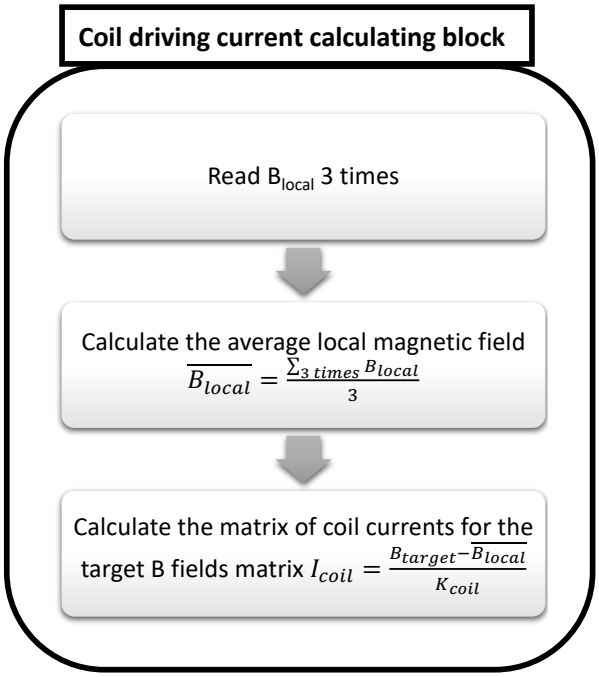

Figure 2.24: Structure for the coil driving current calculating block

Device Sourcing Block: This block provides the target device drive current on the device, namely, it switches on the device as can be seen from Figure 2.25. As indicated by the sequence in Figure 2.20, before switching on the device, the magnetic field

should be set to zero. This is to ensure that the initial state is at zero field instead of some biased magnetic field field where the device might display a magnetic field effect. After settling the magnetic field, the device drive current is applied to switch it on. The last stage of this block is to set the magnetic field to the first target magnetic field for the preparation of the next block after the settling of the device. There is a very important function `Z_KEI(magnetic field)`, which is built to input any target magnetic field and transfer it to the Z coil power supply (Keithley, 2400 SourceMeter) to make coil Z generate the target magnetic field which can be defined as follows:

```
   Sub Z_KEI(ByVal Current As Single)
Dim GpibDevice = New Device(0, CInt(GPIBKeith)) 'declaire the new
variable GpibDevice as a Device type
GpibDevice.Writer(":SOUR:CURR " & Trim(Current)) 'write the tar-
get current into the Keithley power supply by its own programming
language
System.Threading.Thread.Sleep(100)'wait for 100 ms for the equip-
ment to response
GpibDevice.Dispose() 'dispose the temporary buffer for storing this
information
End Sub
```

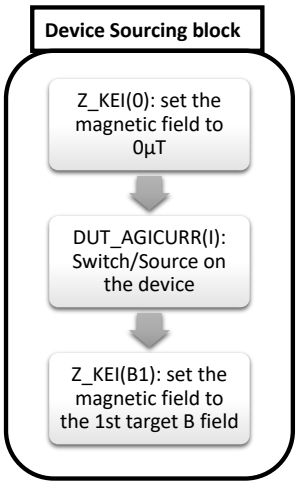

Figure 2.25: Structure for the device sourcing block

Measurement Block: Every measurement (magnetoconductance and magneto-electroluminescence) occurs in this block. As shown in Figure 2.26 that this block consists of a nested loop, which facilitates the whole measurement process of the MC and MEL of the device over all the target magnetic fields. There are four important functions used in this block: `Z_KEI(magnetic field)`, `B_Reading()`, `KeiVoltReading()` and `IntenReading()`, where the first two functions have been defined previously. The function `KeiVoltReading()` and `IntenReading()` measure the device voltage using the initiated "voltmeter" Keithley Semiconductor Characterization System and the light output from the device using the optical power meter, respectively. The three functions `B_Reading()`, `KeiVoltReading()` and `IntenReading()` directly correspond to $\mathbf{B}_{measure}$, $\mathbf{V}_{dev}$ and $\mathbf{El}_{dev}$ shown in the control sequence in Figure 2.20.

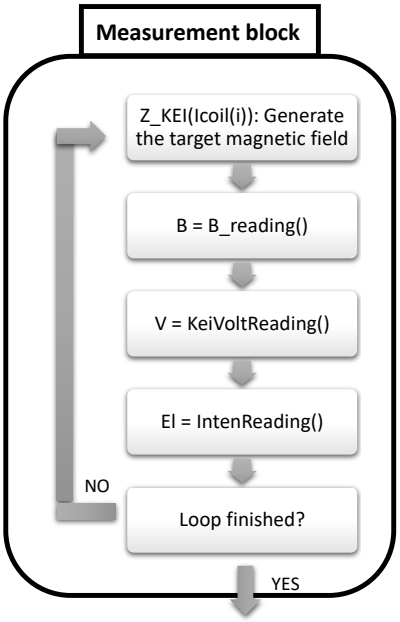

Figure 2.26: Structure for the device measurement block

Output Block: The purpose of this block is to collect all the stored data and format them into a text file which is output to a computer local folder. The process can be seen in Figure 2.28. Because this block is the last operating block in the software top level flowchart shown in Figure 2.21, and this occurs after all the measurements are completed, thus, the device has to be switched off before outputting the data. This

data outputting time can be set for the "device resting time" to prevent the device from overheating due to long operating time. The coil magnetic field is set to 0 μT so as to be the exactly the same as the initial stage where the measurement starts. Lastly, the data stored in the matrices during the measurement is collected and reformatted to a text file. As shown in Figure 2.28, an example of the output text file is displayed. There are three columns in this file – Bfield, Voltage and El which correspond to the measured magnetic field (μT), device voltage (V) and electroluminescence (W) at that magnetic field. This is a measurement of voltage and electroluminescence at different magnetic fields and no direct information on MC and MEL is included. This is only one measurement consisting of hundreds of points, and there are at least 100 repetitions of this measurement (meaning that there are hundreds of data text files output for a single measurement). The size of the data to be analysed is significant and cannot possibly be analysed manually. Therefore a specific data analysis algorithm should be programmed to process these huge amount of data and yield the final MC and MEL. This analysis technique will be covered in section **2.3**.

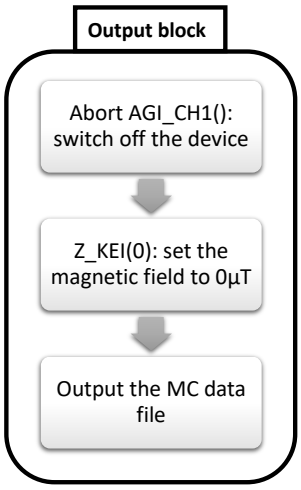

Figure 2.27: Structure for the device output block

2.2.3 Current-Voltage-Luminescence Characteristics software design

It is also important to measure the current-voltage-luminescence characteristics of each device as this can directly determine the quality of the device, based on parameters,

0.0000020000 A -1.txt

Bfield	Voltage	El
-0.467	3.167917E+000	9.870000E-011
-1503.28	3.167868E+000	9.970000E-011
-0.184	3.167895E+000	9.900000E-011
-1503.21	3.167867E+000	9.970000E-011
-0.29	3.167912E+000	9.840000E-011
-1503.22	3.167895E+000	9.970000E-011
-0.413	3.167936E+000	9.810000E-011
-1503.27	3.167942E+000	9.900000E-011
-0.5	3.167985E+000	9.870000E-011
-1503.08	3.167969E+000	1.000000E-010
0.144	3.168026E+000	9.810000E-011
-1503.49	3.168098E+000	9.900000E-011
0.118	3.168073E+000	9.810000E-011
-1503.46	3.168071E+000	9.940000E-011
0.047	3.168103E+000	9.840000E-011
-1503.54	3.168109E+000	9.940000E-011
0.052	3.168140E+000	9.840000E-011
-1503.02	3.168138E+000	9.970000E-011
-0.496	3.168197E+000	9.870000E-011
-1502.66	3.168180E+000	9.870000E-011
-0.457	3.168208E+000	9.870000E-011
-1502.69	3.168227E+000	9.870000E-011
-0.37	3.168256E+000	9.870000E-011
-1502.95	3.168256E+000	9.940000E-011
-0.345	3.168301E+000	9.840000E-011
-1493.61	3.168300E+000	9.940000E-011
-0.36	3.168334E+000	9.870000E-011
-1483.17	3.168344E+000	9.900000E-011
-0.148	3.168374E+000	9.740000E-011

Figure 2.28: An example of the output textfile

such as the turn-on voltage, the efficiency of the device, etc.

It is necessary to build the current-voltage luminescence (I-V-L) characteristics measurement software carefully so as to carry out a reliable measurement.

Figure 2.29 shows the top level flowchart of the algorithm for current-voltage luminescence characteristics measurement.

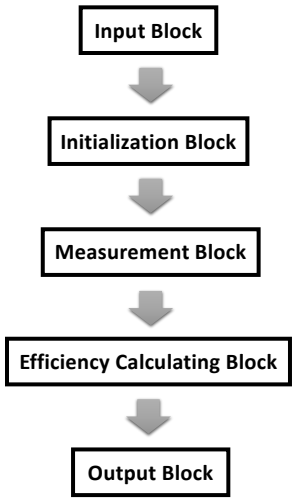

Figure 2.29: The top level flowchart of the current-voltage luminescence characteristics measurement algorithm

There follows an explanation for each block.

Input Block: The input block requires the input of the target device voltages, storing them into a matrix for later use.

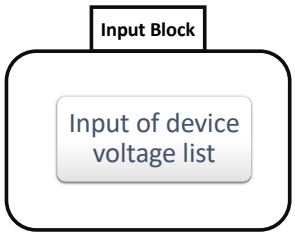

Figure 2.30: Input Block

Initialization Block: In this block, the Keithley Semiconductor Characterization System acts as an ammeter to measure the device current and initialises the light detector.

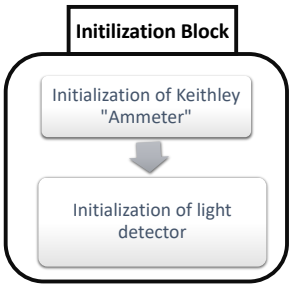

Figure 2.31: Initialization Block

Measurement Block: In this block as indicated in Figure 2.32. The measurement starts with the application of the target device voltage and is followed by the measurement of the device current and light output. Generally, this measurement block consists of a loop over all the target device voltages.

Efficiency Calculation Block: After obtaining the data of device voltage, current and luminescence, the power efficiency (or optical efficiency) can be obtained by using equation 2.23. For the same reason of protecting the device from overheating, the device is switched off first before the calculation of the efficiency. And the code for calculating the the efficiency of the device is as follows:

$$\eta_{efficiency} = \frac{El}{I \times V} \times 100\% \tag{2.23}$$

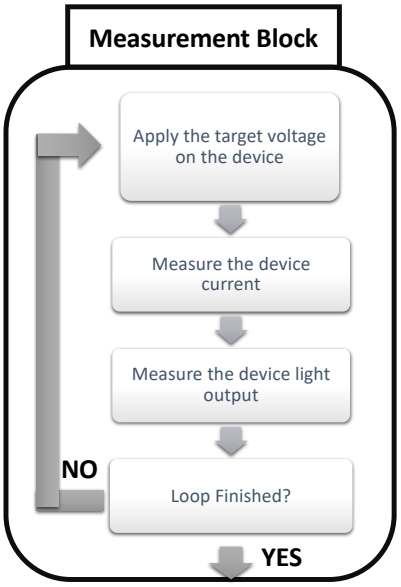

Figure 2.32: Measurement Block

```
   i = 0
Do Until i = size
EffRd(i) = ElRd(i) / (CurrentRd(i) * Voltlist(i)) 'calculating the
efficiency of each data point
i = i + 1
Loop
```

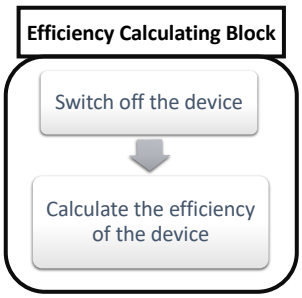

Figure 2.33: Efficiency Calculating Block

Output Block: After obtaining all results, this block reformats the data into a text file for subsequent data analysis and an example of the text file is shown in Figure 2.35. As can be seen in Figure 2.35, there are four columns corresponding to the device voltage (V), device current (A), light output (W) and the efficiency. A specific

programme for plotting the data out is required and will be covered in section **2.3**.

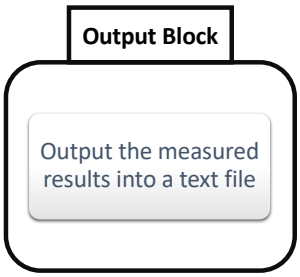

Figure 2.34: Output Block

0-IVL.txt

Voltage	Current	El	Efficiency
-3	3.157810E-009	0.000000E+000	0.000000E+000
-2.9	1.970618E-009	0.000000E+000	0.000000E+000
-2.8	1.843723E-009	0.000000E+000	0.000000E+000
-2.7	1.669252E-009	0.000000E+000	0.000000E+000
-2.6	1.549411E-009	0.000000E+000	0.000000E+000
-2.5	1.401571E-009	0.000000E+000	0.000000E+000
-2.4	1.270070E-009	0.000000E+000	0.000000E+000
-2.3	1.175199E-009	0.000000E+000	0.000000E+000
-2.2	1.057883E-009	0.000000E+000	0.000000E+000
-2.1	9.629131E-010	0.000000E+000	0.000000E+000
-2	8.621910E-010	0.000000E+000	0.000000E+000
-1.9	7.653660E-010	0.000000E+000	0.000000E+000
-1.8	6.820422E-010	0.000000E+000	0.000000E+000
-1.7	6.201620E-010	0.000000E+000	0.000000E+000
-1.6	5.448250E-010	0.000000E+000	0.000000E+000
-1.5	4.696508E-010	0.000000E+000	0.000000E+000
-1.4	4.465343E-010	0.000000E+000	0.000000E+000
-1.3	8.826401E-011	0.000000E+000	0.000000E+000
-1.2	2.407342E-010	0.000000E+000	0.000000E+000
-1.1	2.045046E-010	0.000000E+000	0.000000E+000
-1	1.594113E-010	0.000000E+000	0.000000E+000
-0.9	1.092486E-010	0.000000E+000	0.000000E+000
-0.8	7.480058E-011	0.000000E+000	0.000000E+000
-0.7	4.709614E-011	0.000000E+000	0.000000E+000
-0.6	2.665262E-011	0.000000E+000	0.000000E+000
-0.5	1.185186E-011	0.000000E+000	0.000000E+000
-0.4	2.795767E-012	0.000000E+000	0.000000E+000
-0.3	1.284756E-011	0.000000E+000	0.000000E+000
-0.2	2.055819E-011	0.000000E+000	0.000000E+000

Figure 2.35: Example of the output text file of the I-V-L Characteristics measurement

2.3 Measurement and Data Analysis

2.3.1 Current-Voltage-Luminescence Characteristics

After the device fabrication, it is important to check if the device made is of satisfactory quality using the turn-on voltage, efficiency and reproducibility. This information can be extracted from the I-V-L Characteristics. Thus the experiment of I-V-L Characteristics measurement should be conducted carefully. Figure 2.36 shows the system used for the I-V-L Characteristics, with the control software as described previously. The

device voltage is applied before the measurement, and then the device current and light output are collected by the programmed "ammeter" and the light detector.

All the data (including device voltages, currents and light outputs) is output and analysed using Matlab. The IVL data are plotted and shown in Figure 2.37. Each measurement is repeated 3 times and the error bars shown are the standard deviations of the corresponding data. As shown in Figure 2.37(a), the forward bias current before device switch on of TPD is larger than NPB, which suggests that there might be more trapped charges within NPB. Both devices have very similar switch on voltage of around $\sim 2.3V$, which suggests that the bipolar injection starts at this point for both. The fact that TPD and NPB devices have similar turn on voltage can also be seen from Figure 2.37(b) where both devices start to emit light after the device voltage of $\sim 2.3V$. The noise shown in Figure 2.37(b) is caused by the environment as the light-proof sealing cannot perfectly prevent any residual light getting into the light detector, and is not caused by the noise level of the light detector itself. However, the noise level of this is below the the signal level and thus can be neglected. Figure 2.37(c) shows the results of calculated efficiencies for both devices. It also indicates a very similar peak efficiency for both devices ($\sim 0.6\%$ at around $2\mu A$). Noticeably, the efficiency of the devices is not as high as reported in the literature. This is because my work focuses on the stability and reproducibility of the device instead of fabricating high performance devices.

The reproducibility of I-V-L Characteristics of NPB devices made at different times can be seen from Figure 2.38. From Figure 2.38(a), all fabricated devices show approximately the same turn on voltage of around $\sim 2.2V$, with some variations on the high voltage currents, which might be caused by the thickness differences in active organic layers during the device fabrication. As the whole device fabrication (especially the process of the organic thin film deposition) is based on manual operation rather than being automated. Variations in device fabrication are inevitable even following exactly the same procedure. The similar turn-on voltage indicates the bipolar injection in the devices is occurring approximately at the same point and this suggests the fabricated devices have very similar and reproducible electrode-organic interfaces.

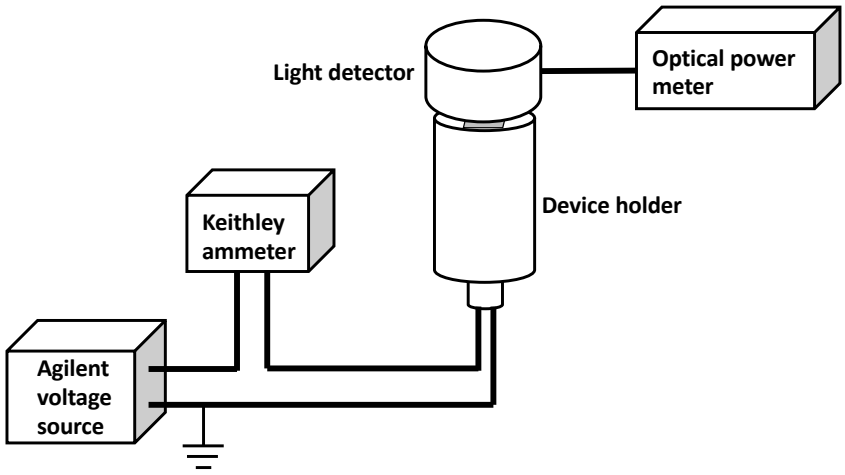

Figure 2.36: The system for I-V-L Characteristics measurement

Likewise, the reproducibility in turn-on voltage can also be seen in Figure 2.38(b). Noticeably, the light output in Figure 2.38(b) is 3 orders of magnitude smaller than that shown in Figure 2.37(b). This is because in the experiment of Figure 2.37(b), the light detector is directly placed on the device with a seal to ensure the maximum light output collection, however, the steel screws inside this light detector can display quite a disturbing residual magnetic field which can have an effect on the ultra-small magnetic field effect measurements. Thus a special non-ferrous metal (Aluminium) cap is made and to put directly on top of the device to transfer the light output from the device illumination to the end connected to the light detector that the distance between the device and the light detector is long enough to ensure no signs of residual magnetic fields due to the steel screws inside the light detector. An illustration of the non-ferrous cap is shown in Figure 2.39. The process of sealing the non-ferrous cap to the device and the other cap to the light detector can introduce extra light output loss, as well as losses in the bundled optical fibre. This is the main reason for the 3 orders magnitude smaller measured light output. However, as the Figure 2.38 (b) suggests, even with reduced light intensity, the resolution of the obtained El data is still clear and can be differentiated from the noise level. This is also the same reason why the efficiencies of all fabricated device in Figure 2.38 (c) are lower than those shown in Figure 2.37 (c). Despite of the efficiency drop, the peak efficiencies measured for all

the NPB devices are reproducible within errors ranging from 0.14% to 0.19%.

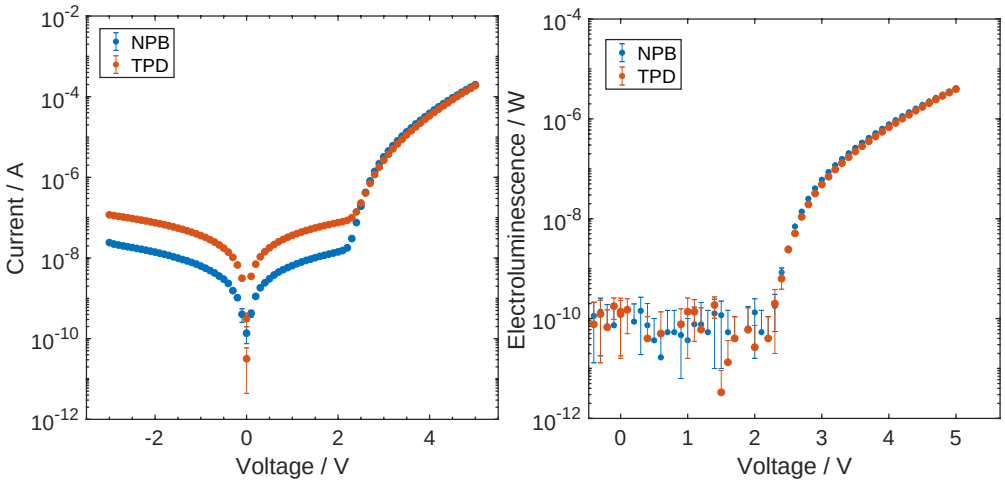

(a) I-V Characteristics of the devices (b) L-V Characteristics of the devices

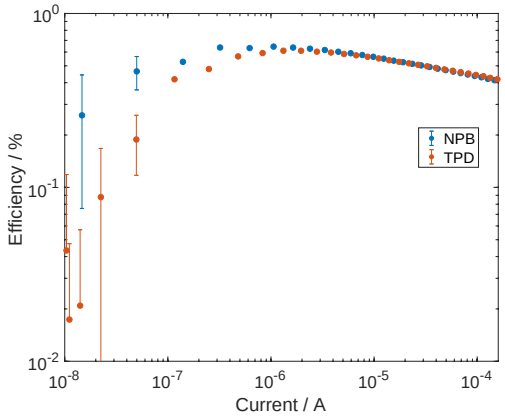

(c) Efficiency of the devices

Figure 2.37: I-V-L Characteristics Measurement of the devices based on NPB and TPD

2.3.2 Magnetoconductance and Magnetoelectroluminescence

Having chosen a stable device it is possible to measure the magnetic field effect. The measurement setup is shown in Figure 2.19 and the device-under-test (DUT) is located at the centre of the 3D Helmholtz coil system. The Z coil pair generates the target measurement magnetic fields required for the ultra-small magnetic field effect and the other two pairs (X coil pair and Y coil pair) provide the magnetic field to cancel the environmental field (such as the Earth's magnetic field in X and Y direction in the system coordinate).

For the measurement of the ultra-small magnetic field effect, the magnetic field

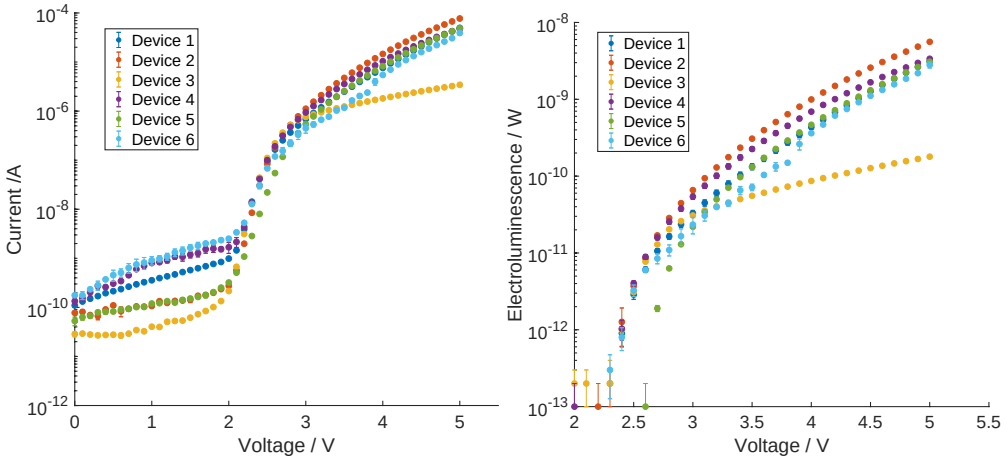

(a) I-V Characteristics of different NPB devices

(b) L-V Characteristics of different NPB devices

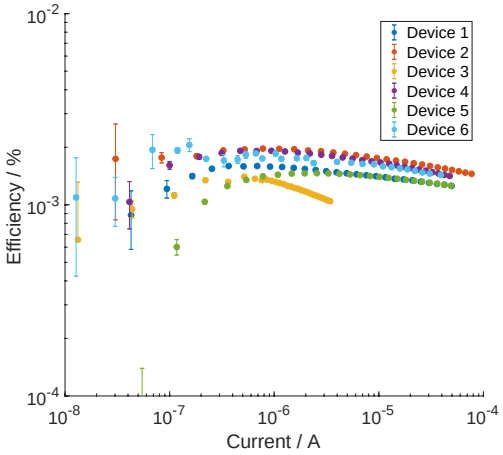

(c) Efficiency of different NPB devices

Figure 2.38: Reproducibility checks on I-V-L on different NPB devices

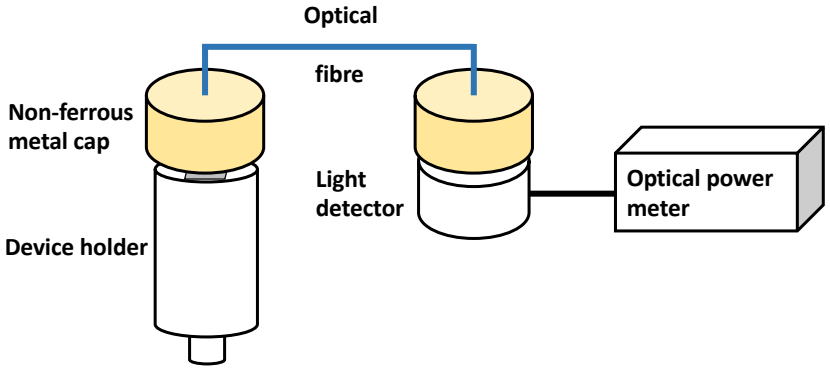

Figure 2.39: The non-ferrous cap for transferring the light output from the device.

chosen is from -500μT to 500μT with different resolutions of 5μT, 2.5μT and 1μT in the range |300–500|μT, |100–300|μT and |0–100|μT, respectively. During the

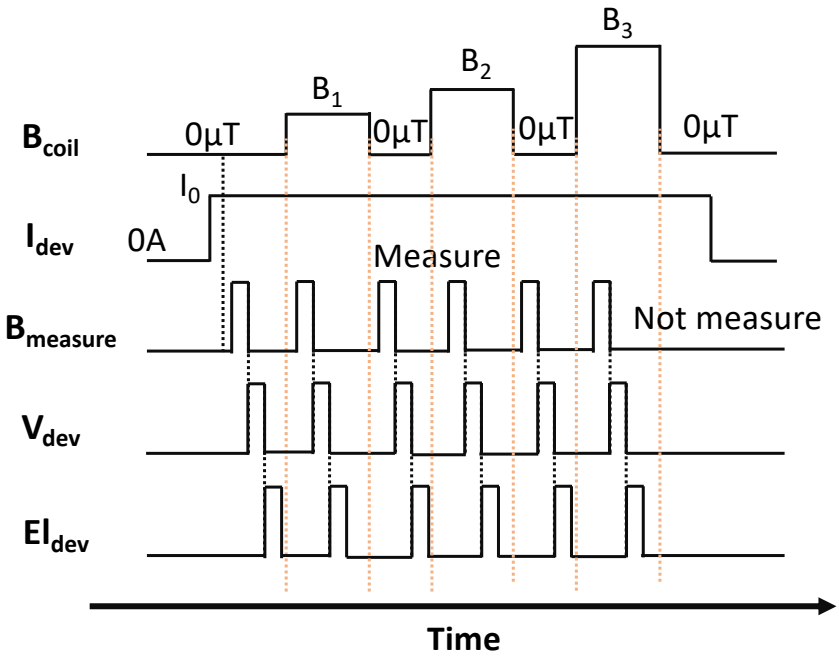

Figure 2.40: The controlling sequence for ultra-small magnetic field effect measurement

measurement of magnetic field effects, the device current drifts. But this drifting effect can be counteracted using some specific measurements.

An edited array of target magnetic fields is generated and measured instead of a continuous ascending magnetic field. In this array of target magnetic fields, a zero field ("null" field) is generated between each ascending target magnetic field ("on" field), for example, $0\mu T$, -$500\mu T$, $0\mu T$, -$400\mu T$, $0\mu T$, -$300\mu T$.... the sequence is shown in Figure 2.40. The ascending magnetic fields are target fields and the neighbouring null fields are used to obtain the net magnetic field effect using background subtraction.

The MC and MEL can be calculated using equations from 2.24 to 2.28:

$$V(0)_{ave} = \frac{V(0)_{before} + V(0)_{after}}{2}, \tag{2.24}$$

$$El(0)_{ave} = \frac{El(0)_{before} + El(0)_{after}}{2}, \tag{2.25}$$

$$MC(B) = \frac{C(B) - C(0)}{C(0)} = \frac{\frac{1}{R(B)} - \frac{1}{R(0)}}{\frac{1}{R(0)}} \tag{2.26}$$

$$= \frac{\frac{I_{dev}}{V(B)} - \frac{I_{dev}}{V(0)_{ave}}}{\frac{I_{dev}}{V(0)_{ave}}} = \frac{V(0)_{ave} - V(B)}{V(B)}, \tag{2.27}$$

$$MEL(B) = \frac{El(B) - El(0)_{ave}}{El(0)_{ave}} \tag{2.28}$$

where the $V(0)_{before}$ and $V(0)_{after}$ (or $El(0)_{before}$ and $El(0)_{after}$) are the device voltage (or device electroluminescence) under zero field before and after the target magnetic field, C is the conductance of the device and I_{dev} is the device sourcing current which is the same for all target magnetic fields.

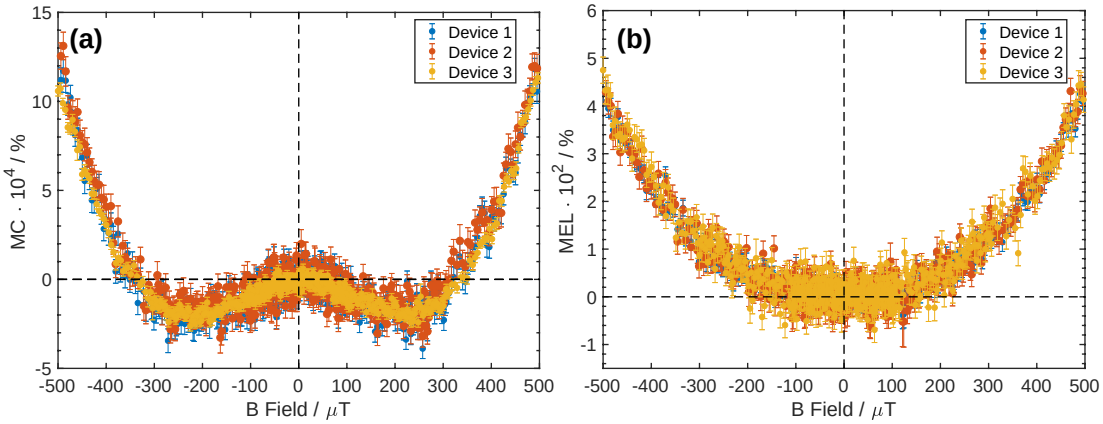

Figure 2.41: Ultra-small magnetic field effect (a) MC (b) MEL for different NPB devices: Reproducibility check

The results of the MC and MEL measurements are shown in Figure 2.41. From the MC results, all measured MC behaves as a "W" shape, and the dip of the "W" shape is at approximately $|250|\mu$T for all the devices. This reproducibility of the dip position enables later work in model fitting.

As indicated in Figure 2.41, the duration for a single scan from -500μT to 500μT is around 30mins and the data is averaged over 100 scans, which takes around 2 days. This long operation time clearly do not have any visible or significant effect on the behaviour of the magnetic field effect measurement on the device, and this suggests long life time and good stability of fabricated devices. Noticeably, the two fabricated devices (TPD-based and NPB-based) show different stabilities during the same long measurement time. TPD-based device is significantly less stable than the NPB-based device, the reason could be the significantly low glass-transition temperature of TPD ($\sim$62.8^{o}C) compared to the glass-transition temperature of NPB

($\sim$100^{o}C). By definition, the glass-transition temperature is the temperature where the organic material starts to change from the hard, glassy behaviour to a soft, rubbery behaviour. In the deposited thin film, if the film starts to change texture to the soft and rubbery, this would affect the device behaviour to a large degree. This texture change can change the device topography and this can re-modify the structure of the device, hence can result in unexpected results which are unpredictable. Consequently all later work was carried out on the stable devices based on NPB.

Generally, the measurements are highly reproducible within the signifiant error bars, especially in the field range -250μT to 250μT. The magnetic field effect within this range is dominated by the polaron pair model (as discussed in chapter 3) hence the high reproducibility of the magnetic field effect within this range ensures the validity of the experiments and fitting procedure.

Chapter 3

Single Proton PP Model Fitting MC to Yield A Realistic Local Hyperfine Field For Holes in Alq_3

3.1 Introduction

The PP model is currently the only quantitative theory used to explain the phenomenon of ultra-small magnetic field effects occurring in organic diodes [51–61, 63]. In the literature, the PP model is able to reproduce the "W" shape MC observed experimentally by simulation [52–55, 57], which shows the potential and the validity of the PP model. Although the simulated shape of MC generated using the Polaron Pair model reproduces the shape of the experimentally obtained MC (i.e. they all behave in a "W" like shape) there is lack of direct comparison between the simulated results and the experiment results. For example, there have been several instances of the MC resulting from these models being plotted, using representative B_{hf} values between 1 and 5 mT [53–55, 57], which corresponds to the fields obtained by empirical (usually Lorentzian) fitting[18, 69, 70] of experimental MCs. These traditional approaches have been successful in reproducing the functional forms of experimentally obtained MC data for a number of systems[52–55, 57], but they are based on calculating the MC resulting from PP models using historically reported or "typical" hyperfine field values

for organic systems.

In this work, a specific PP model fitting technique is carried out on MC data with no assumptions regarding microscopic parameter values such as the (average local) hyperfine field experienced by the polaron. This fundamentally differentiates this work from the literature. In order to develop this fitting technique, a successful and simplified PP model from literature is directly used [48, 53] with only three physical parameters (hyperfine field B_{hf}, decay rate k and a weight factor δ_{TS}). This PP model with small numbers of fitting parameters makes it more reliable for the developed model fitting technique. This simplified PP model will be further developed and justified in Chapter 4.

The small applied field MC on the common organic semiconductor tris-(8-hydroxyquinoline)aluminium (Alq_3) is studied, and the typical W-shaped USMFE MC below 500μT is obtained. The MC measured is used to demonstrate successful PP model fitting, returning physically significant parameters, such as the local hyperfine field strength, B_{hf}. Sufficiently high quality data including errors is obtained to perform fitting of the PP model and returns model parameters with associated uncertainties. The fitting has been carried out on data obtained from several devices and over a range of drive conditions and returns consistent fitting parameters within error. This raises the exciting prospect that PP model fitting to experimental MC data can be used more generally as a method of obtaining microscopic parameters (e.g. average local B_{hf}) in a variety of organic systems.

3.2 Experiments

In this section, the details of the experiments and techniques about this work are extensively discussed.

3.2.1 Device Fabrication

Device fabrication was carried out in section **2.1.2**, and the specific device structure is shown in Figure 3.1.

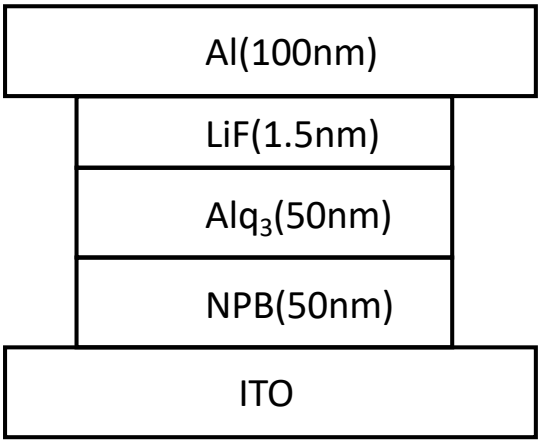

Figure 3.1: Device Configuration

3.2.2 Device Measurement and Data Analysis

After fabrication, the I-V Characteristics were measured as outlined in previous section **2.3.1**. The I-V Characteristics measurement was conducted with the device under vacuum at $\sim 10^{-6}$ mbar at room temperature ($\sim 23^{o}$C) using the setup in Figure 2.39. The device voltage was swept through from -3V to 5V by the source and the device current were measured by the instrument. I-V data was then collected and analysed as described in section **2.3.1**.

The magnetic field effect measurement consists of two kinds of measurements corresponding to the ultra-small magnetic field effect and high field magnetic field effect, respectively.

The measurement of ultra-small magnetic field effect magnetoconductance was carried out as shown in Figure 2.19, which is the same condition as used in the I-V-L measurement. The device was sourced under a constant driving current of 2μA. The raw data of magnetic field experienced by the device and the device voltage change are collected and recorded to file. As described in section **2.3.2**, the same MC analysis was carried out on the raw data. In order to reduce the noise level in the final MC results, the MC measurement was repeated 240 times and the averaged MC analysed with significantly smaller error bars (or standard errors), which is graphically summerized in Figure 3.2.

The coil setup and device were located where the Earth magnetic field components

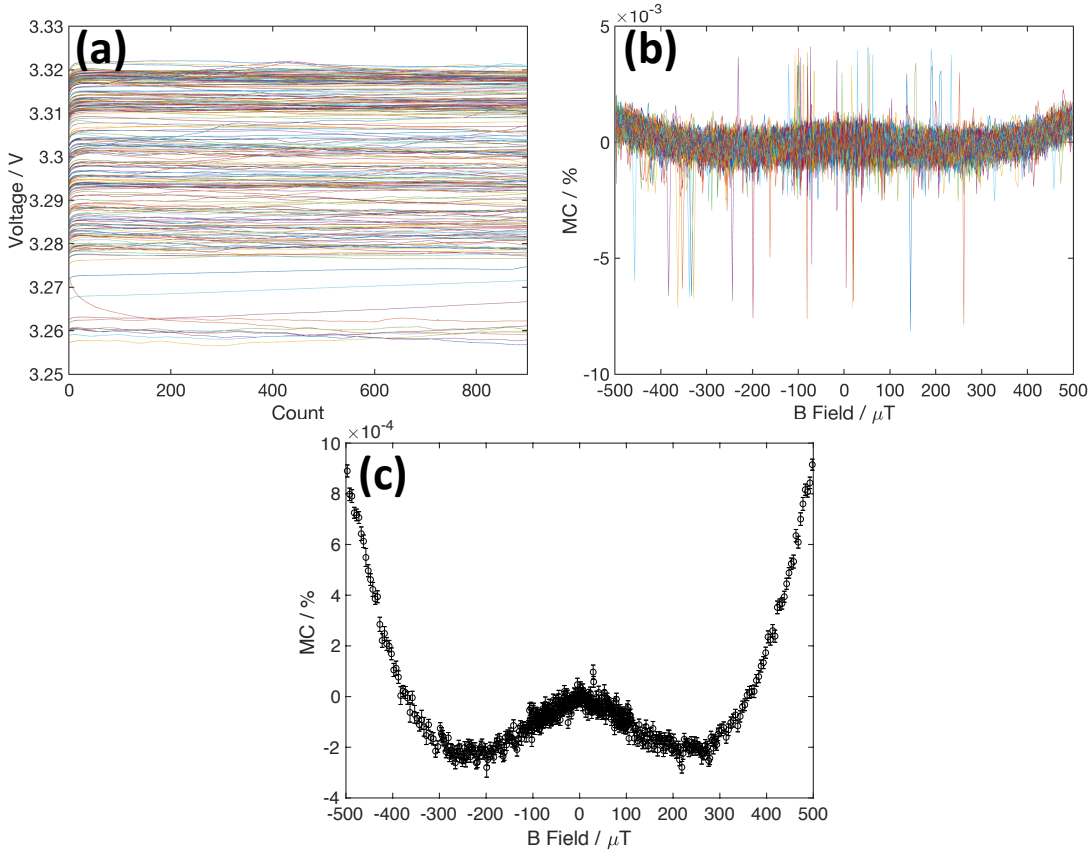

Figure 3.2: MC Averaging Process: (a)Raw data of the device voltage versus measurement counts (b)Calculated MC values for each set of raw data (c)Averaged MC data

along the x, y and z directions were measured to be approximately 14μT, 42μT and 10μT respectively. The magnetic field along the z direction was chosen as the scanning B field and the x and y applied DC fields simply used to cancel the Earth's field components. The x and y coils were connected to a DC power supply (Siglent SPD3303X) while the z coils were connected to a source measure unit (Keithley 2400 SourceMeter).

As the MC was measured under constant drive current, Figure 3.2(a) represents the measured device voltage versus measurement count, where the count represents any applied magnetic field and includes the alternating null field measurement. Thus, the very small device drift, <2%, over the whole measurement time. Evident in Figure 3.2(a)-(c) is eliminated from the MC calculation. Equation 3.1 was applied to calculate the MC value for each of the 100 repeated datasets (the raw MC data is shown in

Figure 3.2(b)). The arithmetic mean and standard error were calculated from these 100 datasets using equations shown in Equation 3.1(a)-(c):

$$MC_{mean}(B) = \frac{1}{N}\sum_{n=1}^{N} MC_n(B) \text{ (where N = 100).....}(a),$$
$$\textit{Standard Err.} = \frac{\sigma_{MC}}{\sqrt{n}}\text{.....}(b), \quad (3.1)$$
$$\sigma_{MC} = \sqrt{\frac{1}{N}\sum_{n=1}^{N}\left[MC_n(B) - MC_{mean}(B)\right]^2} \text{ (where N = 100).....}(c)$$

where MC_n(B) is the MC value of the n^{th} repeated dataset at a specific applied magnetic field and can be calculated using equations **2.24 - 2.28** with σ_{MC} being the standard deviation of each data point from the 100 experiments. The calculated MC_{mean} and *Standard Err.* correspond to the MC values and error bars shown in Figure 3.2(c).

For measurements of the high magnetic field effects (HFE), different equipment was utilised to achieve the generation of the high magnetic field (up to 250mT), namely, LakeShore Electromagnet (Model EM4-HVA). This electromagnet is consisted of a pair of large coils with iron cores in. The device-under-test was located in between the coils where the magnetic field is believed to be uniform. The electromagnet was controlled by a central PID (proportional integral and derivative) controlling power supply unit (PSU), and the whole system was connected to a PC so that commands can be sent to the electromagnet. No other coil pairs in orthogonal directions were used to cancel the environmental residual magnetic fields as the applied magnetic field was significantly larger (tens to hundreds of mT). The residual magnetic field effect is neglected in the measurement of the high magnetic field effect. In a manner similar to the USMFE measurement, the external magnetic field was applied from an array of target ascending magnetic field values with alternating 0μT in between and the MC was calculated in the same manner.

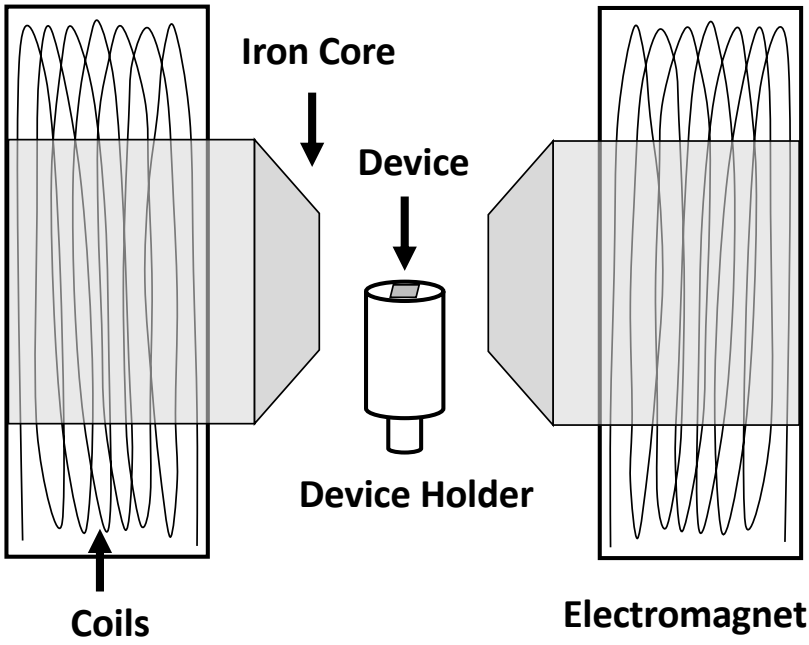

Figure 3.3: The schematic of the LakeShore Electromagnet

3.2.3 Single Proton Polaron Pair Model

The polaron pair model has been previously applied [52–55, 57, 58, 63] based on a magnetic field dependent singlet-triplet interconversion. Singlet or triplet polaron pairs interconvert into each other over time and a magnetic field affects this behaviour, determining the ultimate singlet and triplet polaron pair yields. The polaron pair, an electron-hole pair bound within a Coulomb radius, can either combine to form a tightly bound exciton or dissociate back into free charges. Since singlet excitons decay radiatively, magnetically induced changes in the singlet exciton yield will appear as magnetoelectroluminescence. In parallel, since singlet and triplet polaron pairs contribute differently to dissociated carriers, any changes in singlet (or triplet) yield will result in a different number of free carriers due to dissociation. These will change the overall carrier density and result in MC.

The same approach is taken as in literature [71] using the stochastic Liouville von Neumann equation to calculate the spin density σ as shown in equation 3.2

$$\frac{d\sigma(t)}{dt} = [\mathbf{H}, \sigma] \tag{3.2}$$

Where the Hamiltonian **H** is in angular frequency units. The solution to equation 3.2 can be obtained [48, 71] as in equation 3.3.

$$\sigma(t) = e^{-iHt}\sigma(0)e^{iHt} \tag{3.3}$$

There is an initial assumption of the formation of singlet polaron pairs (this is arbitrary and the same physics can be obtained by assuming initial triplet formation) with initial singlet density, $\sigma(0)$ [48] (in reality, the initial spin states are: 25% are singlet and 75% are triplet). **H** is the spin Hamiltonian describing the interactions between the polaron pair and the external magnetic field. In general, the Hamiltonian is expected to contain the Zeeman interaction between the polaron and the external magnetic field, the hyperfine interaction between the polaron and the hydrogen nuclei, dipolar interactions and exchange interactions between the spins of each polaron etc. For simplicity a reduced, one proton, Hamiltonian is used containing only the Zeeman and hyperfine interactions, shown in equation 3.4 and this single proton hyperfine coupling can be illustrated in Figure 3.4, where only one charge in the polaron pair is coupled to a neighbouring nuclear field and the other polaron is non-coupled.

$$\begin{aligned} H &= H_{Zeeman} + H_{Hyperfine}, \\ H_{Zeeman} &= g\mu_B B \cdot (S_{1z} + S_{2z}), \\ H_{Hyperfine} &= g\mu_B B_{hfc1} \cdot (S_1 \cdot \mathrm{I}) \end{aligned} \tag{3.4}$$

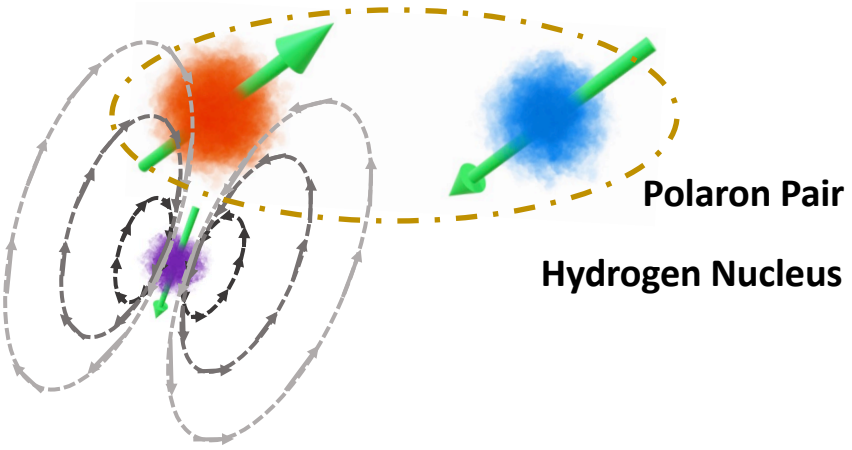

Figure 3.4: The illustration of the single proton hyperfine coupling

Where g is the g-factor and approximately equals to 2.002, μ_B is the Bohr magneton and is approximately 5.788×10^{-5} ev$\cdot$T^{-1}, B is the applied magnetic field, S_{1z} and S_{2z} are the z components of the spin operators for the two polarons and B_{hfc1} is the local hyperfine field due to a single proton. S_1 is the spin operator including all components for one polaron and I is the spin operator for the hydrogen nucleus. The term $S_1 \cdot I$ can be defined in equation 3.5

$$S_1 \cdot \mathrm{I} = \mathrm{S}_{1x} \cdot \mathrm{I}_x + \mathrm{S}_{1y} \cdot \mathrm{I}_y + \mathrm{S}_{1z} \cdot \mathrm{I}_z \tag{3.5}$$

Physically, S_1 and I with different x, y and z subscripts correspond to the Pauli matrices for the polaron and the hydrogen nucleus respectively.

Noticeably, the dipolar and exchange interactions are omitted here in the Hamiltonian. Because the Coulomb radius (the maximum distance between polarons in the PP state, $r_c = \frac{e^2}{4\pi\epsilon_r\epsilon_0 kT}$, e: unit charge, ϵ_0 and ϵ_r are vacuum and relative dielectric constants and $\epsilon_r\sim3$ for Alq_3. kT is the thermal energy at room temperature.) was calculated to be around 19nm for Alq_3 and dipolar and exchange interaction during this long range could be negligibly small.

To calculate the singlet fraction, ρ_S, the trace of the singlet projection operator, P_S, on $\sigma(t)$, as shown in equation 3.6, is required.

$$\rho_S = Tr\left[P_S\sigma(t)\right] \tag{3.6}$$

Intuitively, the singlet-triplet basis matrix is defined as in equation 3.7.

$$P_e = \begin{pmatrix} 1 & 0 & 0 & 0 \\ 0 & \frac{1}{\sqrt{2}} & \frac{1}{\sqrt{2}} & 0 \\ 0 & -\frac{1}{\sqrt{2}} & \frac{1}{\sqrt{2}} & 0 \\ 0 & 0 & 0 & 1 \end{pmatrix} \tag{3.7}$$

Where the second column represents singlet component while the other three columns represent three different triplet components. For consistency of the quantum calculation, all the spin components should stay in the same singlet-triplet basis as

shown in equation 3.7, such a transformation can be achieved using equation 3.8.[72]

$$P = P_e \otimes I_{e2\times 2} = \begin{pmatrix} 1 & 0 & 0 & 0 & 0 & 0 & 0 & 0 \\ 0 & 1 & 0 & 0 & 0 & 0 & 0 & 0 \\ 0 & 0 & \frac{1}{\sqrt{2}} & 0 & \frac{1}{\sqrt{2}} & 0 & 0 & 0 \\ 0 & 0 & 0 & \frac{1}{\sqrt{2}} & 0 & \frac{1}{\sqrt{2}} & 0 & 0 \\ 0 & 0 & -\frac{1}{\sqrt{2}} & 0 & \frac{1}{\sqrt{2}} & 0 & 0 & 0 \\ 0 & 0 & 0 & -\frac{1}{\sqrt{2}} & 0 & \frac{1}{\sqrt{2}} & 0 & 0 \\ 0 & 0 & 0 & 0 & 0 & 0 & 1 & 0 \\ 0 & 0 & 0 & 0 & 0 & 0 & 0 & 1 \end{pmatrix} \tag{3.8}$$

A specific form of the singlet projection operator in equation 3.9 is used, which differs from the generalised operator appearing in reference [48] and is based on the singlet-triplet basis previously defined.

$$P_S = \frac{1}{4} \times I_{e8\times 8} - I_{Ax} \otimes I_{Bx} \otimes I_{e2\times 2} - I_{Ay} \otimes I_{By} \otimes I_{e2\times 2} - I_{Az} \otimes I_{Bz} \otimes I_{e2\times 2} \tag{3.9}$$

Where $I_{e8\times 8}$ is an 8×8 unit matrix and I_A and I_B, subscript x, y and z, are the corresponding components of the Pauli matrices of each polaron. The effect of the singlet projection operator as used in equation 3.6 is to "filter out" all the singlet components among all spin configurations.

Finally, the steady state singlet yield, Φ_S, is obtained by integrating the singlet fraction over all time, assuming a single rate constant, k, to account for the disappearance of the singlets by various mechanisms, using equation 3.10.

$$\Phi_S = k \cdot \int_0^\infty \rho_S(t) e^{-kt} dt \tag{3.10}$$

According to the literature[48], spin selective radical-radical reactions (here, polaron-polaron interactions, such as the dissociation or recombination of polaron pairs) can occur, resulting in the disappearance of singlet and triplet excited states. Thus, the corresponding fractions decay with time and can be described by first-order kinetics. The polaron-polaron interaction occurs for both singlet and triplet polaron pairs, however, although they possess different spin configurations, the large inter-polaron distance

can make the energy difference between the two relatively small. Additionally, the spin-dependent recombination kinetics become inter-twined with the spin-dependent coherent evolution[48]. A more developed model with two different protons coupled to each of the polaron pairs and with different decay rates is extensively discussed in Chapter **4**

Notably, the final form of the singlet yield can be expressed in the form in equation 3.11[48]:

$$\begin{aligned}\Phi_S = \frac{3}{8} + \frac{1}{8}\frac{\omega^2}{\Omega^2} + \frac{1}{8}\frac{a^2}{\Omega^2}f(\Omega) + \frac{1}{8}\Big[1 - \frac{\omega}{\Omega}\Big]f(\frac{1}{2}a + \frac{1}{2}\omega + \frac{1}{2}\Omega) + \\ \frac{1}{8}\Big[1 - \frac{\omega}{\Omega}\Big]f(\frac{1}{2}a - \frac{1}{2}\omega - \frac{1}{2}\Omega) + \frac{1}{8}\Big[1 + \frac{\omega}{\Omega}\Big]f(\frac{1}{2}a - \frac{1}{2}\omega + \frac{1}{2}\Omega) + \\ \frac{1}{8}\Big[1 + \frac{\omega}{\Omega}\Big]f(\frac{1}{2}a + \frac{1}{2}\omega - \frac{1}{2}\Omega)\end{aligned} \tag{3.11}$$

where a = $\frac{g\mu_B B_{hf}}{\hbar}$, ω = $\frac{g\mu_B B_{external}}{\hbar}$, Ω = $\sqrt{a^2+\omega^2}$ and f(x) = $\frac{k^2}{x^2+k^2}$. Again, B_{hf} is the local hyperfine field, μ_B is Bohr magneton, g is the g-factor, $\hbar$ is the reduced Planck constant. a is the hyperfine coupling constant. $B_{external}$ is the externally applied magnetic field, ω is the Larmor frequency under applied magnetic field. k is the rate constant as discussed in equation 3.10. From literature [48], it is intuitive to think that in order for observing the USMFE, the lifetime (which can be related to the slow decay rate constant) of a polaron pairs should be long enough for S-T interconversion process induced by hyperfine and Zeeman interaction, therefore, the slow spin relaxation process is ignored in this model.

By using different values for the applied magnetic field throughout the calculation, one can obtain the magnetic field dependent singlet yield, $\Phi_S(B)$. From this the triplet yield, $\Phi_T(B)$, can be evaluated simply, using $\Phi_S(B)$ + $\Phi_T(B)$ = 1. Similarly to Nguyen and co-workers [53, 54] the yields are used to evaluate the MC at a given field using equation 3.12

$$MC(B) = \frac{\Phi_S(B) + \delta_{TS}\Phi_T(B)}{\Phi_S(B=0) + \delta_{TS}\Phi_T(B=0)} - 1 \tag{3.12}$$

It has been noted that making a direct link between the magnetic field dependent singlet (or triplet) yield and the MEL is straightforward since only singlet states are emissive (for example, see reference [52]), but the relationship between the yields

and the resultant MC is not as simple. Equation 3.12 is used to relate yields to MC and ultimately model the experimental data, as it has been shown to be successful in the literature [53, 54], but no more detailed a mechanism is offered than to simply state that different polaron pair dissociation (singlet, triplet) will alter the number of free charge carriers contributing to conduction. The significance of the dimensionless factor, δ_{TS}, in equation 3.12 is to describe the relative contributions of singlet and triplet polaron pairs to conduction via dissociation, offering a microscopic mechanism for MC.

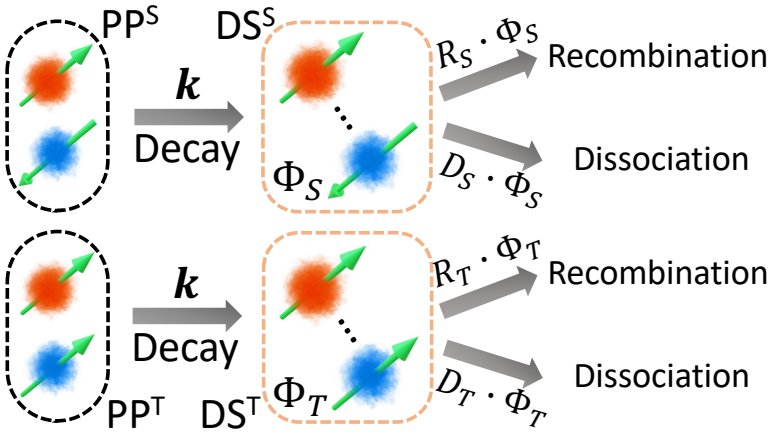

Figure 3.5: The schematic of the single proton polaron pair magnetoconductance model based on a reduced Liouville equation, which introduces the approximation that energy is conserved for the quantum states (for singlets and triplets)

This microscopic process behind the magnetoconductance of the organic device is illustrated in Figure 3.5. Because the polaron pair model is based on a reduced stochastic Liouville von Neumann equation as shown in equation 3.2, and the Hamiltonian used in equation 3.4 is a Hermitian operator which conserves energy[57], the reduced stochastic Liouville Equation has a restriction in use that the energy of the particle system (in my case: the polaron pair) should be conserved. However, the definition of the magnetoconductance in equation 3.12 as appears in literature [53, 54] requires a different polaron pair dissociation (singlet, triplet) will alter the number of free charge carriers contributing to conduction. "Dissociation" of the polaron pair means two of the polarons in the pair state separate and, the energy conservation in the system in dissociation does not apply. However, in order to conserve the polaron pair system

energy, the "recombination" of the separated polarons to reform polaron pair should also be included. Technically, a more accurate stochastic Liouville Equation has been constructed from literature [57, 73] with the non-Hermitian Hamiltonian terms and some dissipative terms added to the current stochastic Liouville Equation. However, it is computationally complex and the reduced stochastic Liouville Equation is used in this work.

As shown in Figure 3.5, the polaron pair (singlet or triplet polaron pair state) disappears (or decay) with a rate of k. Generally, in the literature [48], the static state singlet yield is calculated as shown in equation 3.10, and this is generally for radical pairs which mainly exist in chemical or biological reactions. However, in order to make a counterpart of this singlet yield that can be descriptive in organic electronics, the "singlet yield", is referred to as "decayed state (DS) yield" with the same notation as Φ_S (or triplet yield, Φ_T), although this hypothisized decayed state has no physical reality. For the dissociation and recombination of the polaron pairs, the weight factors R_S and D_S (or R_T and D_T) were used to denote different contributions to singlet DS dissociation and singlet DS recombination (or triplet DS dissociation and triplet DS recombination). Specifically, for the consideration of the particle conservation, the relation of $R_S + D_S = 1$ is required for this model. Therefore, with the help of the illustration in Figure 3.5, it is possible to express the MC as follows as in equation 3.13:

$$\begin{aligned} MC(B) &= \frac{[\Phi_{S,diss}(B) + \Phi_{T,diss}(B)] - [\Phi_{S,diss}(B=0) + \Phi_{T,diss}(B=0)]}{\Phi_{S,diss}(B=0) + \Phi_{T,diss}(B=0)} \\ &= \frac{\Phi_{S,diss}(B) + \Phi_{T,diss}(B)}{\Phi_{S,diss}(B=0) + \Phi_{T,diss}(B=0)} - 1 \\ &= \frac{D_s \cdot \Phi_S(B) + D_T \cdot \Phi_T(B)}{D_S \cdot \Phi_S(B=0) + D_T \cdot \Phi_T(B=0)} - 1 \\ &= \frac{\Phi_S(B) + \frac{D_T}{D_S} \cdot \Phi_T(B)}{\Phi_S(B=0) + \frac{D_T}{D_S} \cdot \Phi_T(B=0)} - 1 \\ &= \frac{\Phi_S(B) + \delta_{TS} \cdot \Phi_T(B)}{\Phi_S(B=0) + \delta_{TS} \cdot \Phi_T(B=0)} - 1 \end{aligned} \tag{3.13}$$

where the δ_{TS} denotes the relative contributions of singlet and triplet polaron pairs to conduction via dissociation as reported from the literature [53, 54]. And in this case, it is given by $\delta_{TS} = \frac{D_T}{D_S}$.

Therefore, as shown in equation 3.13, by considering the contribution weight factors D_S and D_T, the MC constructed by a modelled microscopic process as shown in Figure 3.5 can be transformed into the MC measured using δ_{TS} [53, 54](equation 3.12).

3.2.4 Model Fitting Technique and Algorithm

The process of fitting the Polaron Pair model to the experimentally obtained MC data minimises the reduced Chi-square value (χ^2_{red}) between the two. The reduced Chi-square value can be defined in equation 3.14:

$$\begin{aligned} \chi^2 &= \sum_1^N \left[\frac{MC(B)_{experiment} - MC(B)_{model}}{\sigma_{experiment}} \right]^2, \\ \chi^2_{red} &= \frac{\chi^2}{K} \end{aligned} \tag{3.14}$$

Where: $\mathrm{MC(B)}_{experiment}$ is the experimental data, $\mathrm{MC(B)}_{model}$ is the value obtained by the P-P model (equation 3.12), $\sigma_{experiment}$ is the error on each experimental data point, N is the number of data points and K the number of degrees of freedom. In fitting, χ^2_{red} has been minimised using the approximation K $\approx$ N (given that N is 375).

The overall minimisation method used is to generate a matrix of χ^2 values using a range of the fitting parameter numerical values (B_{hf}, k and δ_{TS}), over a region of the three dimensional parameter space available. The χ^2 thus generated is then searched numerically to find the minimum global χ^2 value. The set of fitting parameters (B_{hf}, k and δ_{TS}), corresponding to the minimum global χ^2 and the reduced value, $\chi^2_{red,Global}$, are then chosen as the minimisation output.

More specifically, there are two programmed function RChi() and RChi3() that play an important role in this whole minimisation process. The function RChi generates a two dimensional matrix of χ^2 values parametric in l and δ_{TS} at a given value of B_{hf}. It does this by running the model to evaluate the MC over all applied magnetic fields and compares to the measured MC (calculating the χ^2). This is done by two nested loops, the outer running over values of l and the inner over values of δ_{TS}. It also selects the minimum χ^2 for that specific value of B_{hf} which it outputs. The function RChi itself is run within a loop, over different values of B_{hf}, in RChi3 which generates

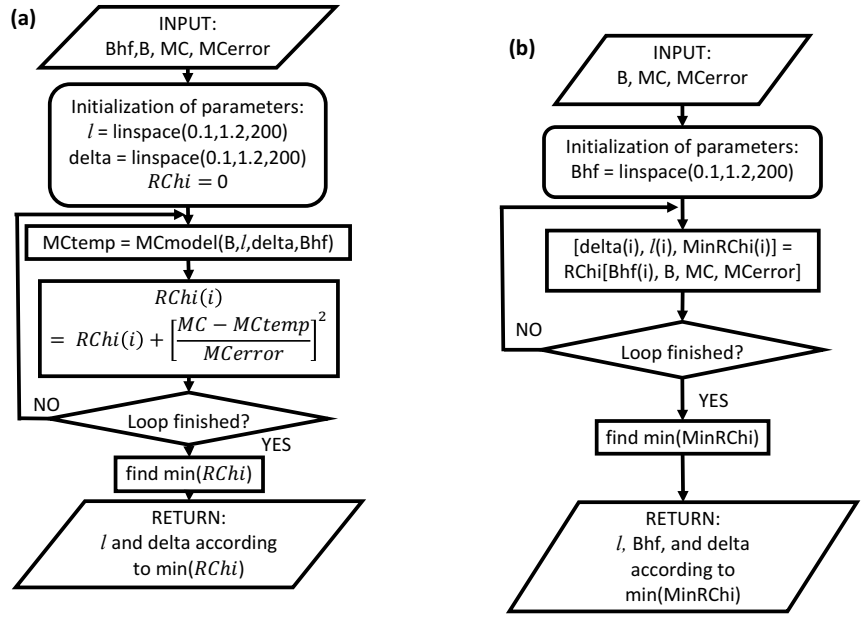

(a) The flowchart of function RChi(). $l = \frac{k}{a}$, a is hyperfine coupling constant

(b) The flowchart of function RChi3()

Figure 3.6: Flowcharts of functions used in minimization

an array of χ^2 values. This array is then searched for the global χ^2 minimum. The reduced $\chi^2_{red,Global}$ is calculated and returned, together with the corresponding set of B_{hf}, k and δ_{TS} values.

Figure 3.6(a) is a flowchart of the function RChi and it is noted that the indicated loop consists of two nested loops, over different values of l and δ_{TS}. Figure 3.6(b) is a flowchart of function RChi3 and the single loop is run over different values of B_{hf}.

Mathematically, individual χ^2 values used in function RChi are defined in equation 3.15.

$$\chi^2_{\delta_m,l_n}(B_{hf},l,\delta_{TS}) = \sum_{\text{over all } B_{applied}} \left(\frac{MC(B_{applied}) - Model(B_{applied})}{MCError(B_{applied})}\right)^2\Bigg|_{B_{hf}} \tag{3.15}$$

Where MC($B_{applied}$) is the experimentally obtained magnetoconductance at a given applied field and MCError($B_{applied}$) is the experimentally obtained error (3.1(b)) associated with every specific value of magnetoconductance. Model($B_{applied}$) is the calculated magnetoconductance using the model at specific values of B_{hf}, l, δ_{TS}. A two dimensional matrix of χ^2 values at a given B_{hf} is generated by the function RChi

as shown in equation 3.16

$$\chi_{\delta_m,l_n} = \begin{pmatrix} \chi_{\delta_1,l_1} & \chi_{\delta_1,l_2} & \cdots & \chi_{\delta_1,l_N} \\ \chi_{\delta_2,l_1} & \chi_{\delta_2,l_2} & \cdots & \chi_{\delta_2,l_N} \\ \vdots & \vdots & \ddots & \vdots \\ \chi_{\delta_N,l_1} & \chi_{\delta_N,l_2} & \cdots & \chi_{\delta_N,l_N} \end{pmatrix} \tag{3.16}$$

The minimum value of χ^2 at a given B_{hf} is selected from the χ_{δ_m,l_n} matrix, as shown in equation 3.17, and the corresponding local values of $\delta_{local}, l_{local}$ are noted.

$$\chi_{\delta_m,l_n}\Big|_{minimum} = \chi^2_{min}(B_{hf})\Big|_{\delta_{local},l_{local}} \tag{3.17}$$

The outputs of the function RChi are used by function RChi3 to construct an array of the χ^2 and associated δ_{TS} and l, over different values of B_{hf} as shown in equation 3.18.

$$\chi^2_{min_{Bhf_m}} = \begin{pmatrix} \chi^2_{min}(B_{hf1}) & \delta_{local1} & l_{local1} \\ \chi^2_{min}(B_{hf2}) & \delta_{local2} & l_{local2} \\ \vdots & \vdots & \vdots \\ \chi^2_{min}(B_{hfN}) & \delta_{localN} & l_{localN} \end{pmatrix} \tag{3.18}$$

The minimum value of χ^2 in the array defined by equation 3.19 corresponds to the global minimum χ^2, as defined in equation 3.19.

$$\chi_{min_{Bhf_m}}\Big|_{minimum} = \chi_{global\ min.}\Big|_{\delta_{global},Bhf_{global},l_{global}} \tag{3.19}$$

The reduced global $\chi^2_{red,Global}$ is then evaluated using $\chi^2_{min_{Bhf_m}}$ and equation 3.14. The corresponding values of B_{hf} and δ_{TS} are reported directly as fitting parameters and the decay rate, k, is calculated using the value for l at minimum χ^2 and $l = \frac{k}{a}$.

3.3 Results and Discussions

3.3.1 I-V Characteristics

Typical results of the Current (Density)-Voltage Characteristics measurements are shown in Figure 3.7

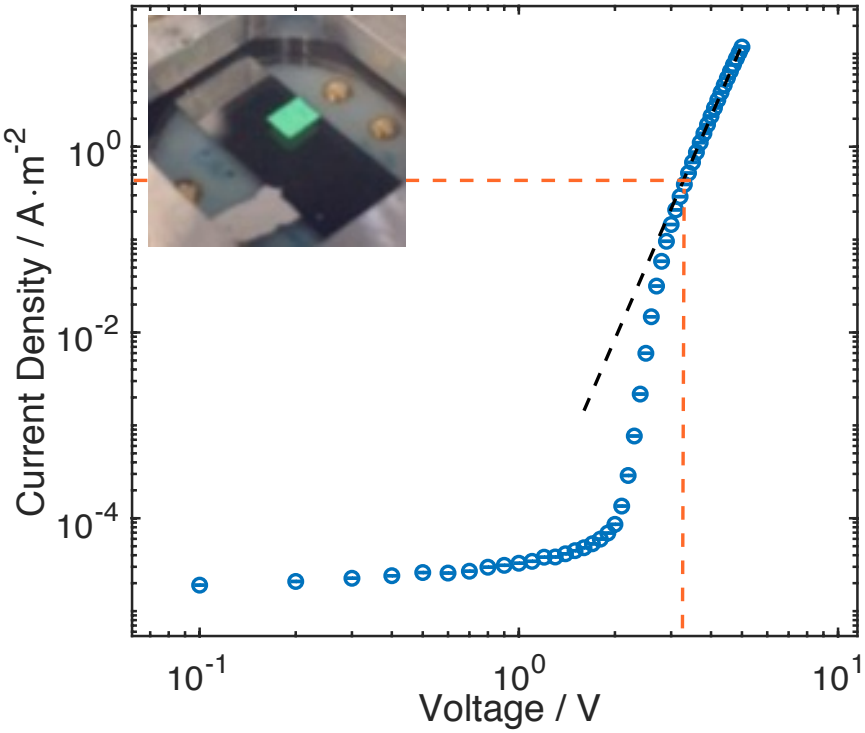

Figure 3.7: The Current (Density)-Voltage Characteristics of the device in log-log scale. The inset is a photo of a working OLED

The I-V measurement results are shown in Figure 3.7. Above 3V, the device is operating in ambipolar mode as evidenced by visible electroluminescence shown in 3.7 (inset). The red dashed line at $\sim$0.5 A·m^{-2} represents 2 μA drive current at around 3.4 V bias. The I-V is clearly superlinear in these conditions and the device is operating above any "turn on" threshold.

3.3.2 Magnetic Field Effect – Magnetoconductance (USMFE and HFE)

Figure 3.8 displays the USMFE MC results obtained from a device under 2 μA constant current in the presence and absence of the Earth's magnetic field (i.e. nulled in the two orthogonal directions to the varied field). In both cases the results show a minimum MC magnetic field (B_m) at approximately $\pm$ 240 μT and 2×10^{-4} % magnitude. The standard error for each data point is 3.6×10^{-5} % and the two plots are essentially identical above 100 μT. The insets show the MC below 100 μT. The two data sets only differ slightly for applied fields below $\sim$ 45 μT, i.e. for fields smaller or equal to the vector sum of the components of Earth's magnetic field orthogonal to the applied

field direction. In the presence of the Earth's field, the sample shows little MC below 45 μT in contrast to Figure 3.8(b) (inset) where a slightly steeper, but noisier, MC is obtained. This is expected since the external field is applied in an arbitrary direction (in this case horizontally at a bearing of 60^oC) and the measurable effects should be obtained once the externally applied field exceeds the component of Earth's field that has not been nulled. No "shifts" of the MC response were seen, in contrast to some literature results[58], where measurements were deliberately carried out parallel and antiparallel to the Earth's field. Figure 3.8(b) demonstrates that it is possible to carry out μT resolution MC measurements at fields smaller than the Earth's field with a MC sensitivity below 10^{-6} (1 ppm, 10^{-4} %), using external field cancelling.

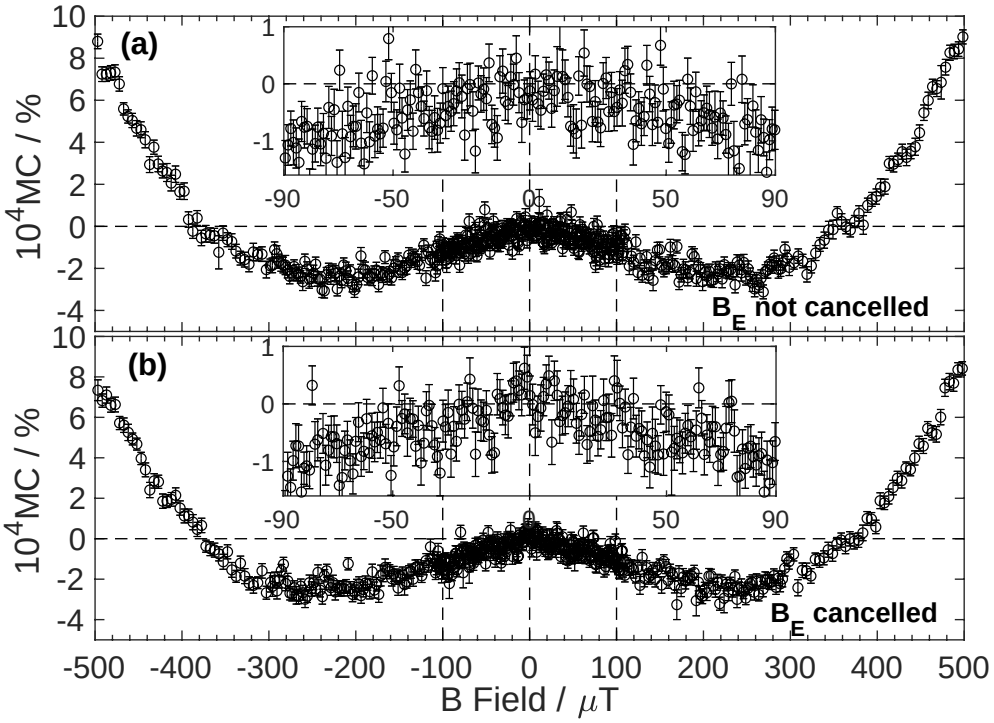

Figure 3.8: Ultra-Small Magnetic Field Effect in the device (a) with and (b) without the Earth magnetic field cancelled

The USMFE MC measurement was repeated on 3 freshly made individual devices, based on the same device structure as stated in subsection **3.2.1** with the measured results shown in Figure 3.9. This shows in the figure, the high reproducibility of the functional form of the USMFE MC, including the position of the "W" shape. In Figure 3.9, only the data within the magnetic field range of $\pm 300\mu$T are shown as this regime

is dominated by the polaron pair model and is the focus of the present work. This will be further addressed in section **3.3.5**.

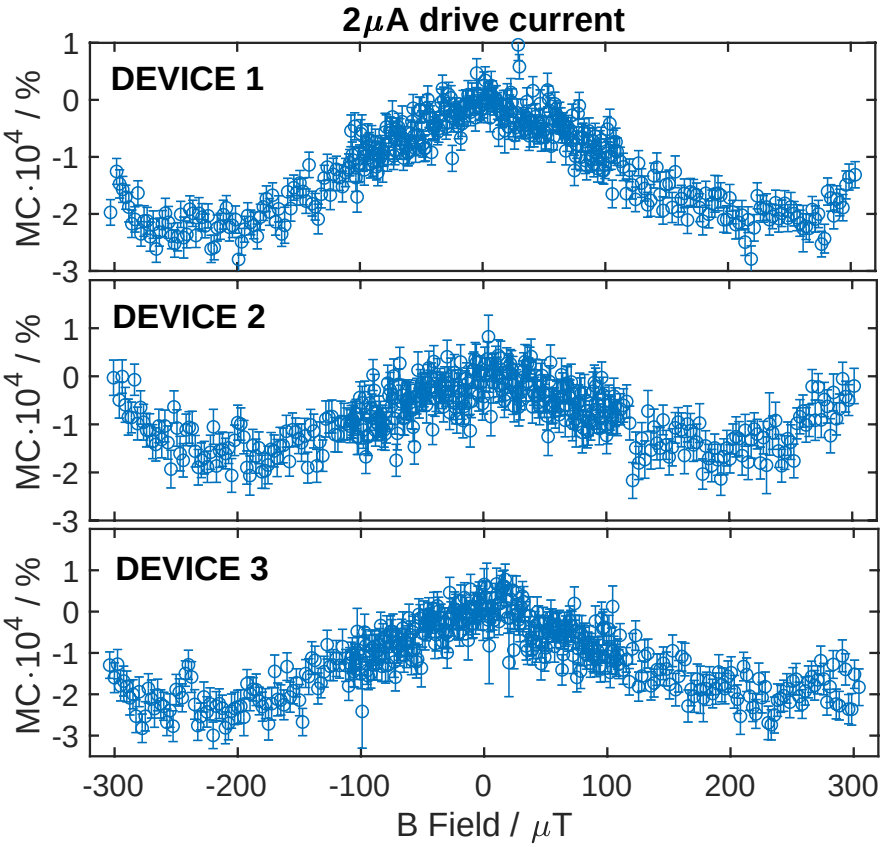

Figure 3.9: Reproducibility of the USMFE MC on different devices within the magnetic field ranges of $\pm 300\mu$T

To place the results in context, the normalised MC (or MR) for a variety of different organic materials is shown in Figure 3.10, including those obtained in the previous work, and from references[52–55, 58, 59, 61, 62, 74]. The normalisation was carried out using equation 3.20.

$$MC_{normalised} = \frac{MC(B)}{MC(B = B_m)} \tag{3.20}$$

Where MC(B) is the MC at a given field and MC(B=B_m) is the MC at the magnetic field where it reaches its minimum (or maximum) value, B_m. The data shown in Figure 3.8 and Figure 3.9 yield $|B_m| \sim 240$ μT, placing the results within the USMFE range. Note that there are variations in USMFE results, even for the same (nominal) system, for example in the H-DOO-PPV results of Nguyen and co-workers (references[53, 58]),

as well as variations in MC for the same system between different groups, e.g. the present Alq_3 results compared to reference[55]. The discrepancies between the two references[55] could be due to a number of factors: different device architectures, drive conditions, magnetic field range and instrumental resolution. In any case, they are not addressed further as they fall outside the scope of the current work. It has also been noted that the smallest literature B_m fields are displayed by deuterated samples [53, 58], as expected given that deuterated samples display smaller hyperfine magnetic fields compared to protonated samples. Measurement conditions and architectures (unipolar, ambipolar) can also yield variations in USMFE results as demonstrated by the MEH-PPV MC of references [53, 62].

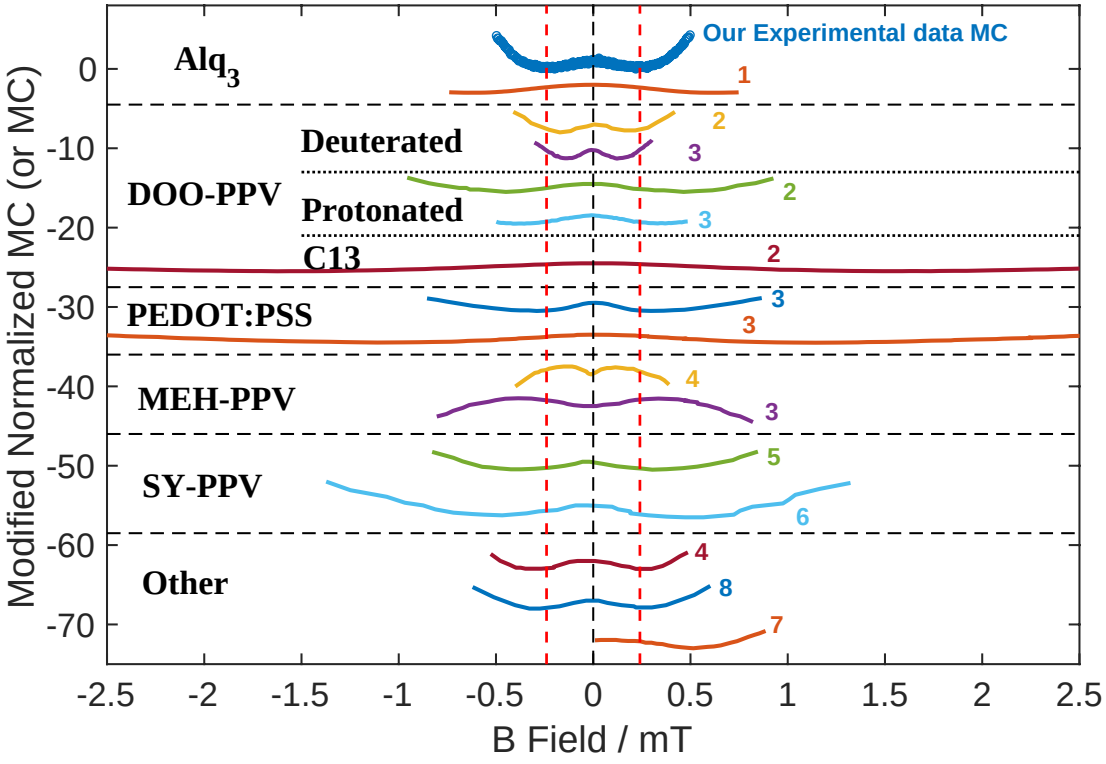

Figure 3.10: Modified (or Offset) normalized MC in comparison with literature. 1:[55] 2:[54] 3:[58] 4:[53] 5:[61] 6:[59] 7:[74] 8:[61]

Apart from the results of the ultra-small magnetic field effect, for completeness of the magnetic field effect measurements, the magnetic field effect measurements were also carried out and the result is shown in Figure 3.11

From Figure 3.11, the applied external magnetic field ranges from -250mT to 250mT. The high magnetic field effect is 3 orders of magnitude larger than the ultra-small

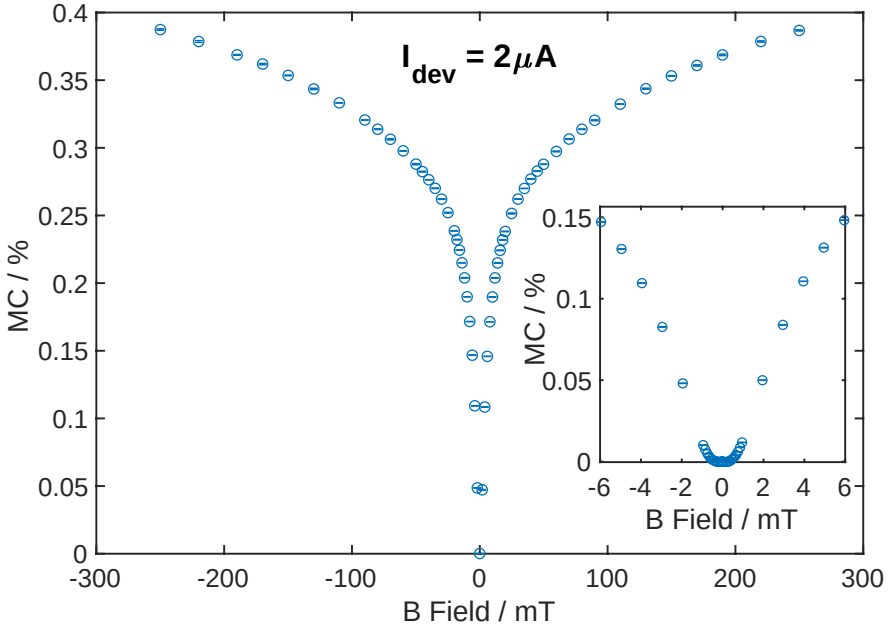

Figure 3.11: The high magnetic field effect measured under a device drive current of 2μA

magnetic field effect. Additionally, the HFE behaves in a monotonic way, which is also different from the "sign reversal" behaviour of the USMFE.

3.3.3 Device Stability Test

Noticeably, devices used to produce the MC results have not undergone any visible degradation, that can be observed in the MC results. As shown in Figure 3.12, there are a total of 240 measurements taken to yield the total averaged dataset and this whole measurement takes ∼120 hours to complete. In order to see the effect of any possible degradation on the MC, the first and last 10 measurements of 240 measurement dataset were each averaged. From Figure 3.12, there is no significant difference between the first 10 and last 10 averaged datasets or compared to average of all 240 (with the exception of the noise level), and this demonstrates that the device behaves in a reproducible manner at the very beginning of the measurements and after a hundred hours of measuring.

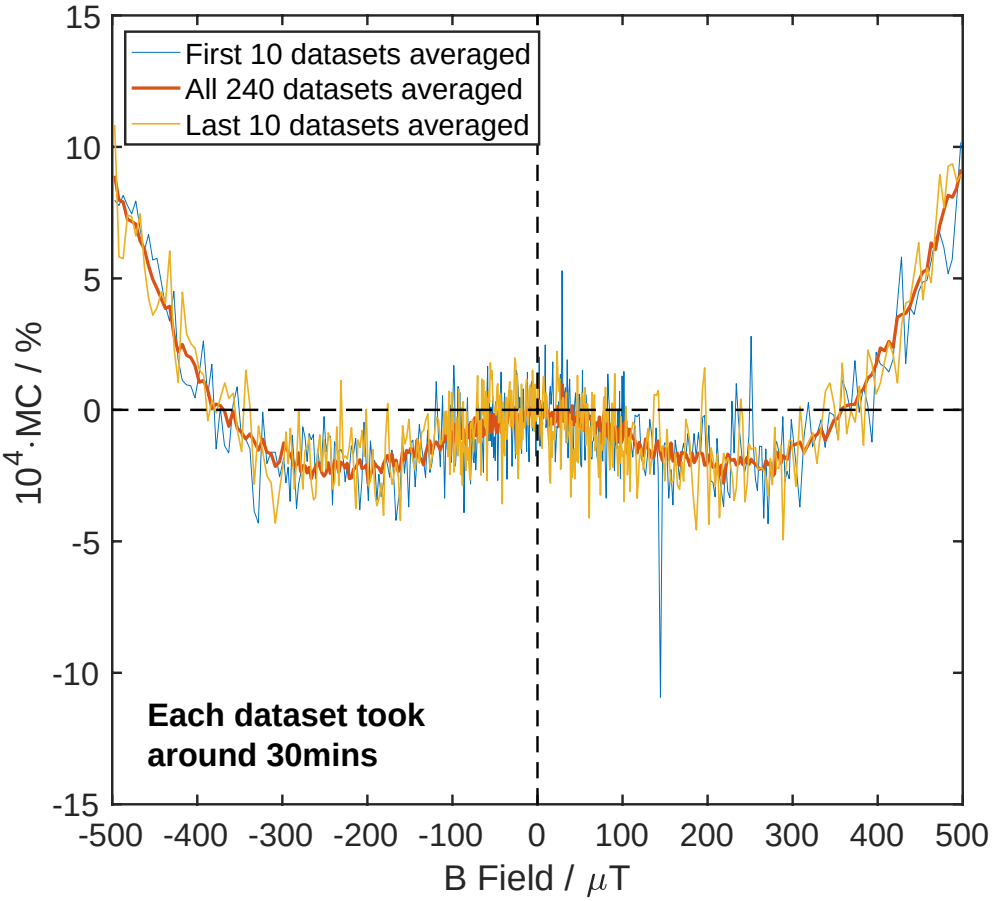

Figure 3.12: Device stability check

3.3.4 Single Proton Polaron Pair Model Simulation

The single proton modelling has been described in subsection **3.2.3**, and in this subsection, the simulation results based on this model are shown. Equation 3.6 shows the calculation of the singlet fraction ρ_S after applying the singlet project operator P_S on the spin density. Figure 3.13 shows the results of the magnetic field dependent singlet fraction time evolution using a simulation parameter B_{hf} = 0.34mT at different applied external magnetic fields. The singlet fraction as defined in equation 3.6 is the precursor of the singlet yield calculation as shown in equation 3.10 with the later requiring delay indicated by the decay rate, k. Figure 3.13 shows the simulation results when the external magnetic fields are (a) 0μT (b) 50μT (c) 250μT (d) 500μT, respectively.

The singlet fraction ρ_S in the absence of any decay will oscillate indefinitely under

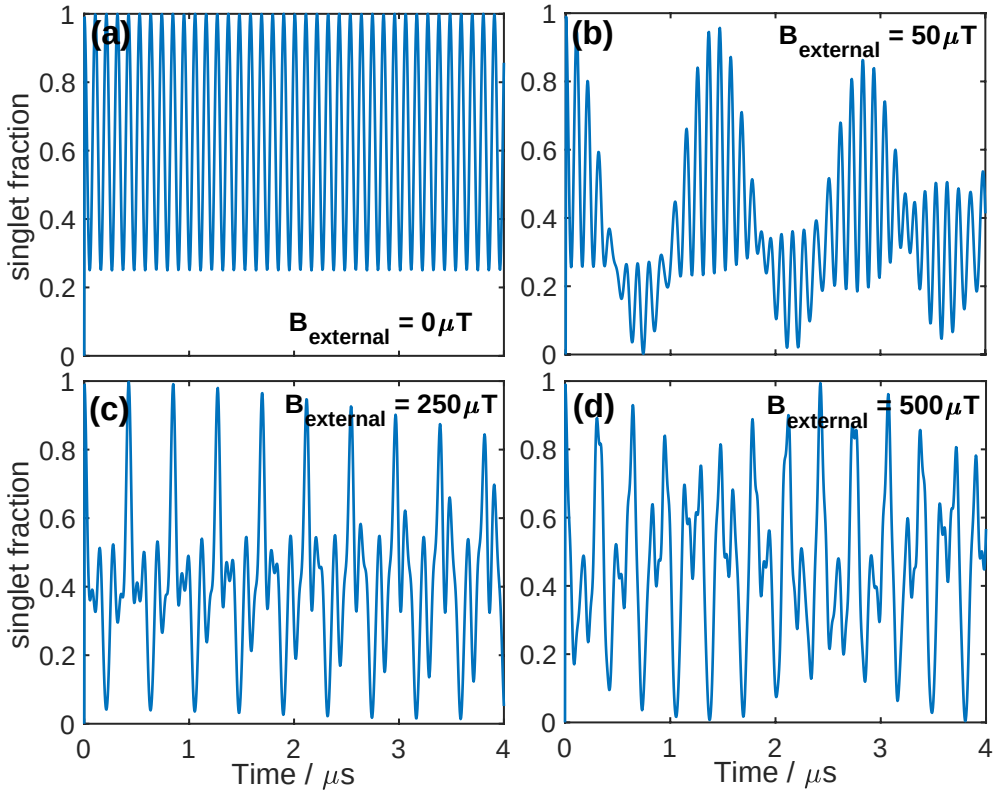

Figure 3.13: Magnetic field dependent singlet fraction ρ_S using the simulation parameter B_{hf} = 0.34mT at different external magnetic fields

the effect of the hyperfine and applied magnetic fields as shown in Figure 3.13. It is noted that the integral appearing in the definition of the steady state singlet yield in equation 3.10 will only converge for non-zero decay rate, k. Nevertheless, even in the absence of a decay rate, the singlet yield is affected by the external field as shown in Figure 3.13. At zero field, Figure 3.13(a), the singlet fraction ρ_S simply oscillates at the hyperfine precession frequency, and this shows that the hyperfine interaction plays an important role in singlet-triplet interconversion. When the external magnetic field is applied, degenerate triplet excited states start to split due to the Zeeman interaction even at fields smaller than the hyperfine field of 0.34mT, as shown in Figures 3.13(b) and (c). Finally, when the external magnetic field exceeds the hyperfine field, the Zeeman interaction starts to dominate in the singlet-triplet mixing processes, Figure 3.13(d). The magnetic field dependent changes in singlet fractions based on the hyperfine and Zeeman interactions lie at the very foundation of the Polaron Pair model.

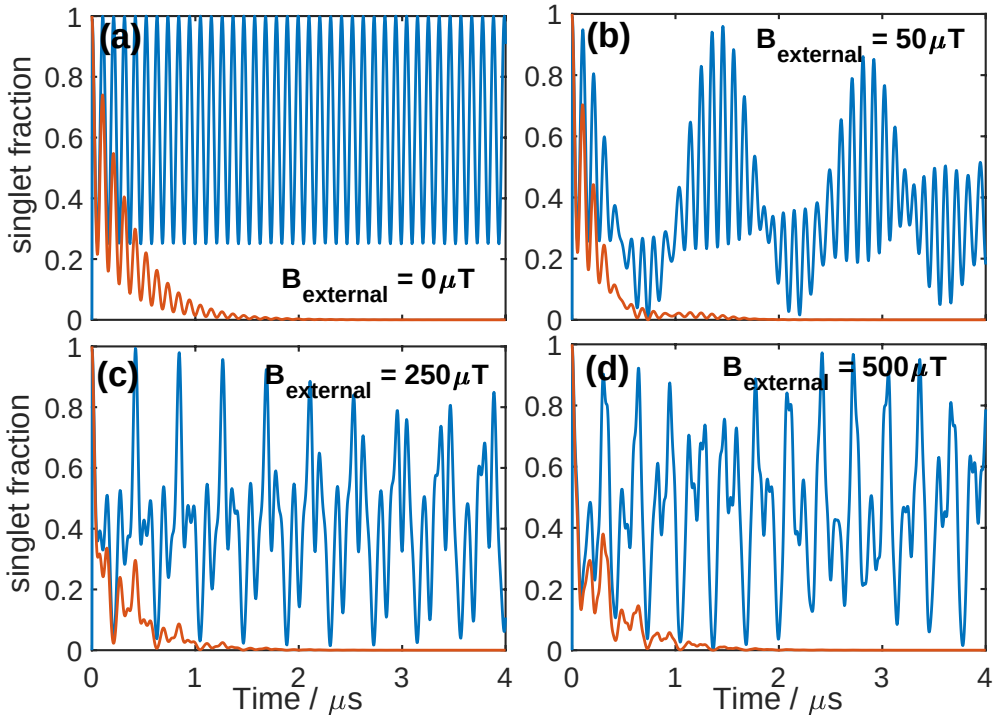

Figure 3.14: Magnetic field dependent singlet fraction ρ_S using the simulation parameter B_{hf} = 0.34mT. The orange line included is the product of a singlet fraction and an exponential decay at a rate of 2.88MHz, i.e. $\rho_S \cdot e^{-kt}$

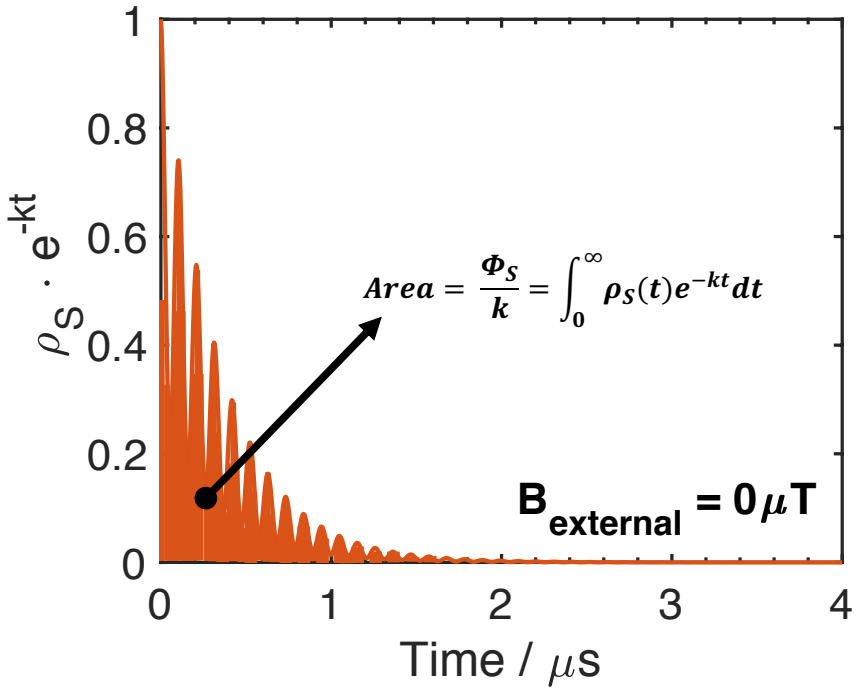

Figure 3.15: The schematic of how the singlet yield is calculated using the integral in equation 3.10.

A steady state of the singlet fraction needed for the subsequent calculation of the singlet yield can be shown in equation 3.10, which is the basis of the polaron pair magnetoconductance model. This steady state singlet fraction can be achieved via a multiplication by a first order kinetic decay (i.e. an exponential decay) as stated in the literature [48]. The time evolution of the singlet fraction including the effect of the decay simulation results are shown in Figure 3.14. As can be seen from the results, it is clear that the periodic oscillations of the singlet fraction due to the hyperfine fields and external magnetic fields (shown in blue line in Figure 3.14) is greatly reduced by the exponential decay term (i.e. $\rho_S \cdot e^{-kt}$) and the value of the singlet fraction can converge to a static value at a specific rate constant. And for this simulation results in Figure 3.14, all the singlet yield would become stable after approximately 2 $\sim$ 3 μs under the decay rate of 2.88MHz. Figure 3.15 shows the schematic of singlet yield calculation using the integral of product between the singlet fraction and an exponential decay.

Simulation results of MC based on single proton polaron pair model were investigated using different parameters (B_{hf}, k and δ_{TS}) for their effects on the shape of the calculated MC results.

A clearly visible "W" shape MC, which is typically observed in ultra-small magnetic field effect experiments was produced by the single proton polaron pair model. The inset in Figure 3.16 is a magnified MC within the magnetic field range of $\pm 400\mu$A. The simulation parameters used are B_{hf}=0.34mT, k=35.67MHz and δ_{TS}=0.99. From Figure 3.16, the overall shape of the simulation saturates quickly above fields of $\pm$1mT, and this indicates that the single proton PP model is possibly suitable within the magnetic field of $\pm$1mT for these specific simulation parameters at larger magnetic fields (larger than $\pm$1mT in this case), high magnetic field effects come into play and dominate. This will be further discussed in the next subsection.

The first simulation parameter to be investigated is the decay rate, k, of the polaron pair with results shown in Figure 3.17. The inset is a magnification of the effect within the magnetic field ranges of $\pm 500\mu$T. The simulation parameters for this simulation are B_{hf}=0.34mT, and δ_{TS}=0.99 and the corresponding hyperfine precession frequency

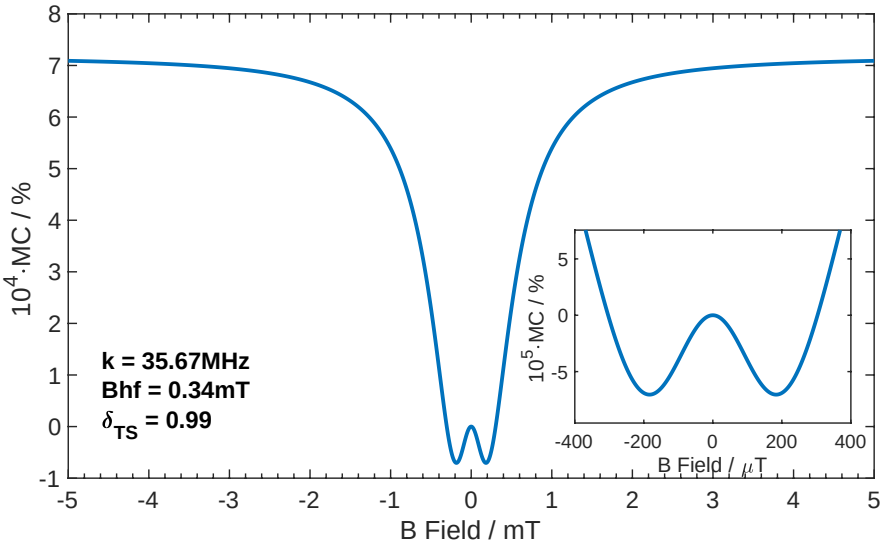

Figure 3.16: Single proton polaron pair magnetoconductance simulation

can be calculated to be $\omega_{hf} = 59.45MHz$. (ω_{hf} is the Larmor frequency at hyperfine magnetic field) and the parameter of the decay rate is changing on different values (k = 11.89MHz, 23.78MHz, 35.67MHz, 47.56MHz and 59.45MHz and they correspond to different l values of 0.2, 0.4, 0.6, 0.8 and 1). In Figure 3.17, the magnitude of the "W" shape MC is decreasing with increasing decay rates. Noticeably, when the decay rates are close to the hyperfine precession frequency (in this case, $\omega_{hf} = 59.45MHz$), the typical "W" shape MC is hardly visible in the form and a ultra-small magnetic field effect begins to vanish. This is in accord with the literature [48] insofar as only when the decay rate is small compared to the hyperfine precession frequency can the ultra-small magnetic field effect be clearly shown. The B field corresponding to the minimum MC does not depend on the decay rate k as indicated by the green dotted line in Figure 3.17. This means that this minimum MC position is independent of the decay rates. Additionally, the approach to the Full-Width at Half-Maximum (FWHM) indicated by the red dashed line is also independent on the decay rate k.

The second simulation parameter to be studied is the hyperfine field B_{hf} while the other simulation parameters remain constant (k=35.67MHz and δ_{TS}=0.99). Figure 3.18 shows simulated MC using k = 35.67MHz and δ_{TS} = 0.99 with different hyperfine values of B_{hf} – 0.14mT, 0.24mT, 0.34mT, 0.44mT and 0.54mT. The inset is the zoom in of the part within the magnetic fields of $\pm 500\mu$T. From the result, it is obvious that

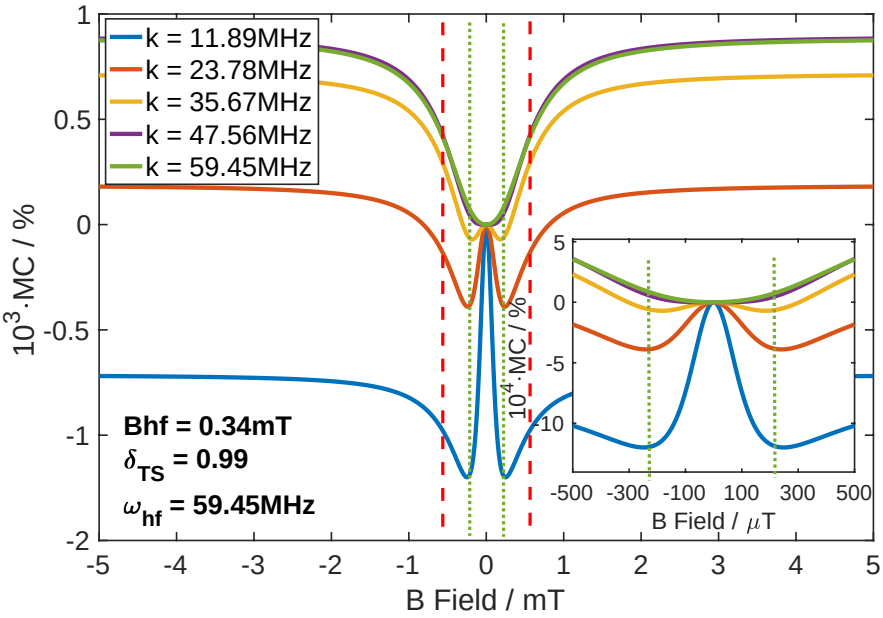

Figure 3.17: Single proton polaron pair magnetoconductance simulation: decay rate change

the minimum MC position of the "W" shape is dependent on the value of B_{hf}, and the minimum MC B field increases with increasing values of B_{hf}. Although the asymptotic saturation value is independent of B_{hf}, the FWHM increases with increasing B_{hf}.

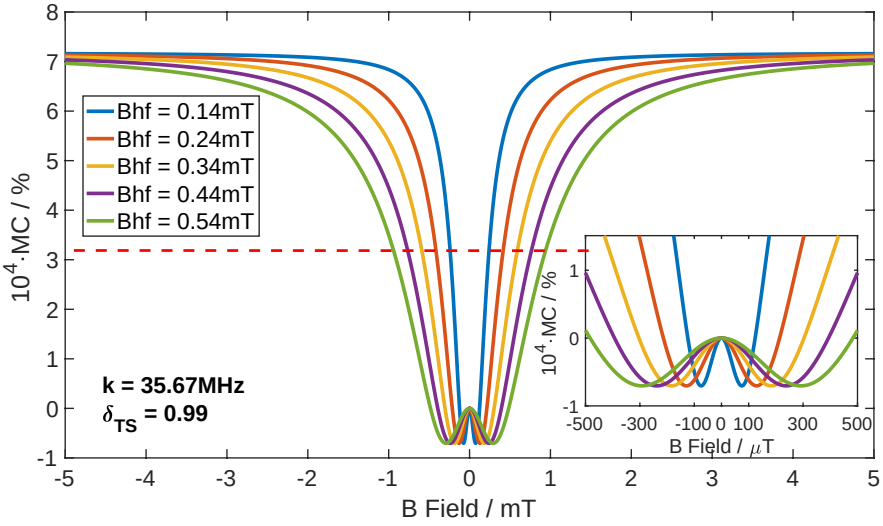

Figure 3.18: Single proton polaron pair magnetoconductance simulation: hyperfine field change. Red dashed line: FWHM

The last simulation parameter to be valued is the relative weight factor δ_{TS} as defined by equation 3.13. Figure 3.19 shows simulated MC using k = 35.67MHz and B_{hf} = 0.34mT with different values of δ_{TS} of 0.79, 0.89, 0.99, 1.09 and 1.19. When the

parameter δ_{TS} is smaller than 1, the singlet polaron pairs contribute more than the triplet counterparts. For values greater than 1, the simulation result is reversed. In Figure 3.19 when δ_{TS} is smaller than 1, i.e. that when singlet polaron pairs contribute dominantly in the dissociation process, the high field saturation MC (larger than 1mT) is positive while the sign reversal part of the effect is negative. While for δ_{TS} greater than 1, the saturation regime becomes negative. Therefore, the relative contributions of singlet and triplet polaron pair dissociation to free carriers process determine the sign of the MC in both the high field regime and the USMFE regime. Noticeably, the shape of the MC, including the minimum MC position is still independent on the relative weight factor δ_{TS}.

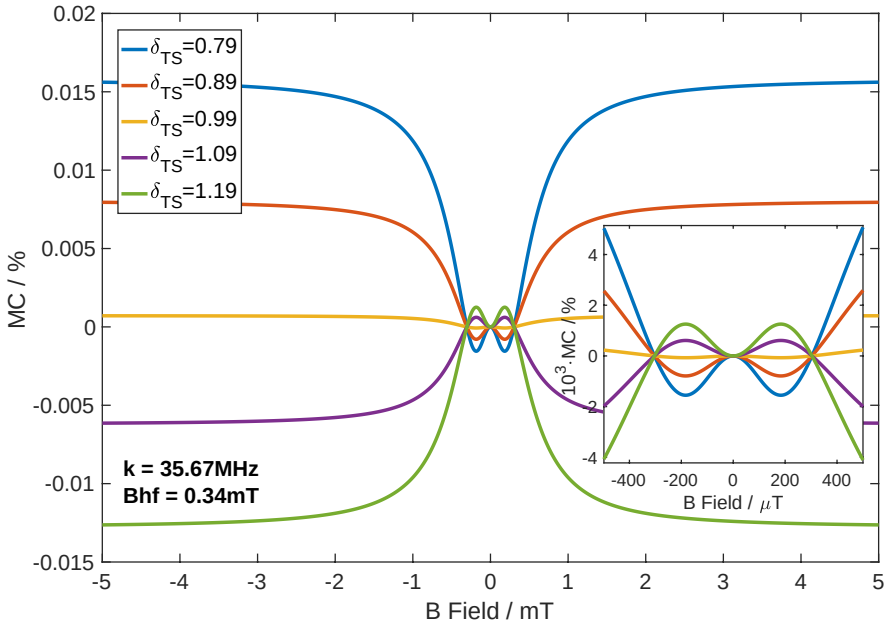

Figure 3.19: Single proton polaron pair magnetoconductance simulation: relative weight factor change

The three simulation parameters in this single proton polaron pair model, namely, the hyperfine field B_{hf}, the decay rate, k, and the relative weight factor δ_{TS} have different effects on the ultimate shape of the simulated MC. Specifically, the magnitude of the decay rate, k, can determine the appearance and the intensity of the USMFE MC local minimum, while the hyperfine field, B_{hf}, can determine the position of the "W" shape local minimum. Lastly, the relative weight factor δ_{TS} can determine the sign of the magnetoconductance. Although δ_{TS} and k are independent variables, they

tend to have similar effects of scaling the magnitude of the formed MC (while only δ_{TS} can change the sign of the MC).

3.3.5 Single Proton PP Model Fitting Results

Before discussing the model fitting results, it is important to determine which regime of the USMFE MC experimental results is suitable for polaron pair model fitting. Specifically, it is necessary to determine the magnetic field range where the polaron pair mechanism dominates and apply only the polaron pair model fitting over this range.

For high magnetic field MC measurements, the device drive current dependence and the resulting MC is shown in Figure 3.20. From Figure 3.20, the high field MC effect is dependent on device drive current (in this case, 0.2μA, 2μA, 20μA and 200μA), and this current dependence might be explained by different large field MC models as mentioned in introduction section **1.4.1**. Thus, the current dependence of the MC is a sign of operating within the high field effect (HFE) zone.

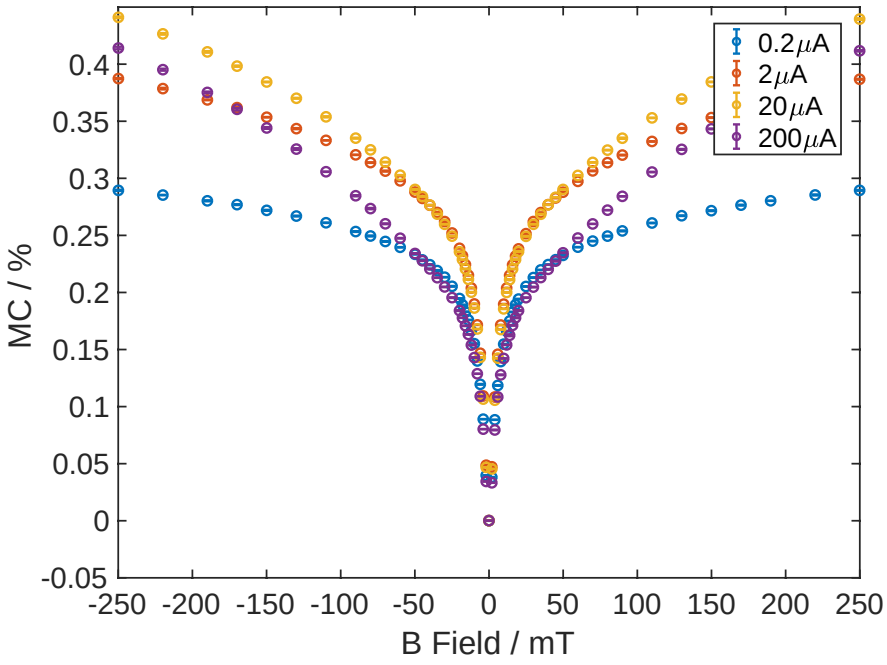

Figure 3.20: High magnetic field effect MC: drive current dependence measurement

The same drive current dependence measurement is carried out in the ultra-small magnetic field range (-500μT$\sim$+500μT) under the same drive currents (0.2μA, 2μA,

20μA and 200μA). The current dependence results are shown in Figure 3.21(a). It is clear that the USMFE MCs start to show the current dependence effect when the external magnetic field exceeds approximately $\pm 300\mu$T. The current dependence indicates that the HFE becomes significant above $\pm 300\mu$T, which can be explained by those four HFE models mentioned in Chapter 1. However, in PP model, there is no drive current related terms included in the modelling (there are only three quantitative parameters: k, $\delta_{T,S}$ and B_{hf}). Therefore only the drive current independent regime is considered to be PP model dominant regime. Below the field of $\pm 300\mu$T, within the small error bars of $\sim 10^{-6}$, there is no obvious sign of any current dependence. This is in agreement with the Polaron Pair model where there are only three model parameters (hyperfine field B_{hf}, decay rate k, and the relative weight factor δ_{TS}) and no current related parameters are included. Therefore, from the current dependence result in Figure 3.21, it can be confirmed that the PP model dominates below magnetic fields of $\pm 300\mu$T and the PP model fitting technique is applied only in this magnetic field regime.

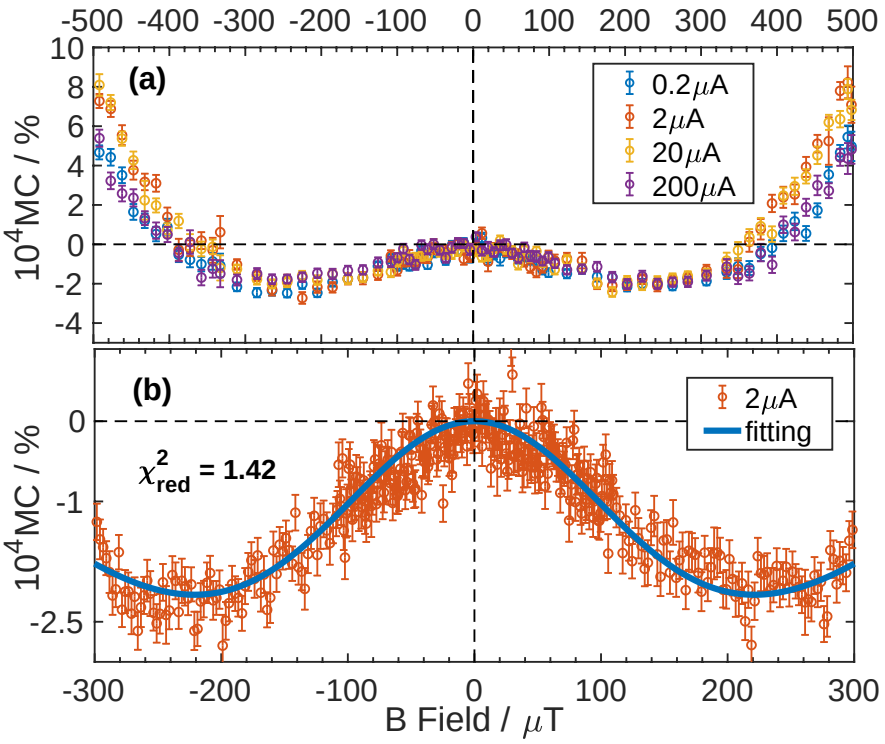

Figure 3.21: Drive current dependence of USMFE MC and the single proton PP model fitting result

Table 3.1: Fitting parameters for 3 individual devices within $\pm 300\mu$T

	Device 1 (Figure 3.21)	Device 2	Device 3
B_{hf}	(0.34 $\pm$ 0.04)mT	(0.30$\pm$ 0.03)mT	(0.34 $\pm$ 0.02)mT
k	(28.6 $\pm$ 9.7)MHz	(20.2 $\pm$ 2.6)MHz	(35.7 $\pm$ 2.2)MHz
δ_{TS}	0.99 $\pm$ 0.01	0.99 $\pm$ 0.01	0.98 $\pm$ 0.01

The algorithm described extensively in section **3.2.4** is applied within this range. The fitting result is shown in Figure 3.21(b) for experimental MC data measured under a drive current of 2μA. The minimum χ^2_{red} set of parameters obtained by the fit in Figure 3.21(b) are: k = 28.6 $\pm$ 9.7 MHz, B_{hf} = 0.34 $\pm$ 0.04 mT and δ_{TS} = 0.99 $\pm$ 0.01, with a χ^2_{red} = 1.42. The errors in the fitting parameters returned by the procedure are recorded to be within one standard error of the minimum χ^2_{red} value, $\sigma_{\chi^2_{red}}$, given by: $\sigma_{\chi^2_{red}}=\sqrt{2/N}$ where N is the number of data points.

To show the reproducibility of the single proton polaron pair model fitting, the same fitting procedure is applied to fit MC results from three individual devices and the results are shown in Table 3.1. From Table 3.1, all the parameters are consistent with each other within error with exceptions of the k values obtained from device 3.

Additionally, fitting was performed for each of the drive currents used in Figure 3.21 and the results are shown in Table 3.2. In the model fitting, as extensively discussed in section **3.2.4**, B_{hf} largely determines the horizontal positions (magnetic field) of the "W" shape MC while k determines the vertical position of the two dips (the magnitude of MC). For device 1, 240 averages were taken and for the other two devices only 100 averages were taken, the errors in the data obtained from device 2 and 3 are therefore slightly larger than device 1. As the Helmholtz coils and gaussmeter are stable and precise there is little effect on the errors on the horizontal positions (B field values) of minimum MC (magnetic field). Therefore, the main error is in the vertical position of the two dips (the magnitude of MC). The change in MC magnitudes and increased errors due to different averaging would result in slightly different values of k as shown in Table 3.1 . The consistency and reproducibility of the model fitting across the returned values is pleasing. The 2μA is chosen for the majority of measurements as the low drive current condition (0.2μA) generates noisier MC compared to 2μA,

Table 3.2: Fitting parameters for different drive conditions of device 1 within $\pm 300\mu$T

	0.2μA	2μA	20μA	200μA
B_{hf}	(0.32 $\pm$ 0.06)mT	(0.34$\pm$ 0.04)mT	(0.32 $\pm$ 0.07)mT	(0.34 $\pm$ 0.07)mT
k	(20.7 $\pm$ 4.9)MHz	(28.6 $\pm$ 9.7)MHz	(22.2 $\pm$ 5.8)MHz	(24.5 $\pm$ 6.8)MHz
δ_{TS}	0.99 $\pm$ 0.01	0.99 $\pm$ 0.01	0.99 $\pm$ 0.01	0.99 $\pm$ 0.01

and high drive conditions (20μA and 200μA) increase the potential to degrade the device. Although 100 averages are used for the drive conditions of 0.2μA, 20μA and 200μA, 240 averages are used for the 2μA drive condition, to generate data for model fitting. A single device has been mesured for a total of $\sim$7000 scans, with a total on-time of $\sim$200 days and the same fitting parameters were returned by the aged device as a new devcie.

At this point, the parameter values obtained by fitting and their physical significance must be addressed. Let's begin by considering the disappearance rate constant, k, and hyperfine field B_{hf}. This is consistent with the value of B_{hf}, since the rate constant has to be smaller than the Larmor precession frequency for the corresponding hyperfine field, which in this case is 59.45 MHz [48]. The local B_{hf} of 0.34 mT, is much smaller than typical hyperfine fields quoted in the literature [18, 69, 70], but is comparable to local hyperfine fields calculated by Marumoto et al using Density Functional Theory (DFT) for an Alq_3 anion [75] where different local hyperfine field magnitudes between 0.01 mT and 1.43 mT are reported.

In trying to assess the relevant local hyperfine field experienced by a polaron one has to take into account the spatial distribution and location of the Highest Occupied Molecular Orbital (HOMO) and Lowest Unoccupied Molecular Orbital (LUMO) wavefunctions in Alq_3. Using available literature calculations [76, 77] for the spatial distribution of the HOMO and LUMO in the system, it is possible to calculate the average local hyperfine field in each case using the literature numerical values [75] and averaging methods [63]. Thus an average local hyperfine field value for the HOMO of approximately 200 μT is obtained and for the LUMO approximately 1.8 mT. The fitted B_{hf} value of 0.34 mT therefore appears to correspond to the average local field for the HOMO and thus should correspond to the field experienced by

the hole in the polaron pair and not the electron. Since the data obtained is limited to small (hundreds of μT) fields, it is not expected to detect large hyperfine field component contributions, such as those resulting from the electron (LUMO) average local hyperfine fields. In terms of the single proton model, the choice is entirely justified as in this model only one of the polaron pair charges is coupled to the hyperfine field, which in this case is the positive (hole) polaron. Furthermore, the fitted B_{hf} value of 0.34 mT can be compared to local fields measured by an entirely independent method. Drew et al have obtained neighbouring proton nuclear spins coupling to electrons, using muon spin relaxation measurements, below approximately 0.3 mT [78] in Alq_3. Thus, the local B_{hf} value returned by the Polaron Pair theoretical fit to my experimental data is in excellent agreement with relevant local hyperfine fields calculated, for this molecule, entirely independently by two different methods. Additionally, Electron Spin Resonance spectroscopy has been used to measure the local hyperfine field in the organic semiconductor H-DOO-PPV and returned a value of 0.37 mT (which compares favourably to the fitted B_{hf} value for Alq_3)[63]. It has been noted that "hyperfine" fields of order 3-5 mT reported in literature[18, 69, 70] for different organic semiconductors, including Alq_3, are obtained using empirical (usually Lorentzian) fits to MC data, but some empirical line-shapes, such as those used by Janssen et al[61], do yield "hyperfine" fields below 1 mT.

The δ_{TS} value of 0.99 indicates that triplet polaron pairs contribute less to dissociation than singlet polaron pairs, in agreement with reference[54] who also report a δ_{TS} of less than but closed to one, meaning that triplet polaron pairs can be expected to be slightly more strongly bound than singlets. This is certainly true of triplet versus singlet excitons[79] and a much more strongly bound triplet exciton is expected to have a smaller probability of dissociation. The microscopic parameters obtained by fitting the sample results in Figure 3.21 are consistent (within error) with those obtained from different diodes measured at the same drive current and with the parameters obtained from a single sample at drive currents between 0.2 μA and 200 μA as shown in Table 3.2. Additionally, there is no evidence of device degradation, despite the large number of repetitions, as evidenced by comparing the MC obtained over different

numbers of repetitions, at the beginning and end of a given experiment, and over all averages shown in Figure 3.12. Notably, a small local B_{hf} of ~300 μT is always obtained, vindicating the approach of modelling a single average local hyperfine field. It should be stressed that the PP model plots appearing in the literature[53] using larger (1mT, 3mT) two proton fields are not fits to data and are used solely as demonstrations that the model can reproduce the correct "W" MC shape, that is, the functional form of the MC.

3.4 Conclusions

In conclusion, the USMFE MC measurements in Alq_3 based devices with μT resolution and ppm sensitivity at fields comparable to the Earth's magnetic field (with careful external coil cancellation) are presented and discussed. The MC measured displays one of the smallest minimum field values ($B_m \sim 240$ μT) reported for protonated organic systems and is not a function of drive current (unlike the HFE MC measured).

A successful single proton Polaron Pair model from literature was chosen for the fitting technique. This model has three physical parameters: the decay rate k, the local hyperfine field B_{hf} and the weight factor δ_{TS}. A series of simulations had been done in order to view the effects of different parameters on the final shape of the simulated MC. Increasing decay rates k can decrease the magnitude of the "W" shape MC, and finally diminishes the "W" functional shape when the decay rate is comparable to the hyperfine precession frequency. In terms of the parameter B_{hf}, the minimum MC B field and FWHM of the MC increase with increasing values of B_{hf} while the asymptotic saturation value is independent of B_{hf}. The last parameter δ_{TS} can effectively tune the sign of the MC. A δ_{TS} smaller than 1, meaning that singlet PP contributes more than triplet PP in dissociation can yield a positive HFE MC and a negative USMFE MC, and vice versa.

The data has been successfully fitted using the single proton Polaron Pair model for organic magnetoconductance and returns physically significant values for three fitting parameters: k = 28.6 $\pm$ 9.7 MHz, B_{hf} = 0.34 $\pm$ 0.04 mT and δ_{TS} = 0.99 $\pm$ 0.01. The

parameter values are mutually consistent, and the average local hyperfine field value of 340 μT obtained for Alq_3 agrees with literature DFT modelling (the local hyperfine field in HOMO of Alq_3) and muon based measurements for this material. Additionally, it is considerably smaller than the Lorentzian empirical fit values in the range 1-5 mT reported in the literature for organic systems. The $\sim$ 340 μT value of B_{hf} obtained for Alq_3 does not depend on individual device drive conditions and is reproducible across different devices, indicating that it represents an actual microscopic material property, within the context of the PP model, rather than depending on individual experimental conditions. Thus, this work demonstrates that Polaron Pair based theoretical fitting of experimentally obtained MC data can be a viable method of obtaining values for physically significant microscopic quantities such as B_{hf} in any organic system.

However, the PP model used in this chapter still has following limitations: 1. It has been simplified that there is only one polaron in the pair state that is coupled to a proton hyperfine field. 2. A reduced Liouville equation is used (without considering the explicit spin-selective radical-radical interaction) and the decay process (recombination and dissociation) is forced into the model by using equation 3.10. 3. The polaron interactions considered are only Zeeman and Hyperfine interactions. 4. The use of singlet initial state 5. The use of the ambiguous parameter $\delta_{T,S}$ in the MC formulation. 6. The neglect of electron coupling. Only three fitting parameters of this model makes the model fitting technique more reliable. In Chapter 4, the PP model will be developed to include two protons coupled to each charge of the polaron pair, and the universal decay rate in this simplified model will be differentiated for singlet and triplet polaron pair states. This developed PP model will make it more realistic for the polaron pair and further justify this model fitting technique.

Moreover, there are only MC data measured and fitted in this work because of the problem measuring MEL with a ferrous light detector, which would have stray magnetic field influencing the measurement of USMFE. However, this problem is addressed by using optical fiber coupling between the device and light detector, elongating the distance between those two would significantly prevent the device from those stray fields.

Chapter 4

Two-Proton PP Model Fitting in MC and MEL data in Alq_3

4.1 Introduction

In Chapter 3, the polaron pair model was used to yield realistic local hyperfine field for holes in Alq_3. However, the microscopic picture between the model and ultra-small magnetic field effects is not clear. In particular, the relative weight factor δ_{TS}, which describes the contribution to the dissociation between singlet and triplet polaron pairs in the formulation of the MC, is ambiguous. The unclear physical significance of this weight factor weakens the physical validity of the model.

In this chapter, the model fitting technique is developed based on the previous work, and to fit both the MC and MEL globally and yield both local hyperfine fields without the use of the elusive parameter δ_{TS}.

In the literature, USMFE MC and MEL of different organic materials are reported to always share the same "W" shape behaviour within the same magnetic field range, as described by conventional polaron pair model [52, 55, 57, 58]. However, in this work, a completely different behaviour of MC and MEL is observed within the same ultra small magnetic field range (-500μT $\sim$ +500μT). This is done using the same OLED based on tris-(8-hydroxyquinoline)aluminium (or Alq_3) by applying constant driving current to the working device instead of the reported method of constant

driving voltage. This difference between MC and MEL behaviour has also been noticed recently by Ratzke, et al.[80], who used the same method as approached in this work. The different behaviour of the MC and MEL suggests that different processes of polaron pair evolution, i.e., exciton formation for MEL and polaron pair dissociation for MC, are necessary to be included in the modelling.

These concerns are addressed in the present chpater, where the developed model is used to fit the experimentally obtained MC and MEL data. Fitting yields some physically significant parameters, including the local hyperfine fields of the material for different charge polarity. The fitting procedure validates the model by correlating it with experimental data and distinguishes this work from literature [52–58, 61, 63], where there is only the reproduction of the "W" shape of the simulated MC and MEL results. The procedure of model development and fitting to experiment data can help us better understand the microscopic processes of singlet and triplet polaron pair evolution and the different behaviours contributing to the ultimate MC and MEL effect of an OLED.

4.2 Experiments

4.2.1 Device Fabrication

The OLED is prepared in the same manner and has the same configuration as described in Chapter 3.

4.2.2 Measurement and Data Analysis

A 3D Helmholtz coil system was used both to cancel the Earth's magnetic field and provide the applied field for the MC measurements (as described in section **2.3.2**). The applied field coils were driven by a Keithley 2400 SourceMeter unit while the current through the diode was provided by an Agilent B2902A source-measure unit, the voltage across the device was measured using a Keithley 4200 semiconductor characterisation system. The light output of the device was measured by the photodetector and an optical power meter (Newport 1830-C). Magnetic field

measurements were made using a LakeShore 475 DSP Gaussmeter and all equipment was controlled via GPIB using custom written software. The B values plotted are the actual B-fields recorded by the gaussmeter at each data point. Typical B-field step sizes are $\sim 1\mu$T, 2.5μT and 5μT in the B field regimes of $\pm 100\mu$T, $\pm$ (100$\sim$300)μT and $\pm$ (300$\sim$500)μT, respectively. The device voltage at different fields was recorded under constant current and readings were repeated 870 times for averaging. Voltage measurements with applied field, V(B), were alternated with zero field measurements, V(0), to eliminate device drift by averaging the two zero field readings (before and after). Likewise, the luminescence of the device is measured the same way with El(B) and El(0). The MC and MEL were calculated using equations 4.1 (a) and (b).

$$\begin{aligned} MC(B) &= \frac{V(0) - V(B)}{V(B)} \times 100\% \text{.....}(a), \\ MEL(B) &= \frac{El(B) - El(0)}{El(0)} \times 100\% \text{.....}(b) \end{aligned} \tag{4.1}$$

All measurements were carried out with the diode under vacuum ($10^{-5}\sim10^{-6}$ mbar) at room temperature($\sim 23^{o}$C).

4.2.3 Two-Proton Polaron Pair Model

Similar to the modelling of the single proton polaron pair, a reduced energy-conserved stochastic Liouville von Neumann is applied as shown in equation 4.2

$$\frac{d\sigma(t)}{dt} = [\mathbf{H}, \sigma] \tag{4.2}$$

Where the Hamiltonian **H** is in angular frequency unit. The solution to equation 4.2 can be obtained [48, 71] as in equation 4.3:

$$\sigma(t) = e^{-iHt}\sigma(0)e^{iHt} \tag{4.3}$$

where the initial assumption of the formation of singlet polaron pair is made (this is arbitrary and the same physics can be obtained by assuming initial triplet formation) with initial singlet density, $\sigma(0)$ [48] as in Chapter 3. **H** is the spin Hamiltonian consisting of different interactions among polaron pairs and the external magnetic field.

Those interactions include Zeeman interaction between each polaron and the external magnetic field, the hyperfine interaction between the polaron and its surrounding hydrogen nuclei, the dipolar interactions and exchange interactions between the spins of each polaron, etc. However, as in Chapter 3, a reduced Hamiltonian containing only the Zeeman and hyperfine interactions is applied for simplicity of calculation. For this work, the hyperfine interaction has two protons, one coupling to each of the polarons as shown in equations 4.4

$$\begin{aligned} H &= H_{Zeeman} + H_{Hyperfine}.....(a), \\ H_{Zeeman} &= g\mu_B B \cdot (S_{1z} + S_{2z}).....(b), \\ H_{Hyperfine} &= g\mu_B \Big[B_{hfc1} \cdot (S_1 \cdot \mathrm{I}_1) + \mathrm{B}_{hfc2} \cdot (S_2 \cdot \mathrm{I}_2) .....(c) \end{aligned} \tag{4.4}$$

Where g is the g-factor that is approximately equal to 2.002, μ_B is the Bohr magneton 5.788×10^{-5} eV·T^{-1}, B is the applied magnetic field, S_{1z} and S_{2z} are the z components of the spin operators for the two polarons and B_{hfc1}, B_{hfc2} are the local hyperfine fields due to two protons. S_1 and S_2 are the spin operators including all components for both polarons and I_1 and I_2 are the spin operators for the hydrogen nuclei. Noticeably, the dipolar and exchange interactions are omitted here in the Hamiltonian. Because the Coulomb radius (the maximum distance between polarons in the PP state, $\mathrm{r}_c = \frac{e^2}{4\pi\epsilon_r\epsilon_0 kT}$, e: unit charge, ϵ_0 and ϵ_r are vacuum and relative dielectric constants and $\epsilon_r \sim 3$ for Alq_3. kT is the thermal energy at room temperature.) was calculated to be around 19nm for Alq_3 and dipolar and exchange interaction during this long range could be negligibly small.

The terms $\mathrm{S}_1 \cdot \mathrm{I}_1$ and $\mathrm{S}_2 \cdot \mathrm{I}_2$ can be defined in equations 4.5 (a) and (b)

$$\begin{aligned} S_1 \cdot \mathrm{I}_1 &= \mathrm{S}_{1x} \cdot \mathrm{I}_{1x} + \mathrm{S}_{1y} \cdot \mathrm{I}_{1y} + \mathrm{S}_{1z} \cdot \mathrm{I}_{1z}.....(\mathrm{a}), \\ S_2 \cdot \mathrm{I}_2 &= \mathrm{S}_{2x} \cdot \mathrm{I}_{2x} + \mathrm{S}_{2y} \cdot \mathrm{I}_{2y} + \mathrm{S}_{2z} \cdot \mathrm{I}_{2z}.....(\mathrm{b}) \end{aligned} \tag{4.5}$$

Likewise, S_1, I_1, S_2 and I_2 with different x, y and z subscripts correspond to the Pauli matrices for the polarons and the hydrogen nuclei respectively.

Figure 4.1 is a schematic of the two-proton hyperfine coupling situation, where each polaron is coupled to its neighbouring hyperfine field.

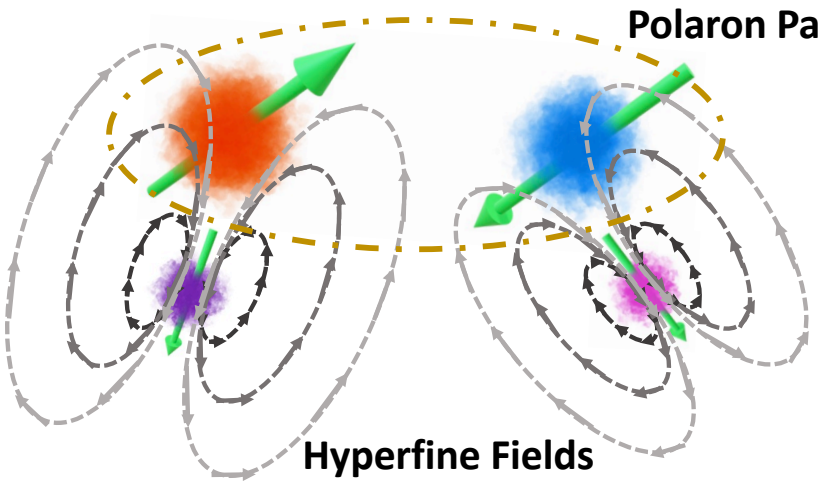

Figure 4.1: The illustration of the so-called two-proton hyperfine coupling

Similarly to Chapter 3, The singlet fraction, ρ_S, is calculated via the trace of the singlet projection operator, P_S, operating on σ(t) as shown in equation 4.6:

$$\rho_S = Tr\left[P_S \sigma(t)\right] \tag{4.6}$$

The singlet-triplet transformation basis is necessary for later calculation basis transformation as given in Equation 4.7

$$P_e = \begin{pmatrix} 1 & 0 & 0 & 0 \\ 0 & \frac{1}{\sqrt{2}} & \frac{1}{\sqrt{2}} & 0 \\ 0 & -\frac{1}{\sqrt{2}} & \frac{1}{\sqrt{2}} & 0 \\ 0 & 0 & 0 & 1 \end{pmatrix} \tag{4.7}$$

Where the second column represents singlet component while the other three columns represent three different triplet components. For consistency of the quantum calculation, all the spin components should stay in the same singlet-triplet basis as shown in equation 4.7. For a two-proton polaron pair system, there are 4 particles in total (2 polarons and 2 nuclei). The calculation of the four particles based on this

singlet-triplet basis can be expressed as the equations given in Equations 4.8 and 4.9.

$$P = P_e \otimes I_{e2\times 2} \otimes I_{e2\times 2} = \begin{pmatrix} 1 & 0 & 0 & 0 & 0 & 0 & 0 & 0 \\ 0 & 1 & 0 & 0 & 0 & 0 & 0 & 0 \\ 0 & 0 & \frac{1}{\sqrt{2}} & 0 & \frac{1}{\sqrt{2}} & 0 & 0 & 0 \\ 0 & 0 & 0 & \frac{1}{\sqrt{2}} & 0 & \frac{1}{\sqrt{2}} & 0 & 0 \\ 0 & 0 & -\frac{1}{\sqrt{2}} & 0 & \frac{1}{\sqrt{2}} & 0 & 0 & 0 \\ 0 & 0 & 0 & -\frac{1}{\sqrt{2}} & 0 & \frac{1}{\sqrt{2}} & 0 & 0 \\ 0 & 0 & 0 & 0 & 0 & 0 & 1 & 0 \\ 0 & 0 & 0 & 0 & 0 & 0 & 0 & 1 \end{pmatrix} \otimes I_{e2\times 2} \tag{4.8}$$

$$= \begin{pmatrix} 1 & 0 & 0 & 0 & 0 & 0 & 0 & 0 & 0 & 0 & 0 & 0 & 0 & 0 & 0 & 0 \\ 0 & 1 & 0 & 0 & 0 & 0 & 0 & 0 & 0 & 0 & 0 & 0 & 0 & 0 & 0 & 0 \\ 0 & 0 & 1 & 0 & 0 & 0 & 0 & 0 & 0 & 0 & 0 & 0 & 0 & 0 & 0 & 0 \\ 0 & 0 & 0 & 1 & 0 & 0 & 0 & 0 & 0 & 0 & 0 & 0 & 0 & 0 & 0 & 0 \\ 0 & 0 & 0 & 0 & \frac{1}{\sqrt{2}} & 0 & 0 & 0 & \frac{1}{\sqrt{2}} & 0 & 0 & 0 & 0 & 0 & 0 & 0 \\ 0 & 0 & 0 & 0 & 0 & \frac{1}{\sqrt{2}} & 0 & 0 & 0 & \frac{1}{\sqrt{2}} & 0 & 0 & 0 & 0 & 0 & 0 \\ 0 & 0 & 0 & 0 & 0 & 0 & \frac{1}{\sqrt{2}} & 0 & 0 & 0 & \frac{1}{\sqrt{2}} & 0 & 0 & 0 & 0 & 0 \\ 0 & 0 & 0 & 0 & 0 & 0 & 0 & \frac{1}{\sqrt{2}} & 0 & 0 & 0 & \frac{1}{\sqrt{2}} & 0 & 0 & 0 & 0 \\ 0 & 0 & 0 & 0 & -\frac{1}{\sqrt{2}} & 0 & 0 & 0 & \frac{1}{\sqrt{2}} & 0 & 0 & 0 & 0 & 0 & 0 & 0 \\ 0 & 0 & 0 & 0 & 0 & -\frac{1}{\sqrt{2}} & 0 & 0 & 0 & \frac{1}{\sqrt{2}} & 0 & 0 & 0 & 0 & 0 & 0 \\ 0 & 0 & 0 & 0 & 0 & 0 & -\frac{1}{\sqrt{2}} & 0 & 0 & 0 & \frac{1}{\sqrt{2}} & 0 & 0 & 0 & 0 & 0 \\ 0 & 0 & 0 & 0 & 0 & 0 & 0 & -\frac{1}{\sqrt{2}} & 0 & 0 & 0 & \frac{1}{\sqrt{2}} & 0 & 0 & 0 & 0 \\ 0 & 0 & 0 & 0 & 0 & 0 & 0 & 0 & 0 & 0 & 0 & 0 & 1 & 0 & 0 & 0 \\ 0 & 0 & 0 & 0 & 0 & 0 & 0 & 0 & 0 & 0 & 0 & 0 & 0 & 1 & 0 & 0 \\ 0 & 0 & 0 & 0 & 0 & 0 & 0 & 0 & 0 & 0 & 0 & 0 & 0 & 0 & 1 & 0 \\ 0 & 0 & 0 & 0 & 0 & 0 & 0 & 0 & 0 & 0 & 0 & 0 & 0 & 0 & 0 & 1 \end{pmatrix} \tag{4.9}$$

The matrix in equation 4.9 is a 16×16 matrix which represents the 16 quantum states for this four-particle system. The physical meaning of the Kronecker product $\otimes$ in equation 4.8 is the combinations of the possible quantum states that exist in the four-particle system (or singlet-triplet-proton-proton system).

Therefore, accordingly, the singlet projection operator P_S in equation 4.6 can be expressed in Equation 4.10:

$$P_S = \frac{1}{4} \times I_{e16\times16} - I_{Ax} \otimes I_{Bx} \otimes I_{e2\times2} \otimes I_{e2\times2} - I_{Ay} \otimes I_{By} \otimes I_{e2\times2} \otimes I_{e2\times2} - I_{Az} \otimes I_{Bz} \otimes I_{e2\times2} \otimes I_{e2\times2} \tag{4.10}$$

Where $I_{e16\times16}$ is a 16×16 unity matrix and I_A and I_B, subscript x, y and z, are the corresponding components of the Pauli matrices of each polaron. The effect of the singlet projection operator as used in equation 4.6 is to "filter out" all the singlet components among all spin configurations.

Noticeably, the subsequent definition of steady state singlet and triplet yield is different from the previous work, and is defined by the new Different-Rate-Polaron-Pair Model. In this model, not only are the two hyperfine fields (two protons) considered in the hyperfine coupling, also included are two different decay pathways for singlet and triplet polaron pair fractions, which contains dissociation and recombination. For different pathways, it is assumed that different rate constants applied to different processes. i.e., $k_{S,d}$, $k_{T,d}$ and $k_{S,r}$, which correspond to the dissociation rates of singlet polaron pair and triplet polaron pair into free charges and the recombination rates of singlet polaron pair into singlet exciton, respectively. Straightforwardly, the steady state yields can be expressed using equations 4.11(a), (b) and (c).

$$\begin{aligned} \Phi_{S,r} &= k_{S,r} \cdot \int_0^\infty \rho_S(t) e^{-k_{S,r} \cdot t} dt \text{.....}(a), \\ \Phi_{S,d} &= k_{S,d} \cdot \int_0^\infty \rho_S(t) e^{-k_{S,d} \cdot t} dt \text{.....}(b), \\ \Phi_{T,d} &= k_{T,d} \cdot \int_0^\infty \rho_T(t) e^{-k_{T,d} \cdot t} dt \text{.....}(c) \end{aligned} \tag{4.11}$$

where $\Phi_{S,r}$ is the steady state singlet exciton yield due to singlet polaron pair recombination, $\Phi_{S,d}$ is the steady state singlet yield due to singlet polaron pair dissociation, $\Phi_{T,d}$ is the steady state triplet yield due to triplet polaron pair dissociation. $\Phi_{T,r}$, the steady state triplet exciton yield due to triplet polaron pair recombination, is not included as the triplet recombination process can neither contribute to the total current nor the luminescence of the device. ρ_S is the singlet fraction, and ρ_T is the triplet fraction which can be evaluated using $\rho_S + \rho_T = 1$. In this way the magnetic field dependent yields $\Phi_{S,r}(B)$, $\Phi_{S,d}(B)$ and $\Phi_{T,d}(B)$ are obtained as shown

in equation 4.11. Electroluminescence is directly related to the radiative recombination of singlet excitons, and magnetoconductance is linked to the dissociation of singlet and triplet polaron pairs as suggested in literature[53]. For the magnetoconductance, the approach by Nguyen and co-workers[53] is used but noticeably, with different rates for dissociation for singlets and triplets in order for the contribution to MC from singlets and triplets to be calculated. This removes the relative weight factor δ_{TS} used in previous work. In this way, intuitively, the expressions for magnetoconductance and magnetoelectroluminescence can be defined as in equations 4.12(a) and (b).

$$\begin{aligned} MEL(B) &= \frac{\Phi_{S,r}(B) - \Phi_{S,r}(B=0)}{\Phi_{S,r}(B=0)} .....(a), \\ MC(B) &= \frac{[\Phi_{S,d}(B) + \Phi_{T,d}(B)] - [\Phi_{S,d}(B=0) + \Phi_{T,d}(B=0)]}{\Phi_{S,d}(B=0) + \Phi_{T,d}(B=0)} \\ &= \frac{\Phi_{S,d}(B) + \Phi_{T,d}(B)}{\Phi_{S,d}(B=0) + \Phi_{T,d}(B=0)} - 1 .....(b) \end{aligned} \tag{4.12}$$

The expressions for MC and MEL in equations 4.12(a) and (b) are the foundation for the newly developed fitting procedure discussed in subsection **4.2.4**.

A schematic showing the process of this two-hyperfine field (two-proton) polaron pair model is illustrated in Figure 4.2

In this model, the same reduced stochastic Liouville von Neumann equation is applied as stated in equation 4.2, thus the rule of conservation energy in the system must be obeyed as stated in Chapter 3. Similarly, for the purpose of the "energy conservation" applied to the dissociation of the polaron pairs, there must be a counterpart as the recombination of the same pair system. Therefore, when the singlet or triplet polaron pair state evolves into the decayed state, the decayed pair state separate into long-distance uncorrelated free charges, or simultaneously, the decayed pair state has the probability of reforming the previous polaron pair state. This is to make sure the energy is conserved in the system. These are indicated in Figure 4.2 by the notation of "reformation" and "separation". Noticeably, the weight factor D_S and D_T as shown in Figure 4.2 are assumed to be equal to each other in contrast to the process in Figure 3.5. In this situation, the weight factors describe the contributions of dissociated decayed states to the dissociated free charges. Technically, there should be

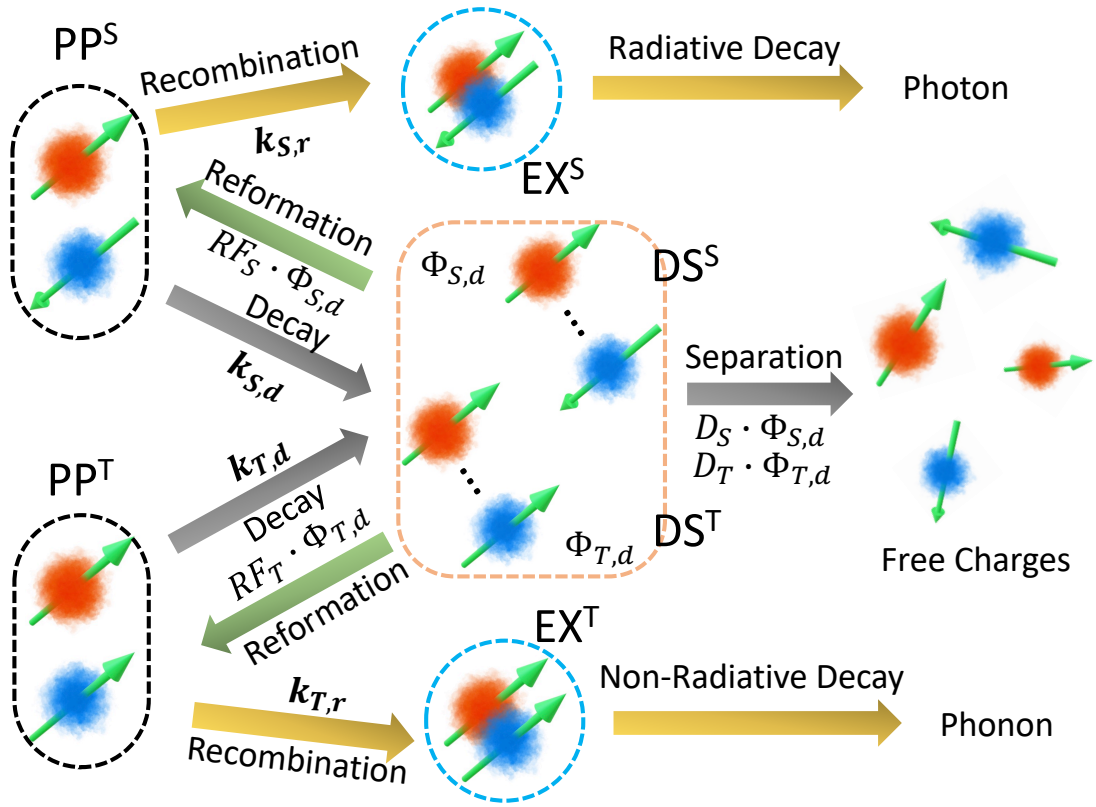

Figure 4.2: The schematic of the microscopic process of the two-proton polaron pair model.

no singlet or triplet states at this decayed stage which is an intermediate state and the two should have approximately the same energetics. Alternatively to the "decaying" process, the polarons in the pair state can also initially approach each other due to the Coulomb attraction in the pair state and to form the exciton state. Recombination of PP states into excitons conserves energy and the reformation and decay processes are use to conserve the energy despite the dissociation into free charges.

4.2.4 Model Fitting Technique and Algorithm

A totally different fitting technique is adopted for this model compared to Chapter 3. Because the single proton polaron pair model in the last chapter only have three fitting parameters and the computation is not complex, thus, a method of trial and error can be applied. However, for this two-hyperfine field (two-proton) polaron pair model, there are more than three fitting parameters and the modelling is more complicated than the first model and evaluating χ^2 values of 5 parameters can be very

inefficient and computationally expensive. Therefore, a more efficient χ^2 minimisation and fitting algorithm is considered.

An efficient and popular optimisation algorithm is Nelder-Mead simplex optimisation algorithm, which was proposed by John Nelder and Roger Mead in 1965. This algorithm is successfully used in non-linear optimisation situations where there can be multiple variables to be optimised and these conditions satisfy the properties that the two-hyperfine field (two-proton) polaron pair model has. The algorithm of Nelder-Mead simplex is discussed extensively as follows.

The simplex, in geometry, can be a line segment when it is in 1 dimensional space, a triangle in 2 dimensional space, a tetrahedron in 3 dimensional space. Since the two-hyperfine field (two-proton) polaron pair model has 5 fitting parameters (the hyperfine fields of two protons B_{hf1} and B_{hf2}, the dissociation rate for singlet and triplet polaron pairs $k_{S,d}$ and $k_{T,d}$ and the recombination rate of singlet polaron pair $k_{S,r}$), the simplex in 5 dimensional space is a 6-simplex. For the purpose of clear demonstration and easy understanding, a situation using a 2 dimensional triangle is applied in explaining the Nelder-Mead optimisation algorithm.

The function to be optimised in this algorithm is called the objective function. The number of variables in the objective function determines the number of vertices in the simplex with a relation of *n* variables corresponding to a *n+1* vertices simplex. For example, an objective function with two variables corresponds to a three vertices simplex, i.e. a triangle.

For the purpose of demonstrating the algorithm, a simple and random objective function shown is used as defined in equation 4.13.

$$f(x_1, x_2) = \frac{1}{7}\sqrt{2500 + x_1^2} + \frac{1}{4}\sqrt{400 + (x_2 - x_1)^2} + \frac{1}{2}\sqrt{900 + (100 - x_2)^2} \qquad (4.13)$$

In order to clarify the optimisation process, a contour map of this objective function is shown in Figure 4.3. There are only 2 variables (x_1 and x_2) in this objective function, a triangle is displayed in Figure 4.3 as the simplex for optimisation. The initial triangle is shown in orange in Figure 4.3(a) with initial vertices A, B and C. The initial vertices

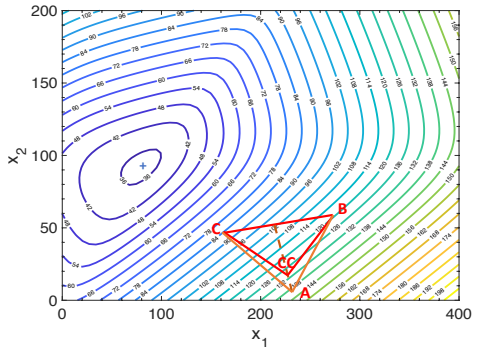

(a) Contraction CC (red) from the initial guess (orange)

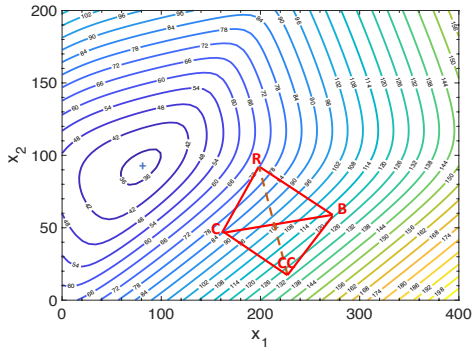

(b) Reflection R

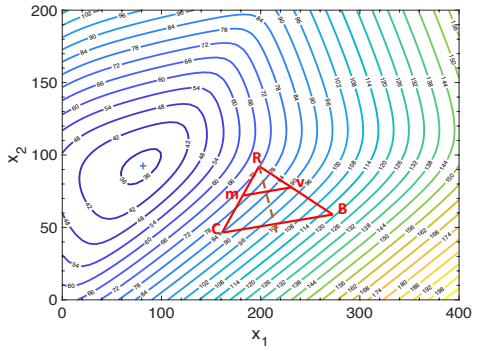

(c) Shrink v

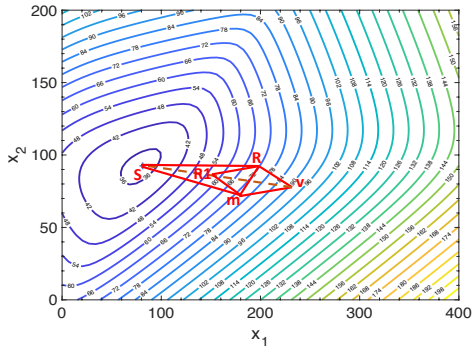

(d) Expansion S1

Figure 4.3: Nelder-Mead Simplex optimisation algorithm

are determined randomly. As the objective function value at vertex A is highest among these three vertices (∼138 in the graph), the first optimisation operation is to contract the triangle ABC with its vertex A to the vertex CC as the objective function at the vertex CC has lower value (∼132 in the graph). CC can be calculated as in equations 4.14 (a) and (b)

$$\begin{aligned} CC &= m + \frac{A - m}{2} \text{.....}(a), \\ m &= \frac{\sum_N \text{all variables}}{N} \text{.....}(b) \end{aligned} \tag{4.14}$$

The algorithm starts to calculate the reflection point R shown in Figure 4.3(b) as defined in Equation 4.15.

$$R = 2m - CC \tag{4.15}$$

As the vertex R has lower function value (∼72) than the vertex CC (∼130), the algorithm replaces the vertex CC with the vertex R and now the triangle becomes CBR

in Figure 4.3(b).

The algorithm starts to improve the total optimisation of all vertices, and shrinks the triangle CBR to mvR where v is expressed in equation 4.16. The shrinking process is shown in Figure 4.3(c).

$$v = R + \frac{B - R}{2} \tag{4.16}$$

Lastly, the algorithm will decide how to converge the optimisation in the last step of expansion as shown in Figure 4.3(d). The algorithm calculates the reflection point R1 first and evaluates the function value at this vertex. Then the algorithm continues to calculate another point called the expansion point S and its corresponding objective function value as defined by Equation 4.17. Importantly, the algorithm will eventually compare the function value at these two points S and R1. For this example, the vertex S has a lower function value and the algorithm will reject the solution of R1 but to accept the vertex S to provide the optimised values. For this simple demonstration, the optimisation algorithm ends at this expansion step as can be seen in Figure 4.3(d) since the vertex S has the lowest objective function value and the values of x_1 and x_2 at the vertex S are finally yielded by the Nelder-Mead simplex optimisation algorithm.

$$S = m + 2(m - v) \tag{4.17}$$

In real situations where there are multiple variables and a more complicated objective function, there can be many simplex transformations and each transformation is carried out iteratively. Thus, the number of the iteration cycles determine how many transformations of simplex or optimisation steps there are in the whole optimisation process.

Particularly for the work in this chapter, the general idea of data fitting is the same in the Chapter 3 where the minimisation of the reduced chi squared value (χ^2_{red}) defined by the experiment data and the model simulation results is applied. However, a major difference is that in this chapter, the chi square (χ^2_{red}) function contains not only an MC term but also an MEL term, which means that this chi squared value is a global chi squared value for all the results and the optimisation on this global χ^2_{red}

achieves the fitting of both MC and MEL data to the model. And the global χ^2_{red} is defined in equation 4.18

$$\chi^2_{global,red} = \sum_N \left[\left(\frac{MC_{exp} - MC_{model}}{MCerror_{exp}} \right)^2 + \left(\frac{MEL_{exp} - MEL_{model}}{MELerror_{exp}} \right)^2 \right] \tag{4.18}$$

Where MC_{exp}, MEL_{exp}, $MCerror_{exp}$ and $MELerror_{exp}$ are the experimentally obtained MC, MEL values with corresponding calculated standard errors, and N is the number of the data points in the measurements. Since the two hyperfine field (two-proton) polaron pair model has 5 fitting parameters, the chi square can be expressed as $\chi^2_{red}(B_{hf1}, B_{hf2}, k_{S,d}, k_{T,d}, k_{S,r})$.

Noticeably for this chapter, this $\chi^2_{red}(B_{hf1}, B_{hf2}, k_{S,d}, k_{T,d}, k_{S,r})$ is treated as the objective function which has been extensively mentioned above, and since this specific objective function has five parameters, the 6-vertices simplex in the 5 dimensional space is applied in the Nelder-Mead optimisation algorithm.

4.3 Results and Discussion

4.3.1 I-V-L Characteristics

Similarly to experiments in Chapter 3, the Current-Voltage-Luminescence Characteristics of the OLED are measured and the result is shown in Figure 4.4 In Figure 4.4 (a)

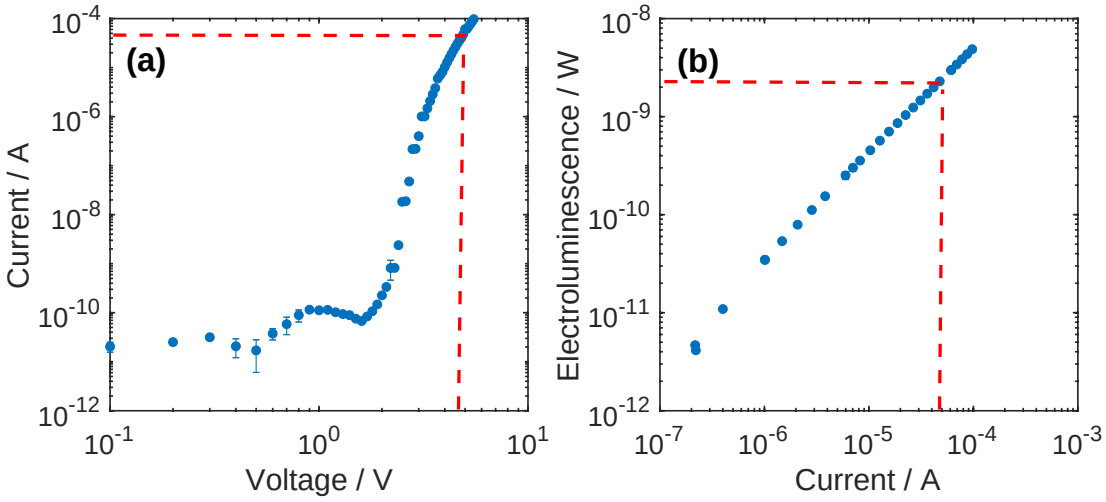

Figure 4.4: The Current-Voltage-Luminescence Characteristics of the OLED

and (b), the Current-Voltage-Electroluminescence Characteristics are shown and the

red dashed line indicates that the device is working in superlinear regime when the device current is above the μA level. Additionally, Figure 4.4 (b) shows a clear near linear Electroluminescence-Current relationship in the device. Both measurements in Figure 4.4 (a) and (b) show significantly reduced noise in the data, achieved by repeating the measurements by 3 times averaging.

4.3.2 Ultra-Small Magnetic Field Effects on MC and MEL

Figure 4.5 (a) and (b) are the results of the magnetic field effect measurements. The device was measured under a constant 39μA drive current with the Earth's magnetic field components in the two orthogonal directions cancelled. The reason 39μA was chosen is that 2μA drive current from the previous work can produce clear MC data but the generated MEL is too noisy. Larger drive currents can generate clear MC and MEL data, however, the higher the drive current is, the higher the probability the device can degrade and destroy the device in an irreversible way[81, 82]. As mentioned in Chapter 3, there is no visibly significant difference on the data between cancelling and not cancelling the residual Earth magnetic field components above approximately 50μT. Although the Earth's field was cancelled in this work. Noticeably, the shape of the obtained MC and MEL data is different. The MC data behaves similarly to results as reported in the literature[52–58, 61–63], however, the MEL data is in a totally different shape compared to the literature [52, 55, 57, 58]. This is due to a different device drive conditions as the device is used in constant current mode in contrast to the literature where constant voltage mode is common. The different MC and MEL shapes have been reported recently by Ratzke, et al. using the constant drive current condition [80], and this rules out the possibility that the different shapes are the experiment artefacts. As can be seen from Figure 4.4(b), the relation between the electroluminescence and the device current is linear while the relation between the electroluminescence and the device voltage is non-linear (Figure 2.38(b)). Because of the effect of magnetoresistance, the device current will change upon different applied external magnetic fields in constant voltage mode, and thus, the device current can be considered as a function of the external magnetic fields. From the linear relation

between electroluminescence and device current, the electroluminescence can be affected by current changes to the external magnetic fields. Therefore, the USMFE measurements with the device under constant voltage will yield the same behaviour in MC and MEL (both like "W" shaped). These constant drive voltage experiments appear in the literature [52, 55, 57, 58]. However, when measuring the USMFE by driving the device in constant current and measuring the device voltage, the device depend on the external magnetic field, however, due to the non-linear relation between the device voltage and the electroluminescence, the electroluminescence is not simply proportional to the device voltage and this will yield a different shape of MEL from the MC data. This rules out the confusion between the charge transport and the optical observable, and makes probing of the spin-dependent recombination more selective and accurate[80].

The reason why the MEL can be modelled and fitted in my work is that under constant current bias, the densities of injected electrons and holes are fixed, ensuring all the other simulation parameters to be controllable (e.g. $\Phi_{S,r}$), and this laid the foundation for the MEL data fitting under constant drive current.

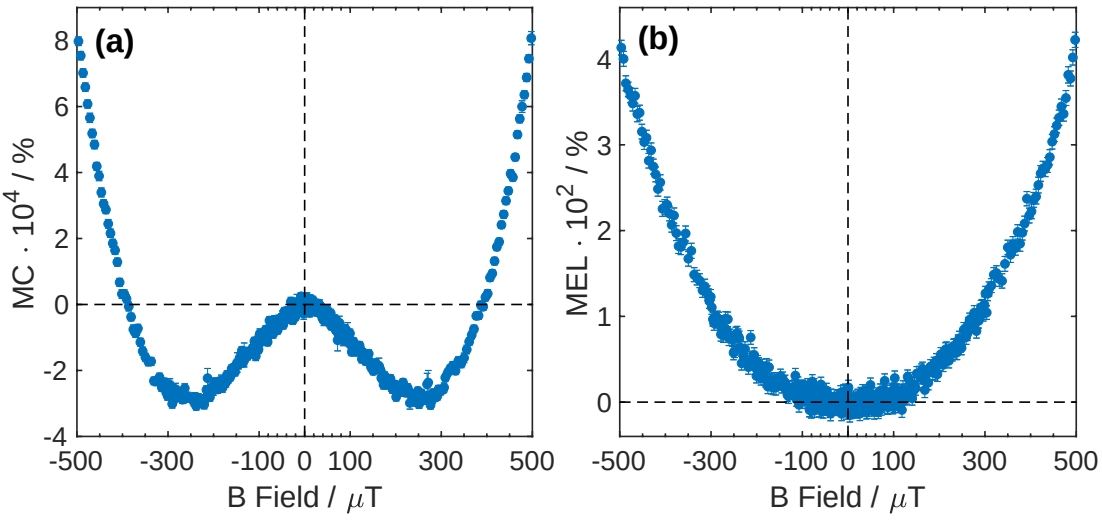

Figure 4.5: The experiment results of measured USMFE (a)MC and (b)MEL with 870 repetitions.

4.3.3 Two-Proton Polaron Pair Model Simulation

Before fitting using the two-proton polaron pair model, it is important to simulate the singlet fraction time evolution and check the validity and consistency of the model as was done in section **3.3.4**. The singlet fraction in equation 4.6 is simulated using the two simulation hyperfine fields of B_{hf1} = 1.55mT and B_{hf2} = 0.39mT under different external magnetic fields of 0μT, 50μT, 250μT and 500μT as shown in Figure 4.7(a), (b), (c) and (d). Because there are two hyperfine fields in this two-proton polaron pair model, there are two hyperfine precession frequencies, namely, 272.8MHz and 67.8MHz, respectively. According to equation 4.11, the yield is calculated via integral of different charge fractions (singlet or triplet fraction). Numerically, the integration is carried out discretely in the calculation. It is important to investigate the effect of the size of the interval on the final result of the yield during integration before the simulation. The check was carried out via the calculation of the singlet fraction using different integral rates (or intervals). A range of rates were chosen including the minimum rate corresponding to the rate 10 times larger than the Larmor precession frequency at 500 μT (i.e. 0.366 ns/step in Figure 4.6). Noticeably, in data sampling theorem, a specific sampling frequency is defined as Nyquist frequency which is the half of the frequency of the original dataset, and is defined to be the minimum of the sampling frequency for replicating original data. In this case, the Nyquist rate is calculated to be 1.83 ns/step. The check results are shown in Figure 4.6.

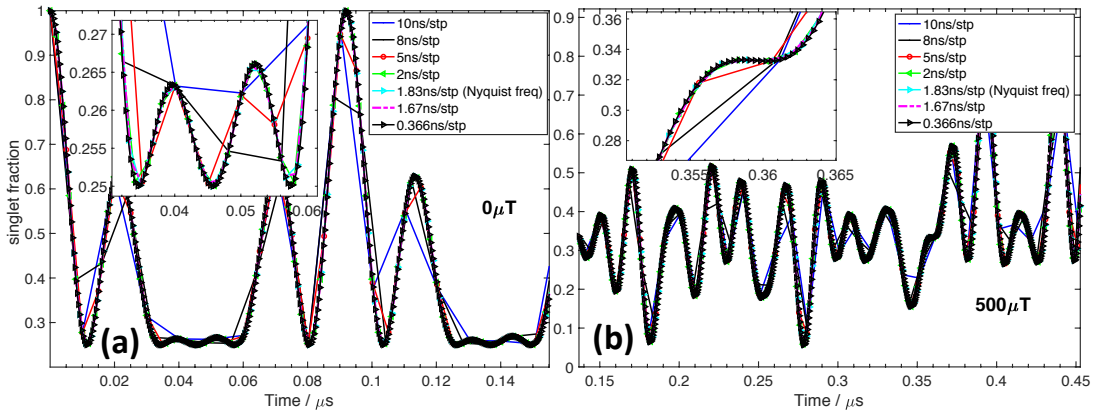

Figure 4.6: Integral interval check at (a) 0μT (b) 500 μT. Insets: the detail of the minimum oscillation frequency. Legends: showing all the integral intervals

The black triangle curve corresponds to the minimum frequency in the data and can be approximated as the "original data form". The details of the minimum oscillation frequency were picked out in insets in Figure 4.6. It is intuitive to consider that if the chosen rate can properly approximate the details of those minimum oscillations (largest possible oscillation frequency) it would be more precise in describing the waveform with smaller oscillation frequencies. Comparing the results in Figure 4.6 (a) and (b), it is clear that when the integral interval is below 2 ns/step the details of the minimum oscillations can be properly sampled.

According to the simulation results from Figure 4.6, the rate of 1.67 ns/step is chosen for the subsequent simulation. In the two proton Polaron Pair model, there are two components of the hyperfine field corresponding to two hyperfine precession frequencies. These two frequencies can be seen in Figure 4.7(a) which is different to the single oscillation phase caused by a single hyperfine field in Figure 3.13. Under zero external magnetic field and this intertwined oscillation consists of multi-oscillations due to the two different hyperfine precession frequencies. In Figure 4.7(b), when the external magnetic field is 50μT, which is larger than the smaller component of the two hyperfine fields (39μT), but smaller than the larger hyperfine component (1.55mT), the oscillation envelope changes and is affected by the Zeeman interaction of the external magnetic field. When the external magnetic field increases to 250μT, which is significantly larger than the smaller hyperfine field component (39μT), as shown in Figure 4.7(c), the effect of the hyperfine precession of the slow frequency (67.8MHz) is totally eliminated (the envelope in Figure 4.7 (a) and (b)) and dominated by the much larger effect of the Zeeman interaction with the external magnetic field. However, as the external field is still much smaller than the larger hyperfine field (1.55mT), the high precession frequency is still visible in the oscillation. Similar for Figure 4.7(d), the only effect is the Zeeman interaction getting more intense as the oscillation envelope becomes faster.

In the simulation of singlet fraction time evolution with different decay rates is also carried out and the results are shown in Figure 4.8. In Figure 4.8, the blue lines are the same results as in Figure 4.7 before the decay rates are introduced. The

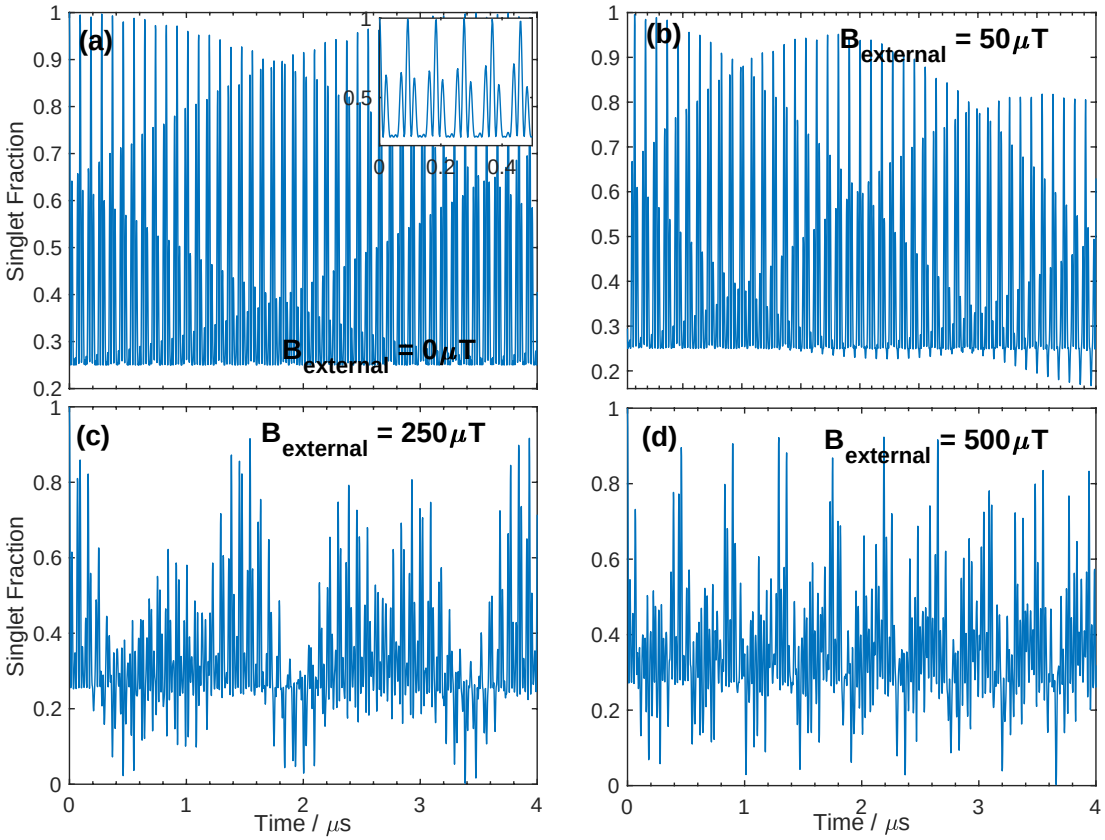

Figure 4.7: The singlet fraction time evolution under different external magnetic fields using B_{hf1} = 1.55mT and B_{hf2} = 0.39mT. The inset in (a) is a detail of the singlet fraction from 0 to 0.5μs.

red lines represent the result of the singlet fraction decay into a static state due to the recombination process with a simulated recombination rate of $k_{S,r}$ = 1.94MHz. As shown in equation 4.11, there are two "decay" or disappearing routes for singlet fraction - recombination and dissociation pathways (also indicated in Figure 4.2). Both of the pathways begin at an initial singlet fraction. When the singlet polaron pair moves towards the recombination pathway, it "decays" with a rate $k_{S,r}$ and is shown in red in Figure 4.8(a). Similarly, when the singlet polaron pair turns to the "decay" pathway – dissociation pathway, the time evolution of the state is determined by rate $k_{S,d}$ and is shown in yellow line in Figure 4.8(a).

In Figure 4.8(a), (b), (c) and (d), the simulations are carried out under different external magnetic fields of 0μT, 50μT, 250μT and 500μT using the same two hyperfine field components of B_{hf1} = 1.55mT and B_{hf2} = 0.39mT. For all the decays due to recombination (red), a slow decay rate of 1.94MHz is chosen for clear demonstration,

similarly for the dissociation process (yellow) as a much slower rate of 0.6MHz is chosen.

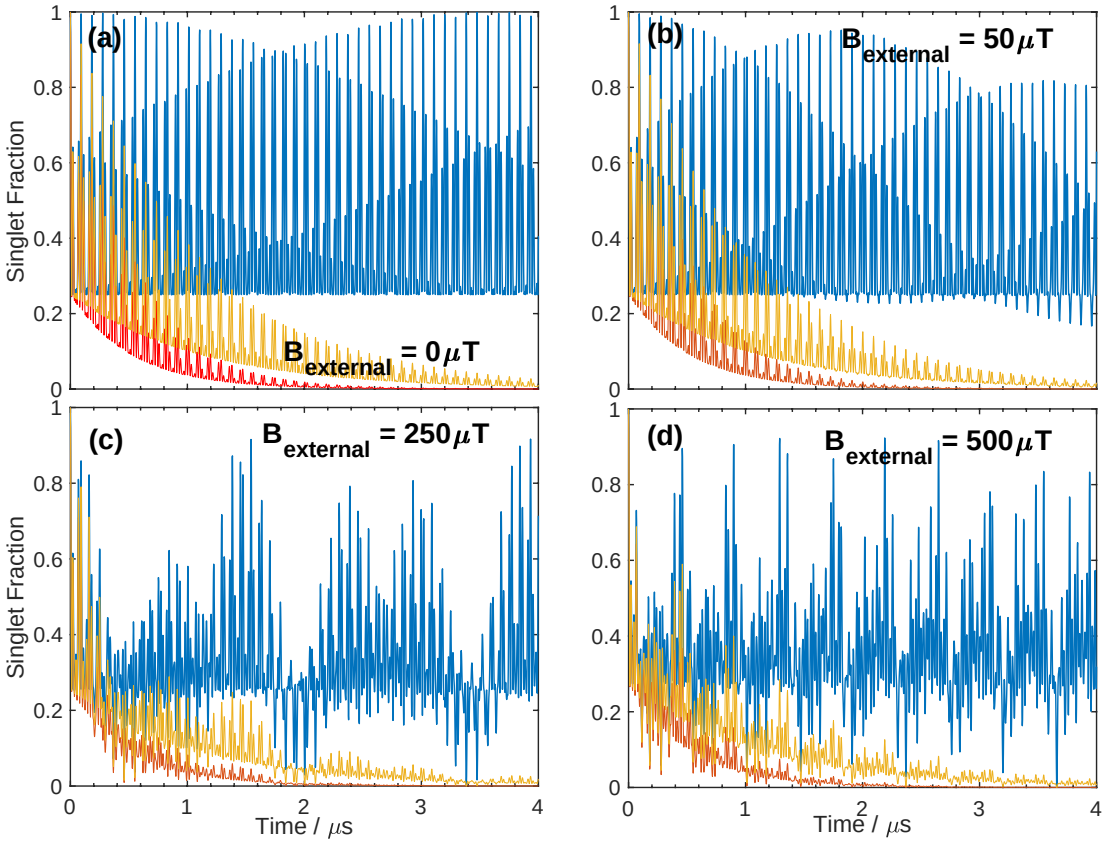

Figure 4.8: The singlet fraction time evolution with different decay rates. Red: Recombination with decay rate of $k_{S,r}$ = 1.94MHz. Yellow: Dissociation with decay rate of $k_{S,d}$ = 0.6MHz. Blue: No decay. The simulated two hyperfine fields are B_{hf1} = 1.55mT and B_{hf2} = 0.39mT.

In this chapter, the MC and MEL are modelled as in equation 4.12 (a) and (b). In Figure 4.9, the MC and MEL over a large range of magnetic fields (±20mT) are simulated with model parameters: B_{hf1} = 1.55mT, B_{hf2} = 0.39mT, $k_{S,r}$ = 237.7MHz, $k_{S,d}$ = 104.6MHz and $k_{T,d}$ = 96.5MHz. In Figure 4.9(a), the magnetic field ranges from -20mT to 20mT and the inset is the ultra-small magnetic field region (below 1mT) where the typical "W" shape MC manifests. Similar to the simulation result in Figure 3.16, the simulated MC and MEL using two-proton polaron pair model also tend to saturate at relatively larger magnetic field (approximately larger than |6mT|). This indicates that the polaron pair model is not dominant at high fields, and other HFE starts to play an important role. Evidently, from the HFE measurement experiments in

Figure 3.20 and the current dependence experiments within the ultra-small magnetic field range shown in Figure 3.21, it is clear to see that the HFE start to dominate the MC effect when the external magnetic field exceeds approximately $\pm 300\mu$T. The MC rises rapidly compared to below $\pm 300\mu$T, and is orders of magnitude larger than that of the saturated MC level shown in Figure 4.9(a). This is similar for MEL simulation results in Figure 4.9(b). Again the HFE starts to dominate the high fields and the PP model is no longer applicable.

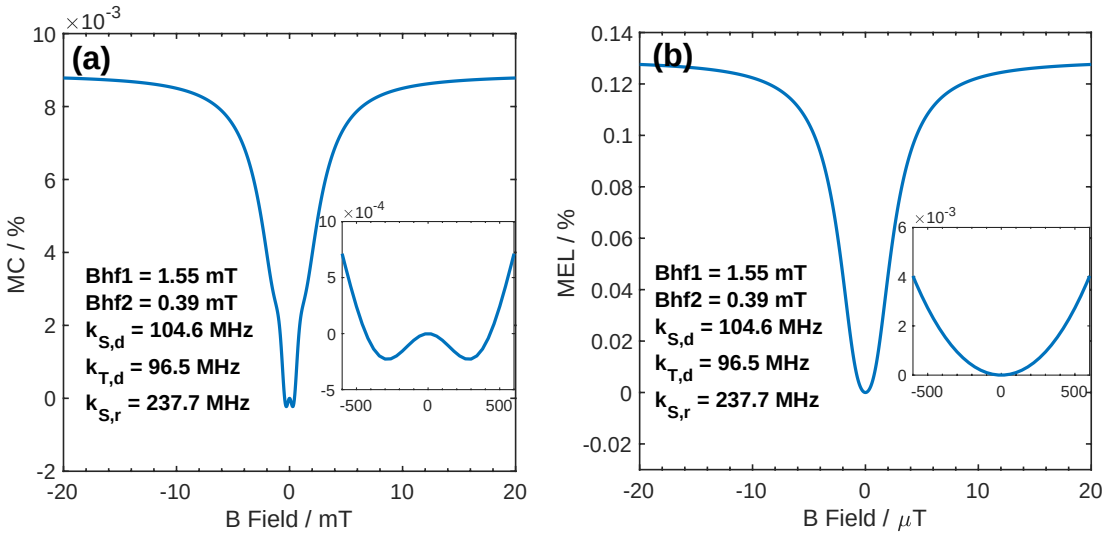

Figure 4.9: Simulated (a) MC and (b) MEL. The insets in (a) and (b) are USMFE regions of the simulations

In Figure 4.10, the simulation results of MC and MEL under different B_{hf1} (1.15mT, 1.35mT, 1.55mT, 1.75mT and 1.95mT) are shown at a fixed B_{hf2} = 0.39mT. The shape of the MC can be determined by the magnitude of B_{hf1}, as the larger B_{hf1} tends to diminish the characteristic "W" shape of the USMFE MC. Additionally, the magnitude of the MEL can also be tuned by B_{hf1} as shown in Figure 4.10(b).

The effect of the smaller hyperfine component B_{hf2} is investigated and the results are shown in Figure 4.11. The values of B_{hf2} used in the simulation are 0.09mT, 0.19mT, 0.39mT, 0.59mT and 0.79mT with a fixed B_{hf1} = 1.55mT. From Figure 4.11(a), B_{hf2} can also determine the appearance of the characteristic "W" shape of the MC. It can also tune the magnitude of the MEL as shown in Figure 4.11(b).

The effect of varying the model parameter of $k_{S,d}$ is studied and the results are

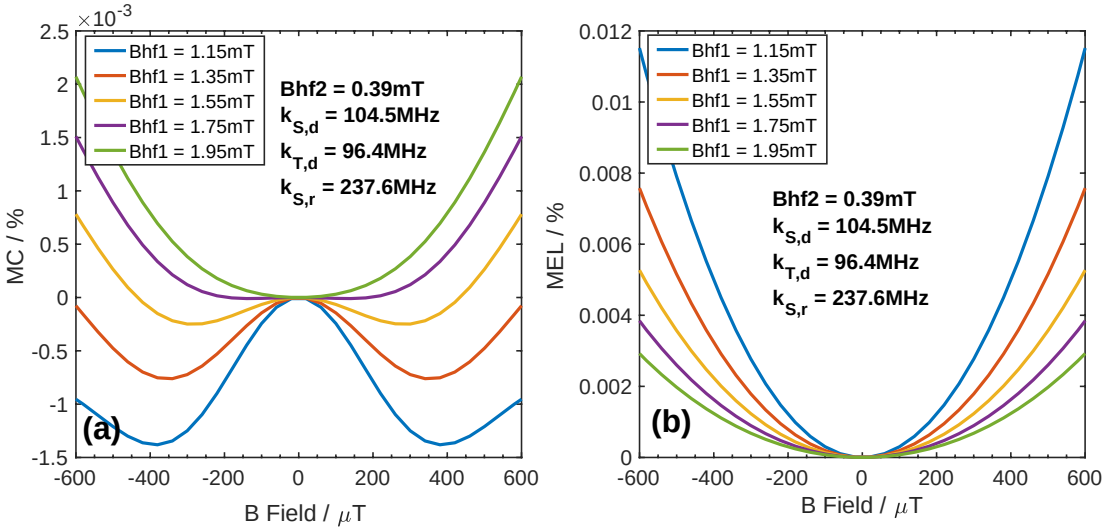

Figure 4.10: Simulated MC and MEL under different B_{hf1}. B_{hf2} = 0.39mT

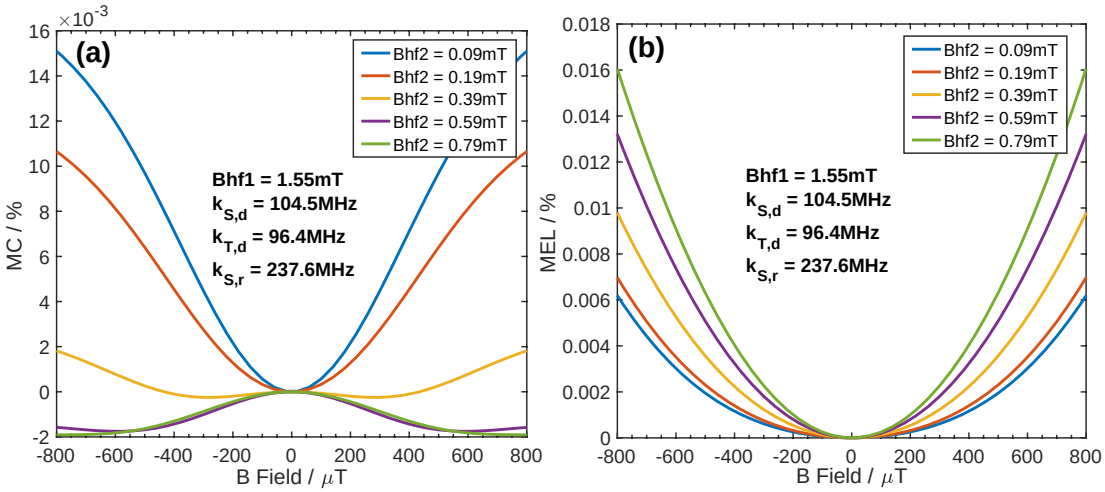

Figure 4.11: Simulated MC and MEL under different B_{hf2}. B_{hf1} = 1.55mT

shown in Figure 4.12. The simulated singlet polaron pair dissociation rates are 22.7MHz, 50.0MHz, 104.5MHz, 159.1MHz and 213.6MHz. Figure 4.12(a) indicates that $k_{S,d}$ has a significant effect on the sign and shape of the resultant MC. It has no effect at all on the MEL from the results in Figure 4.12(b) as expected, given in equation 4.12.

Variations on the model parameter $k_{T,d}$ (the triplet polaron pair dissociation rate) at 14.6MHz, 41.9MHz, 96.4MHz, 151.0MHz and 205.5MHz, are simulated in Figure 4.13. This parameter also has a shape tuning effect on the MC. Faster triplet PP dissociation rate can increase B_m (the magnetic field value at minimum MC), and finally diminish the functional "W" shape MC if the rate is faster enough. As expected by equation 4.12,

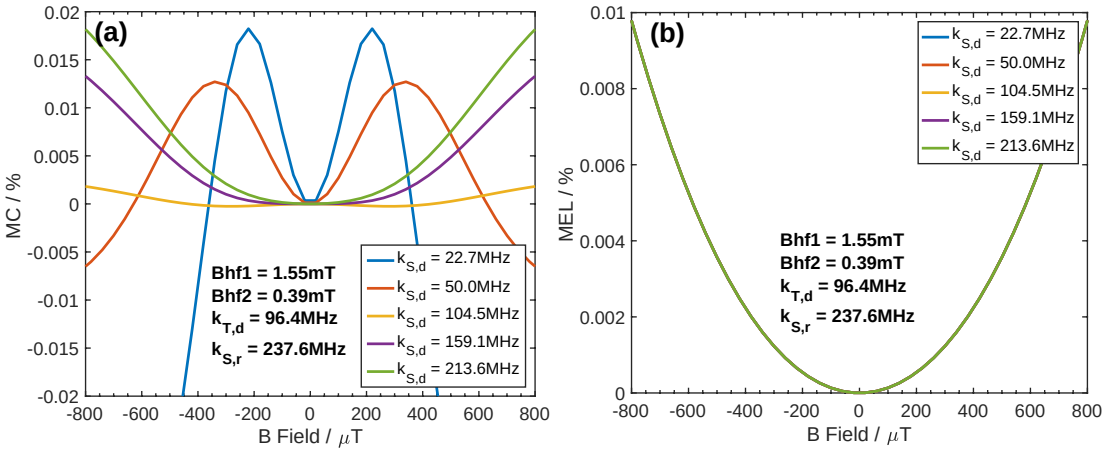

Figure 4.12: The simulated MC and MEL for different $k_{S,d}$. B_{hf1} = 1.55mT and B_{hf2} = 0.39mT

the triplet polaron pair dissociation rate has no effect on the result of MEL (Figure 4.13(b)).

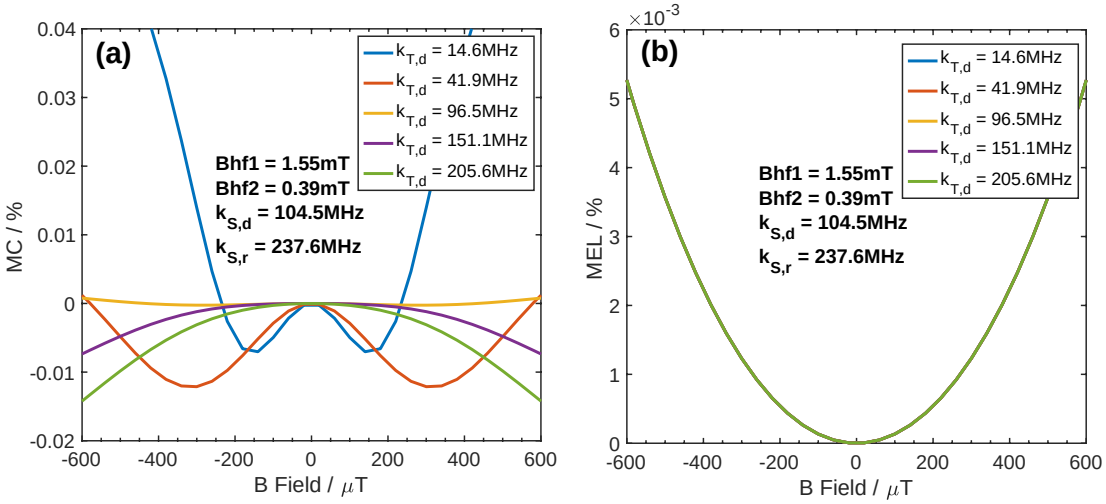

Figure 4.13: The simulated MC and MEL under different $k_{T,d}$. B_{hf1} = 1.55mT and B_{hf2} = 0.39mT

In Figure 4.14, the simulation based on different recombination rates $k_{S,r}$ (128.5MHz, 183.1MHz, 237.6MHz, 292.2MHz and 346.7MHz) is presented. As expected by equation 4.12, the singlet polaron pair recombination rate has no effect on the simulated MC (Figure 4.14(a)). As for MELs, they become intertwined and very similar to each other when at larger recombination rate. However, when the recombination rate is sufficiantly small (in this case, ∼128.5MHz), the MEL will show the characteristic "W" shape obtained in MC. However, the minima points of the MEL B_m occured at larger

field ($\sim$650μT) than those of the simulated MC ($\sim$300μT). This indicates that, although the shape of the MC and MEL might be similar and show the characteristic "W" shape, the minimum value field B_m of the MC and MEL of the same device can be different.

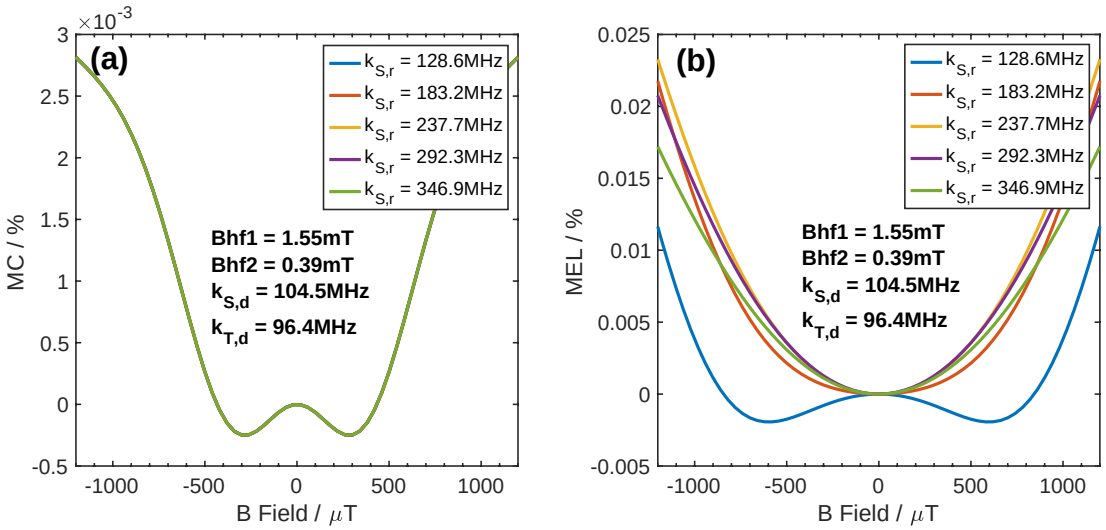

Figure 4.14: The simulated MC and MEL for different $k_{S,r}$. B_{hf1} = 1.55mT and B_{hf2} = 0.39mT

Different model parameters have different effects on the shape, sign and magnitude of both MC and MEL, and in the fitting procedure, the algorithm takes all the effects into considerations fitting to both MC and MEL data and yielding fitting results for the model parameters.

4.3.4 Approximation of Average Local Hyperfine Fields for HOMO and LUMO in Alq_3 From DFT calculations

Before discussing about the fitting results of the two-proton PP model and the validity of the hyperfine fields obtained, a method of approximating local hyperfine fields on the Alq_3 molecule is presented. In particular, the hyperfine fields in the local areas of the Lowest Unoccupied Molecular Orbital (LUMO) and Highest Occupied Molecular Orbital (HOMO), according to Density Functional Theory (DFT) calculated distributions reported by different literatureare used [76, 77, 83–86]. The purpose of this analysis is to approximate local hyperfine fields within the Alq_3 molecule, to allow for later comparisons between the fitted local hyperfine fields and the theoretical

DFT computed values.

In order to carry out the approximation and to describe the Alq_3 molecule using the same referencing number system, the atomic numbering sequence in reference [75] is applied to all the Alq_3 molecules described in references [76, 77, 83–86]. The results of labelling are shown in Figure 4.15. From reference [75], the calculated local hyperfine fields of an anion Alq_3 based on DFT are shown in Table 4.1. There are three columns of hyperfine field information, corresponding to the x, y and z components of the anisotropic hyperfine field of a given atom.

After obtaining information on the local hyperfine fields, the local hyperfine fields can be approximated through an average of the hyperfine fields at given atom's position. The averaging method is presented in references [63, 87] and can be expressed as in equation 4.19

$$\langle a \rangle = \sqrt{\sum_k a_k^2 I_k (I_k + 1)} \tag{4.19}$$

Where $\langle a \rangle$ is the average local hyperfine field, a_k is the total local hyperfine field for the specific atom(or hyperfine coupling constant), I_k is the spin quantum number of that atom.

A specific example for the LUMO in Figure 4.15(c) is presented for clarification. As can be seen, the LUMO spatial distribution in Figure 4.15(c) is indicated by the probability clouds according to the DFT calculation. The LUMO occupied regions include the following atoms: N2,H7, H8, H9, H10, H11, H12, N3, H13, H15. Using the labelling described in Figure 4.15(a), Table 4.2 is constructed using X, Y and Z components of the hyperfine field given in reference [75] (also in Table 4.1). The resultant total field (or a_k) is calculated using $a_k = \sqrt{X^2 + Y^2 + Z^2}$. I_{spin} is the spin quantum number for each atom and B1 is evaluated using $a_k^2 I_{spin}(I_{spin}+1)$ as shown in equation 4.19.

Lastly, the $\langle a \rangle$ of the whole LUMO region can be calculated as in equation 4.20, yielding an average hyperfine field for the LUMO region of 2.13mT.

$$\begin{aligned} \langle a \rangle &= \sqrt{\sum_{\text{all LUMO covered atoms}} B1(n)} \\ &= \sqrt{1.1 + 0.55 + ... + 0.62} \approx 2.13mT \end{aligned} \tag{4.20}$$

Table 4.1: DFT calculated local hyperfine fields of an anion Alq_3. Reproduced from [75]

Atom	ρ	s	hfc (mT)		
Al	1.981	0.001	−0.189	−0.172	−0.116
N1	−0.532	0.004	0.047	0.053	0.095
O1	−0.791	0.001			
C1	0.055	0.002			
C2	−0.286	−0.000			
C3	−0.178	0.007			
C4	−0.081	−0.001			
C5	−0.297	0.001			
C6	−0.212	0.000			
C7	−0.324	0.000			
C8	0.398	0.001			
C9	0.147	0.002			
H1	0.240	−0.000	−0.059	−0.044	0.066
H2	0.235	0.000	−0.014	−0.008	0.019
H3	0.228	−0.000	−0.067	−0.048	−0.011
H4	0.219	−0.000	−0.010	−0.009	0.007
H5	0.222	−0.000	−0.006	−0.006	0.008
H6	0.234	−0.000	−0.010	−0.006	0.012
N2	−0.673	0.068	0.057	0.064	0.739
O2	−0.849	0.002			
C10	−0.013	0.071			
C11	−0.297	−0.018			
C12	−0.257	0.133			
C13	−0.080	−0.015			
C14	−0.296	0.022			
C15	−0.237	0.007			
C16	−0.327	0.008			
C17	0.347	0.016			
C18	0.129	0.013			
H7	0.232	−0.002	−0.666	−0.496	−0.201
H8	0.223	0.000	−0.010	0.070	0.119
H9	0.214	−0.004	−1.152	−0.781	−0.336
H10	0.212	−0.001	−0.171	−0.165	−0.039
H11	0.214	−0.000	−0.093	−0.080	0.009
H12	0.225	−0.000	−0.093	−0.080	−0.001
N3	−0.620	0.040	0.045	0.054	0.453
O3	−0.837	0.002			
C19	0.026	0.045			
C20	−0.291	−0.011			
C21	−0.225	0.083			
C22	−0.079	−0.010			
C23	−0.294	0.014			
C24	−0.228	0.004			
C25	−0.327	0.004			
C26	0.364	0.010			
C27	0.140	0.009			
H13	0.238	−0.001	−0.418	−0.306	−0.136
H14	0.227	0.000	−0.006	0.040	0.081
H15	0.219	−0.003	−0.731	−0.497	−0.213
H16	0.215	−0.000	−0.108	−0.103	−0.020
H17	0.217	−0.000	−0.059	−0.050	0.009
H18	0.227	−0.000	−0.059	−0.041	−0.001

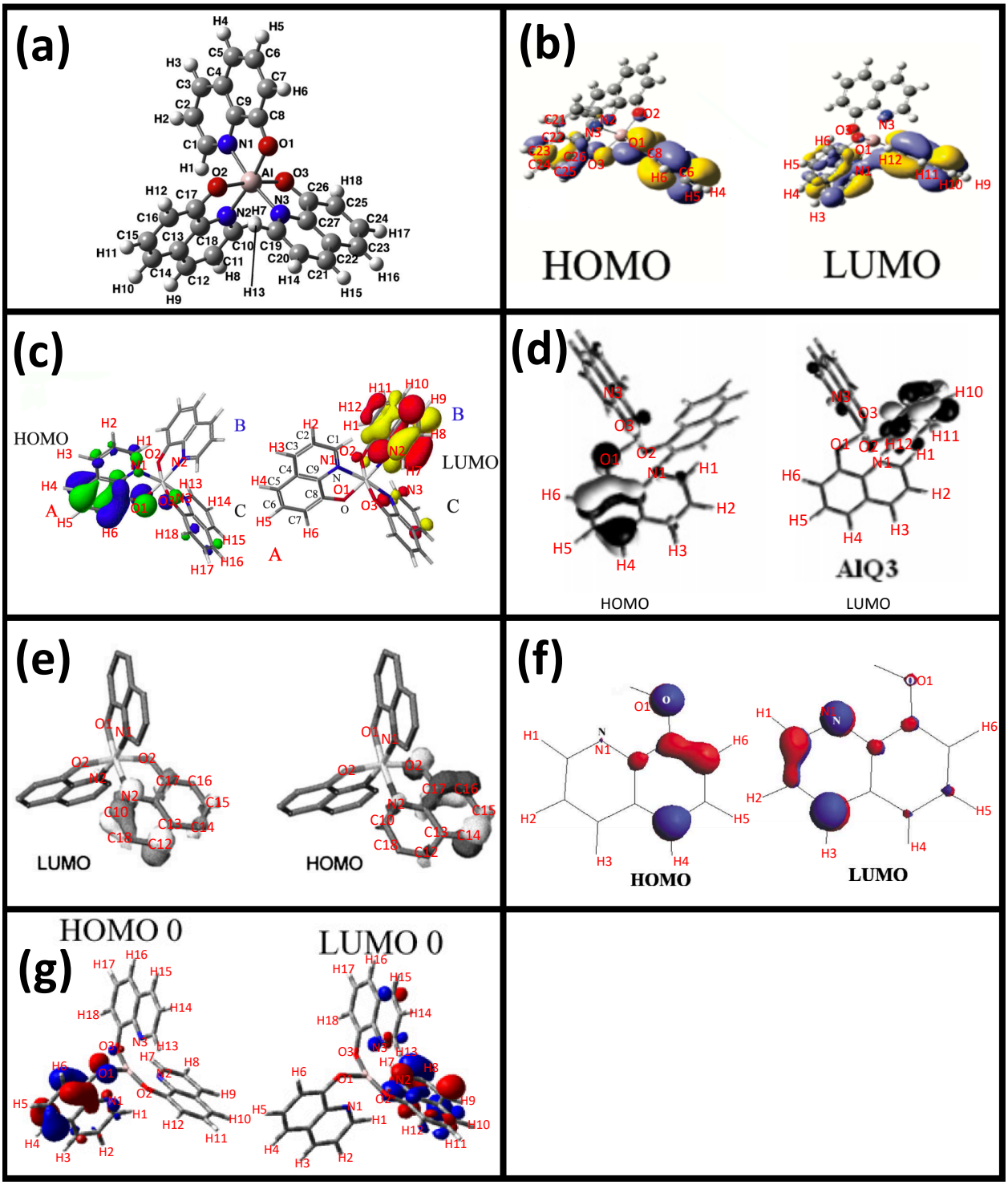

Figure 4.15: Literature HOMO and LUMO spatial distributions and atomic numbering in Alq_3 molecule. (a) the referencing atomic numbering. Reproduced from [75] (b)∼(g): Reference 1∼6 atomic numbering. Reproduced from [76, 77, 83–86], respectively.

Hence, the averaged local LUMO hyperfine field is approximately 2.13mT using the data in reference [77].

Table 4.2: An example calculation of the average local hyperfine field of the LUMO of Alq_3

	X / mT	Y / mT	Z / mT	a_k	I_{spin}	B1
N2	0.057	0.064	0.739	0.744	1	1.10
H7	-0.666	-0.496	-0.201	0.854	0.5	0.55
H8	-0.01	0.07	0.119	0.138	0.5	0.01
H9	-1.152	-0.781	-0.336	1.432	0.5	1.54
H10	-0.171	-0.165	-0.039	0.241	0.5	0.04
H11	-0.093	-0.08	0.009	0.123	0.5	0.01
H12	-0.093	-0.08	-0.001	0.123	0.5	0.01
N3	0.045	0.054	0.453	0.458	1	0.42
H13	-0.418	-0.306	-0.136	0.54	0.5	0.22
H15	-0.731	-0.497	-0.213	0.91	0.5	0.62

In order to compare the calculated LUMO and HOMO regions in a single Alq_3 molecule, atoms corresponding to HOMO and LUMO regions from different works are illustrated in Figure 4.16 where the 1st to 6th paper refers to the literature [76, 77, 83–86], respectively. The bar chart in Figure 4.16 shows occurrences of different atoms in Alq_3 in LUMO or HOMO from the six different papers. The occupied atoms in LUMO or HOMO are also highlighted in Figure 4.16 as indicated. It is clear that the HOMO and LUMO spatial distributions is clearly separated from the DFT computations from the literature. It is this spatial separation of HOMO and LUMO, where the holes and electrons resides in the molecule, that makes the local hyperfine fields for electrons and holes different.

As can be seen from the bar charts in Figure 4.16, different references yield different distributions for HOMO and LUMO regions. In order to include all the possibilities in the calculations, all atoms corresponding to either HOMO or LUMO in all references are included in the sum of Equation 4.20. Therefore, for the LUMO, atoms N2, H7, H8, H9, H10, H11, H12, H13, H14, H15 and H16 are included. For HOMO, atoms N1, H1, H2, H3, H4, H5, H6, H10, H11, H12, H16, H17 and H18 are included.

Similarly, using this approximation method, the average local hyperfine fields are found to be $\langle a_{LUMO} \rangle \approx 2.13$mT and $\langle a_{HOMO} \rangle \approx 0.36$mT. These two different numerical values suggest the different local hyperfine environments for electrons and holes. Although these are only approximations within quantified errors. The

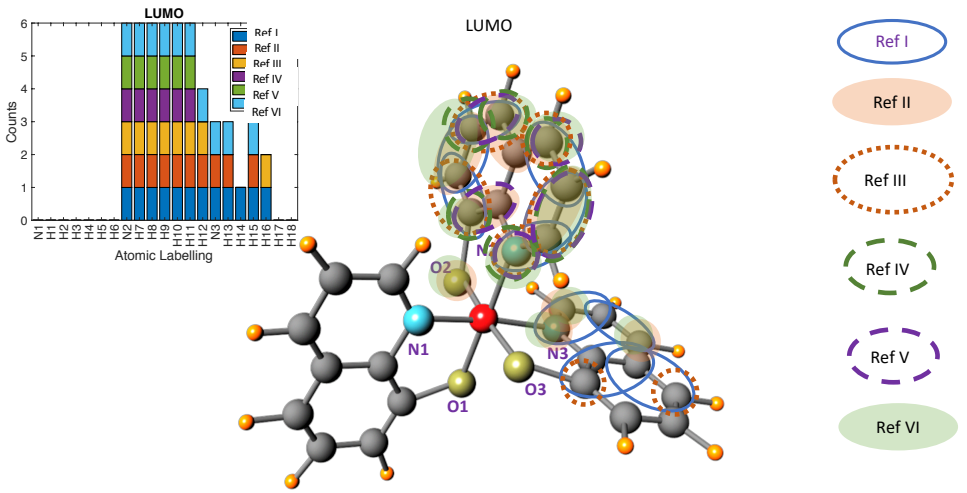

(a)

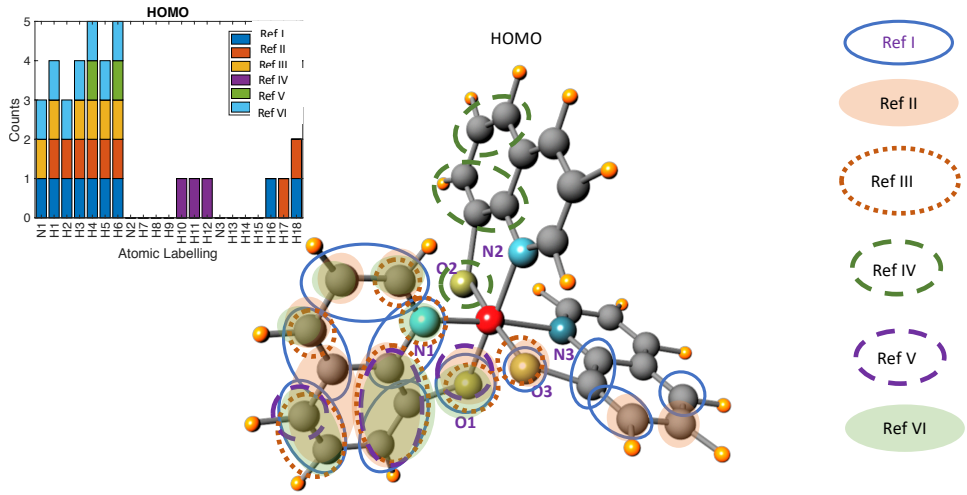

(b)

Figure 4.16: Spatial distribution of (a) LUMO and (b) HOMO in Alq_3 using different literature sources. The insets in (a) and (b) show the atom occurrence in different sources. Ref I: [76] Ref II: [77] Ref III: [83] Ref IV: [84] Ref V: [85] Ref VI: [86]

errors can arise in many ways, including the different DFT calculation processes and methods used by different authors. The averaging formula in equation 4.19 is itself an approximation, and identifying individual atoms for LUMO and HOMO in different papers can be hard to determine. Additionally, the sum in Equation 4.20 has no weighting corresponding to the HOMO and LUMO probability density.

4.3.5 Two-Proton PP Model Fitting Results

The two-proton polaron pair model using the Nelder-Mead Simplex Optimisation algorithm is applied to the MC and MEL results as discussed in subsection **4.2.4**. Figure 4.17 shows the fitting result.

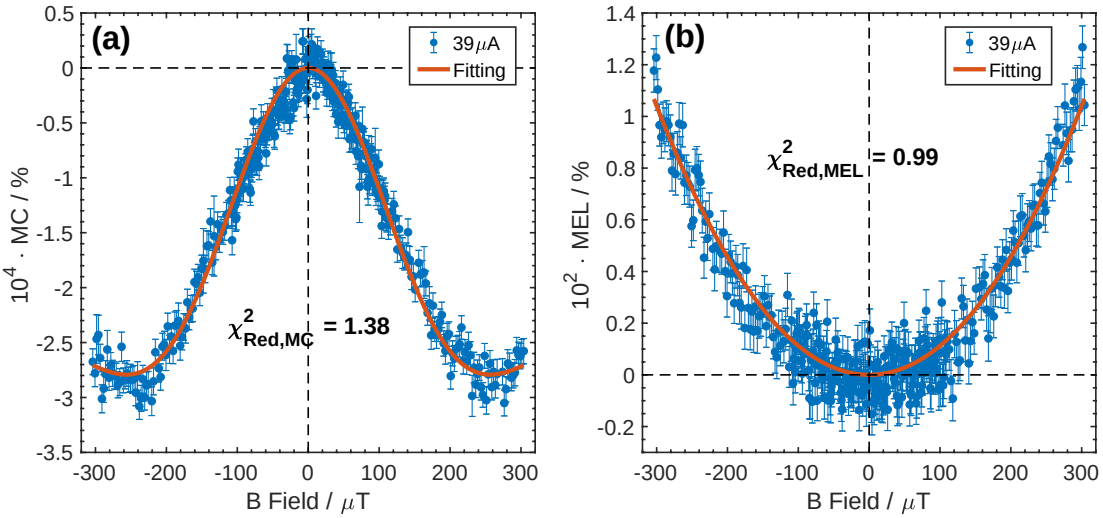

Figure 4.17: Two-proton polaron pair model fits to (a) MC and (b) MEL within the B field range of $\pm 300\mu$T.

As previously discussed, the experimentally obtained MC and MEL data is obtained within the magnetic field range of $\pm 300\mu$T to avoid current dependence of the MC for fields larger than $\pm 300\mu$T.

As mentioned in the subsection **4.2.4**, the model optimisation process starts by randomly choosing initial points for the simplex in the space. Likewise in the fitting procedure, a set of random numbers are chosen for the five parameters (B_{hf1}, B_{hf2}, $k_{S,d}$, $k_{T,d}$ and $k_{S,r}$) before the fitting. There might be an issue of finding a local minimum of the functions (let's make a hypothesis, the function might have another minimum when B_{hf1} = 100mT and B_{hf2} = 0.0001mT, this might yield a mathematical local minimum, however, the number of two hyperfine fields are not physically significant.), therefore, careful initialisation of fitting parameters are carried out by randomly choosing the numbers within some physically significant ranges, for instance, hyperfine field parameters are initiated within the hyperfine field range of 0 to 3 mT.

The parameter values obtained by the fitting results in Figure 4.17 are: B_{hf1} =

(0.63±0.01)mT, B_{hf2} = (0.24±0.01)mT, $k_{S,d}$ = (44.59±0.01)MHz, $k_{T,d}$ = (43.97±0.01)MHz and $k_{S,r}$ = (87.97±5.56)MHz with $\chi^2_{red,MC}$ = 1.38 and $\chi^2_{red,MEL}$ = 0.99. The errors in the returned parameters are calculated using the same technique mentioned in Chapter 3, namely, by considering the error in χ^2 value itself. Noticeably, the Larmor frequency for B_{hf1}, B_{hf2} are approximately 111MHz and 42MHz, respectively. The much slower rate of $k_{S,d}$ and $k_{T,d}$ meaning that the "lifetime" of the predefined Decayed States (DS^S and DS^T) are long enough to be involved in hyperfine interaction induced ST interconversions. However, the faster rate of the $k_{S,r}$ means that the shorter "lifetime" of singlet exciton formation process might not be long enough to be significantly perturbed by the hyperfine interactions, thus showing no sign of functional "W" shape USMFE in the MEL data and simulation.

However, before continuing with further physical analysis of the yielded parameters, it is important to check if the fitting process is mathematically sensible. As mentioned in subsection **4.3.3**, the integral rate of 1.67 ns/step is chosen for the simulation as this rate can approximate the detail of the singlet fraction oscillation at up to 500 μT (so it would be more precise in sampling lower frequency oscillations at up to 300 μT). Although this rate (1.67 ns/step) can be fixed during simulation and fitting, the effect of different integral time windows on the fitting results needs further investigation.

In the simulation of Figure 4.18, the y-axis $\chi^2_{red,Global}$ is calculated using the yielded parameters from the fitting result in Figure 4.17. A fixed integral interval (1.67 ns/step) is applied while varying different integral windows. As clearly indicated in Figure 4.18, the $\chi^2_{red,Global}$ reduces exponentially with increasing numbers of integral time windows, and reaches a static value of 2.37 when the integral time windows exceeds the number of 213 ns. Conclusively, it means that using an integral time window larger than 213 ns in the fitting process the yielded $\chi^2_{red,Global}$ and the corresponding fitting parameters could reach and remain consistency. In the fitting of Figure 4.17, the integral time window is chosen to be 3000 ns (the rate is still 1.67 ns/step) which falls very well in the consistency region. Importantly, for the fitting process, it is vital to take a safe guess initially for the integral time window in the simulation. After the

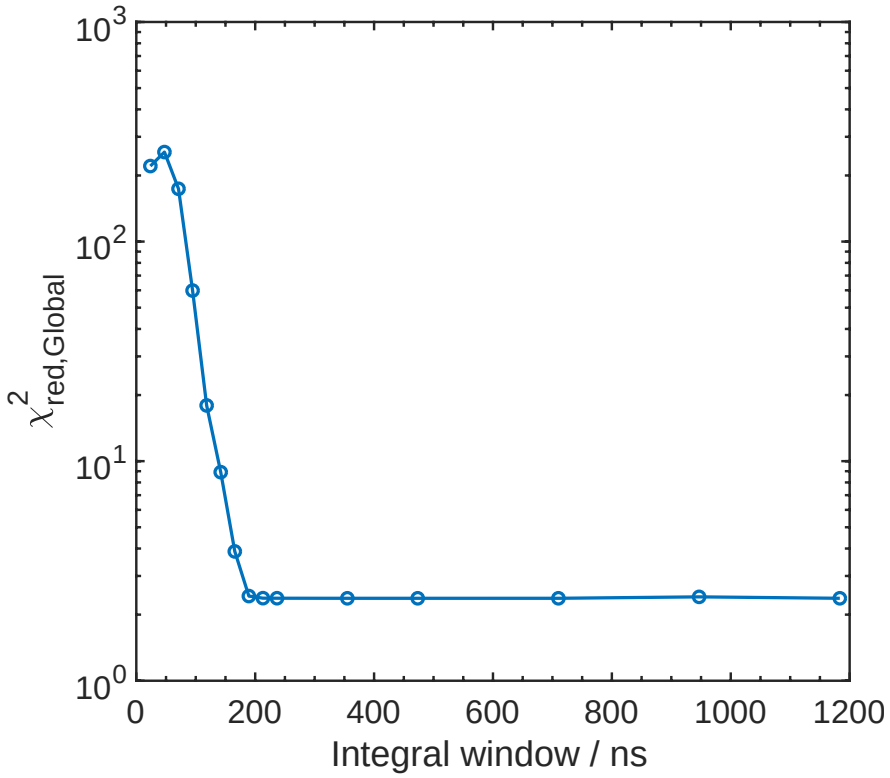

Figure 4.18: Integral time window check with a fixed ratio of 1.67 ns/step

simulation it is necessary to do a $\chi^2_{red,Global}$ check experiment as mentioned in Figure 4.18 to make sure if the initial guess is significant or not.

Noticeably, the B_{hf} yielded using the single proton PP model from Chapter 3 ($\sim$0.34mT) corresponds approximately to the small component B_{hf2} ($\sim$0.24mT) from the two-proton PP model within 2.4 standard deviations. From the extensive discussions about the approximated average of the local hyperfine fields from DFT results, although within errors, my fitted two local hyperfine fields ($B_{hf1} \sim 0.63$mT, $B_{hf2} \sim 0.24$mT) are in agreement with two local hyperfine fields for the HOMO and the LUMO – that is a distinctively large local hyperfine field component and a small one. From subsection **4.3.4**, the larger hyperfine component corresponds to the LUMO region averaged local hyperfine fields (i.e. the local hyperfine environment experienced by an electron), and the smaller hyperfine component matches with the HOMO region (i.e. the local hyperfine environment experienced by a hole), therefore, this indicates that of the two local hyperfine fields, the larger one ($B_{hf1} \sim 0.63$mT) corresponds to the local hyperfine field for the electron, and the smaller one ($B_{hf2} \sim 0.24$mT) corresponds

to the local hyperfine field for the hole. There are significant discrepancies between the local hyperfine fields ($B_{hf1} \sim 0.63$mT, $B_{hf2} \sim 0.24$mT) obtained by fitting and the approximated averaged local hyperfine fields from DFTs ($B_{LUMO} \sim 2.13$mT, $B_{HOMO} \sim 0.36$mT), especially between B_{hf1} and B_{LUMO} values. Given the unknown errors introduced in the approximation of B_{LUMO} (and B_{HOMO}), the discrepancy is not surprising. Accurate approximations of B_{LUMO} (and B_{HOMO}) fall out of the scope of the current work as this is mainly focused on the technique of fitting the two-proton PP model to the experimentally obtained MC and MEL data. Thus, the approximation results can only be considered as an indicator that the local environment hyperfine fields are distinctive for electrons and holes, and that the electron experiences significantly larger local hyperfine field value compared to the hole. This different electron and hole local hyperfine environments have also been experimentally observed from literature [53, 88] based on different kinds of experiments. Nguyen, et al. measured the USMFE MC on the electron-only and hole-only diodes, and observed a much larger B_m for electron-only device compared to the hole-only device [53]. Additionally, McCamey, et al. used Pulsed Electrically Detected Magnetic Resonance (PEDMR) technique on OLED to detect two significantly different components in the measured resonance spectrum via fitting. The different fitting lines correspond to different charges in the polaron pair state, and they estimated the two hyperfine fields to be $B_{hf1}\sim$2.72mT and $B_{hf2}\sim$0.79mT [88]. In terms of this significant difference, my fitted two local hyperfine fields ($B_{hf1} \sim 0.63$mT, $B_{hf2} \sim 0.24$mT) are in agreement with this. Since the work in Chapter 3, where the single proton polaron pair model is applied yielded a local hyperfine value of $\sim$0.34mT, it is in accord with the smaller component of the two local hyperfine fields meaning that the single proton PP model yielded the local hyperfine field environment for hole charge carriers in the molecule (in this case, an Alq_3 molecule).

Considering the fitting parameters for the decay rates ($k_{S,d}$, $k_{T,d}$ and $k_{S,r}$), namely, $k_{S,d}$ = (44.59$\pm$0.01)MHz, $k_{T,d}$ = (43.97$\pm$0.01)MHz and $k_{S,r}$ = (87.97$\pm$5.56)MHz. For the dissociation process, the singlet polaron pair has a significantly higher rate ($\sim$44.59MHz) than the triplet polaron pair ($\sim$43.97MHz) with the small error bar

(0.01MHz) considered (over 43 standard deviations apart). This agrees with the result from the work in Chapter 3, where a δ_{TS} less than one (δ_{TS}~0.99) is obtained indicating that singlet contributes more to the dissociation than the triplet polaron pairs. This might be explained in terms of the higher binding energy of triplet polaron pairs compared to the singlet counterpart, thus, it is more difficult for triplet polaron pairs to dissociate. On the other hand, for the recombination process, a much higher rate of recombination is obtained (~87.97MHz) compared to the dissociation rates (for both singlet and triplet). This indicates that the formed singlet polaron pairs are more inclined to recombine into singlet excitons instead of separating and dissociating into free charge carriers. This might be explained by large Coulomb attraction between the positive and the negative polarons in the pair state driving the electron-hole charge pair closer to each other, and forming a singlet exciton, which is responsible for the subsequent electroluminescence from the OLED. This is also reflected by the great magnitude difference between the obtained MC (~10^{-4}%) and MEL (~10^{-2}%) with the weaker MC signal indicating a much weaker or slower process of dissociation of polaron pairs (singlet and triplet).

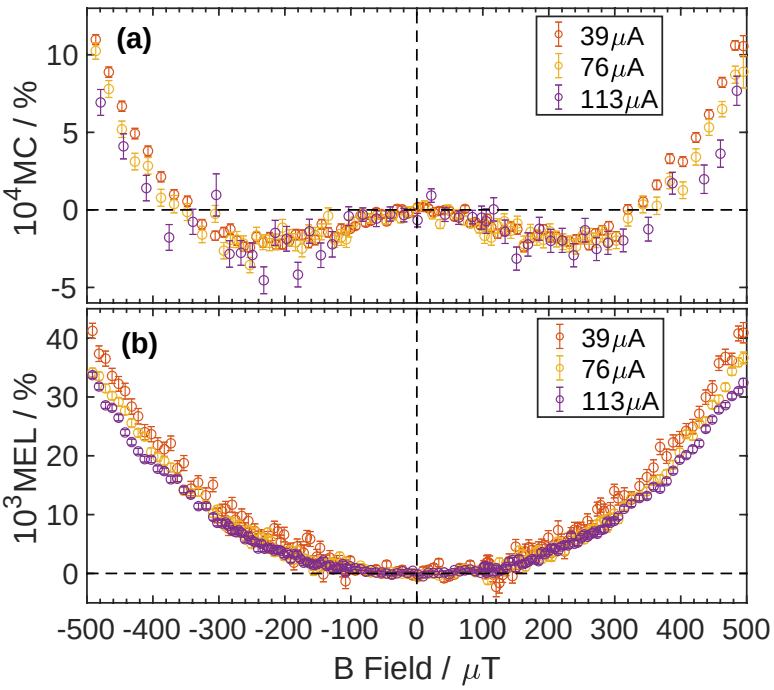

Figure 4.19: The current dependence of the MC and MEL experiments in the device used in the PP model fitting

Table 4.3: Fitting parameters for different drive currents of the same device within $\pm 300\mu$T

Drive Current	B_{hf1} / mT	B_{hf2} / mT	$k_{S,r}$ / MHz	$k_{S,d}$ / MHz	$k_{T,d}$ / MHz
39μA (text)	0.63±0.01	0.24±0.01	87.97±5.56	44.59±0.01	43.97±0.01
76μA	0.66±0.02	0.24±0.01	92.37±8.73	46.82±0.16	46.16±0.15
113μA	0.66±0.02	0.22±0.02	95.15±5.77	46.80±0.14	46.23±0.14

The reproducibility checks are carried out to ensure both of the working device performance and the two-proton polaron pair model fitting procedure are valid. First, the current dependence of the MC and MEL on the device is carried out with different device drive currents (39μA, 76μA and 113μA) as shown in Figure 4.19. Figure 4.19 (a) shows the current dependence of the MC, and the data shown were averaged using a moving average of 10 points along the whole magnetic field range ($\pm 500\mu$T) to reduce the noise in the raw data. The MC begins to show a clear current dependence when the magnetic field exceeds approximately 400 μT as suggested in Chapter 3. From Figure 4.19 (b), the MEL shows a strong dependence on the device drive current even at significantly small magnetic field. The increased device drive current corresponds to increased charge injection in the device. The changing current density (and charge density) will reduce the inter-charge distance between two polarons in the pair state and could subsequently affect the recombination process between polarons in the pair state.

The two-proton polaron pair model fitting to the data has been conducted using the raw data in Figure 4.19. The fitting results for different drive current are shown in Table 4.3.

From Table 4.3, all the fitted parameters (B_{hf1}, B_{hf2}, $k_{S,r}$, $k_{S,d}$ and $k_{T,d}$) are consistent within errors in the same device within the magnetic field range of $\pm 300\mu$T. The discrepancies between numbers can be due to the different number of repetitions of experiments, resulting in different errors and slight deviations as shown in the Figure 4.19. As the MC is averaged over 800 times at a drive current of 39μA while the others are only averaged for around 100 times (76μA and 113μA). The consistency in the data fitting results in Table 4.3 suggests that it is valid to fit both MC and MEL below $\pm 300\mu$T.

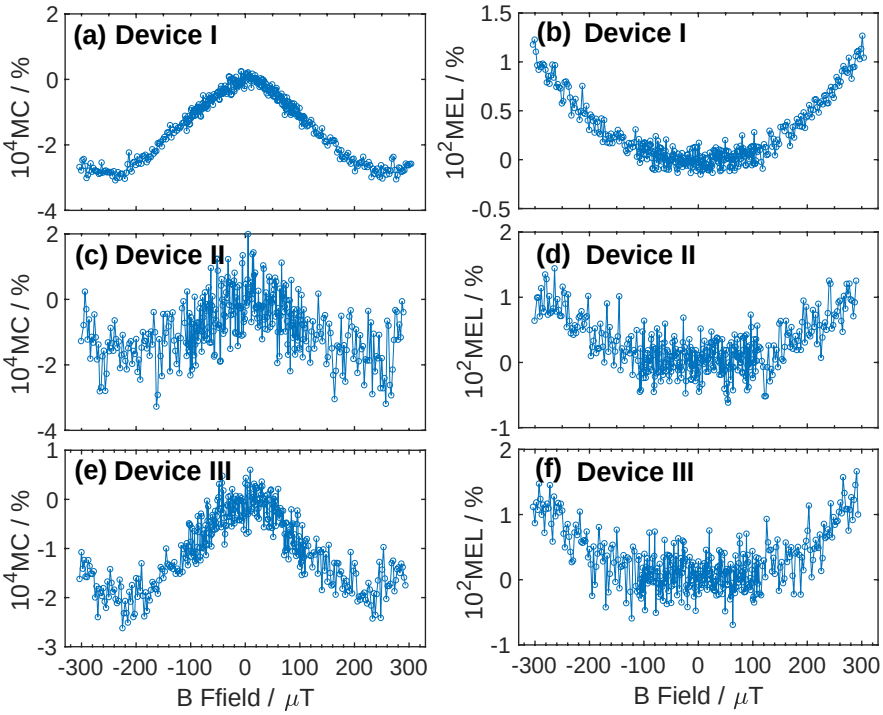

Figure 4.20: The MC and MEL within $\pm 300\mu$T at a drive current of 39μA for three different devices

Table 4.4: Fitting parameters for different devices under the drive current of 39μA within $\pm 300\mu$T

Device	B_{hf1} / mT	B_{hf2} / mT	$k_{S,r}$ / MHz	$k_{S,d}$ / MHz	$k_{T,d}$ / MHz
Device I (text)	0.63±0.01	0.24±0.01	87.97±5.56	44.59±0.01	43.97±0.01
Device II	0.64±0.02	0.23±0.01	90.69±9.47	45.30±0.03	44.82±0.03
Device III	0.64±0.03	0.24±0.02	89.47±7.88	45.17±0.02	44.69±0.11

In order to check if the device performance can be reproducible, three different devices were fabricated and the same measurement of the MC and MEL conducted under a drive current of 39μA has been carried out. The results of this reproducibility test are shown in Figure 4.20. It is noticeable that the noise level in Figure 4.20 (c), (d), (e) and (f) are much larger than in (a) and (b). This is only due to large number of averages in (a) and (b) (more than 800 repetitions) compared to (c), (d), (e) and (f) (only 100 repetitions). Despite the noise level, the dip position in the MC and the overall magnitudes of the MC and MEL are consistent across different devices as can be seen from Figure 4.20. The same fitting process is carried out on each of the data sets and the results are shown in Table 4.4. All the fitting parameters are significantly

and statistically consistent across devices.

4.4 Conclusions

Both the magnetoconductance (MC) and the magnetoelectroluminescence (MEL) were measured on devices with the same structure as those in Chapter 3. The results with μT resolution and ppm sensitivity were obtained with the Earth's magnetic field components cancelled. Different shapes of MC and MEL were observed, in contrast to some of the literature where the MC and MEL share the same characteristic "W" shape [52, 55, 57, 58]. This is caused by the constant voltage mode measurement condition used in some literature. However, the drive condition used in the work presented is constant current mode, and this shape difference between MC and MEL has also been reported by Ratzke, et al. [80], who used the same drive condition. Additionally, the magnitude of the MEL is approximately 100 times larger than the MC, suggesting that the recombination process dominates the Polaron Pair dynamics.

A two-proton Polaron Pair model was used in the simulation. There are five physical parameters in the model: two local hyperfine fields for each of the polaron in the pair states B_{hf1} and B_{hf2}, dissociation rates for singlet and triplet PP states $k_{S,d}$ and $k_{T,d}$, and recombination rate for singlet PP state $k_{S,r}$. Simulations have been carried out to show the effects of different parameters on the MC and MEL. B_{hf1} (or the large hyperfine component) can determine the shape of the MC and the magnitude of the MEL as sufficiently large B_{hf1} can diminish the functional "W" shape in MC. This is the same for the second parameter B_{hf2} (also the small hyperfine component). Both $k_{S,d}$ and $k_{T,d}$ have similar effects on the MC and MEL. They can both change the shape of the simulated MC while having no effect on the MEL. In terms of $k_{S,r}$, increasing values of the parameter generates a set of similar results of MEL while having no effect on MC. Noticeably, a sufficiently small $k_{S,r}$ can result in a "W" shape MEL with a minimum MEL B field ($\sim$650μT) larger than the minimum MC B field ($\sim$300μT).

By fitting the MC and MEL globally using the developed analysis technique and the two-proton polaron pair model, the yielded results are: B_{hf1} = (0.63$\pm$0.01)mT,

B_{hf2} = (0.24±0.01)mT, $k_{S,d}$ = (44.59±0.01)MHz, $k_{T,d}$ = (43.97±0.01)MHz and $k_{S,r}$ = (87.97±5.56)MHz. The results are reproducible across devices, and no current dependence is shown within ±300μT. The two yielded hyperfine fields are distinct from each other. This is in accord with the difference estimated based on averaging the local hyperfine fields for electron and hole from DFT calculations, which yields sufficiently different values of 2.13mT (for electrons) and 0.36mT (for holes). Noticeably, the small component of the yielded hyperfine fields in this chapter (B_{hf2} = (0.24±0.01)mT) corresponds to the local hyperfine field of a hole, and this is in agreement with the yielded hole local hyperfine field ((B_{hf}=0.34±0.04)mT) in Chapter 3. Furthermore, in dissociation, the singlet polaron pair has a significantly higher rate (∼44.59MHz) than the triplet polaron pair (∼43.97MHz) with the small error bar (0.01MHz) considered (over 43 standard deviations apart). This agrees with the result from the work in Chapter 3, where a δ_{TS} less than one (δ_{TS}∼0.99) is obtained indicating that singlet contributes more to the dissociation than the triplet polaron pairs. For recombination, a much higher rate of recombination is obtained (∼87.97MHz) compared to the dissociation rates (for both singlet and triplet), indicating that the formed singlet polaron pairs are more inclined to recombine into singlet excitons instead of separating and dissociating into free charge carriers.

However, the two-proton polaron pair model is developed based on the single proton polaron pair model in Chapter 3, and both of them were built upon a reduced and simplified stochastic Liouville von Neumann equation which requires energy conservation in the modelling. A more universal and general Liouville equation needs to be investigated to further justify the model fitting technique.

Chapter 5

Conclusions

The work presented mainly focuses on the technique of fitting the polaron pair model (single proton and two proton versions) to the experimentally obtained MC and MEL data to yield physically significant parameters, such as the local hyperfine fields B_{hf} for hole and electron polarons in Alq_3 molecule.

The results with μT resolution and ppm sensitivity results are obtained using OLEDs that are carefully fabricated and measured. The devices operate under a vacuum of 10^{-6} mbar and do not show any degradation over approximately 120 hours of measurement. The obtained magnetoconductance (MC) has one of the smallest minimum field values ($B_m \sim 240\mu$T) reported for protonated organic system. The MC measurements are carried out with the Earth's magnetic field (B_E) present or cancelled, and the results suggest that a clear MC effect appears at values below Earth's magnetic field ($\sim 50\mu$T) with B_E cancelled. The data has been successfully fitted using the single proton Polaron Pair model (PP model), yielding the parameters: k = (28.6$\pm$9.7) MHz, B_{hf} = (0.34$\pm$0.04) mT and δ_{TS} = (0.99$\pm$0.01). The obtained values are reproducible across devices and are independent of the drive current within the small magnetic field range (smaller than $\sim |300| \mu$T). Noticeably, the yielded hyperfine field B_{hf} = (0.34$\pm$0.04) mT is consistent with the average hole polaron local hyperfine field estimated using DFT calculations and measurement results from μSR. The slow decay rate of the PP state k = (28.6$\pm$9.7) MHz, which is much smaller than the hyperfine precession frequency 59.45MHz, is a necessary precondition for showing the USMFE.

The yielded weight factor δ_{TS} = (0.99±0.01) is smaller than 1, meaning that singlet is contributing more to the MC than the triplet counterpart.

Additionally, the theoretical model has been further developed into a two-proton PP model. The MC and MEL are obtained experimentally and globally fitted using the two proton polaron pair model and analysis. Noticeably, the shapes of obtained MC and MEL are different as a result of the constant current measurement condition. The parameters obtained by fitting are: B_{hf1} = (0.63±0.01) mT, B_{hf2} = (0.24±0.01) mT, $k_{S,d}$ = (44.59±0.01) MHz, $k_{T,d}$ = (43.97±0.01) MHz and $k_{S,r}$ = (87.97±5.56) MHz. All the results are highly reproducible across devices and are independent on the drive currents. The two hyperfine fields obtained B_{hf1} = (0.63±0.01) mT and B_{hf2} = (0.24±0.01) mT are sufficiently distinct from each other, which is in accord with the estimated local hyperfine environments of electrons and holes by DFT calculations. The larger hyperfine field (B_{hf1}) corresponds to electron environment while the smaller one corresponds to the hole environment. Additionally, the obtained singlet PP dissociation rate is significantly larger than the triplet PP dissociation rate and this is in agreement with the yielded δ_{TS} from single proton PP model fitting. The singlet PP recombination rate is much higher than the dissociation rate, indicating that the recombination process is dominant. This is in agreement with the result that the measured MEL has the magnitude approximately 100 times larger than the MC. Noticeably, the obtained MC and MEL have different functional shapes when the device was measured under constant current mode, which is different from the reports in literature. This difference shows that there should be two different pathways for the polaron pair dynamics–the dissociation and the recombination of the pair states.

The technique of fitting the Polaron Pair model (single-proton and two-proton) to the obtained MC and MEL data further helps to better understand the microscopic proccesses within an Alq_3 molecule and can be applied to any organic semiconductor systems. However, further developments and investigations on the Polaron Pair model in the fitting technique need to be carried out in the future and to further justify this technique.

Chapter 6

Future Work

As the work presented is the prototype work of using the polaron pair model to fit the experimentally obtained MC and MEL data to yield physically significant parameters such as the local hyperfine field(s) in the molecule, there are further steps in the development of this methodology.

Firstly, in order to further justify the technique of data fitting using PP models, OLEDs made of different kinds of organic semiconductor materials are required for the testing. This work could be further verified comparing the yielded physical parameters, for instance, the local hyperfine field B_{hf} of the material, with the simulated local hyperfine field from literature about that specific organic semiconductor.

Secondly, since the polaron pair model (single proton and two-proton versions) utilises a reduced and simplified stochastic Liouville von Neumann equation to calculate the singlet fraction and the singlet yield, the energy has to be conserved in the model system. However, for a more general and universal situation, a more complete Liouville equation with dissipative and non-dissipative terms is required and a more complete Hamiltonian consisting of multiple interactions including the Zeeman interaction, hyperfine interaction, exchange interaction and dipolar interaction, etc. should be applied.

Thirdly, the shape of the MC changes by varying parameter of the hyperfine field B_{hf} in one proton PP model. In order to verify this, measurement on the USMFE MC and/or MEL of OLEDs using protonated and deuterated Alq_3 material should be

conducted and fitted to yield the fitted hyperfine field. In this way, the validity of the single proton PP model can be tested.

Additionally, reports in the literature [62, 80] of a new phenomenon characterised by a "double W" shape of the MC have been noted (in Figure 1.20). The underlying mechanisms, however, have not been discussed in the literature. During the simulation of the two-proton polaron pair model in section **4.3.3**, similar results of a "double W shape" MC have been observed. This is shown in Figure 6.1. The generation of double "W" shape by simulation which replicates experiments should be further investigated. The simulation conditions for generating such a shape require very low dissociation rates (for both singlets and triplets). Because this is only theoretical, some related experiments should be designed to prove the validity of this prediction. Intuitively, the operation temperature of a working OLED is related to the dissociation rate of polaron pairs. Hence a temperature dependent experiment is ideal to test the validity of this prediction by the two proton PP model.

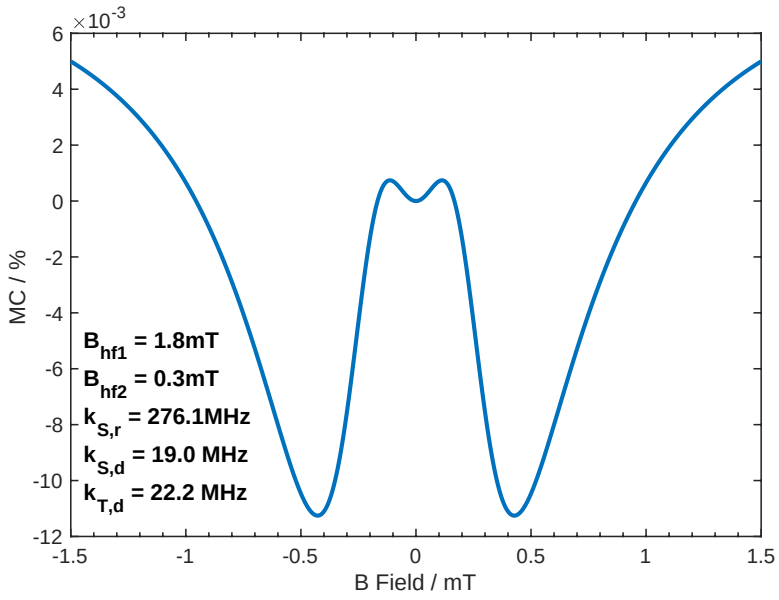

Figure 6.1: The "double W" shape of the generated MC

Further developments of the work can also help to discover new phenomena in the USMFE and not limited to detecting local hyperfine environments within the molecule.

References

1. Kattnig, D. R., Solov'yov, I. A. & Hore, P. J. Electron spin relaxation in cryptochrome-based magnetoreception. *Phys. Chem. Chem. Phys.* **18,** 12443–12456. ISSN: 1463-9076. http://xlink.rsc.org/?DOI=C5CP06731F (2016).

2. Giffin, R., Pool, R. & Robinson, S. *Emerging Safety Science : Workshop Summary* 51–52 (National Academies Press, 2008).

3. Geoghegan, M. & Hadziioannou, G. *Polymer Electronics* 26–29 (Oxford University Press, 2013).

4. Tang, C. W. & Vanslyke, S. A. Organic electroluminescent diodes. *Appl. Phys. Lett.* **51,** 913–915. ISSN: 00036951. arXiv: arXiv:1011.1669v3 (1987).

5. Shi, J. & Tang, C. W. Doped organic electroluminescent devices with improved stability. *Appl. Phys. Lett.* **70,** 1665–1667. ISSN: 00036951 (1997).

6. Lu, J. *et al.* Synthesis and Characterization of a Novel AlQ3 -Containing Polymer. *J. Polym. Sci. A* **38,** 2887–2892 (2000).

7. Neogi, I. *et al.* Organic amorphous hole-transporting materials based on Tröger's Base: Alternatives to NPB. *RSC Adv.* **5,** 26806–26810. ISSN: 20462069 (2015).

8. M.Schwoerer; H.Wolf. *Organic Molecular Solids* 149–151. ISBN: 9783527405404 (WILEY-VCH Verlag GmbH & Co. KGaA, 2007).

9. Hadir, S. A. K. *et al.* Exciton enhancement and exciplex quenching by plasmonic effect of Aluminum nanoparticle arrays in a blue organic light emitting diode. **25,** 9812–9822 (2017).

10. Taliani, C. *et al.* Organic-Inorganic Hybrid Spin-Valve : A Novel Approach to Spintronics. *Phase. Transit.* **75,** 1049–1058 (2002).

11. Kalinowski, J., Cocchi, M., Virgili, D., Di Marco, P. & Fattori, V. Magnetic field effects on emission and current in Alq3-based electroluminescent diodes. *Chem. Phys. Lett.* **380,** 710–715. ISSN: 00092614 (2003).

12. Xiong, Z. H., Wu, D., Vardeny, Z. V. & Shi, J. Giant magnetoresistance in organic spin-valves. *Nature* **427,** 821–824. ISSN: 00280836 (2004).

13. Kalinowski, J., Cocchi, M., Virgili, D., Fattori, V. & Di Marco, P. Magnetic field effects on organic electrophosphorescence. *Phys. Rev. B* **70,** 1–7. ISSN: 01631829 (2004).

14. Mermer, Ö., Veeraraghavan, G., Francis, T. L. & Wohlgenannt, M. Large magnetoresistance at room-temperature in small-molecular-weight organic semiconductor sandwich devices. *Solid State Commun.* **134,** 631–636. ISSN: 00381098. arXiv: `0501124 [cond-mat]` (2005).

15. Mermer, Ö., Wohlgenannt, M., Francis, T. L. & Veeraraghavan, G. Large Magnetoresistance at Room Temperature in Organic Semiconductor Devices. *IEEE Trans Magn* **41,** 3682–3684 (2005).

16. Mermer, Ö. *et al.* Large magnetoresistance in nonmagnetic π-conjugated semiconductor thin film devices. *Phys. Rev. B* **72,** 1–12. ISSN: 10980121. arXiv: `0504738 [cond-mat]` (2005).

17. Gärditz, C., Mückl, A. G. & Cölle, M. Influence of an external magnetic field on the singlet and triplet emissions of tris- (8- hydroxyquinoline) aluminum (III) (Alq3). *J. Appl. Phys.* **98,** 1–5 (2005).

18. Sheng, Y. *et al.* Hyperfine interaction and magnetoresistance in organic semiconductors. *Phys. Rev. B* **74.** ISSN: 10980121. arXiv: `0602282 [cond-mat]` (2006).

19. Prigodin, V. N., Bergeson, J. D., Lincoln, D. M. & Epstein, A. J. Anomalous room temperature magnetoresistance in organic semiconductors. *Synth. Met.* **156,** 757–761. ISSN: 03796779 (2006).

20. Desai, P. *et al.* Magnetoresistance and efficiency measurements of Alq3 -based OLEDs. *Phys. Rev. B* **75,** 1–5. ISSN: 10980121 (2007).

21. Hu, B. & Wu, Y. Tuning magnetoresistance between positive and negative values in organicsemiconductors. *Nat. Mater.* **6,** 985–991. ISSN: 14764660 (2007).

22. Bobbert, P. A., Nguyen, T. D., Van Oost, F. W., Koopmans, B. & Wohlgenannt, M. Bipolaron mechanism for organic magnetoresistance. *Phys. Rev. Lett.* **99,** 1–4. ISSN: 00319007 (2007).

23. Baldo, M., Adachi, C. & Forrest, S. R. Transient analysis of organic electrophosphorescence.II. Transient analysis of triplet-triplet annihilation. *Phys. Rev. B* **62,** 10967–10977. ISSN: 1098-0121. s:%7B%5C%%7D5CAG%7B%5C_%7DLemmer%7B%5C%%7D5CForschungsprojekte%7B%5C%%7D5Corganische%7B%5C%%7D5CnBauelemente%7B%5C%%7D5Corganische%7B%5C%%7D5CnLaser%7B%5C%%7D5CoLAS%7B%5C%%7D5Cpapers%7B%5C%%7D5CBaldo%7B%5C_%7DPhys%7B%5C_%7DRev%7B%5C_%7DB%7B%5C_%7D2000.pdf (2000).

24. Ern, V. & Merrifield, R. E. Magnetic field effect on triplet exciton quenching in organic crystals. *Phys. Rev. Lett.* **21,** 609–611. ISSN: 00319007. arXiv: arXiv:1011.1669v3 (1968).

25. K. Fesser; A.R.Bishop; D.K.Campbell. Optical absorption from polarons in a model of polyacetylene. *Phys. Rev. B* **27,** 4804–4825 (1983).

26. Bässler, H. Injection , Transport and Recombination of Charge Carriers in Organic Light-emitting Diodes. *Polym. Adv. Technol.* **418,** 402–418 (1998).

27. Kalinowski, J., Szmytkowski, J. & Stampor, W. Magnetic hyperfine modulation of charge photogeneration in solid films of Alq3. *Chem. Phys. Lett.* **378,** 380–387. ISSN: 00092614 (2003).

28. Wilkinson, J., Davis, A. H., Bussmann, K. & Long, J. P. Evidence for charge-carrier mediated magnetic-field modulation of electroluminescence in organic light-emitting diodes. *Appl. Phys. Lett.* **86,** 1–4 (2005).

29. Köhlerl, A. *et al.* UV photocurrent spectroscopy in poly(p-phenylene vinylene) and derivatives. *Synth. Met.* **84,** 675–676 (1997).

30. Müller, J. G., Lupton, J. M. & Feldmann, J. Ultrafast dynamics of charge carrier photogeneration and geminate recombination in conjugated polymer : fullerene solar cells. *Phys. Rev. B* **72,** 1–10 (2005).

31. Szmytkowski, J., Stampor, W., Kalinowski, J. & Kafafi, Z. H. Electric field-assisted dissociation of singlet excitons in tris-(8-hydroxyquinolinato)aluminum (III). *Appl. Phys. Lett.* **1465,** 1–4 (2002).

32. Kalinowski, J. *et al.* Coexistence of dissociation and annihilation of excitons on charge carriers in organic phosphorescent emitters. *Phys. Rev. B* **74,** 1–11 (2006).

33. Wittmer, M. & Zschokke-Gränacher, I. Exciton-charge carrier interactions in the electroluminescence of crystalline anthracene. *J. Chem. Phys.* **63,** 4187–4194 (1975).

34. Tolstov, I. V. *et al.* On the role of magnetic field spin effect in photoconductivity of composite films of MEH-PPV and nanosized particles of PbS. *J. Lumin.* **112,** 368–371 (2005).

35. Kalinowski, J. & Signerski, R. Exciton-enhanced double injection currents in tetracene crystals. *Phys. Stat. Sol. (B)* **147,** 13–16 (1983).

36. Kalinowski, J., Szmytkowski, J. & Stampor, W. Magnetic hyperfine modulation of charge photogeneration in solid films of Alq3. *Chem. Phys. Lett.* **378,** 380–387 (2003).

37. Wohlgenannt, M. & Vardeny, Z. V. Spin-dependent exciton formation rates in π-conjugated materials. *J. Phys.: Condens. Matter* **15,** 83–107 (2003).

38. Levinson, J., Weisz, S. Z., Cobas, A. & Rolón, A. Determination of the Triplet Exciton-Trapped Electron Interaction Rate Constant in Anthracene Crystals. *J. Chem. Phys* **52,** 2794–2795 (1970).

39. W. Helfrich. Destruction of triplet excitons in anthracene by injected electrons. *Phys. Rev. Lett.* **16,** 401–403 (1966).

40. Xu, Z., Wu, Y. & Hu, B. Dissociation processes of singlet and triplet excitons in organic photovoltaic cells. *Appl. Phys. Lett.* **89,** 1–4 (2006).

41. Kalinowski, J. Electroluminescence in organics. *J. Phys. D: Appl. Phys.* **179,** 179–244 (1999).

42. Bussas, M. & Zuppiroli, L. Bipolaron singlet and triplet states in disordered conducting polymers. *Phys. Rev. B* **47,** 5493–5496 (1993).

43. Chauvet, O., Sienkiewicz, A., Forro, L. & Zuppiroli, L. High-pressure electron-spin dynamics in disordered conducting polymers. *Phys. Rev. B* **52,** 118–121 (1995).

44. Brocklehurst, B. Spin correlation in the geminate recombination of radical ions in hydrocarbons. *J. Chem. Soc. Faraday Trans II* **72,** 1869–1884. ISSN: 0300-9238 (1976).

45. Werner, H. J., Schulten, Z. & Schulten, K. Theory of the magnetic field modulated geminate recombination of radical ion pairs in polar solvents: Application to the pyrene-N, N-dimethylaniline system. *J. Chem. Phys.* **67,** 646–663. http://jcp.aip.org/resource/1/jcpsa6/v67/i2/p646%7B%5C_%7Ds1?isAuthorized=no (1977).

46. Tang, J. & Norris, J. R. Theoretical calculations of kinetics of the radical pair PF state in bacterial photosynthesis. *Chem. Phys. Lett.* **92,** 136–140. ISSN: 00092614 (1982).

47. Brocklehurst, B. Free radical m echanism for the effects of environmental electromagnetic fields on biological systems. *Int. J. Radiat. Biol.* **69,** 3–24 (1996).

48. Timmel, C. R., Till, U., Brocklehurst, B., McLauchlan, K. A. & Hore, P. J. Effects of weak magnetic fields on free radical recombination reactions. *Mol. Phys.* **95,** 71–89. ISSN: 13623028 (1998).

49. Rodgers, C. T. & Hore, P. J. Chemical magnetoreception in birds: The radical pair mechanism. *PNAS* **106,** 353–360. ISSN: 0027-8424. http://www.pnas.org/cgi/doi/10.1073/pnas.0711968106 (2009).

50. Hore, P. J. & Mouritsen, H. The Radical-Pair Mechanism of Magnetoreception. *Annu. Rev. Biophys.* **45,** 299–344. ISSN: 1936-122X. http://www.annualreviews.org/doi/10.1146/annurev-biophys-032116-094545 (2016).

51. Wang, F. J., Bässler, H. & Vardeny, Z. V. Magnetic field effects in π-conjugated polymer-fullerene blends: Evidence for multiple components. *Phys. Rev. Lett.* **101,** 1–4. ISSN: 00319007 (2008).

52. Nguyen, T. D. *et al.* Isotope effect in spin response of π-conjugated polymer films and devices. *Nat. Mater.* **9,** 345–352. ISSN: 14764660 (2010).

53. Nguyen, T. D., Gautam, B. R., Ehrenfreund, E. & Vardeny, Z. V. Magnetoconductance response in unipolar and bipolar organic diodes at ultrasmall fields. *Phys. Rev. Lett.* **105,** 1–4. ISSN: 00319007 (2010).

54. Nguyen, T. D., Gautam, B. R., Ehrenfreund, E. & Vardeny, Z. V. Magnetoconductance of π-conjugated polymer based unipolar and bipolar diodes. *Synth. Met.* **161,** 604–607. ISSN: 03796779. http://dx.doi.org/10.1016/j.synthmet.2010.11.051 (2011).

55. Nguyen, T. D. *et al.* Isotope effect in the spin response of aluminum tris(8-hydroxyquinoline) based devices. *Phys. Rev. B* **85,** 1–7. ISSN: 10980121 (2012).

56. Gautam, B. R., Nguyen, T. D., Ehrenfreund, E. & Vardeny, Z. V. Magnetic field effect on excited-state spectroscopies of pi-conjugated polymer films. *Phys. Rev. B* **85,** 205207. ISSN: 1098-0121. https://link.aps.org/doi/10.1103/PhysRevB.85.205207 (2012).

57. Ehrenfreund, E. & Vardeny, Z. V. Effects of magnetic field on conductance and electroluminescence in organic devices. *Isr. J. Chem* **52,** 552–562. ISSN: 00212148 (2012).

58. Nguyen, T. D., Ehrenfreund, E. & Vardeny, Z. V. Organic magneto-resistance at small magnetic fields; compass effect. *Org. Electron.* **14,** 1852–1855. ISSN: 15661199. http://dx.doi.org/10.1016/j.orgel.2013.04.031 (2013).

59. Zhang, Q. *et al.* Modulating the competition between dissociation and spin mixing in electron-hole pairs: An investigation of ultra-small field induced magnetoconductance responses in blended devices. *Org. Electron.* **14,** 2875–2879. ISSN: 15661199. http://dx.doi.org/10.1016/j.orgel.2013.08.011 (2013).

60. Janssen, P. *et al.* Tuning organic magnetoresistance in polymer-fullerene blends by controlling spin reaction pathways. *Nat. Commun.* **4,** 1–8. ISSN: 20411723. arXiv: 9809069v1 [arXiv:gr-qc]. http://dx.doi.org/10.1038/ncomms3286 (2013).

61. Janssen, P., Wouters, S. H., Cox, M. & Koopmans, B. The influence of the triplet exciton and charge transfer state energy alignment on organic magnetoresistance. *Org. Electron.* **15,** 743–750. ISSN: 15661199. http://dx.doi.org/10.1016/j.orgel.2014.01.010 (2014).

62. Klemm, P., Bange, S., Pöllmann, A., Boehme, C. & Lupton, J. M. Nanotesla magnetoresistance in π-conjugated polymer devices. *Phys. Rev. B* **95,** 1–6. ISSN: 24699969 (2017).

63. Lawrence, J. E., Lewis, A. M., Manolopoulos, D. E. & Hore, P. J. Magnetoelectroluminescence in organic light-emitting diodes. *J. Chem. Phys.* **144,** 1–10 (2016).

64. Wu, C. C., Wu, C. I., Sturm, J. & Kahn, A. Surface modification of indium tin oxide by plasma treatment : An effective method to improve the efficiency , brightness , and reliability of organic light emitting devices. *Appl. Phys. Lett.* **70,** 3–6 (2000).

65. Chen, S.-h. Work-function changes of treated indium- tin-oxide films for organic light-emitting diodes investigated using scanning surface-potential microscopy. *J. Appl. Phys.* **073713,** 1–4 (2005).

66. Huang, W., Mi, B. & Gao, Z. *Organic Electronics* 301–302 (2010).

67. DeTroye, D. J. & Chase, R. J. *The Calculation and Measurement of Helmholtz Coil Fields* tech. rep. (1994), 1–22.

68. Johansson, T., Jensen, P. & Krag, C. *Helmholtz coils for characterization of magentic sensors* PhD thesis (Technical University of Denmark, 2003), 1–61.

69. Shakya, P. *et al.* The magnetic field effect on the transport and efficiency of group III tris(8-hydroxyquinoline) organic light emitting diodes. *J. Appl. Phys.* **103.** ISSN: 00218979 (2008).

70. Gu, H. *et al.* Annealing and doping-dependent magnetoresistance in single layer poly(3-hexyl-thiophene) organic semiconductor device. *Org. Electron.* **17,** 51–56. ISSN: 15661199. http://dx.doi.org/10.1016/j.orgel.2014.11.019 (2015).

71. Hayashi, H. *Introduction to Dynamic Spin Chemistry* 239–244. ISBN: 978-981-238-423-2. http://www.worldscientific.com/worldscibooks/10.1142/5316 (World Scientific Publishing Co. Pte. Ltd., 2004).

72. Konowalczyk, M. *https://uk.mathworks.com/matlabcentral/fileexchange/64703-liouville-von-neumann- simulation-by-density-matrix-propagation* 2017. https://uk.mathworks.com/matlabcentral/fileexchange/64703-liouville-von-neumann-%20simulation-by-density-matrix-propagation.

73. Schellekens, A. J., Wagemans, W., Kersten, S. P., Bobbert, P. A. & Koopmans, B. Microscopic modeling of magnetic-field effects on charge transport in organic semiconductors. *Phys. Rev. B* **84,** 075204. ISSN: 1098-0121. https://link.aps.org/doi/10.1103/PhysRevB.84.075204 (2011).

74. Reichert, T. & Saragi, T. P. Ultrasmall magnetic field-effect and sign reversal in transistors based on donor/acceptor systems. *Beilstein J. Nanotechnol.* **8,** 1104–1114. ISSN: 21904286 (2017).

75. Son, D., Marumoto, K., Kizuka, T. & Shimoi, Y. Electron spin resonance of thin films of organic light-emitting material tris (8-hydroxyquinoline) aluminum doped by magnesium. *Synth. Met.* **162,** 2451–2454. ISSN: 0379-6779. http://dx.doi.org/10.1016/j.synthmet.2012.11.009 (2012).

76. Gao, H., Zhang, H., Zhang, H., Gen, Y. & Su, Z.-m. Theoretical Study of Isomerism / Phase Dependent Charge Transport Properties in Tris (8-hydroxyquinolinato) aluminum (III). *J. Phys. Chem. A* **115,** 9259–9264 (2011).

77. Demasi, A. *et al.* Electronic structure of the organic semiconductor Alq 3 (aluminum tris-8-hydroxyquinoline) from soft x-ray spectroscopies and density functional theory calculations. *J. Chem. Phys.* **129,** 1–7 (2008).

78. Drew, A. J. *et al.* Intrinsic mobility limit for anisotropic electron transport in Alq3. *Phys. Rev. Lett.* **100,** 1–4. ISSN: 00319007 (2008).

79. Singh, J., Narayan, M. & Ompong, D. Comparative contributions of singlet and triplet excitons in the performance of organic devices. *Phys. Stat. Sol. (C)* **13,** 77–80. ISSN: 16101642 (2016).

80. Ratzke, W., Bange, S. & Lupton, J. M. Direct Detection of Singlet-Triplet Interconversion in OLED Magnetoelectroluminescence with a Metal-Free Fluorescence-Phosphorescence Dual Emitter. *Phys. Rev. Applied* **9,** 54038. ISSN: 23317019. https://doi.org/10.1103/PhysRevApplied.9.054038 (2018).

81. Kwak, K., Cho, K. & Kim, S. Analysis of thermal degradation of organic light-emitting diodes with infrared imaging and impedance spectroscopy. *Opt. Express* **21,** 29558. ISSN: 1094-4087. https://www.osapublishing.org/oe/abstract.cfm?uri=oe-21-24-29558 (2013).

82. Lee, Y. J. *et al.* Study of thermal degradation of organic light emitting device structures by X-ray scattering. *Thin Solid Films* **515,** 5674–5677. ISSN: 00406090 (2007).

83. Gahungu, G. & Zhang, J. " CH "/ N Substituted mer -Gaq3 and mer -Alq3 Derivatives : An Effective Approach for the Tuning of Emitting Color. *J. Phys. Chem. B* **109,** 17762–17767 (2005).

84. Anderson, S., Weaver, M. S. & Hudson, A. J. Materials for organic electroluminescence : aluminium vs . boron. *Synth. Met.* **111-112,** 459–463 (2000).

85. Han, Y.-k. & Lee, S. U. Molecular orbital study on the ground and excited states of methyl substituted tris (8-hydroxyquinoline) aluminum (III). *Chem. Phys. Lett.* **366,** 9–16 (2002).

86. Laxmikanth, R. J. & Bhanuprakash, K. Structure and electronic properties of tris(4-hydroxy-1,5-naphthyridinato) aluminum (AIND3) and its methyl derivatives: a theoretical study. *Theor. Chem. Acc.* **129,** 131–139 (2011).

87. Rodgers, C. T., Henbest, K. B., Kukura, P., Timmel, C. R. & Hore, P. J. Low-field optically detected EPR spectroscopy of transient photoinduced radical pairs. *J. Phys. Chem. A* **109,** 5035–5041. ISSN: 10895639 (2005).

88. McCamey, D. R. *et al.* Hyperfine-Field-Mediated Spin Beating in Electrostatically Bound Charge Carrier Pairs. *Phys. Rev. Lett.* **104,** 1–4 (2010).